

Analysis of the unusually cold Arctic winter 2015/16 lowermost stratosphere by airborne and satellite observations and atmospheric models

Zur Erlangung des akademischen Grades eines
DOKTORS DER NATURWISSENSCHAFTEN (Dr. rer. nat.)
von der KIT-Fakultät für Physik des
Karlsruher Instituts für Technologie (KIT)

angenommene

DISSERTATION

von

M. Sc. Sören Johansson
geboren am 21.08.1989 in Erfurt

Tag der mündlichen Prüfung: 18. Januar 2019
Referent: PD Dr. Michael Höpfner
Korreferent: Prof. Dr. Johannes Orphal
Dekan: Prof. Dr. Georg Weiß

Sofern nicht anders angegeben, ist dieses Werk lizenziert unter einer Creative Commons Namensnennung 4.0 International Lizenz.

Except where otherwise noted, this work is licensed under a Creative Commons Attribution 4.0 International License.



Abstract

This thesis presents a comprehensive view of the temporal evolution of trace gases relevant for chlorine chemistry in the lowermost stratosphere (**LMS**) over the course of the Arctic winter 2015/16. This particular winter was characterized by unusually cold stratospheric temperatures. Two-dimensional vertical cross sections of trace gases, measured by the airborne limb-imager **GLORIA** (Gimballed Limb Observer for Radiance Imaging of the Atmosphere) during the so-called **PGS**¹ campaign, are utilized to investigate in detail the upper troposphere lower stratosphere (**UTLS**).

GLORIA was operated on board the German High Altitude and Long range research aircraft (**HALO**) during the **PGS** aircraft campaign. Research flights were conducted from 17 December 2015 until 18 March 2016 within 25–87° N and 80° W–30° E. During 15 scientific flights, the **GLORIA** instrument measured more than 15 000 atmospheric profiles at high spectral resolution. From these measurements, two-dimensional cross sections of temperature, nitric acid (**HNO₃**), ozone (**O₃**), chlorine nitrate (**ClONO₂**), water vapor (**H₂O**), and dichlorodifluoromethane (**CFC-12**) were retrieved. Dependent on flight altitude and tropospheric cloud cover, the vertical range of profiles retrieved from the measurements was typically between 5 and 14 km. A vertical resolution between 400 and 1000 m was achieved. The profiles were validated at flight altitude by simultaneous in situ measurements. Comparisons with the spatially lower resolved Microwave Limb Sounder (**MLS**) satellite instrument show highly consistent structures.

Three long-distance flights in January, February and March 2016 are discussed in detail regarding horizontal and vertical structures of **O₃**, **ClONO₂**, and **HNO₃**, which show a large horizontal and vertical variability. **ClONO₂** volume mixing ratios up to 1100 pptv were measured at 380 K potential temperature in mesoscale structures. Similar mesoscale structures are also visible in **GLORIA O₃** and **HNO₃** cross sections.

Satellite measurements from **MLS** and **ACE-FTS** (Atmospheric Chemistry Experiment – Fourier Transform Spectrometer) provide an overview over the whole winter and information about the stratospheric situation above flight altitude. Time series of these satellite measurements reveal unusually low abundances of hydrogen chloride (**HCl**) and **ClONO₂** inside the polar vortex at 380 K from the beginning of January to the end of February 2016, while strongly enhanced chlorine monoxide (**ClO**) is observed. In March 2016, unusually rapid chlorine deactivation into **HCl** is observed instead of deactivation into **ClONO₂**, the more typical pathway for chlorine deactivation in the Arctic.

¹POLSTRACC / GW-LCYCLE II / GWEX / SALSA

The measurements are applied to evaluate simulation results from the chemistry transport model **CLaMS** (Chemical Lagrangian Model of the Stratosphere) and the chemistry climate model **EMAC** (ECHAM/MESSy Atmospheric Chemistry). The comparisons show agreement within the expected performance of these models. Because of the more detailed agreement between **GLORIA** measurements and **CLaMS** simulations, only this model is used for further analyses. Chlorine deactivation observed in the satellite time series is well reproduced by **CLaMS**, therefore this model is used for sensitivity studies regarding the influence of low abundances of O_3 and reactive nitrogen (NO_y). The availability of O_3 is reduced by ozone depletion, and NO_y is reduced by sedimentation. On the basis of the different altitude and time ranges of these effects, this thesis concludes that the substantial chlorine deactivation into **HCl** at 380 K arose as a result of very low ozone abundances together with low temperatures. **CLaMS** estimates ozone depletion of at least 0.4 ppmv at 380 K and 1.75 ppmv at 490 K. A “Match-based” analysis of **MLS** O_3 measurements estimates chemical ozone loss with 0.8 ppmv at 375 K and 1.7 ppmv at 475 K. Differences are contributed to underestimation of downwelling in the model.

CLaMS trajectories are used to analyze the history of enhanced **ClONO₂** measured by **GLORIA**. In February 2016, most of the enhanced **ClONO₂** is traced back to chlorine deactivation that had occurred within the past five days prior to the **GLORIA** measurement. In March, after the final warming, air masses, in which chlorine has previously been deactivated into **ClONO₂**, have been transported within the remnants of polar vortex air towards the location of measurement for at least 11 days.

This thesis presents a study based on aircraft and satellite measurements, which demonstrate unusual Arctic chlorine deactivation due to low ozone abundances. Atmospheric models are evaluated, and measured **ClONO₂** is linked to transport and in situ deactivation in the **LMS**.

Zusammenfassung

In dieser Dissertation wird der zeitliche Verlauf der für die stratosphärische Chlorchemie relevanten Spurengase in der untersten Stratosphäre (lowermost stratosphere, **LMS**) während des arktischen Winters 2015/16 umfassend dargestellt und analysiert. Dieser Winter zeichnete sich durch außergewöhnlich niedrige stratosphärische Temperaturen aus. Horizontal und vertikal aufgelöste Spurengasmessungen des flugzeuggebundenen abbildenden Horizontsondierers **GLORIA** (Gimballed Limb Observer for Radiance Imaging of the Atmosphere) von der sogenannten **PGS²**-Messkampagne wurden für eine detaillierte Analyse der oberen Troposphäre und unteren Stratosphäre (**UTLS**) verwendet.

GLORIA wurde während dieser **PGS**-Messkampagne auf dem deutschen Forschungsflugzeug **HALO** (High Altitude and Long range research aircraft) verwendet. Die wissenschaftlichen Flüge fanden zwischen dem 17. Dezember 2015 und dem 18. März 2016 statt und erstreckten sich über eine Region von 25–87° N und 80° W–30° O. Auf 15 wissenschaftlichen Flügen hat das **GLORIA**-Messinstrument mehr als 15 000 atmosphärische Profile in hoher spektraler Auflösung gemessen. Von diesen Messungen wurden zweidimensionale Verteilungen von Temperatur und den Spurengasen Salpetersäure (**HNO₃**), Ozon (**O₃**), Chlornitrat (**ClONO₂**), Wasserdampf (**H₂O**) und Dichlordifluormethan (**CFC-12**) abgeleitet. Abhängig von der Flughöhe und der troposphärischen Wolkenoberkante reichen die Temperatur- und Spurengasprofile von 5 bis 14 km Höhe. Die vertikale Auflösung dieser Profile beträgt zwischen 400 und 1000 m. Die Profile wurden auf Flughöhe mit simultan gemessenen *in situ*-Messungen validiert. Vergleiche mit den räumlich geringer aufgelösten Satellitenmessungen des Microwave Limb Sounder (**MLS**) zeigen übereinstimmende Strukturen.

Drei Messflüge im Januar, Februar und März 2016 werden bezüglich horizontaler und vertikaler Strukturen von **O₃**, **ClONO₂** und **HNO₃** detailliert analysiert. Diese Gase zeigen eine starke horizontale und vertikale Variabilität. **ClONO₂**-Volumenmischungsverhältnisse von bis zu 1100 pptv wurden in feinen atmosphärischen Strukturen auf einer Höhe von 380 K potentieller Temperatur gemessen. Ähnliche feine Strukturen sind in **O₃**- und **HNO₃**-Messungen von **GLORIA** zu erkennen.

Satellitenmessungen von **MLS** und **ACE-FTS** (Atmospheric Chemistry Experiment – Fourier Transform Spectrometer) bieten einen Überblick über den gesamten arktischen Winter sowie über die Zusammensetzung der Stratosphäre oberhalb der **HALO**-Flughöhe. Zeitreihen dieser Satellitenmessungen zeigen im Zeitraum von Januar bis

²POLSTRACC / GW-LCYCLE II / GWEX / SALSA

Februar 2016 ungewöhnlich niedrige Vorkommen von Salzsäure (HCl) und ClONO_2 auf einer Höhe von 380 K potentieller Temperatur, während Chlormonoxid (ClO) deutlich erhöht war. Im März 2016 wurde aktives Chlor außergewöhnlich schnell in HCl deaktiviert, anstelle der für die Arktis üblichen Deaktivierung in ClONO_2 .

Die Messungen werden verwendet, um das Chemietransportmodell CLaMS (Chemical Lagrangian Model of the Stratosphere) sowie das Chemie-Klima-Modell EMAC (ECHAM/MESSy Atmospheric Chemistry) zu überprüfen. Die Übereinstimmungen mit den Messungen entsprechen den Erwartungen für das jeweilige Modell. Weil der Vergleich zwischen GLORIA und CLaMS detaillierter Übereinstimmungen zeigt, wird nur dieses Modell für die weiteren Analysen verwendet. Die von den Zeitreihen aus Satellitendaten beobachtete Chlordeaktivierung wird durch CLaMS besonders gut wiedergegeben, so dass dieses Modell verwendet werden konnte, um Sensitivitätsstudien bezüglich des Einflusses von geringer Verfügbarkeit von O_3 sowie reaktivem Stickstoff (NO_y) durchzuführen. Die Verfügbarkeit von O_3 wird durch Ozonabbau reduziert, die Verfügbarkeit von NO_y durch Sedimentierung eingeschränkt. Aufgrund der unterschiedlichen Zeit- und Höhenbereiche, in denen diese Effekte wirken, lässt sich schließen, dass die erhebliche Deaktivierung in HCl auf einer Höhe von 380 K potentieller Temperatur mit der geringen Verfügbarkeit von O_3 sowie niedrigen Temperaturen zusammenhängt. Mit Hilfe von CLaMS wurde der chemische Ozonverlust für den arktischen Winter 2015/16 auf 0.4 ppmv auf 380 K und 1.75 ppmv auf 490 K potentieller Temperatur abgeschätzt. Eine Analyse von Ozonmessungen mit MLS dagegen schätzt den Ozonverlust auf 0.8 ppmv auf 375 K und 1.7 ppmv auf 475 K. Dieser Unterschied lässt sich damit erklären, dass das Absinken im Polarwirbel vom Modell unterschätzt wird.

Die chemische Zusammensetzung entlang Rückwärtstrajektorien von CLaMS zeigt für die GLORIA -Messungen, dass im Februar 2016 der Großteil der erhöhten ClONO_2 -Werte auf Chloraktivierung in der LMS während der vorangegangenen fünf Tage zurückzuführen ist. Im März 2016 dagegen wurden Luftmassen mit bereits erhöhten ClONO_2 -Werten aus Überresten des Polarwirbels länger als 11 Tage bis zum Messort transportiert.

Diese Dissertation zeigt durch Analyse der flugzeug- und satellitengebundenen Messungen, dass im Winter 2015/16 in der Arktis eine ungewöhnliche Chlordeaktivierung aufgrund der niedrigen Ozonkonzentrationen stattgefunden hat. Zwei atmosphärische Modelle wurden evaluiert, und das CLaMS -Modell wurde verwendet, um gemessene ClONO_2 -Konzentrationen auf Transport bzw. *in situ*-Deaktivierung in der LMS zurückzuführen.

List of Author's Publications

- Johansson, S.**, Woiwode, W., Höpfner, M., Friedl-Vallon, F., Kleinert, A., Kretschmer, E., Latzko, T., Orphal, J., Preusse, P., Ungermann, J., Santee, M. L., Jurkat-Witschas, T., Marsing, A., Voigt, C., Giez, A., Krämer, M., Rolf, C., Zahn, A., Engel, A., Sinnhuber, B.-M., and Oelhaf, H.: Airborne limb-imaging measurements of temperature, HNO₃, O₃, ClONO₂, H₂O and CFC-12 during the Arctic winter 2015/2016: Characterization, in situ validation and comparison to Aura/MLS, Atmospheric Measurement Techniques, 11, 4737–4756, doi:10.5194/amt-11-4737-2018, 2018.
- Johansson, S.**, Santee, M. L., Groß, J.-U., Höpfner, M., Braun, M., Friedl-Vallon, F., Khosrawi, F., Kirner, O., Kretschmer, E., Oelhaf, H., Orphal, J., Sinnhuber, B.-M., Ungermann, J., Walker, K. A., and Woiwode, W.: Unusual chlorine partitioning in the 2015/16 Arctic winter lowermost stratosphere: Observations and simulations, Atmospheric Chemistry and Physics Discussions, submitted, 2019.
- Clarmann, T. V. and **Johansson, S.**: Chlorine nitrate in the atmosphere, Atmospheric Chemistry and Physics, 18, 15 363–15 386, doi:10.5194/acp-18-15363-2018, 2018.
- Braun, M., Groß, J.-U., Woiwode, W., **Johansson, S.**, Höpfner, M., Friedl-Vallon, F., Oelhaf, H., Preusse, P., Ungermann, J., Sinnhuber, B.-M., Ziereis, H., and Braesicke, P.: Nitrification of the lowermost stratosphere during the exceptionally cold Arctic winter 2015/16: Manuscript in preparation, Atmospheric Chemistry and Physics Discussions, 2019.
- Khosrawi, F., Kirner, O., Sinnhuber, B.-M., **Johansson, S.**, Höpfner, M., Santee, M. L., Froidevaux, L., Ungermann, J., Ruhnke, R., Woiwode, W., Oelhaf, H., and Braesicke, P.: Denitrification, dehydration and ozone loss during the 2015/2016 Arctic winter, Atmospheric Chemistry and Physics, 17, 12 893–12 910, doi:10.5194/acp-17-12893-2017, 2017.
- Woiwode, W., Dörnbrack, A., Bramberger, M., Friedl-Vallon, F., Haenel, F., Höpfner, M., **Johansson, S.**, Kretschmer, E., Krisch, I., Latzko, T., Oelhaf, H., Orphal, J., Preusse, P., Sinnhuber, B.-M., and Ungermann, J.: Mesoscale fine structure of a tropopause fold over mountains, Atmospheric Chemistry and Physics, 18, 15 643–15 667, doi:10.5194/acp-18-15643-2018, 2018.

Contents

Abstract	iii
Zusammenfassung	v
List of Author's Publications	vii
1 Introduction	1
2 The polar UTLS: background and state of knowledge	3
2.1 Vertical structure and circulation	3
2.2 Stratospheric polar vortex	6
2.3 Trace gases and particles in the polar vortex	8
2.4 Stratospheric ozone layer	10
2.5 Polar chlorine chemistry	12
2.6 Interactions of climate change and ozone depletion	15
2.7 Observations	17
3 GLORIA airborne atmospheric limb emission measurements	19
3.1 Imaging Fourier Transform Spectrometer	19
3.2 GLORIA instrument overview	21
3.3 Infrared emission spectroscopy	24
3.4 Limb measurement geometry	27
3.5 Radiative transfer	28
3.6 Information retrieval theory	29
4 Data sets	35
4.1 PGS campaign	35
4.2 In situ instruments	36
4.3 Satellite observations	37
4.3.1 Aura/MLS	37
4.3.2 SCISAT/ACE-FTS	38
4.3.3 CALIPSO/CALIOP	39
4.4 Model simulations	39
4.4.1 CLaMS	39
4.4.2 EMAC	40
4.5 Meteorological data	40

5	Measurement characterization and validation	41
5.1	Meteorological situation for flight PGS19 on 13 March 2016	42
5.2	Characterization of example profiles	44
5.3	GLORIA results	46
5.3.1	Line of sight	46
5.3.2	Temperature	47
5.3.3	Nitric acid	48
5.3.4	Ozone	50
5.3.5	Chlorine nitrate	51
5.3.6	Water vapor	52
5.3.7	Chlorofluorocarbon 12	53
5.4	Overview of in situ comparisons for the PGS campaign	54
5.5	Vertical validation of temperature and O ₃ profiles	56
6	Chlorine partitioning and ozone loss in the LMS	59
6.1	Measurements and model evaluation	59
6.1.1	Time series	60
6.1.2	Comparison of satellite measurements to model simulations . . .	62
6.1.3	Aircraft measurements	66
6.1.4	Comparison of aircraft measurements to model simulations . . .	70
6.1.5	Correlations	74
6.2	Chemical ozone loss	76
6.3	CLaMS investigations of chemical evolution	79
6.3.1	Influence of ozone depletion and denitrification on chlorine deac- tivation	79
6.3.2	Temperature sensitivity	82
6.3.3	Origin of ClONO ₂ measured by GLORIA	84
7	Summary, conclusions and outlook	91
	List of Abbreviations	95
	List of Figures	99
	List of Tables	101
	Bibliography	103
	Acknowledgments	135

Chapter 1

Introduction

Trace gases only constitute a small fraction of the chemical composition of the Earth's atmosphere. However, they play a major role in the radiation budget and temperature on the Earth's surface and are therefore vital. Changes in ozone (O_3) influence the amount of ultraviolet (UV) radiation that reaches the surface, and it is well established that changes in greenhouse gases (GHGs), such as CO_2 , CH_4 , or tropospheric O_3 , have an impact on global tropospheric temperatures. In addition, the influence of ozone depletion on climate (in particular in the Antarctic) has been shown (e.g., Hartmann et al., 2000; Thompson and Solomon, 2002; Perlwitz et al., 2008; WMO, 2015). Swart et al. (2018) presented evidence that recent warming of the Southern Ocean is not only caused by GHG emissions, but also by ozone depletion. International treaties acknowledge the importance of an unharmed atmospheric composition: The Montreal protocol successfully regulated the emission of ozone depleting substances (ODS) to protect the stratospheric ozone layer (WMO, 1987), and the Paris agreement attempts to reduce the emissions of GHG globally (United Nations, 2015).

The upper troposphere lower stratosphere (UTLS) is vertically located approximately ± 5 km around the tropopause (Gettelman et al., 2011). Despite its relatively small fraction of the total atmosphere, it is important for the radiation budget due to minimum temperatures in the tropopause region (Forster and Shine, 1997). This importance is also reflected in the sensitivity of ground temperatures to changes in the UTLS. This strong influence on the total radiation budget is caused by steep gradients in O_3 and H_2O profiles, by mixing, and by a large variability in high altitude cloud formation (Riese et al., 2012, and references therein). In the UTLS region, O_3 is efficiently acting as a GHG and has an important influence on the radiation budget (Xia et al., 2017).

The polar part of the UTLS is also important regarding ozone depletion. While most of polar ozone depletion takes place in the ozone layer in the middle stratosphere, substantial chlorine activation and catalytic ozone depletion also occur in the lower-most stratosphere (LMS), which can be regarded as the stratospheric part of the UTLS (Lelieveld et al., 1999). In the Arctic LMS, chemical ozone loss is fostered for particular cold conditions, which allow for chlorine activation (von Hobe and Stroh, 2012, and references therein). Due to changes in temperature and dynamics in the UTLS, caused by climate change, enhanced chlorine activation and ozone depletion is expected (Dameris

and Baldwin, 2012). In this work, ozone depletion processes are observed and studied for the unusually cold Arctic winter 2015/16. The focus of this study is on the **UTLS** region, where increased **GHG** concentrations are expected to result in colder temperatures (Fels et al., 1980). Based on the important role of the polar **UTLS**, the following research questions are addressed in this thesis:

- How are ozone and trace gases, which are related to catalytic ozone depletion, distributed horizontally and vertically in the **UTLS** region over the course of the exceptionally cold Arctic winter 2015/16?
- What is the context of small-scale structures in trace gases, and how can this context be evaluated using satellite observations of related trace gases?
- To what extent are atmospheric models capable of reproducing these structures?
- How does O_3 loss of the Arctic winter 2015/16 compare to other Arctic winters?
- How much chlorine is activated and deactivated in the **LMS** and how much chlorine is transported in form of reservoir species from higher altitudes to the **LMS**?
- What are the primary reasons for changes in chlorine activation and deactivation during Arctic winters with colder temperatures in the **LMS**?

Despite its importance, observations are sparse for the **UTLS**. Current and previous spaceborne instruments only partially cover this region, and the vertical and horizontal resolution is rather coarse. This shortage in high spatial resolution is a result of rather aged instruments in orbit, which were built with technology available at their time. Airborne measurements with the Gimballed Limb Observer for Radiance Imaging of the Atmosphere (**GLORIA**) during the Arctic winter 2015/16 provide spatially highly resolved temperature and trace gas information. This new data set is characterized and validated in this thesis with a detailed discussion of the retrieval approach, error estimation, and vertical resolution. Furthermore, comparisons with satellite measurements, airborne in situ measurements and ozone sonde data are shown to establish this new data set for further scientific studies. These recent measurements are then used to evaluate two different approaches of atmospheric models and to examine the origin of small scale atmospheric structures in trace gases. Satellite measurements provide a broader context for these **GLORIA** measurements and emphasize that the Arctic winter 2015/16 was unusual regarding chlorine activation and chemical ozone loss.

This thesis starts with the theoretical background of polar winter **UTLS** processes and recent research in this field. Chapter 3 introduces the method of airborne atmospheric limb-emission spectroscopy, followed by a chapter describing the measurements and atmospheric models used in this thesis. The **GLORIA** data set for the 2015/16 campaign is described, characterized and validated in Chapter 5. These measurements are interpreted in the context of chlorine activation and deactivation together with satellite measurements and atmospheric model simulation results in the following chapter.

In parts of this thesis, text, tables and figures are taken from Johansson et al. (2018) and Johansson et al. (2019, licensed with CC BY 4.0). This material has been prepared by the author of this thesis. Relevant passages are not marked as direct quotations.

Chapter 2

The polar UTLS: background and state of knowledge

Measurements of extremely low total ozone column amounts (Chubachi et al., 1984; Farman et al., 1985) drew attention toward polar winter chemistry, which is relevant for ozone depletion. This chapter provides background information about the polar atmosphere and summarizes chlorine related processes significant for polar ozone depletion in a brief overview. For a detailed description and explanation of polar winter chemistry, textbooks (e.g. Brasseur and Solomon, 2005; Müller, 2012; Seinfeld and Pandis, 2016; Roedel and Wagner, 2017) and review articles (e.g. Solomon, 1999; von Clarmann, 2013; Solomon et al., 2015) are recommended.

2.1 Vertical structure and circulation

The vertical structure of the atmosphere is described by several altitude regimes, which are characterized by different temperature gradients. A typical temperature profile from ground up to 50 km is shown in Fig. 2.1. In the troposphere, temperatures are decreasing with altitude until the tropopause, whereas the stratosphere is characterized by increasing temperatures with increasing altitude. Troposphere and stratosphere also differ significantly in their chemical composition and relevant chemical reactions. Some gases are present in considerably higher concentrations in the troposphere (e.g., H₂O, N₂O, CH₃Cl, CCl₄, CFC-11, and CFC-12), while other gases have higher concentrations in the stratosphere (e.g., O₃, HNO₃, ClO, HCl, and ClONO₂). CO₂ shows similar volume mixing ratios (VMRs) over the whole altitude range presented.

For the vertical coordinate, different variables are presented: Besides absolute altitude, also pressure and potential temperature (θ) are used in this thesis. The relationship between these measures is illustrated in Fig. 2.1 as well.

This work focuses on the upper troposphere lower stratosphere (UTLS), which is the region around the tropopause. There are several definitions of the tropopause: The thermal tropopause (also called “WMO tropopause”) is defined as the altitude, which is

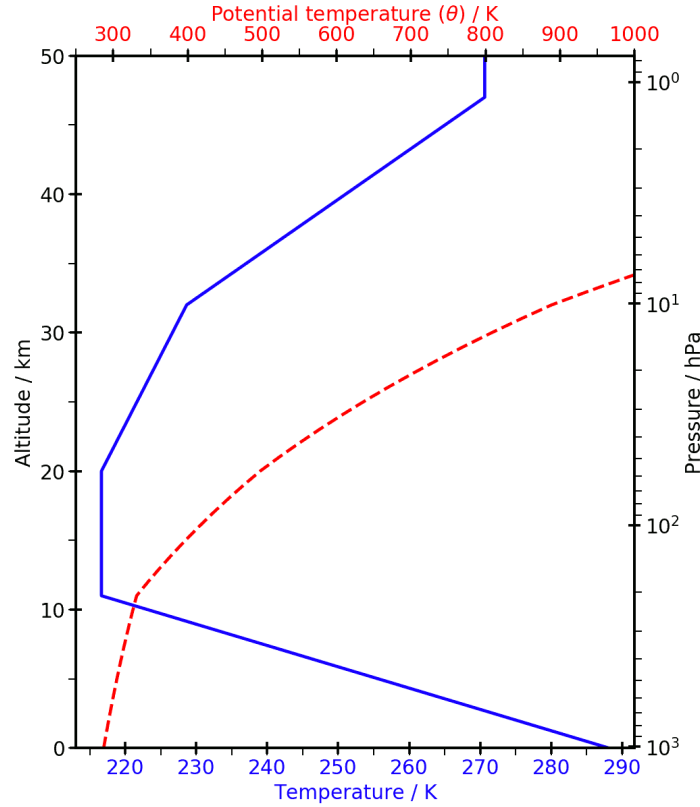


Figure 2.1: Temperature (blue) and potential temperature (θ , red) profile of the U.S. 1976 standard atmosphere (NOAA, 1976).

followed by altitudes with a temperature lapse rate decreasing to less than 2 K/km for at least 2 km (WMO, 1992). This altitude is visible slightly above 10 km in the exemplary temperature profile in Fig. 2.1. In addition, a dynamical tropopause is defined outside the tropics for a constant potential vorticity (PV) level of 2 potential vorticity units ($1 \text{ PVU} = 1 \cdot 10^{-6} \text{ K m}^2 \text{ kg}^{-1} \text{ s}^{-1}$). Inside the tropics, a cold point tropopause at the minimal temperature (which is difficult to define in the exemplary profile in Fig. 2.1) and a potential temperature tropopause at $\theta=380 \text{ K}$ are used. In this work, the dynamical tropopause is marked in several figures, because this tropopause is well defined in the polar UTLS. In contrast, the thermal tropopause is often not well defined, because of double tropopause occurrences.

The meridional stratospheric circulation is dominated by the Brewer Dobson circulation (BDC), which transports mass from the equator polewards (Brewer, 1949; Dobson, 1956). Fig. 2.2 shows the equator to winter pole transport of the deep and shallow branch of the BDC. The BDC is mainly driven by dissipating Rossby waves (Butchart, 2014, and references therein). Diffusive mixing processes, which may occur at different altitude regimes, are shown with wavy arrows. The zonal mass transport in the lower stratosphere is dominated by the Quasi-Biennial-Oscillation (Baldwin and Dunkerton, 2001) in the tropics, by the subtropical jets in the mid latitudes, and by strong westerly

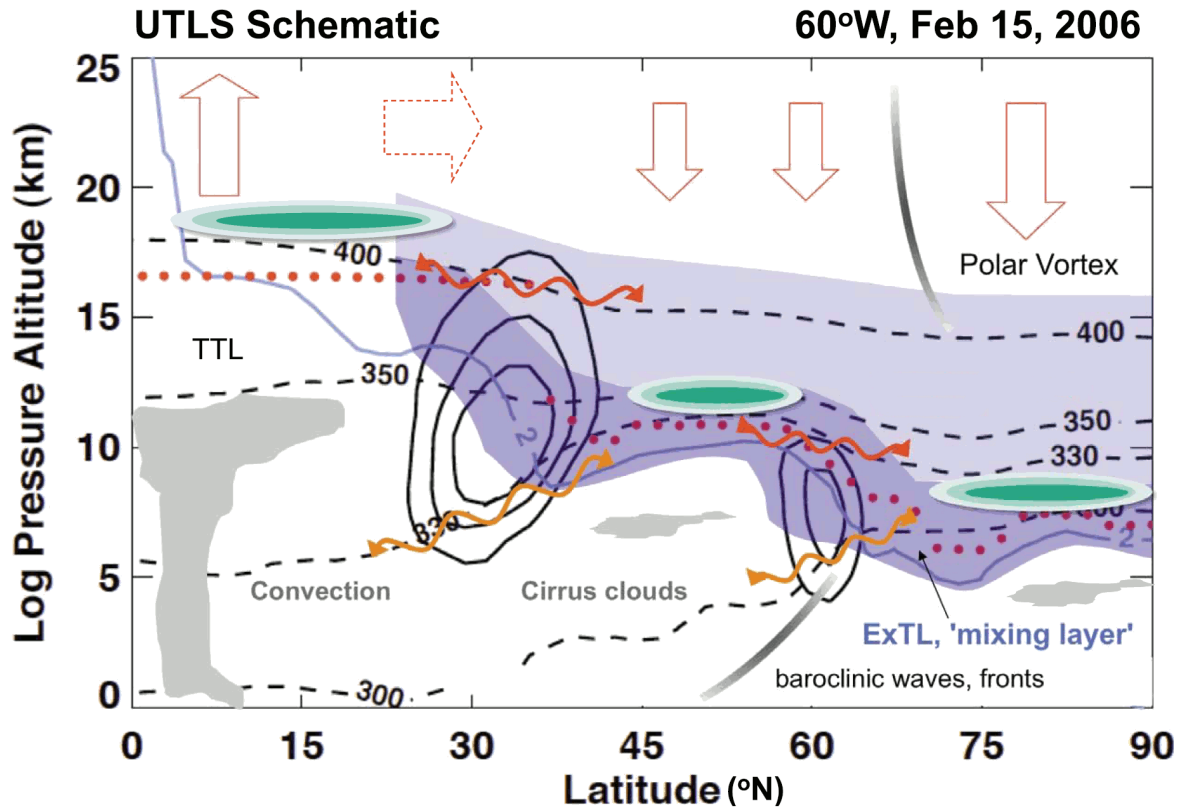


Figure 2.2: Schematic of the transport and mixing processes in the UTLS. Closed black solid lines show wind contours (subtropical jet at $\approx 30^\circ\text{N}$, polar jet at $\approx 60^\circ\text{N}$), dashed black lines show potential temperature surfaces, red dots mark the thermal tropopause, and the blue solid line shows the 2 PVU dynamical tropopause. Mixing barriers are marked as bold black lines with changing intensity (according to their permeability at different altitudes). Dark and light blue shadings show the extratropical UTLS, the dark blue shading the extratropical Transition Layer, and grey shadings show clouds and fronts. Green regions mark the position of tropopause inversion layers, red wavy arrows show quasi-isentropic exchange, and orange wavy arrows show cross-isentropic exchange. The Brewer-Dobson Circulation is indicated by large red arrows with the solid arrows for the deep branch and the dotted arrows for the shallow branch. Approved modified reprint from Gettelman et al. (2011, Figure 1, © John Wiley and Sons).

winds in the polar winter stratosphere (polar vortex).

Besides global circulations (e.g., **BDC**), exchange between troposphere and stratosphere is also fostered by small-scale processes, which influence the transport across the tropopause (Holton et al., 1995; Stohl et al., 2003; Bönisch et al., 2011; Konopka and Pan, 2012). These processes allow for mass transport between the troposphere with its usually fast transport (e.g., convection) and the stratosphere with slow transport timescales. The lowermost stratosphere (**LMS**), which is significantly different to the troposphere with respect to chemical composition and dynamical processes, is also different to the rest of the stratosphere by its accessibility for stratosphere-troposphere exchange (**STE**). This **STE** is in large parts conducted by mixing processes (Krause et al., 2018). Preferred regions for **STE** are tropopause folds (Shapiro, 1980; Woiwode et al., 2018).

2.2 Stratospheric polar vortex

The stratospheric polar vortex is a low pressure system, located poleward of, and above of the polar jet (see also Fig. 2.2). The surrounding winds of the polar vortex are also referenced as the polar night jet. It develops above the poles of both hemispheres during winter. Toward the end of autumn, zonal winds increase in intensity, and potential vorticity is raised in this region. This forms an area, which is characterized by cold temperatures, a transport barrier to air masses from lower latitudes, and well mixed air masses inside (Schoeberl and Hartmann, 1991; Schoeberl et al., 1992). Due to dynamical processes, stratospheric warmings can occur over the course of the winter. These warmings are disrupting the stability of the polar vortex. The winter polar vortex dissolves after the final stratospheric sudden warming (**SSW**, Matthewman et al., 2009). The temporal evolution of the polar vortex during the Arctic winter 2015/16 is shown in Fig. 2.3. The absolute number of **PV** increases with level of θ , but at all levels, a region of enhanced **PV** can be identified. At lower θ levels, this region has less defined borders. This lower level of confinement is also observed at all levels for 18 March 2016, which has been after the final stratospheric sudden warming (**SSW**).

During winter, air masses cool down and diabatic descent is observed (Schoeberl and Hartmann, 1991; Schoeberl et al., 1992). In addition, the wave-driven **BDC** results in a downwelling within the polar vortex over the course of the winter (Rosenfield et al., 1994; Butchart, 2014). Several techniques have been developed to define the border of the polar vortex using the strong horizontal gradient in **PV** (Nash et al., 1996; Manney et al., 2009). In the **LMS**, the lower boundary of the polar vortex (also called subvortex at this altitude) is difficult to define, and the transport barrier is not as strong as in the middle stratosphere (Gettelman et al., 2011; Lawrence et al., 2018). In this thesis, it was decided to use two vortex filters: The first method calculates the **PV** determining the edge of the polar vortex according to Nash et al. (1996). The polar vortex at 370 K θ is shown on maps in order to illustrate its position. The second method uses scaled potential vorticity (**sPV**), which is the **PV** divided by the factor $\partial\theta/\partial p$ (where p denotes the pressure), to exclude the altitude dependency from the **PV** (Dunkerton and Delisi,

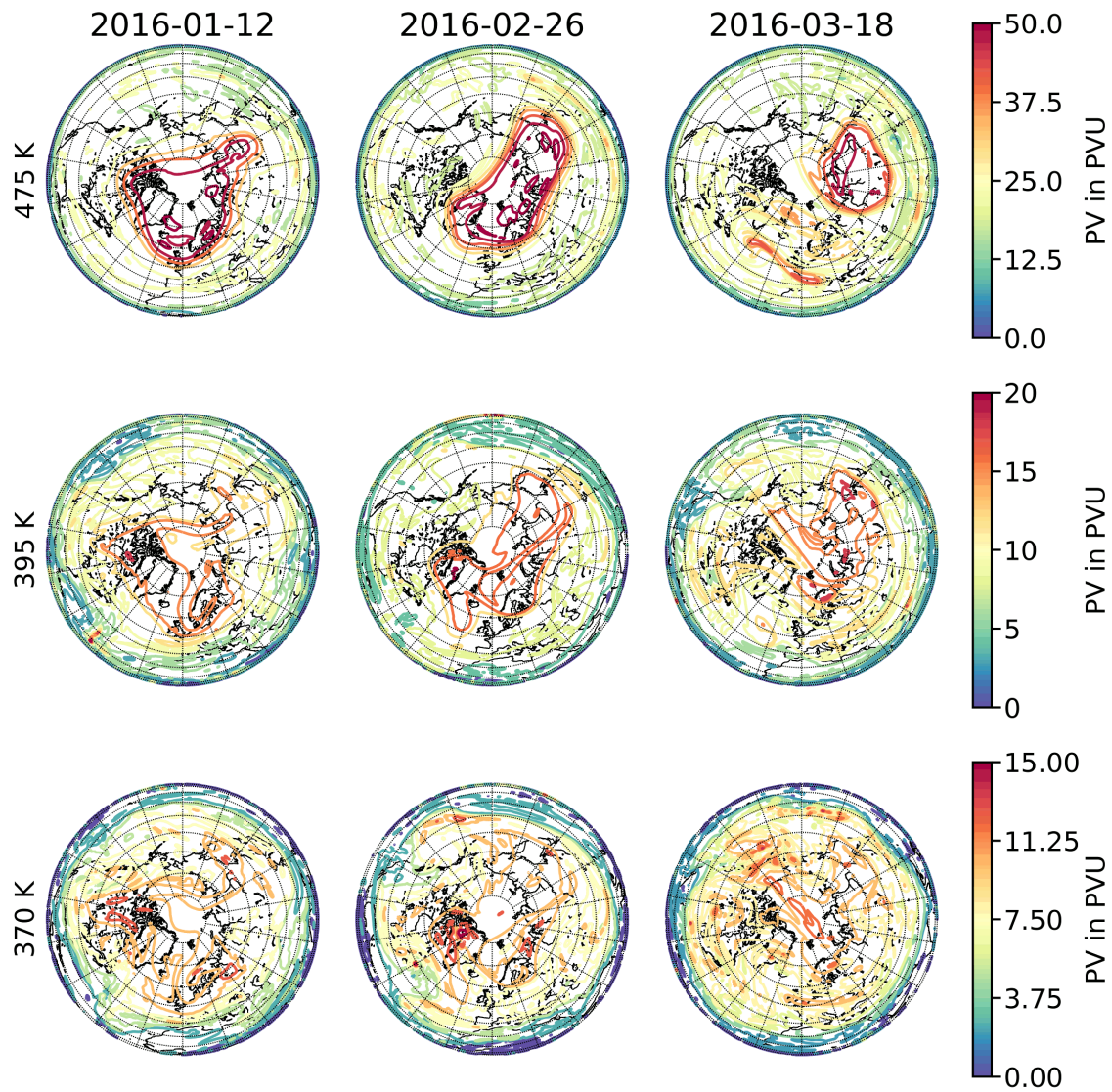


Figure 2.3: The polar vortex over the course of the Arctic winter 2015/16: Potential vorticity at different levels of potential temperature. Data from the NASA MERRA2 reanalysis.

1986; Manney et al., 1994). Measurements with a corresponding $\text{sPV} < 1.2 \cdot 10^{-4} \text{ s}^{-1}$ are considered to be outside the polar vortex.

A schematic of the dynamical situation of the polar vortex and the UTLS can be seen in the right part of Fig. 2.2: The polar vortex with its transport barrier and the downwelling as a consequence of the BDC are visible in the LMS (which is the polar part of the light blue region). Below the 400 K isentrope, the schematic shows that this subvortex region is influenced by many exchange and mixing processes, and that the transport barrier around this subvortex is not as strong as the transport barrier around the vortex in the stratosphere.

While polar vortices are present during wintertime in both hemispheres, there are differences in stability, temperature and duration. The Arctic vortex is typically warmer, less persistent, and exhibits the break-up on average one month earlier, compared to the Antarctic (Waugh and Randel, 1999). Also, the vortex is more volatile and less focused in its geographic position relative to the geographic pole. It is also more likely to split due to stratospheric warming events (Manney et al., 2009). Reasons for the less stable Arctic polar vortex are stronger planetary wave activity in the Northern hemisphere. Still, vortex splits are also reported for the Antarctic (Charlton et al., 2005).

The timing of the break-up date of the vortices has been monitored over several years. It shows a large variability, but no sign of a specific trend (WMO, 2015).

2.3 Trace gases and particles in the polar vortex

A climatological overview of Arctic winter trace gas profiles is shown in Fig. 2.4, together with a typical temperature profile. In this profile, the temperature decreases until the thermal tropopause at 10 km. In the stratosphere, the temperature does not increase as expected, and slightly decrease until 30 km. Tropospheric trace gases (such as, e.g., CFC-11, CFC-12, and CH_3Cl) show minor vertical variation in the troposphere and constantly decrease in the stratosphere, which makes them useful as tracers of stratospheric air masses. Stratospheric trace gases (such as, e.g., O_3 , HNO_3 , and ClONO_2) show low abundances in the troposphere and typically increase with altitude in the LMS. Many of these trace gases are involved in chemical reactions, which only occur during polar winter. Some of these processes are discussed in more detail in the following sections. For these processes, also solid particles are of particular importance. Besides the stratospheric aerosol layer (Junge et al., 1961), also polar stratospheric clouds (PSCs) are a source of particles inside the polar vortex.

PSCs are high altitude (usually 15 - 25 km) clouds, which consist of nitric acid trihydrate (NAT, type Ia, Voigt et al., 2000), supercooled ternary solution (STS) of sulfuric and nitric acid (type Ib, Tabazadeh et al., 1994a,b), or water ice (type II, Tabazadeh et al., 1997). They are formed at temperatures below about 195 K (NAT, Hanson and Mauersberger, 1988), 192 K (STS, Carslaw et al., 1995), and 188 K (ice, Murphy and Koop, 2005), respectively. Observation and classification of PSCs are performed by LIDAR (Browell et al., 1990; Pitts et al., 2018) and infrared limb emission measurements

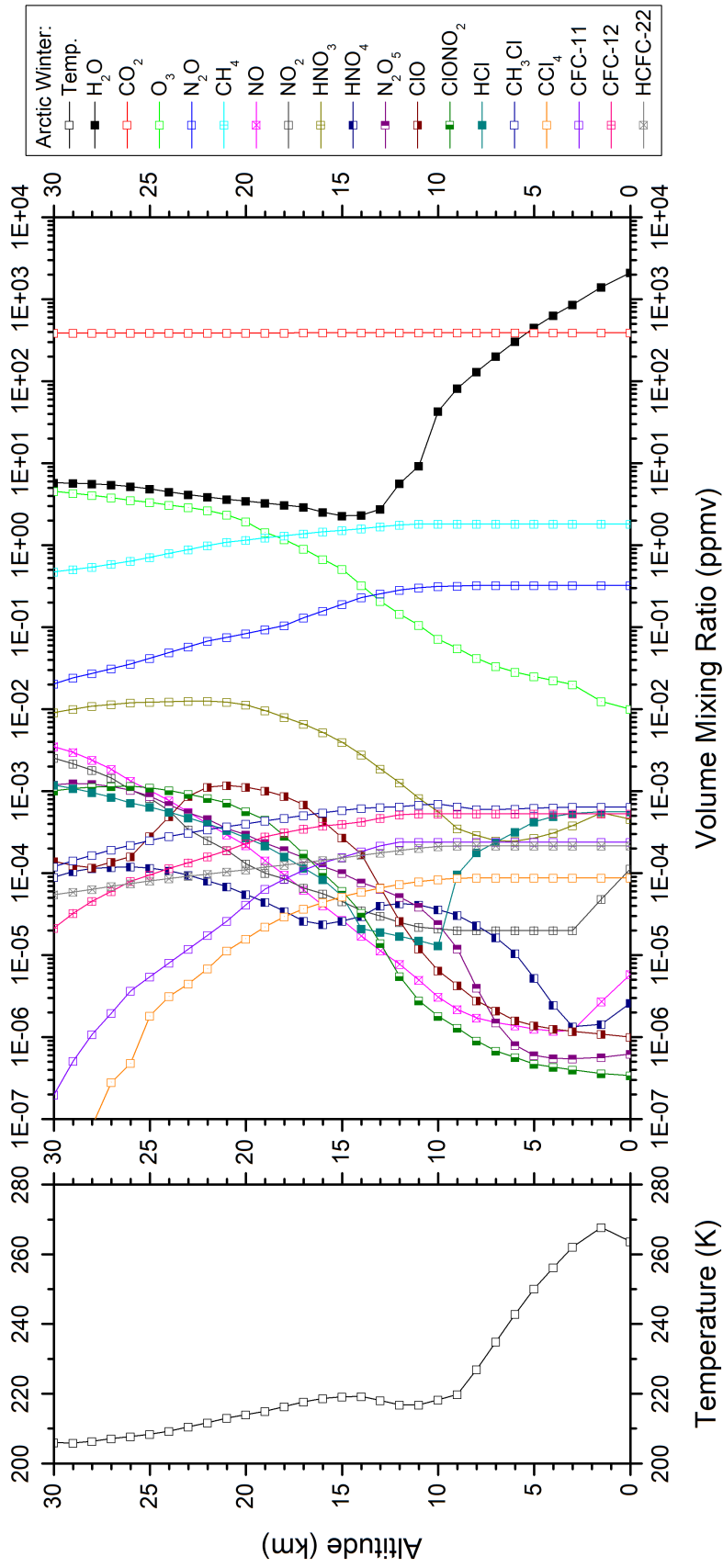


Figure 2.4: Climatological temperature and trace gas profiles for the Arctic winter according to Remedios et al. (2007). Figure courtesy: Gerald Wetzel.

(Höpfner et al., 2006, 2018; Spang et al., 2018). In the UTLS region, low PSCs can occur in a similar altitude region as high cirrus clouds (12 - 13 km), and it is difficult to discriminate PSCs and cirrus clouds in observations.

2.4 Stratospheric ozone layer

The stratospheric ozone (O_3) layer was discovered and measured in the 1920's (Dobson and Harrison, 1926). Chapman (1930) gave the first explanation for the existence of this O_3 layer as an equilibrium of photolysis and synthesis reactions to build and destroy O_3 . O_3 is produced in 20 - 35 km altitude under the presence of sunlight ($\lambda < 240$ nm) and a molecule M, which is necessary to preserve inertia:



Ozone can be photolyzed by the presence of sunlight ($\lambda < 310$ nm):



These natural construction and destruction processes are also called ‘‘Chapman cycle’’ (e.g., Solomon, 1999, and references therein). Reactions R 2.1 and R 2.3 effectively filter ultraviolet radiation from the sun. Above 35 km, low O_2 concentrations limit O_3 production, while at altitudes below 20 km, not enough photons with suitable wavelengths remain to photolyse O_2 . Besides the ozone destruction in this Chapman cycle, other ozone destroying processes occur in the atmosphere. First hypotheses of stratospheric ozone depletion were explained with odd hydrogen (HO_x ; Bates and Nicolet, 1950), odd nitrogen (NO_x ; Crutzen, 1970), and odd chlorine (ClO_x ; Stolarski and Cicerone, 1974; Molina and Molina, 1987) catalytic cycles. Typical reactions for these cycles (with X denoting the radical) are (e.g., Solomon, 1999, and references therein)



Molina and Rowland (1974) identified increasing anthropogenic emissions of chlorofluorocarbons as a potential source of long-lived chlorine. Chlorofluorocarbons are photolyzed in the stratosphere and provide atomic chlorine in the region of highest ozone concentration. Bromine chemistry is also important for ozone depleting processes (von Hobe and Stroh, 2012; WMO, 2015), but it is not in focus of this work and therefore not discussed further. As a consequence of decreasing ozone, production of ozone depleting substances (ODS) was banned by the Montreal protocol (WMO, 1987). Measured and

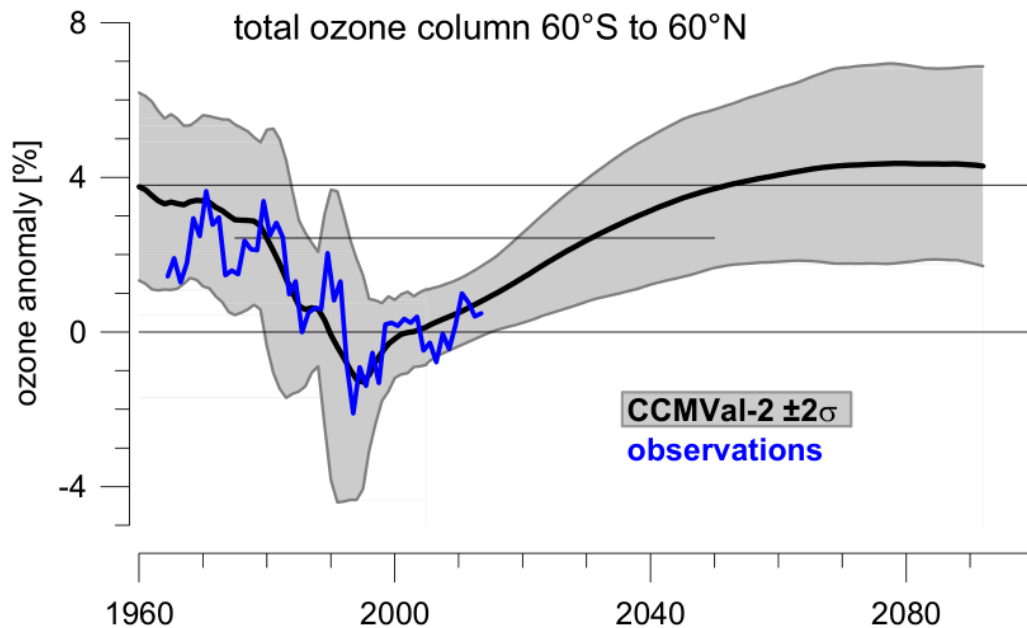


Figure 2.5: Observed (blue) and simulated (black) total ozone column anomalies as time series between 1960 and 2100. Observations are mean values of all in WMO (2015) available ground- and satellite-based information. The black line and grey shadow show the multi model mean and 2σ deviation from the CCMVal-2 data (Eyring et al., 2010). The reference of all data is the 1998 to 2008 period. Reprint from WMO (2015, Figure 2-26).

simulated global ozone trends are shown in Fig. 2.5: After decreasing until the 1990s, global ozone is slowly increasing again (WMO, 2015). Generally, the Montreal protocol is working well and ODS are successfully reduced in the atmosphere (WMO, 2015). Still, Montzka et al. (2018) found that the concentrations of trichlorofluoromethane (CFC-11) declined notably slower after 2012. Their back-trajectory analysis showed that emissions responsible for this slower decrease of CFC-11 are originated in eastern Asia.

Despite the general consensus that the Montreal protocol (and following) is working, Ball et al. (2018) showed that no sign of ozone recovery was ascertained by measurements. They analyzed a large number of observational data sets of stratospheric ozone and concluded a continued decrease of lower stratospheric (147 - 32 hPa) ozone since 1998 outside the polar regions (between 60°S and 60°N). This is in contrast to the trend of increasing total ozone columns (from ground to the top of the atmosphere) for the same latitudinal region, as shown in Fig. 2.5. Stone et al. (2018) tried to reproduce this trend with model simulations, but concluded from the simulation results it was not possible to deduce a significant trend due to large variability. An overview of scientific analyses related to atmospheric ozone was recently published (WMO, 2018).

2.5 Polar chlorine chemistry

Stratospheric chlorine is known to have a major influence on ozone depletion (WMO, 2015), and chlorine chemistry has been thoroughly described and explained (Solomon et al., 1986). Chlorine forms non-reactive reservoirs hydrogen chloride (HCl; Stolarski and Cicerone, 1974) and chlorine nitrate (ClONO₂; Rowland et al., 1976; von Clarmann and Johansson, 2018), which are not able to deplete ozone. PSCs provide surfaces for heterogeneous chemistry, which is essential for chlorine activation of these reservoir gases (Solomon et al., 1986; Crutzen et al., 1992; Peter and Grooß, 2012; WMO, 2015).

During the presence of PSCs, heterogeneous reactions on the surface of these PSCs can occur and produce molecular chlorine (Brasseur and Solomon, 2005)



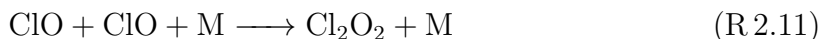
which can be photolyzed in the presence of sunlight



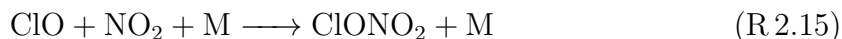
This atomic chlorine can react with ozone to another reactive chlorine species chlorine monoxide (ClO):



which can react in the ClO-dimer (Cl₂O₂) catalytic cycle (Molina and Molina, 1987):



According to Wohltmann et al. (2017), this ClO-dimer cycle contributes to approximately 50% of the vortex averaged ozone loss at altitudes of 54 hPa (about 18 km), while the ClO-BrO cycle (McElroy et al., 1986) contributes to approximately 40%. Furthermore ClO can react with atomic oxygen to Cl. Deactivation of reactive chlorine to reservoirs is mostly conducted via these reactions (Brasseur and Solomon, 2005, see also for an overview of possible reactions):



STS PSCs consist of droplets of 0.3-0.5 μm. They are important for chlorine activation and reversible uptake of nitric acid (HNO₃). Kirner et al. (2015) presented model results indicating that 90% of antarctic ozone depletion is caused by chlorine activation on such liquid particles. Nitric acid trihydrate (NAT) PSCs can play a role in chlorine activation, and large NAT particles can permanently remove HNO₃ from the stratosphere by

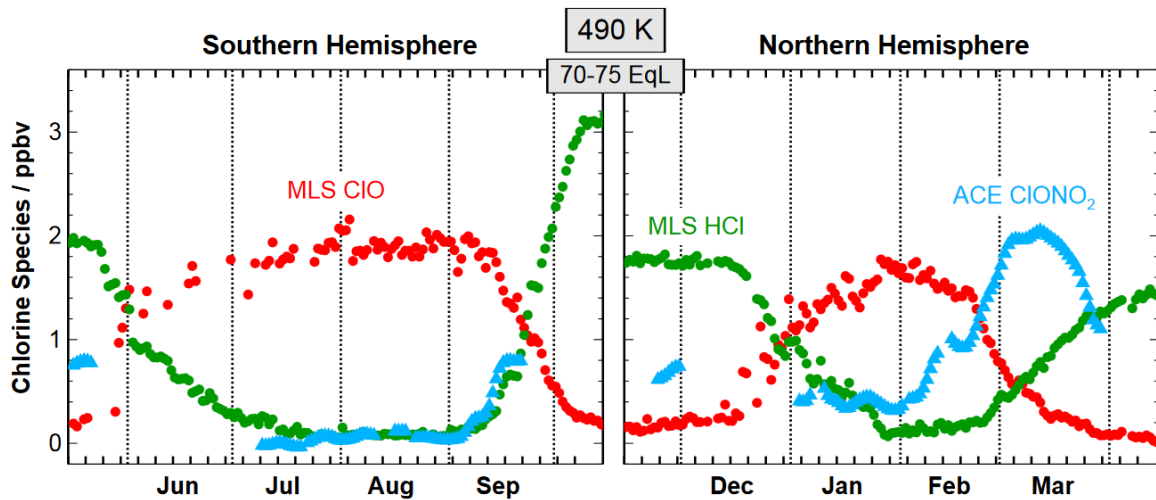


Figure 2.6: Time series of daily 70–75° EqL averages of ACE-FTS ClONO_2 (blue triangles), Aura/MLS HCl (green dots), and Aura/MLS daytime ClO (red dots) at 490 K potential temperature altitude. The left panel shows the 2005 Antarctic winter, the right panel shows the 2004/2005 Arctic winter. Reprint from WMO (2007, Figure 4-10).

sedimentation (denitrification, Toon et al., 1990). After resublimation to the gas phase, these particles add HNO_3 at lower altitudes (re-nitrification). Typically, NAT particles have radii of 1 μm , but “NAT-rocks” with radii up to 10 μm have been observed (von Hobe et al., 2013). Woitode et al. (2016) showed that highly aspherical NAT particles are involved in the denitrification process in the Arctic. Ice PSCs have little influence on chlorine activation, but when sedimented, they cause dehydration of the stratosphere (Gandrud et al., 1990). They typically consist of 1–10 μm large particles (WMO, 2015).

Due to the different temperatures of the polar vortices on both hemispheres (see Sec. 2.2), time periods and spatial extent of PSCs are different in the Arctic and Antarctic, resulting in different typical temporal evolution of chlorine species. During austral winter, a stable vortex with cold stratospheric temperatures and thus frequent occurrences of PSCs is observed. Therefore, usually extensive chlorine activation occurs together with ozone depletion (Stolarski et al., 1986) and denitrification in the lower stratosphere (Santee et al., 1998). This denitrification results in a lower availability of NO_y , which prevents chlorine deactivation into ClONO_2 (R 2.15). Additionally, ozone depletion reduces the probability of reaction (R 2.10), which results in more Cl , which is deactivated via (R 2.16) to HCl (Prather and Jaffe, 1990; Douglass et al., 1995; Grooß et al., 1997, 2005; Douglass and Kawa, 1999). Therefore, chlorine deactivation into HCl is the dominating process in the Antarctic (e.g., Santee et al., 2008b). In typical Arctic winters, less denitrification and ozone depletion is reported (Solomon, 1999) and therefore chlorine deactivation into ClONO_2 is observed prior to deactivation into HCl (e.g., Santee et al., 2008b). Typical chlorine partitioning for Antarctic and Arctic winters is shown in Fig. 2.6: In the Antarctic, HCl and ClONO_2 decrease early in the beginning of the winter, and ClO increases over a period of more than three months. Deactivation of ClO goes along with a strong increase of HCl and a smaller increase of ClONO_2 .

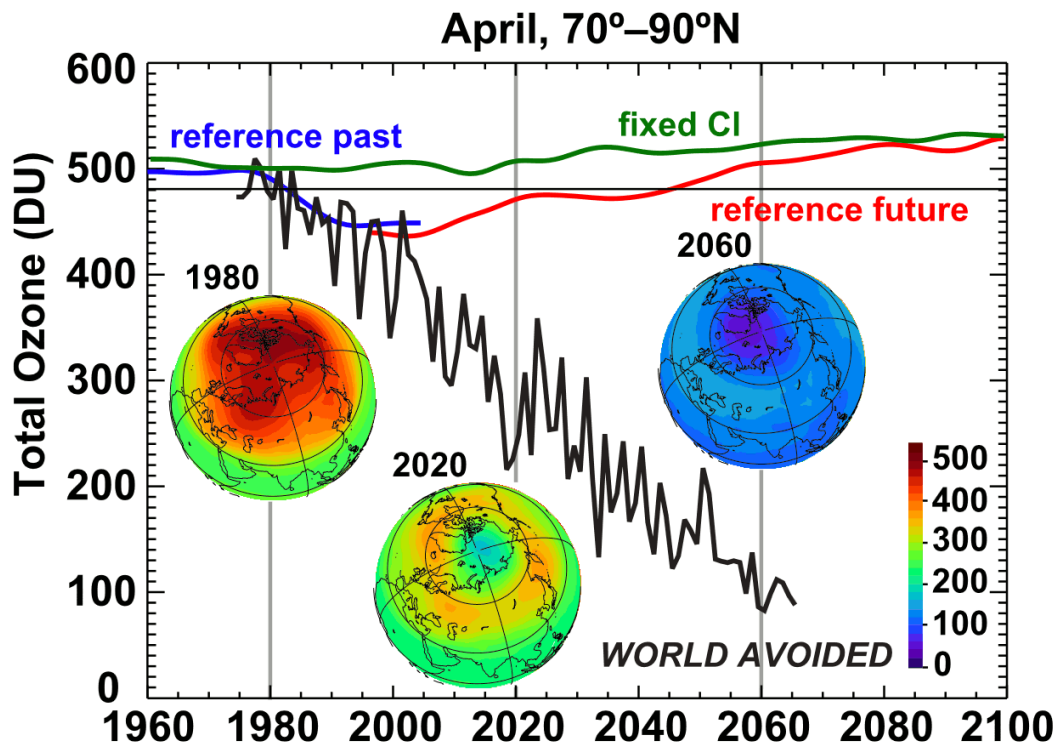


Figure 2.7: Total ozone column in Arctic (70–90°N) April between 1975 and 2065 for the past (blue), a model run with fixed preindustrial chlorine (green), with chlorine emissions according to the Montreal protocol (red), and for the “World avoided” with unregulated chlorine emissions (black). Horizontal distributions are shown for the Arctic region for the years 1980, 2020, and 2060. Reprint from Newman et al. (2009, Figure 4a, CC Attribution 3.0 License).

In the Arctic, activation into ClO starts later in the winter and ClO is increased over a period of approximately two months. Deactivation starts with a strong increase of ClONO_2 , and HCl builds up later in March, when ClONO_2 decreases again. However, there are exceptions to this general picture. For extraordinarily cold Arctic winters, enhanced chlorine activation and atypically strong chlorine deactivation into HCl have been reported (Santee et al., 2008b; Manney et al., 2011). This preferential deactivation into HCl can be caused by the lack of nitrogen dioxide (NO_2) due to strong denitrification, which is usually observed in the Antarctic (e.g., Fahey et al., 1990; Santee et al., 1998) but also occasionally in the Arctic (e.g., Waibel et al., 1999; Santee et al., 2000; Grooß et al., 2005). Additionally, cold temperatures and low O_3 abundances can favor chlorine deactivation into HCl (Prather and Jaffe, 1990; Douglass et al., 1995; Grooß et al., 1997, 2011; Mickley et al., 1997). Douglass and Kawa (1999) also demonstrated that even small decreases in O_3 together with low stratospheric temperatures can shift chlorine deactivation toward HCl . Beside PSC surfaces, also stratospheric background aerosol can to some extent provide surfaces for heterogeneous reactions (WMO, 2015). Volcanic aerosols are also considered to efficiently provide surfaces for heterogeneous reactions (Solomon et al., 2016; Ivy et al., 2017; Zhu et al., 2018).

Rex et al. (2004, 2006) derived a relation between the air volume, which is possibly cold

enough to form PSCs, and the amount of depleted ozone. This shows the crucial role of PSCs (and cold temperatures as prerequisite for their creation) for ozone depletion. Wegner et al. (2016) showed for the Arctic winter 2009/2010 that one mesoscale PSC occurrence over Greenland was responsible for a substantial part of chlorine activation, even though the mesoscale PSC only covered a small part of the total vortex. Their study showed that chlorine activation does not need to occur homogeneously in the vortex, but can occur at mesoscale PSCs, which act as process-reactors. This local confinement emphasizes the importance of spatially highly resolved measurements of ozone and trace gases, which are related to catalytic ozone depletion.

Newman et al. (2009) conducted a model study, showing a “World avoided” by the Montreal (and following) protocol. The temporal evolution of ozone in a world with unregulated chlorine emissions is shown for the Arctic in Fig. 2.7, where total ozone columns of less than 100 DU globally are reached in 2060.

In this thesis, an Arctic winter with atypical chlorine deactivation is discussed, and the primary reasons for changes in chlorine activation and deactivation, in particular due to colder temperatures, are examined.

It is known that the chlorine reservoir species found in the LMS can have two origins. Either they are formed in situ through chlorine deactivation or they are transported to this altitude regime from higher altitudes (e.g., Thornton et al., 2003). However, it is only reported for few examples, how much chlorine is deactivated in the LMS and how much chlorine reservoir is transported from higher altitudes.

2.6 Interactions of climate change and ozone depletion

Anthropogenic emission of greenhouse gases (GHGs) continuously changes the composition of the atmosphere (Charney et al., 1979). These changes in atmospheric composition influence the thermal radiation budget (Pachauri and Mayer, 2015), which in turn affects relevant processes for catalytic ozone depletion (Dameris and Baldwin, 2012). It is commonly known and well established that the presence of GHG influences the temperature of the atmosphere. While the surface temperature is increasing, temperatures in the stratosphere are decreasing (Fels et al., 1980; Randel et al., 2009). As global GHG emissions are expected to continue, also the decreasing temperature trend in the stratosphere is expected to be maintained. This probably leads to longer and more stable vortices, more frequent occurrences of PSCs, and more ozone depletion in the Arctic (Shindell et al., 1998). During recent winters, extremely low temperatures and strong ozone depletion have been reported for the Arctic (Manney et al., 2011). Using the connection between the volume of PSCs and ozone depletion shown by Rex et al. (2004), an additional ozone loss of 15 DU per Kelvin of the average cooling of the stratosphere is estimated. In a time series, Rex et al. (2004, 2006) showed that the extreme cold Arctic winters are getting colder and thus more ozone depletion occurs.

Beside this direct influence of temperature, climate change also affects atmospheric dy-

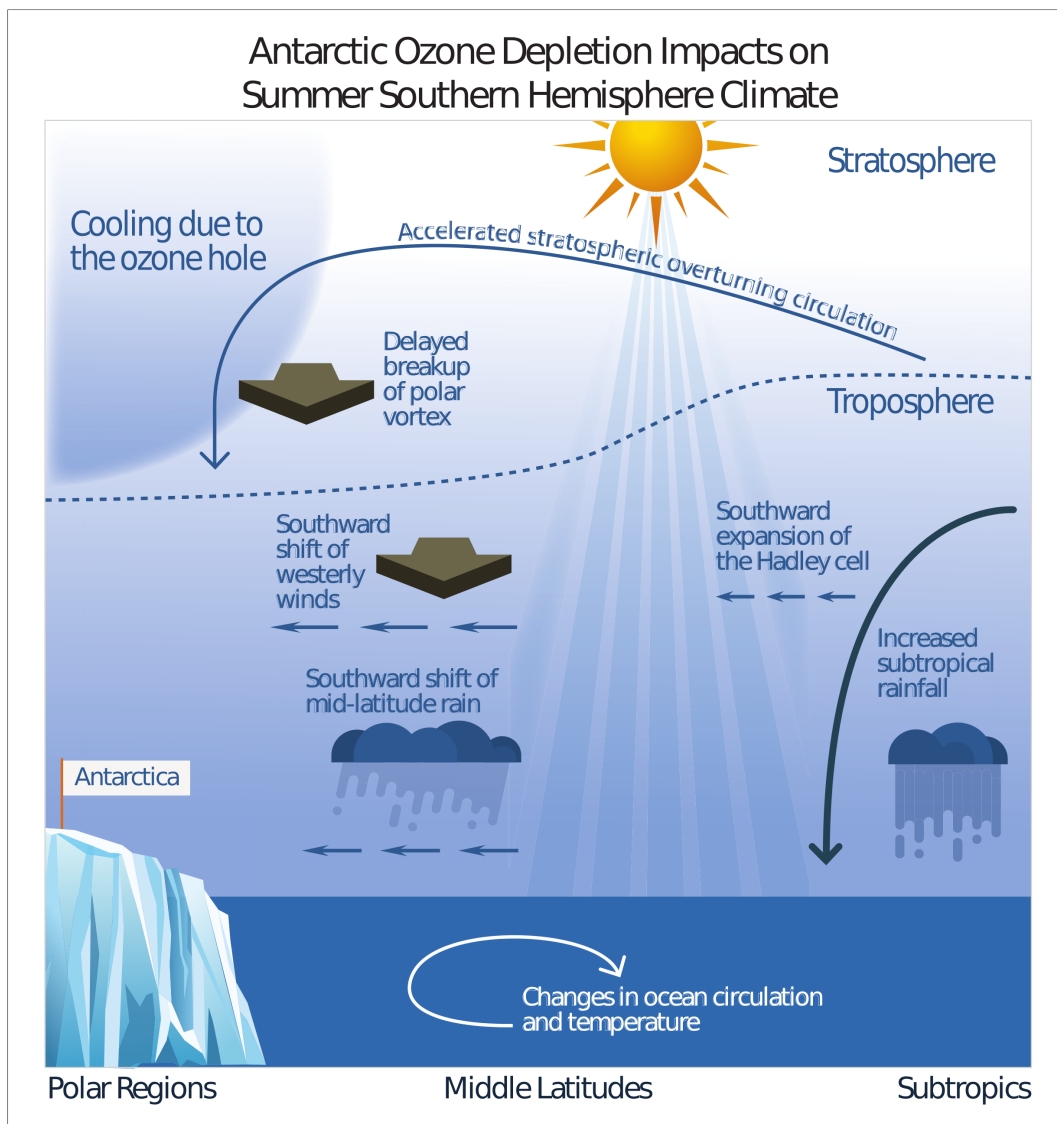


Figure 2.8: Climate impacts due to Antarctic ozone depletion. Reprint from WMO (2018, Figure ES-8).

namics and transport, which are also relevant for the stratospheric ozone layer. A change of the **BDC** is discussed to be connected to climate change (Stiller et al., 2012; Haenel et al., 2015; Dameris and Baldwin, 2012, and references therein), which would also imply considerable changes in stratospheric ozone distribution and changes in ozone depletion. **STE** is also projected to change due to climate change: Increased atmospheric wave activity may change the polar night jet and the North Atlantic Oscillation (Dameris and Baldwin, 2012, and references therein). For future projections of ozone changes due to climate change, it is of particular interest to assess, which effects caused by climate change will alter the atmosphere, and how they interact in combination. While radiative cooling due to **GHG** might increase the stability of the polar vortex, stronger wave activity might decrease this stability. These long term changes are difficult to project with atmospheric models (Dameris and Baldwin, 2012, and references therein) and therefore it is important to closely monitor the atmospheric state during the process of

GHG-induced climate change. Highly resolved measurements in the **UTLS** are therefore important to validate atmospheric models in terms of their capability to reproduce meso-scale structures in trace gases.

Ozone, in particular in the **UTLS** region, also has a great influence on the radiation budget. Variability in distribution of **UTLS** ozone accounts for notable differences in climate simulations (Xia et al., 2017). Potential changes in the radiation budget of the atmosphere due to ozone were already discussed by Forster and Shine (1997). According to the recent summary of the WMO ozone assessment (WMO, 2018), the relative importance of ozone depletion for climate in the southern hemisphere will depend on the evolution of atmospheric **GHG** concentrations. However, low ozone columns in the Antarctic cool the stratosphere, which accelerates stratospheric circulation, delays the breakup of the polar vortex, influences zonal transport and rainfall, and changes ocean temperature and circulation (Hartmann et al., 2014; Butchart, 2014; Gerber and Son, 2014; Swart et al., 2018). The interplay of these processes are depicted schematically in Fig. 2.8.

2.7 Observations

After the discovery of low stratospheric ozone values due to catalytic ozone depletion, observations of trace gases in the stratosphere were required to monitor the ozone layer, to control the emission of substances banned by the Montreal protocol, and to increase the knowledge of ozone depleting processes. A large variety of measurement techniques can be applied for this purpose. In situ instruments, which are deployed on an altitude changing platform such as aircraft or balloon, usually have excellent accuracy and precision, but are spatially limited to the position of the airborne platform. Remote sensing instruments from aircraft and balloon can cover a larger spatial range than in situ instruments but are still limited in spatial and temporal extent. Potentially continuous and global measurements are possible with spaceborne instruments. The total ozone column, which is relevant for the amount of harmful ultraviolet radiation that reaches the Earth's surface, has been monitored by several satellite missions. The **TOMS**¹ series of instruments (Stolarski et al., 1986) started the monitoring of total ozone columns in 1979 and was followed by many instruments, e.g., the **OMI**² or **OMPS**³. Measurements of these instruments are collected by the NASA Ozone Watch website (NASA GSFC, 2018). Besides ozone, also total columns of other trace gases (e.g., HNO_3 , H_2O , NH_3 , CFC-11) are regularly measured by spaceborne instruments in nadir viewing geometry, e.g., by **IASI**⁴. Total columns of trace gases like O_3 , HNO_3 , ClONO_2 , and HCl are also measured by ground based Fourier transform infrared spectrometry (**FTIR**) stations, which are organized in the Network for the Detection of Atmospheric Composition Change (**NDACC**; Mazière et al., 2018).

¹Total Ozone Mapping Spectrometer

²Ozone Monitoring Instrument

³Ozone Mapping Profiler Suite

⁴Infrared Atmospheric Sounding Interferometer

Besides total columns, also vertical profiles can be derived from these measurements, but the vertical resolution is limited. Limb remote sensing instruments provide trace gas profiles with a considerably higher vertical resolution but with lower horizontal resolution, compared to nadir remote sensing instruments. These limb remote sensing instruments are deployed on satellites, balloon platforms, or aircraft. Examples for such remote sensing instruments are the Michelson Interferometer for Passive Atmospheric Sounding (MIPAS; Fischer et al., 2008) on satellite, balloon and aircraft, the spaceborne Microwave Limb Sounder (MLS; Waters et al., 2006) and the Atmospheric Chemistry Experiment – Fourier Transform Spectrometer (ACE-FTS; Bernath, 2017), the balloon-borne Mark 4 (MkIV; Toon, 1991) and the CRISTA – New Frontiers (CRISTA-NF; Offermann et al., 1999) on aircraft. Measurements of chlorine species have been performed from spaceborne instruments for the chlorine reservoirs ClONO_2 (e.g., Zander et al., 1986; Roche et al., 1994; Höpfner et al., 2004; Nakajima et al., 2006; Wolff et al., 2008) and HCl (e.g., Beaver and Russell, 1998; Mahieu et al., 2008; Froidevaux et al., 2008b), and active chlorine such as ClO (e.g., Waters et al., 1993; Glatthor et al., 2004; Urban et al., 2005; Santee et al., 2008a). These satellite measurements can provide global coverage over a long period of time and have been used to investigate for example chlorine partitioning (e.g., Dessler et al., 1995; Dufour et al., 2006; Santee et al., 2008b), and for model evaluation (e.g., Andersson et al., 2016; Grooß et al., 2018).

During several measurement campaigns in the Arctic, important insights into processes related to polar ozone depletion have been gained. The SOLVE / THESEO⁵ (2000) campaign showed evidence of large nitric acid trihydrate (NAT) particles (so called “NAT-rocks”), which significantly increase denitrification (Newman et al., 2002; Fueglistaler et al., 2002). The RECONCILE⁶ (2010/11) campaign revealed essential parameters of the Cl_2O_2 photolysis (von Hobe et al., 2013). Balloon and airborne in situ measurements enabled process studies (e.g., Lelieveld et al., 1999; von Hobe et al., 2013) and studies of chlorine partitioning at flight altitude (e.g., Jurkat et al., 2017) to be performed. Limb remote sensing measurements from balloon and airborne instruments provide trace gas profiles that have been used to study the diurnal cycle of trace gases (Wetzel et al., 2012), chlorine partitioning (von Clarmann et al., 1995; Wetzel et al., 2015), and process studies (e.g., von Hobe et al., 2013, and references therein). Most of these studies focus on altitudes of around 500 K potential temperature, (≈ 20 km altitude) where maximum chlorine activation is typically found.

The POLSTRACC / GW-LCYCLE II / GWEX / SALSA (PGS) campaign, which were conducted during the Arctic winter 2015/16, give insights into horizontal and vertical distributions of ozone and trace gases, which are related to catalytic ozone depletion in the UTLS. Context information on these meso-scale structures is provided by satellite observations of relevant trace gases. The Gimballed Limb Observer for Radiance Imaging of the Atmosphere (GLORIA) instrument and several in situ instruments which were deployed on the High Altitude and Long range research aircraft (HALO) during the PGS campaign are presented in more detail in Sections 3.2 and 4.2.

⁵Stratospheric Aerosol and Gas Experiment (SAGE) III Ozone Loss and Validation Experiment / Third European Stratospheric Experiment on Ozone

⁶Reconciliation of essential process parameters for an enhanced predictability of Arctic stratospheric ozone loss and its climate interactions

Chapter 3

GLORIA airborne atmospheric limb emission measurements

Airborne measurement campaigns with infrared limb-emission remote-sensing instruments have been a source of spatially and/or temporally resolved observations of temperature and a wealth of trace gases (e.g., Piesch et al., 1996; Blom et al., 2003) as well as these campaigns have been important steps for demonstration of technology for future satellite missions (e.g., Fischer et al., 2008).

The Gimballed Limb Observer for Radiance Imaging of the Atmosphere (**GLORIA**; Friedl-Vallon et al., 2014) continues the heritage of the series of Michelson Interferometers for Passive Atmospheric Sounding (**MIPAS**; Fischer and Oelhaf, 1996; Piesch et al., 1996; Friedl-Vallon et al., 2004) and Cryogenic Infrared Spectrometers and Telescopes for the Atmosphere (**CRISTA**; Offermann et al., 1999; Ungermann et al., 2012). One major improvement of **GLORIA** compared to its limb-scanning precursors is the usage of an imaging array detector for significantly higher spatial and temporal sampling and precise relative pointing between vertical limb angles. An overview of scientific objectives and the potential of the **GLORIA** instrument is given by Riese et al. (2014).

This chapter starts with an overview of Fourier transform spectrometers (FTS), explaining the basic concepts, and introducing advantages of the imaging FTS (**iFTS**) concept. Then, the implementation of such an **iFTS** is shown for the **GLORIA** instrument. The theory of infrared emission spectroscopy is summarized in Sec. 3.3, followed by sketches of the limb measurement geometry and radiative transfer theory. These aspects are finally used to explain the theory of the trace gas retrieval method used for the **GLORIA** measurements.

3.1 Imaging Fourier Transform Spectrometer

The usage of FTS for observation of the atmospheric state and composition is an established technique, and many applications have been reported (Beer, 1992; Persky, 1995). The **FTS** of **GLORIA** basically consists of a Michelson interferometer, of which

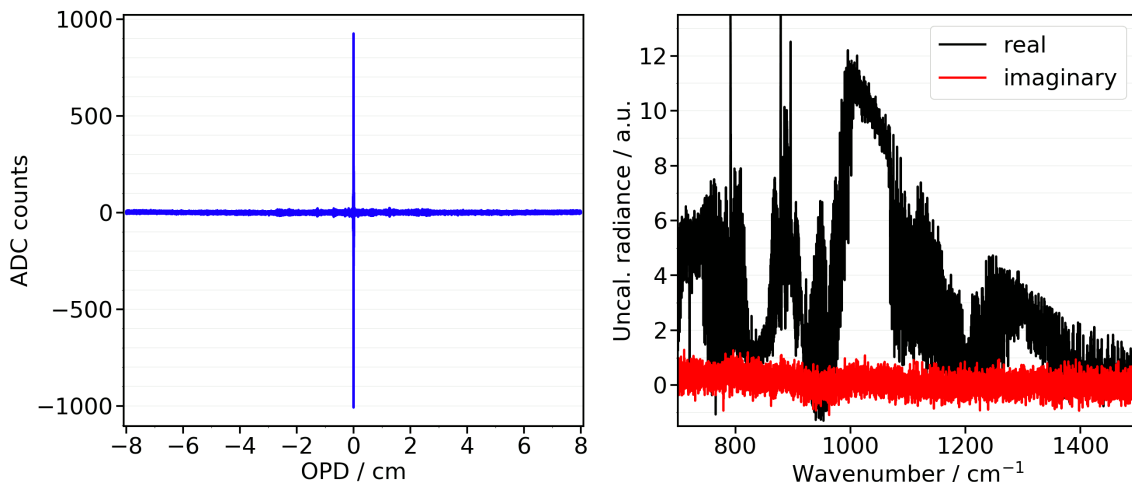


Figure 3.1: Interferogram (high-pass filtered) and corresponding complex spectrum after Fourier transformation and phase correction. Measured by GLORIA on 13 March 2016 10:46:32 UTC at a tangent altitude of 13.7 km.

the optical path difference (**OPD**) is modified (e.g., by moving one mirror back- and forward). The intensity modulation, due to the interference pattern, observed at the detector is correlated with the **OPD**, and the Fourier transform of this interferogram (intensity vs. **OPD**) results in a spectrum. An example of a GLORIA interferogram together with the corresponding complex spectrum as result of a Fourier transformation is shown in Fig. 3.1. The interferogram has been high-pass filtered. This figure displays the maximum **OPD** of GLORIA, which is from -8.0 cm to 8.0 cm. Due to this rather coarse level of detail, only some fine structures in the interference pattern are visible, but not fully resolved in this representation of the interferogram. The corresponding complex spectrum depicted in Fig. 3.1 has been phase corrected after Fourier transform of the presented interferogram. The spectral sampling of such a spectrum is given as the inverse of the **OPD**. For a Michelson interferometer with a maximum **OPD** (OPD_{max}), the spectral sampling $\Delta\nu$ is:

$$\Delta\nu = \frac{1}{2|\text{OPD}_{\text{max}}|} . \quad (3.1)$$

In the **iFTS** approach, a large number of interferograms of different target geolocations is recorded simultaneously by using an imaging array as detector behind the Michelson interferometer. Fig. 3.2 shows exemplary off-axis beams entering from the atmosphere under an angle α with their path through the **FTS** for two different positions of the movable mirror are depicted. It is shown that beams incident under one angle α are focused at one position on the image plane (Genest and Tremblay, 1999; Kretschmer, 2014). Therefore the signal at different pixels on the imaging detector corresponds to a certain range of angles, of which the light is entering from the atmosphere. The significantly higher sampling of the **iFTS GLORIA** compared to the **FTS MIPAS-STR**atospheric aircraft (**MIPAS-STR**) is shown in Fig. 3.3.

This considerably higher number of observations provided, also introduces technological challenges, which need to be addressed. Compared to a single pixel **FTS**, the imaging

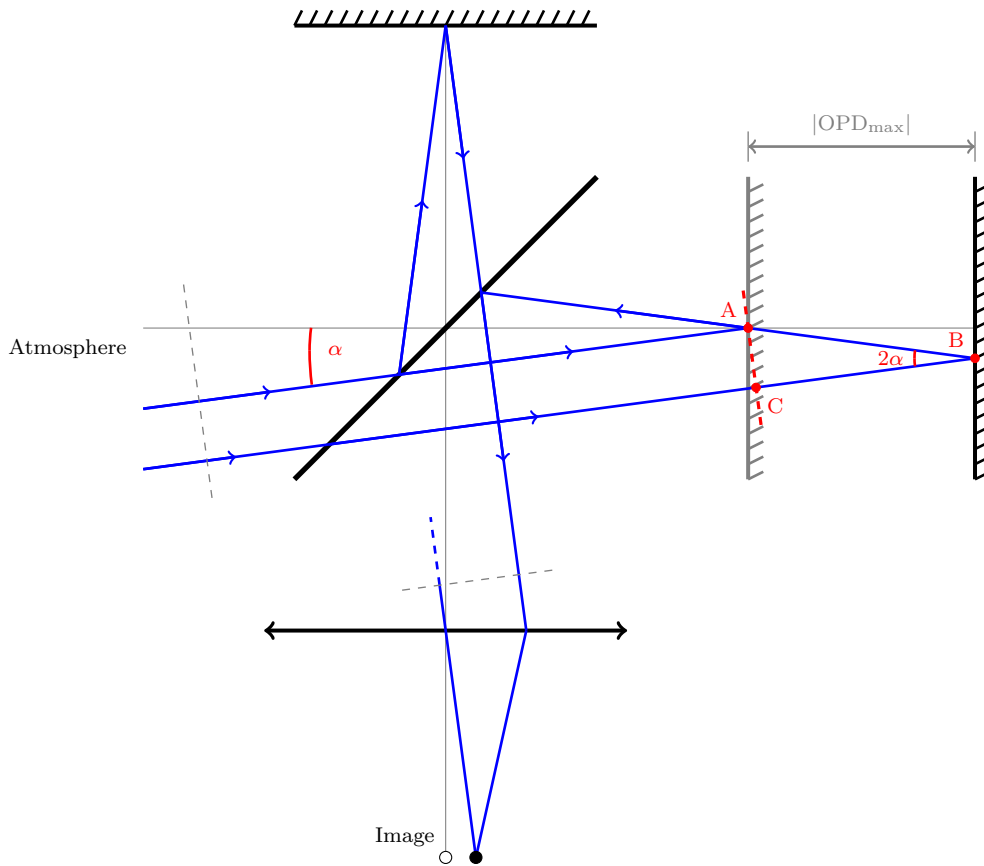


Figure 3.2: Schematic of off-axis beams entering from the atmosphere under an angle α into a FTS. Two exemplary rays are shown for two positions of the movable mirror, which are separated by a distance of $|\text{OPD}_{\text{max}}|$. Adapted from Kretschmer (2014, Fig. 2.5).

array of an **iFTS** is substantially more difficult to characterize, as detector pixels show considerable variations within one detector array, which introduces enhanced uncertainties from the radiometric calibration. In fact, each pixel has to be considered as a unique **FTS** instrument. In addition, an advanced set of electronics is necessary, in order to handle the larger amount (6144 interferograms for the **GLORIA iFTS** instead of one interferogram for the **MIPAS-STR FTS**) of recorded data. The large amount of data also leads to extreme requirements in data transmission, storage, handling and processing. In the following section, the implementation of this **iFTS** concept for **GLORIA** is briefly described.

3.2 GLORIA instrument overview

The **GLORIA** instrument (Friedl-Vallon et al., 2014, and the related AMT special issue) is designed for the deployment on the German **HALO** aircraft (see Fig. 3.4) and the Russian stratospheric research aircraft Geophysica (**M55**). The essential parts of the **GLORIA** instrument are an imaging spectrometer, a gimbaled frame for pointing and line-of-sight stabilization, two blackbodies for radiometric calibration, and a control and

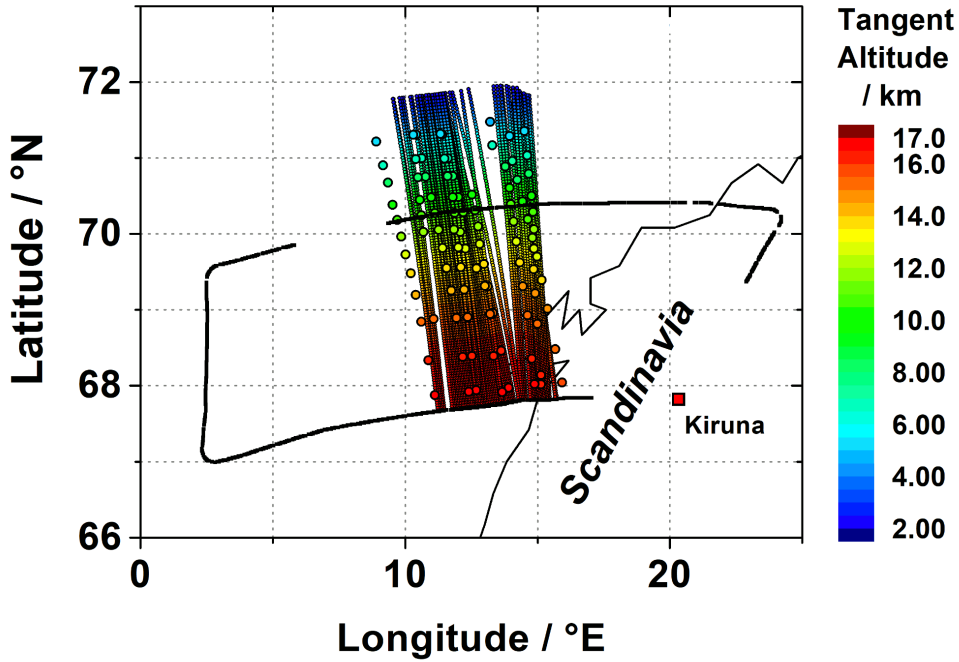


Figure 3.3: Exemplary geolocations sampled by MIPAS-STR (solid large circles, color-coded with altitude) and GLORIA (solid small dots, color-coded with altitude) during the same time period during one flight (6 December 2011). Figure courtesy: Wolfgang Woiwode, adapted from Woiwode et al. (2015).

data acquisition system. The spectrometer is a **FTS** with a HgCdTe long wave infrared detector array. A total of 48×128 (horizontal \times vertical) pixels of this imaging detector are used to record the same number of interferograms simultaneously. In order to reduce thermal noise and increase the instrument sensitivity, the spectrometer is cooled down to -50°C (Piesch et al., 2015). Depending on the scientific goals, the **GLORIA** spectrometer can adapt the maximum **OPD** (i.e., the interferogram length) and therefore with the spectral and temporal sampling. During the **PGS** campaign, **GLORIA** was operated in two different measurement modes: the high-spatial-resolution mode with a spectral sampling of 0.625 cm^{-1} and a temporal resolution of 2 s and the high-spectral-resolution mode (“chemistry mode”) with a sampling of 0.0625 cm^{-1} and 13 s. These spectral sampling characteristics are result of the **GLORIA OPD**, which can be chosen in a range between 0.8 cm and 8.0 cm. In this work, results of measurements at high spectral resolution are discussed. In this measurement configuration, 48×128 interferograms are recorded every 13 s, which corresponds to a displacement of the platform of $\approx 3\text{ km}$ considering typical **HALO** cruise speed. The gimbal frame is used to compensate for the movements of the carrying aircraft and also offers the possibility to point at azimuth angles between 45° and 135° relative to the flight direction for measurements in across-track limb geometry. These different azimuth pointing angles are desired to avoid stray sunlight, to correct for movements of the carrying aircraft due to cross winds or to adopt the measurement line of sight (**LOS**) for expected horizontal gradients in temperature or trace gases. Another application of the adjustable azimuth angle is the feasibility of tomographic measurements, in particular for studies of dynamical



Figure 3.4: GLORIA mounted in the belly pod below the HALO research aircraft. The photograph was taken just before take-off for research flight PGS19 on 13 March 2016. Photographer: Björn-Martin Sinnhuber.

features of the atmosphere (Ungermann et al., 2011; Krisch et al., 2018). With these tomographic measurements, the first three-dimensional observation of a gravity wave was accomplished (Krisch et al., 2017).

The level 0 to level 1 processing comprises the generation of radiometrically and spectrally calibrated spectra from raw measurement data (Kleinert et al., 2014). At first, the interferograms are corrected for spikes and for the nonlinearity of the detector and readout system. Then, they are resampled from the time-equidistant measurement grid onto a space-equidistant grid using information of a reference laser (Brault, 1996). During resampling, the interferograms are corrected for possible shifts due to linear phase drifts, and the optical path difference of each pixel is determined according to its off-axis angle, in order to sample each interferogram onto the correct abscissa in space. After the Fourier transform, a complex calibration according to Revercomb et al. (1988) is performed. Gain and offset are determined from regular in-flight measurements of the two on-board blackbodies (Olschewski et al., 2013). The temperature difference between the two blackbodies is about 30 to 40 K, with the cold blackbody being around or slightly below ambient temperature. The spectra are apodized using the Norton-Beer “strong” apodization (Norton and Beer, 1976, 1977). This processing is done individually for each of the 48×128 interferograms. For noise reduction, the pixels of each detector row are averaged after filtering of bad pixels (typically 5 % to 10 %). As measurements are smeared along track due to the horizontal movement of the aircraft, this averaging does not result in a loss of information. This process results in 128 row-averaged spectra with different elevation angles. After cloud filtering, this set of spectra serves as input for the retrieval of atmospheric parameters. All atmospheric parameters are retrieved

from the same set of averaged spectra.

GLORIA was deployed during the HALO campaigns TACTS/ESMVal¹ (2012), PGS² (2015/2016) and WISE³ (2017) and during the M55 campaigns ESSenCe⁴ (2011) and StratoClim⁵ (2016/2017). During these campaigns, the instrument was constantly improved (Kretschmer et al., 2015), the data processing was revised (Kleinert et al., 2014; Guggenmoser et al., 2015), and the level 2 products (vertical profiles of atmospheric parameters) were validated (Kaufmann et al., 2015; Woiwode et al., 2015; Ungermann et al., 2015). GLORIA data proved to be useful for model validation (Khosrawi et al., 2017) and case studies (Rolf et al., 2015; Krisch et al., 2017; Woiwode et al., 2018). Improvements to the instrument (reduced aero-acoustic noise in the spectra) compared to the results of Woiwode et al. (2015) increased the quality of the measured infrared spectra, resulting in better quality characteristics of the retrieved temperature and trace gas profiles.

The following sections sketch the theory of temperature and trace gas retrievals from spectra, measured by GLORIA.

3.3 Infrared emission spectroscopy

The thermal infrared spectrum of the atmosphere shows numerous contributions from rotational-vibrational transitions of trace gases. An example of a measured atmospheric infrared emission spectrum, with major contributing trace gases marked, is shown in Fig. 3.5. A more detailed view of this spectrum with the major contributing trace gases is presented in Fig. 3.6. Besides numerous spectral features from trace gases of interest in this spectral region, cloud and aerosol emissions strongly affect measurements due to their relatively warm temperatures. Measurements affected by these cloud and aerosol emissions make trace gas retrievals more complicated, but also allow to retrieve information of these clouds and aerosols (e.g., Günther et al., 2017; Höpfner et al., 2018).

Atmospheric trace gas molecules absorb and emit radiation through electronic, rotational, and vibrational transitions. While electronic transitions absorb and emit radiation in the ultraviolet (UV) and visible spectral range, and pure rotational transitions mostly absorb and emit microwave and far-infrared radiation, rotational-vibrational transitions are absorbing and emitting bands in the mid-infrared spectrum. Vibrations of the molecule influence its moment of inertia, and thus, rotational and vibrational transitions are usually coupled (e.g., Bernath, 2005). The resulting energy levels of the molecule can be calculated as the energy eigenvalues E of the time independent

¹Transport and Composition in the UTLS/Earth System Model Validation

²POLar STRATosphere in a Changing Climate/Gravity Wave Life Cycle/Gravity Wave EXperiment/Seasonality of Air mass transport and origin in the Lowermost Stratosphere using the HALO Aircraft

³Wave-driven ISentropic Exchange

⁴ESA Sounder Campaign

⁵Stratospheric and upper tropospheric processes for better climate predictions

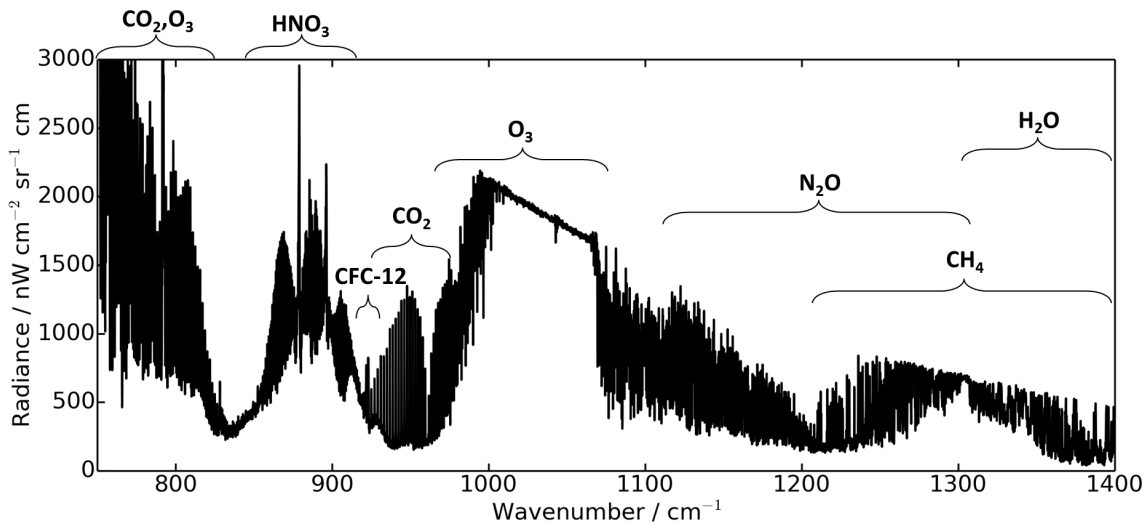


Figure 3.5: Example of an atmospheric limb emission infrared spectrum measured by GLORIA on 13 March 2016 10:46:32 UTC at a tangent altitude of 13.7 km. Trace gas contributions, which are identifiable at this level of detail, are marked.

Schrödinger equation (Schrödinger, 1926)

$$\hat{H}\psi = E\psi, \quad (3.2)$$

where \hat{H} is the Hamiltonian and ψ the wave function. Solutions for energy levels, considering the vibrational state v and the rotational state J , are (Herzberg, 1939):

$$E = \left(v + \frac{1}{2}\right)h\nu_c + B'J(J+1) \quad (3.3)$$

Here, h denotes the Planck constant, and B' and ν_c are characteristic constants of the molecule. Selection rules allow for rotational-vibrational transitions with $\Delta v = \pm 1$ and $\Delta J = \pm 1, 0$. For one vibrational transition $v_2 \rightarrow v_1$, multiple rotational transitions are possible, which form so-called “P” ($\Delta J = J'' - J' = -1$) and “R” ($\Delta J = +1$) branches. For certain transitions of this molecule also a “Q” branch ($\Delta J = 0$) can be allowed, which is located between the “P” and “R” branches (e.g., Hollas, 2010). A detailed discussion of the quantum mechanical motivation for the existence of a “Q” branch in a molecular spectrum is given by Wilson et al. (1955, appendix XVI). An example for a transition having a “Q” branch is the CO_2 band centered at 791 cm^{-1} (shown in Fig. 3.7).

The line strength or intensity is a measure of the transition probability. This probability depends on temperature, on the degeneracy of the relevant energy levels, and on selection rules for the transition (e.g., Bernath, 2005). For increasing J (which corresponds to spectral lines in the band further away from the center frequency), degeneracy of these energy levels ($2J+1$) increases, while for increasing J also the probability of thermal occupation of this rotational level ($e^{-(E_J - E_0)/(k_B T)}$) decreases. This explains the envelope of the “P” and “R” branch (e.g., Haken and Wolf, 2006).

Spectroscopic data, which are necessary for evaluation and processing of atmospheric remote sensing measurements, are provided as line-by-line or cross section data (Flaud,

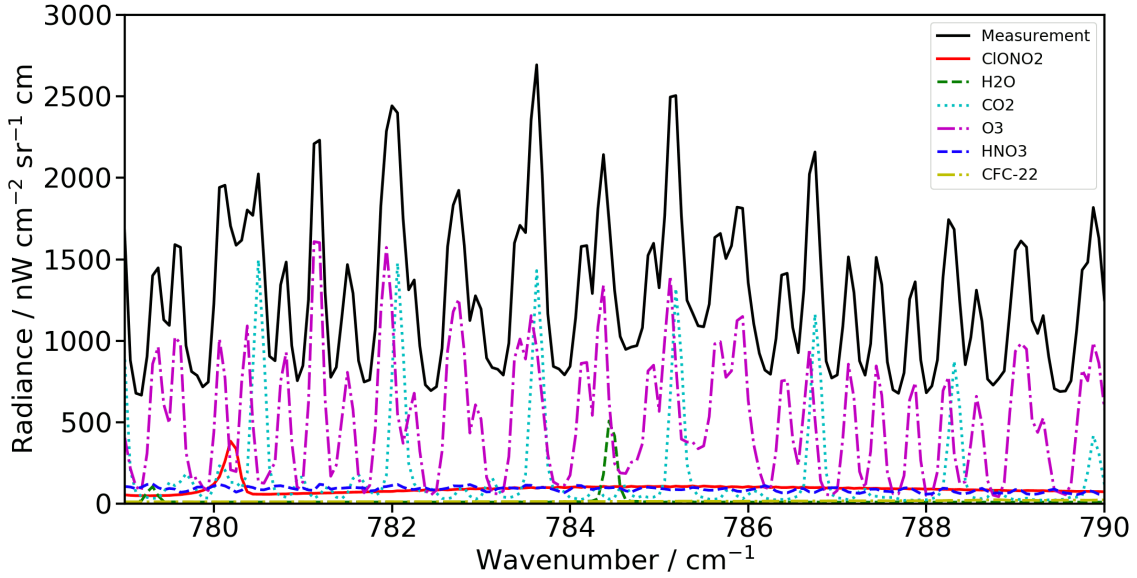


Figure 3.6: Close-up of the example of an atmospheric limb emission infrared spectrum measured by GLORIA on 13 March 2016 10:46:32 UTC at a tangent altitude of 13.7 km (black solid line). The contributions of single gases are calculated with the radiative transfer model *KOPRA* (Stiller, 2000) and shown as colored lines. Measurement noise is estimated to $20 \text{ nW}/(\text{cm}^2 \text{ sr cm}^{-1})$.

1994). A large number of available spectroscopic data is collected in the high-resolution transmission molecular absorption database (*HITRAN*; e.g., Gordon et al., 2017) and in a dedicated *MIPAS* spectroscopy (e.g., Flaud et al., 2003).

According to Eqn. (3.2), spectral lines of rotational-vibrational transitions are calculated to occur at distinct spectral positions, while in observations these spectral lines have a finite width. Broadening of the lines is caused by the natural line shape, pressure broadening, and Doppler broadening. The natural line shape is a result of the finite lifetime of the excited state of the molecule. Due to the uncertainty in energy and time, each spectral line connected to a transition has a minimum line shape in form of a Lorentzian distribution (Spencer and Moore, 2001, chapter B1.1.4.2). Thermal velocity of the radiation emitting molecules causes a temperature-dependent Doppler broadening of the spectral lines. The velocity of the molecules follows a Maxwell distribution and broadens the line in a Gaussian shape (e.g., Hollas, 2010). The probability of molecule collisions is related to pressure and temperature of the atmosphere. If a collision occurs during the emission process, the characteristic lifetime of this process is shortened and, due to the energy-time uncertainty, the energy uncertainty is increased. This pressure broadening results in a Lorentzian line shape (Rabitz, 1974). These effects of line broadening are considered in Voigt-profiles (Armstrong, 1967). Still, this Voigt-profile does not account for the influence of collisions on translations of the molecules, which are visible in line shape measurements of high spectral resolution (Valipour, 2001; Kochanov, 2012; Birk and Wagner, 2016). The Dicke-effect (Dicke, 1953; Wang, 2013) describes the narrowing of the Doppler broadening as a result of changes in velocity

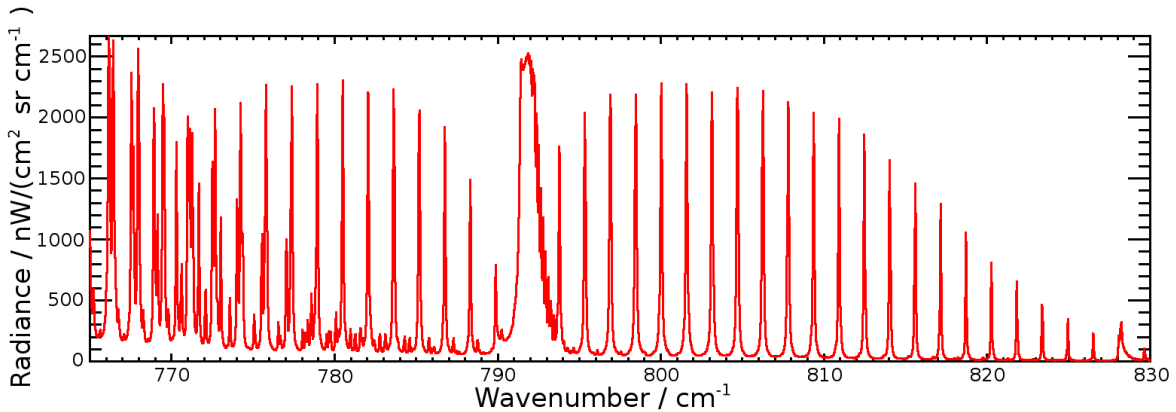


Figure 3.7: Spectrum for a CO₂ molecule showing the P, Q and R branches, simulated with KOPRA with a 0.025 cm⁻¹ sampling. At wavenumbers lower than 780 cm⁻¹, spectral lines from another emission band are visible.

due to collisions between molecules. This effect is considered in sophisticated line shape functions, such as Galatry, Rautian, or velocity dependant Voigt-profiles (Galatry, 1961; Rautian and Sobel'man, 1967; Valipour, 2001). For rotational-vibrational bands, spectral lines of one molecule are located spectrally close. Due to broadening, these lines may overlap significantly. Under these conditions, line-mixing effects, if not considered in the spectroscopic model, may introduce an additional error (e.g., Rosenkranz, 1975; Berman, 1998). In measured spectra, the line shape is, in addition, influenced by the spectral resolution and the instrumental line shape of the spectrometer. In case of spectra measured with GLORIA, the instrumental line shape only allows for observation of pressure broadening.

3.4 Limb measurement geometry

In the limb measurement geometry, observations are taken in long paths through the atmosphere, which are a tangent to a layer parallel to Earth's surface (Livesey, 2014). The lines of sight, together with the position of tangent points and tangent altitudes, are schematically shown in Fig. 3.8. All atmospheric segments along the line of sight contribute to the signal, but most information is considered to come from the tangent point (Gille and House, 1971; Gordley and Russell Iii, 1981). The spectroscopic signature of the target trace gas can be measured in absorption or emission. For solar occultation measurements, the sun is used as background to measure absorption of the atmosphere. While this method provides good signal to noise and vertical resolution, the total number of measurements is limited to the number of occultation possibilities. The Atmospheric Chemistry Experiment – Fourier Transform Spectrometer (ACE-FTS) is an example of a solar occultation infrared limb-sounder (e.g., Bernath, 2017). Emission measurements use the cold deep space as background for each limb measurement to observe the thermal emission of the molecules in the atmosphere. This method allows for a high number of measurements and is independent of the time of the day, but emission measurements demand for an elaborate instrument design. In particular, cooling

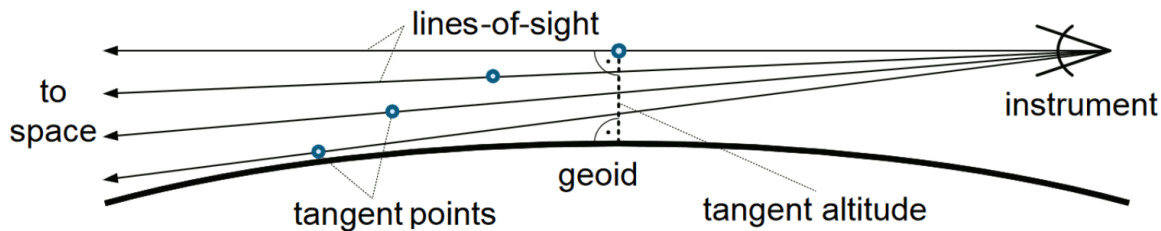


Figure 3.8: Schematic representation of the limb measurement geometry, showing the tangent points located on a slant in the atmosphere. Figure from [Ungermann et al. \(2013\)](#) (CC Attribution 3.0 License).

of the instrument is crucial to reduce thermal emission of the instrument. Examples for limb emission sounders are the Microwave Limb Sounder (**MLS**) instrument in the microwave wavelength range (e.g. [Waters et al., 2006](#)), and the **MIPAS** in the infrared (e.g. [Fischer et al., 2008](#)). Limb measurements have excellent vertical resolution, while their horizontal resolution is limited due to the long paths through the atmosphere (along the **LOS**), on which the signal is averaged. In addition, the horizontal resolution is limited, as the instrumental platform is moving during the time, needed for recording one interferogram. This results in a horizontal averaging of the air masses which are sampled during the time period of the measurement.

3.5 Radiative transfer

The radiation L at the spectral position of a wavenumber ν observed by the instrument depends on the background radiation $L(\nu, 0)$, the transmittance along the path through the atmosphere to the observer $\tau(\nu, z', z)$, and sources J along the path. Radiation after propagation through an atmospheric path z can be formulated as ([Rodgers, 2000](#)):

$$L(\nu, z) = L(\nu, 0) \tau(\nu, 0, z) + \int_0^z J(z') \frac{d}{dz'} \tau(\nu, z', z) dz', \quad (3.4)$$

where τ denotes the transmittance, and J the source function. The background radiance $L(\nu, 0)$ at position 0 is transmitted according to the transmittance $\tau(\nu, 0, z)$ along the path z . Along this path, sources $J(z')$ contribute to the observable radiance again transmitted according to the transmittance $\tau(\nu, z', z)$ between the position of the source and the observer. The source function includes scattering and thermal emission. A detailed discussion of formulations of $\tau(\nu, z', z)$ and $J(z)$ is given by [Liou \(1992\)](#) or [Rodgers \(2000, Chapter 9\)](#).

In case of local thermodynamic equilibrium (**LTE**)⁶, the emission part of the source function J is depending on the Planck function B . This thermal radiance emission B

⁶For higher altitudes (starting from the upper stratosphere), Non-LTE effects become increasingly important (see [Lopez-Puertas, 2001](#)).

of a black-body with the temperature T is given by Planck's law (Planck, 1914):

$$B(\nu, T) = \frac{2h\nu^3}{c^2} \frac{1}{e^{\frac{h\nu}{k_B T}} - 1} \quad (3.5)$$

Here ν denotes the wavenumber, c the speed of light, and k_B the Boltzmann constant. The shape of the Planck function can be seen in the envelope of atmospheric spectral lines. This envelope can be partly observed in Fig. 3.5, particularly in the spectral range of 1000 - 1100 cm^{-1} where the atmosphere is optically thick due to the strong absorption band of ozone.

3.6 Information retrieval theory

With the knowledge of the radiative transfer equation (3.4) and the optical properties of the atmosphere (caused by the atmospheric composition and state), it is possible to calculate the expected radiation for an observer. As remote sensing instruments measure the radiation, an inversion of Eqn. (3.4) is necessary in order to retrieve the atmospheric state and composition from the measurement of the radiation. As this inversion is analytically nonexistent, the retrieval process needs to be performed iteratively. Starting with an initial guess of the atmospheric state and composition (e.g., climatological data), spectra are calculated by radiative transfer models and compared to the profile of measured spectra. For the target parameters, derivatives of the radiance with respect to the parameter are calculated to perform an iterative fit. Typically, this inversion problem is underdetermined and additional a-priori knowledge has to be applied to constrain the retrieval. It is important to carefully select these constraints in order to account for atmospheric features, which do not agree to the prior knowledge (McPeters et al., 1984). More details and explanations of atmospheric retrieval theory are given by Rodgers (2000).

In this work, the retrieval software KOPRAFIT (Höpfner, 2000) is used, in which the forward radiative transfer is calculated by the radiative transfer model KOPRA (Karlsruhe Optimized and Precise Radiative transfer Algorithm; Stiller, 2000). Karlsruhe Optimized and Precise Radiative transfer Algorithm (KOPRA) is a line-by-line radiative transfer model, which is optimized for computationally efficient analyses of highly resolved spectral measurements. This software is used in the processing of spaceborne and airborne MIPAS measurements (von Clarmann et al., 2003; Wetzel et al., 2002; Woiwode et al., 2012). KOPRAFIT employs the Jacobians (derivatives of the radiance with respect to the fitted atmospheric parameters) provided by KOPRA to fit the selected atmospheric parameters to the measured set of spectra. The inverse problem is solved by the Gauss-Newton iterative algorithm (Rodgers, 2000) with Tikhonov-Phillips regularization (Tikhonov and Arsenin, 1977; Phillips, 1962):

$$\vec{x}_{i+1} = \vec{x}_i + (\mathbf{K}_i^T \mathbf{S}_y^{-1} \mathbf{K}_i + \gamma \mathbf{L}^T \mathbf{L})^{-1} (\mathbf{K}_i^T \mathbf{S}_y^{-1} (\vec{y} - \vec{f}(\vec{x}_i)) + \gamma \mathbf{L}^T \mathbf{L} (\vec{x}_a - \vec{x}_i)) \quad (3.6)$$

Here i denotes the iteration index, \vec{x}_i the vector containing the atmospheric state of step i , \vec{y} the radiance measurement vector, \vec{f} the radiative transfer function, \vec{x}_a the a

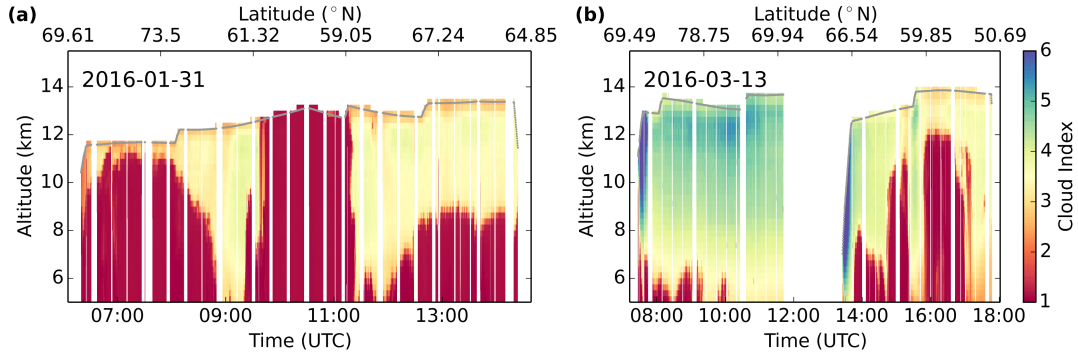


Figure 3.9: Vertical distribution of cloud indices along flights PGS12 (**a**, 31 January 2016) and PGS19 (**b**, 13 March 2016). The lower the cloud index, the more the measured spectrum is affected by clouds. Between 12:00 and 14:00 UTC in PGS19 no atmospheric data were measured due to a refueling stop of the aircraft.

priori profile, \mathbf{K}_i the Jacobian of \vec{f} for \vec{x}_i , \mathbf{S}_y the co-variance matrix of the measurement, \mathbf{L} the first-order differential operator and γ the regularization parameter. The regularization term $\gamma \mathbf{L}^T \mathbf{L}$ constrains the retrieval result to a smooth profile of the retrieved atmospheric quantity. In the applied formulation, the regularization avoids a bias to the retrieval result from an a priori profile (Eriksson, 2000). The regularization parameters are chosen such that high vertical resolutions are obtained while unrealistic oscillations of the retrieved quantity are avoided.

The retrieval strategy in this work follows closely the one described by Woiwode et al. (2012). For the retrieval, the atmospheric parameters are represented on a discrete altitude grid with 250 m spacing in the region of interest (3–17 km) and a coarser grid width below and above (1.5 km for 0–3 km, 2 km for 18–20 km, 2.5 km for 20–30 km and 50 km for 50–100 km). For the first step of the retrieval, trace gas profiles from the climatology by Remedios et al. (2007) are used for all important trace gases in the selected spectral range. Temperature, pressure and water vapor are taken from an interpolation of European Centre for Medium-Range Weather Forecasts (ECMWF) analysis data to the GLORIA tangent points. Only for the retrieval of water vapor, a constant profile of 10 ppmv for H_2O is used as an initial guess (instead of the ECMWF H_2O profile, which is used for retrievals of other atmospheric parameters than H_2O), in order to assure independence of retrieved vertical and horizontal structures in the water vapor distribution of the meteorological analysis. Retrieval quantities are the LOS, temperature, VMR of HNO_3 , O_3 , ClONO_2 and CFC-12 or the logarithm of VMR of H_2O . To consider atmospheric aerosols and thin clouds, the logarithm of an artificial continuum is part of the retrieval vector as described in Woiwode et al. (2015).

For the preparation of the retrieval, spectra affected by thick clouds are filtered. For that purpose, the cloud index (CI) introduced by Spang et al. (2004) is calculated for each measured spectrum as the color ratio between the spectral interval (also known as “micro-windows”) 788.20 to 796.25 cm^{-1} and 832.30 to 834.40 cm^{-1} . The CI is shown in Fig. 3.9 for the flights on 31 January 2016 and on 13 March 2016. Lower CI values indicate a larger influence of clouds on the spectrum. In previous studies using compa-

Retrieval target	Micro-window [cm^{-1}]
LOS and temperature	810.5–812.9
	956.0–958.2
HNO_3	862.0–863.5
	866.1–867.5
	901.3–901.8
O_3	780.6–781.7
	787.0–787.6
ClONO_2	780.0–780.4
H_2O	795.7–796.1
CFC-12	918.9–921.3

Table 3.1: Spectral windows for the different target species of the GLORIA high-spectral-resolution-mode PGS retrieval.

rable airborne limb-emission observations, typically fixed **CI** thresholds between 2 and 4 were used (Ungermann et al., 2012; Woiwode et al., 2012, 2015). In this work, a **CI** threshold of 3 is used for the lowest and 1.8 for the highest limb tangent altitude to preserve observations which are only moderately affected by **PSCs**. The **CI** thresholds for points in between these altitudes are linearly interpolated. This approach is chosen to effectively filter out tropospheric clouds at lower altitudes while optically thin cirrus or polar stratospheric clouds still are allowed for the retrieval.

In the first step, the line of sight is determined to correct a possible misalignment of the **GLORIA** gimbal frame. From this retrieval, a correction for the **LOS** is calculated and applied to all of the following steps. This is discussed in more detail in Chapter 5. Then temperature, **HNO₃**, **O₃**, **CFC-12**, **ClONO₂** and **H₂O** are sequentially retrieved. After each step, the values retrieved for the previous quantities are kept fixed and used as new initial guess profiles.

The spectral windows for the retrieval of the different trace gases are shown in Table 3.1. These spectral ranges were selected to minimize the cross talk of emission lines of other trace gases, as well as saturation of spectral lines, particularly at low limb views.

Error analysis

For the characterization of the results, possible error sources (systematic and noise errors) are estimated, and their influences on the retrieval are calculated. Considered errors are spectroscopic uncertainties (as reported in previous work), radiometric calibration errors (multiplicative gain and additive offset), residual pointing uncertainty, a temperature error for **VMR** retrievals, and an error of the **CO₂** climatology profile (accounting also for errors in the **CO₂** spectroscopic line data).

The spectroscopic error is estimated as 8% for **HNO₃** (Wetzel et al., 2002), 5.5% for **ClONO₂** (Wagner and Birk, 2003) and 10% for **CFC-12** (Moore et al., 2006). For **O₃** and **H₂O**, uncertainties in line intensities are reported (Flaud et al., 2002, 2006), and

the spectroscopic error is estimated as 7% for O_3 and 10% for H_2O . Considering the temperature retrieval, the spectroscopic error can be estimated by assuming an error in the CO_2 profiles as high as 5%, according to [Wetzel et al. \(2002\)](#). In order to quantify the influence of the assumed CO_2 profile, the temperature retrieval has been repeated with a CO_2 profile uniformly decreased by 5%. The differences between these retrievals at each grid point show the sensitivity of the retrieval to the modified CO_2 profile.

In the same way, the impacts of the other error sources on the retrieval are quantified. The results of a retrieval with a perturbed radiometric calibration, LOS or temperature are subtracted from the standard retrieval results to estimate the error at each individual retrieval grid point. With this method, uncertainties in the radiometric calibration are calculated considering uncertainties in the multiplicative gain of 2% and uncertainties in the additive radiance offset of $50.0 \text{ nW cm}^{-2} \text{ sr}^{-1} \text{ cm}$. LOS errors are estimated by retrievals assuming a 0.05° LOS offset. This estimation is based on the short-term profile-to-profile variability found in the LOS retrievals (see Sect. 5.3.1) and systematic uncertainties inherent to the LOS retrieval, such as uncertainties in ECMWF atmospheric temperature and pressure. For trace gas retrievals, the retrieved temperature is used to describe the atmospheric state. The effect of uncertainties in the retrieved temperatures on the trace gas retrievals is estimated by modifying the retrieved temperature profile systematically with the related temperature error (estimated for the temperature retrieval). The retrieval noise is calculated according to [Rodgers \(2000\)](#):

$$\Delta x_{\text{noise}} = \mathbf{G}_y \epsilon = \left((\mathbf{K}^T \mathbf{S}_y^{-1} \mathbf{K} + \gamma \mathbf{L}^T \mathbf{L})^{-1} \mathbf{K}^T \mathbf{S}_y^{-1} \right) \cdot \epsilon. \quad (3.7)$$

Here, Δx_{noise} denotes the noise error, \mathbf{G}_y the retrieval gain matrix, ϵ the measurement error and \mathbf{K} the Jacobian for the last iteration step. This measurement error is estimated as the spectral variance in the micro-window of the imaginary part of the calibrated spectrum ([Kleinert et al., 2014](#)).

The total estimated error for each altitude of each retrieved profile is calculated as the square root of the sum of the squares of each error contribution, as is shown for **VMR** in Eq. (3.8) and for temperature in Eq. (3.9).

$$\Delta x_{\text{vmr}} = \sqrt{\Delta x_{\text{spectroscopy}}^2 + \Delta x_{\text{gain}}^2 + \Delta x_{\text{offset}}^2 + \Delta x_{\text{pointing}}^2 + \Delta x_{\text{temperature}}^2 + \Delta x_{\text{noise}}^2} \quad (3.8)$$

$$\Delta x_{\text{temperature}} = \sqrt{\Delta x_{\text{CO}_2}^2 + \Delta x_{\text{gain}}^2 + \Delta x_{\text{offset}}^2 + \Delta x_{\text{pointing}}^2 + \Delta x_{\text{noise}}^2} \quad (3.9)$$

Vertical resolution and degrees of freedom

An important diagnostic measure is the vertical resolution, which is calculated by using the averaging kernel of the retrieval. The averaging kernel matrix is defined as ([Rodgers, 2000](#))

$$\mathbf{A} = \mathbf{G}_y \cdot \mathbf{K}. \quad (3.10)$$

The vertical resolution at a retrieval grid point is calculated as the full width at half maximum of the averaging kernel row. Another important quantity for a retrieval is

the number of degrees of freedom. These are calculated as the trace of the averaging kernel matrix (Rodgers, 2000), since the diagonal elements of the averaging kernel are a measure of how much measurement information is contained in the retrieval result per level. For the GLORIA retrievals in this work, vertical resolutions of 400 – 1000 m are reached. For an exemplary profile, the retrieved profile had 12 degrees of freedom for 85 used limb angles covering an altitude of 7.5 km.

Chapter 4

Data sets

This chapter introduces other data sets than **GLORIA** measurements, which are also used in this paper. First, the **PGS** campaign is discussed and an overview of the in situ instruments used for validation of **GLORIA** data and their measurement techniques is provided. Then, relevant satellite missions are presented and atmospheric models and meteorological data sets are introduced.

4.1 PGS campaign

The **PGS** mission is the combination of the **POLSTRACC**¹ aircraft campaign (Oelhaf et al., 2015) together with **GW-LCYCLE II**², **GWEX**³ and **SALSA**⁴ campaigns. The combined mission took place in the Arctic winter 2015/2016 with bases in Oberpfaffenhofen (Germany) and Kiruna (Sweden). This particular winter was characterized by exceptionally cold stratospheric temperatures (Manney and Lawrence, 2016; Matthias et al., 2016), by the presence of Polar Stratospheric Clouds (PSCs) down to altitudes lower than 15 km over a long period of time (Pitts et al., 2018; Voigt et al., 2018), and by strong denitrification (Khosrawi et al., 2017). These conditions allowed for extensive activation of chlorine. Among the scientific objectives of the **PGS** campaign are

- investigation of chemical processes such as ozone depletion,
- nitrification and denitrification and chlorine activation and deactivation in the **LMS**,
- mixing and dynamical linkages between the upper troposphere and the lower stratosphere, and between high latitudes and middle latitudes over the course of the winter,

¹POLar STRATosphere in a Changing Climate

²Gravity Wave Life Cycle

³Gravity Wave EXperiment

⁴Seasonality of Air mass transport and origin in the Lowermost Stratosphere using the HALO Aircraft

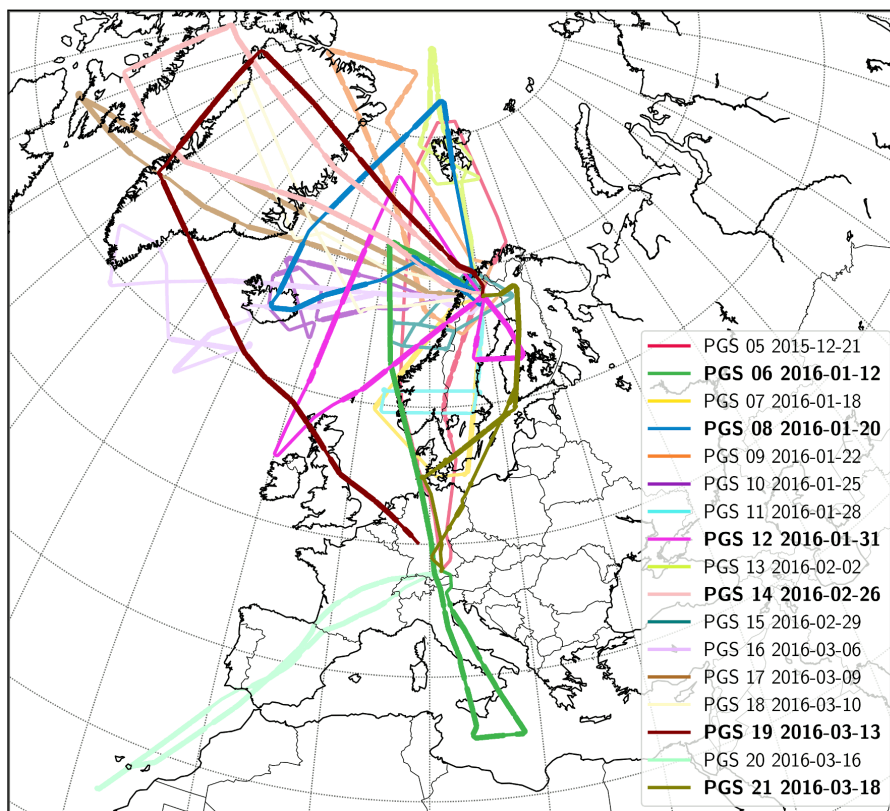


Figure 4.1: Flight paths of all PGS flights with GLORIA measurements. The parts of the flights with GLORIA high-spectral-resolution-mode measurements are represented in bold lines. Flights PGS06 (12 January 2016), PGS08 (20 January 2016), PGS12 (31 January 2016), PGS14 (26 February 2016), PGS19 (13 March 2016), and PGS21 (18 March 2016) are discussed in detail in this work and are highlighted on the map.

- gravity waves.

For that purpose, nine in situ and three remote-sensing instruments probed the UTLS region during 18 HALO research flights between December 2015 and March 2016. The flight paths, covering regions between 80°W - 30°E longitude and 25°N - 87°N latitude, are shown in Fig. 4.1. These 18 PGS research flights, each with a duration of approximately 10 h (up to 8000 km distance), cover the whole time of the Arctic winter and provide a unique data set.

4.2 In situ instruments

The nine in situ instruments that were deployed on board HALO during the PGS campaign measure temperature and trace gases at the position of the aircraft with high precision and temporal resolution. Calibration measurements with reference gases or calibration units assure a high accuracy of the measurements.

The Airborne (chemical ionization) Mass Spectrometer (AIMS) measures HCl, SO₂,

HNO_3 and ClONO_2 at a time resolution of 1.7 s with a detection limit of 6–20 pptv, 10–15 % precision and an accuracy of 12–20 % (Jurkat et al., 2016, 2017). In addition, water vapor in low concentrations is measured in a second configuration (Kaufmann et al., 2016; Voigt et al., 2017).

Water vapor measurements between 1 and 1000 ppmv are performed with the Fast In-situ Stratospheric Hygrometer (**FISH**), which is based on Lyman- α photo-fragment fluorescence (Zöger et al., 1999). **FISH** is one of the core airborne in situ instruments for measuring water vapor in the **UTLS** (Fahey et al., 2014). **FISH** has a time resolution of 1 s and achieved a precision of $0.7\% \times \text{vmr}$ (volume mixing ratio; relative part of the precision) plus 0.35 ppmv (absolute part of the precision) with an overall accuracy of $6.6\% \times \text{vmr}$ during **PGS** (Meyer et al., 2015).

The Basic HALO Measurement and Data System (**BAHAMAS**) consists of a sensor package for basic meteorological parameters – such as temperature, pressure, airflow, wind and humidity – and a data acquisition system which provides additional interfaces into the aircraft avionic system and to an inertial reference system (Krautstrunk and Giez, 2012; Giez et al., 2017). Sensor data are available with a time resolution of 100 Hz; standard processing is based on a 10 Hz time resolution. The temperature measurement is based on an open-wire resistance temperature sensor, which is contained in a special Total Air Temperature (**TAT**) inlet located in the nose section of the aircraft. These housings are heated to prevent ice formation and designed to separate droplets and particles from the probed airflow ahead of the sensor. The airflow is slowed down inside the housing in order to approach **TAT** via adiabatic heating. Data processing contains several corrections to account for deviations from ideal inlet behavior (Bange et al., 2013). These corrections limit the accuracy of the temperature determination to about 0.5 K, while the precision of the measurement is estimated to be about 0.03 K by means of auto-covariance function analysis.

The Fast AIRborne Ozone instrument (**FAIRO**) measures ozone with a time resolution of 10 Hz (Zahn et al., 2012). The O_3 volume mixing ratio has a precision of ≈ 0.3 ppbv (at 10 Hz) and an accuracy (based on systematic errors) of $\approx 1.5\%$.

Additionally, the Gas chromatograph for the Observation of Stratospheric Tracers Mass Spectrometer (**GhOST-MS**) provides measurements of CFC-12 in the electron capture detector channel (Obersteiner et al., 2016).

4.3 Satellite observations

4.3.1 Aura/MLS

The NASA Earth Observing System Aura satellite was launched in July 2004 into a near-polar, sun-synchronous 705 km altitude orbit with the **MLS** deployed on board. The Aura satellite flies in formation in the “A-Train” constellation of satellites and has an approximately 13:45 local Equator-crossing time. The Aura/**MLS** instrument is a successor to the **MLS** instrument on the Upper Atmosphere Research Satellite (**UARS**)

Trace gas	vertical resolution	estimated error	recommended lowest retrieval surface
O ₃	3 km	10%	261 hPa
HNO ₃	4 km	30%	215 hPa
HCl	3 km	20-40%	147 hPa
ClO	3-4.5 km	5-20%	147 hPa
CH ₃ Cl	5-5 km	30-45%	147 hPa

Table 4.1: Approximate vertical resolution, typical estimated error, and recommended lowest (i.e., highest pressure) retrieval surface for MLS version 4 trace gases in the UTLS.

and is a limb sounder analyzing the thermal emission (wavelengths from 2.5 to 0.1 mm) of the atmosphere using seven radiometers to cover five spectral bands (Waters et al., 2006). The along-track scanning radiometers, pointing in the orbital flight direction and vertically scanning the limb of the atmosphere, scan the limb every 165 km along the orbit track. According to the orbit of the Aura spacecraft, the global coverage of measurements is from 82° S to 82° N.

In this work, the current **MLS** version 4.2 (Livesey et al., 2018) data of O₃ (Schwartz et al., 2015), HNO₃ (Manney et al., 2015b), HCl (Froidevaux et al., 2015), ClO (Santee et al., 2015b), and **CH₃Cl** (Santee et al., 2015a) are used. The quality and reliability of the v4 **MLS** data set are described by Livesey et al. (2018); detailed information on the quality of a previous version (v2.2) of **MLS** O₃, HCl, HNO₃, ClO, and **CH₃Cl** measurements can be found in dedicated evaluation papers (Froidevaux et al., 2008b,a; Santee et al., 2007, 2008a, 2013). Retrieval characteristics for **MLS** version 4 trace gases are summarized in Tab. 4.1.

4.3.2 SCISAT/ACE-FTS

The **ACE-FTS** is an infrared limb solar occultation instrument and the main payload of the Canadian SCISAT-1 satellite. The spacecraft was launched in 2003 into a 74° inclination circular orbit at 650 km altitude. In this study we use ClONO₂ from the **ACE-FTS** version 3.5/3.6 data (Bernath, 2017). The ClONO₂ data product has been validated (Sheese et al., 2016) and it has a vertical resolution of 3-4 km and up to 20% estimated error in the **UTLS**. Due to the solar occultation measurement geometry, no measurements are available during polar night and generally, the number of measured profiles is significantly lower (up to 30 per day in two latitude “bands”) compared to **MLS**. This limited sampling makes the usage of **ACE-FTS** daily vortex averaged data difficult, but as shown in various studies the quality of vortex averaged data is good for scientific use (e.g., Dufour et al., 2006; Santee et al., 2008b).

4.3.3 CALIPSO/CALIOP

The Cloud-Aerosol Lidar with Orthogonal Polarization (**CALIOP**) instrument on the Cloud-Aerosol Lidar and Infrared Pathfinder Satellite Observations (**CALIPSO**) satellite provides measurements of high altitude clouds (**PSCs** and cirrus) using backscatter coefficients at 532 nm and 1064 nm of the dual wavelength polarization-sensitive lidar (Winker et al., 2009). The **CALIPSO** satellite was launched 2006 and flies in a 98° inclination orbit at 705 km altitude, together (among others) with the Aura satellite in the NASA “A-train” constellation. This allows for nearly coincident measurements of **PSCs** with Aura/**MLS** trace gases. A detailed discussion of the **CALIOP PSC** climatology is given by Pitts et al. (2018).

4.4 Model simulations

4.4.1 CLaMS

The Chemical Lagrangian Model of the Stratosphere (**CLaMS**, McKenna et al., 2002b,a; Grooß et al., 2014) is a chemistry transport model (**CTM**) that has been utilized to simulate the chemical composition of the Arctic winter 2015/16 (Grooß et al., 2018). The version “PL8” model run was initialized 1 November 2015 with data from **MLS** observations of O₃, N₂O, H₂O, and HCl. The dynamics over the course of the winter have been specified by wind and temperature fields from the ERA-Interim analysis provided by **ECMWF**. **CH₃Cl** has been initialized using a correlation between a 15-day average of **CFC-11** simulated by **CLaMS** and **CH₃Cl** measured by **MLS**. This correlation was used instead of **CFC-11/CH₃Cl** correlations available from **ACE-FTS** (Brown et al., 2013) because **MLS** and **ACE-FTS** show differences in the LMS (Santee et al., 2013), where this study is focused. The model run employs 32 vertical entropy-preserving layers (Konopka et al., 2007) with an altitude-dependent vertical resolution of 400 m at 10 km up to about 800 m between 12 and 24 km altitude and a horizontal resolution of 100 km. The troposphere below 9 km only has a vertical resolution of about 2 km. Recent improvements to the model, such as the influence of galactic cosmic rays (Grooß et al., 2018), are considered in this model run.

For the comparison of **CLaMS** results to **GLORIA** and **MLS** measurements, backward trajectories are calculated from the geolocations of the measurements. At 12:00 UTC, the **CLaMS** output is spatially interpolated linearly onto these trajectory positions. Chemistry relevant for diurnal variations of target trace gases has been calculated along these trajectories.

The **CLaMS** sedimentation module offers the possibility to simulate **NAT** (Grooß et al., 2014) and ice (Tritscher et al., 2018) **PSC** cloud formation and corresponding denitrification and re-nitrification as well as dehydration and re-hydration. Information about the surface area density of ice, **NAT**, and **STS** particles per volume of air is available for every **CLaMS** air parcel. For comparison with the **CALIOP PSC** areal coverage, lower boundaries for the different surface area densities were defined to discriminate

PSCs from background aerosols. In accordance with the CALIOP detection thresholds, PSC thresholds for CLaMS simulations are as follows: $3.3 \mu\text{m}^2 \text{cm}^{-3}$ for STS droplets (Carslaw et al., 1994), $0.25 \mu\text{m}^2 \text{cm}^{-3}$ for NAT, and $0.5 \mu\text{m}^2 \text{cm}^{-3}$ for ice particles. Values exceeding those thresholds are counted as PSCs in those specific composition classes, respectively.

4.4.2 EMAC

The ECHAM5/MESSEy Atmospheric Chemistry (EMAC, Jöckel et al., 2010) model is an Eulerian chemistry climate model (CCM) that uses the fifth-generation European Centre Hamburg general circulation model (ECHAM5 version 5.3.02, Roeckner et al., 2006) and the second version of the Modular Earth Submodel System (MESSEy version 2.52). For the Arctic winter 2015/16 a simulation nudged to the dynamics of the ECMWF operational analyses has been initialized 1 July 2015. This model run was performed with a T106L90MA resolution with a spherical truncation of T106 (which corresponds to a horizontal resolution of approximately $1.125^\circ \times 1.125^\circ$ (latitude \times longitude)) and 90 vertical hybrid pressure levels from the surface up to 0.01 hPa (approx. 80 km). The vertical resolution in the UTLS is about 0.5 km. A comprehensive chemistry set-up with gas-phase and also heterogeneous reactions on PSCs was included using rate constants mainly from the Jet Propulsion Laboratory (JPL, Sander et al., 2011). A detailed description of this model simulation is given by Khosrawi et al. (2017).

4.5 Meteorological data

The input profiles for temperature, pressure and water vapor for GLORIA retrievals are taken from ECMWF analysis data. These meteorological analyses from the “atmospheric model high resolution” (HRES) are available every 6 h with a horizontal resolution of 1° and 137 vertical levels up to a top pressure level of 0.1 hPa. The global fields of temperature, pressure and PV are interpolated on a vertical grid of absolute altitude.

The Modern-Era Retrospective analysis for Research and Applications, Version 2 (MERRA2) is the standard meteorological reanalysis data set of the NASA Global Modeling and Assimilation Office (Gelaro et al., 2017). Global fields of temperature, pressure, θ , and PV at $0.625^\circ \times 0.5^\circ$ (longitude \times latitude) horizontal resolution and 83 vertical levels are used for scientific analyses in Chapter 6 (Pawson and Global Modeling and Assimilation Office, 2015). Note that both atmospheric models used in this thesis, CLaMS and EMAC, apply meteorological data from ECMWF rather than MERRA2.

Chapter 5

Measurement characterization and validation

The goal of this chapter is to characterize and validate the **GLORIA** observations during the course of the Arctic winter, involving measurements under cloud-free conditions and conditions affected by **PSCs**. The data product is characterized considering random and systematic errors. An approach for correcting systematic line-of-sight errors in limb-imaging observations is presented. Finally, the **GLORIA** observations are brought into a broader perspective by comparisons with Aura/**MLS** observations. Furthermore, the capability of **GLORIA** to resolve mesoscale structures in the **UTLS** is demonstrated. This chapter shall provide the baseline for scientific studies in the following chapters using **GLORIA** measurements.

The results of the **GLORIA** measurements for the flight on 13 March 2016 (PGS19) are shown in the following part. Flight PGS19 is selected as an example of continuous measurements in high-spectral-resolution mode and as an example of an illustrative amount of atmospheric variability within the measured air masses. Results for all of the other 14 PGS research flights with **GLORIA** measurements at high spectral resolution are shown in the supplement of Johansson et al. (2018). First, the meteorological and chemical background situation of this flight day and region is discussed on the basis of **MLS** measurements at an altitude level corresponding to a typical flight altitude for this specific flight. Then one exemplary temperature and **HNO₃** profile is characterized in detail. The main part of this section is the discussion of the **GLORIA** retrieval results for flight PGS19. For the discussion of the elevation angle correction, **LOS** results of the flight on 31 January 2016 (PGS12) are shown as an example of a different type of **LOS** distortion and correction. In order to provide a survey of all **GLORIA** measurements and their quality during the whole PGS campaign, comparisons to in situ and **MLS** measurements are presented as an overview. In addition, comparisons of **GLORIA** measurements from flight PGS08 (20 January 2016) with balloon-borne ozone and temperature measurements are shown to validate **GLORIA** vertical profiles.

5.1 Meteorological situation for flight PGS19 on 13 March 2016

The flight PGS19 on 13 March 2016 was the transfer back from the campaign base in Kiruna, Sweden, to Oberpfaffenhofen, Germany. This flight was planned to sample aged vortex air over the northwestern part of Greenland and to cross a region of subtropical air associated with a high tropopause between the east coast of Greenland and Ireland. Takeoff in Kiruna was at 07:08 **UTC**, and touchdown in Oberpfaffenhofen at 18:28 **UTC**. The first part of the flight was directed towards the northwestern coast of Greenland (see Fig. 5.1, way point “A”), flying over the Norwegian Sea and then in a southern direction to a refueling stop at Kangerlussuaq Airport in Greenland (way point “B”). **HALO** reaches its peak ceiling altitude shortly before each landing, when the air frame is at its lightest. Before reaching way point “B”, the flight altitude is high enough to sample subsided polar air masses over the northern part of Greenland. After this stop, the aircraft passed the northern Atlantic Ocean and the British Isles towards Oberpfaffenhofen in southern Germany.

The meteorological situation during this flight is shown in Fig. 5.1 (top row) with temperature (a) and **PV** (b) at a level corresponding to a typical flight altitude of 13 km for this specific flight. At this altitude and time of the winter, the **PV** determining the edge of the polar vortex according to Nash et al. (1996) is estimated as ≈ 9 **PVU**. The first part of the flight (until way point “A”) took place in relatively warm (220 to 230 K) air masses compared to the rest of the flight. **PV** increased along the flight track towards maximum values of more than 12 **PVU**. This indicates that the flight entered the late-winter polar stratosphere and presumably even aged subsided polar vortex air. During the flight leg between the way points “A” and “B”, the aircraft remained within these stratospheric air masses with relatively warm temperatures and high **PV**. On the flight leg from way point “B” towards the final destination, Oberpfaffenhofen, **HALO** left these air masses, with temperatures decreasing to 200 K and **PV** down to 4 **PVU** over the northern Atlantic Ocean. The air masses above the British Isles and central Europe showed temperatures of up to 210 K and **PV** of 6 to 9 **PVU** with fine filaments visible on the **PV** map. This might point to air masses remaining from the dissolving late-winter polar vortex.

For a comparison of the **MLS** measurements with **GLORIA**, the **MLS** data were selected for dates and times (for flight PGS19 between 06:00 and 18:00 **UTC**) of PGS flights, filtered by data quality as recommended by Livesey et al. (2018) and interpolated onto a regular horizontal grid (2° latitude \times 4° longitude) using a squared cosine as the weighting function. The width of this squared cosine function was chosen to be 1.5° for latitudes and 8.0° for longitudes, and a minimum threshold of 0.75 was selected. Additionally, the pressure coordinate of the **MLS** data is interpolated to geometric altitude for an easier comparison to the **GLORIA** data. This interpolation method does not provide meaningful comparisons of water vapor because tropospheric **H₂O** (in contrast to stratospheric **HNO₃** and **O₃**) is likely to vary significantly within the time range of Aura/**MLS**-measured profiles, which are selected for this type of interpolation. For this reason, no comparison of **GLORIA** and Aura/**MLS H₂O** measurements is shown.

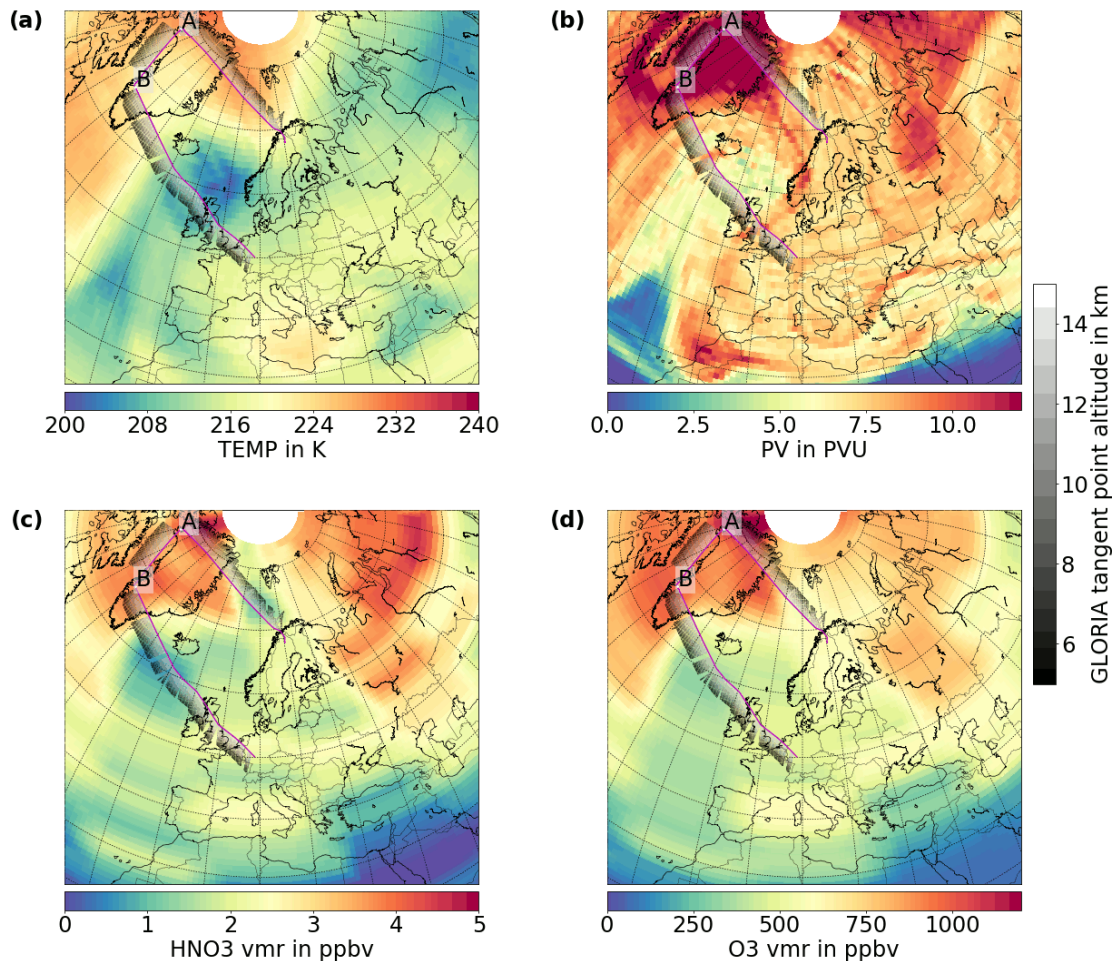


Figure 5.1: (a) Temperature and (b) potential vorticity (PV) from ECMWF meteorological analysis on 13 March 2016 at 12:00 UTC at 13.0 km, and (c) MLS HNO₃ and (d) O₃ measurements on 13 March 2016 between 06:00 and 18:00 UTC (approximation for the time period of flight PGS19) interpolated to a regular latitude–longitude grid and typical HALO cruising altitude of 13.0 km. For flight PGS19 on this day, the ground track of the HALO aircraft is shown with a magenta line, and the geolocations of GLORIA tangent points are shown along the flight track with points in the grayscale color map. Way points of this flight are marked with capital letters.

An overview of these gridded **MLS HNO₃** and **O₃** horizontal distributions is shown in Fig. 5.1 (bottom row) at a typical flight altitude of 13.0 km for flight PGS19 on 13 March 2016. The **HALO** flight track and geolocations (position and altitude) of **GLORIA** tangent points are also shown on these maps. Along the flight track, local minima in **MLS HNO₃** are observed above the Norwegian Sea and south of Iceland. Local maxima in **MLS HNO₃** and **O₃** are present above the northern part of Greenland at way point “A”.

5.2 Characterization of example profiles

The quality of the retrieved **GLORIA** data can be assessed by the estimated errors and by the vertical resolution (see Sect. 3.6). These quantities are shown in Fig. 5.2 as an example of the retrieval result of a temperature and nitric acid profile. In the left column (a, d) of this figure, the retrieval results and the initial-guess profiles are shown; the right panel (c, f) shows the vertical resolution. For these retrievals, a vertical resolution of 400 to 750 m is achieved. It can be seen that the shapes of the retrieved temperature and **VMR** profiles differ significantly from the initial-guess profiles at an altitude range between 5.5 and 13.5 km, reflecting the weak influence by the Tikhonov regularization. Above these altitude ranges, there is a small contribution from measurements with upward looking lines of sight, which explains the small differences in shape at these altitudes. In this region the vertical resolution is poor, and therefore little measurement information is obtained for these parts of the profiles. Below 5.5 km, no information is contributed by the measurement, and the profile shapes resemble those of the initial-guess profile.

In the second column (b, e) of Fig. 5.2, individual 1σ error contributions are shown. For the temperature, the total estimated error is predominantly influenced by the radiometric gain calibration (up to 1.0 K) and pointing uncertainties (in the range of 0.5 to 1.5 K). In case of **HNO₃**, the total estimated error is dominated by the spectroscopy error estimated as a constant relative fraction of 8.0% (as assumed in Sect. 3.6) and the uncertainties due to the previously retrieved temperature data (up to 0.3 ppbv). The pointing error has large contributions (up to 0.6 ppbv) to the total estimated error at altitude ranges where large vertical gradients in the profiles occur. At these altitude ranges with large vertical gradients even small changes in the elevation pointing have large influence on the absolute differences between the perturbed and the reference retrieval result. The radiometric offset and the retrieval noise error only contribute a minor part of the total error (≤ 0.5 K for temperature and ≤ 0.2 ppbv for **HNO₃**).

In the following discussion of the results, the retrieved profile, vertical resolution and total estimated error are presented as certain plots for a whole research flight. This simultaneously gives an overview of the whole data set measured by **GLORIA** and allows the characteristics of the results to be shown in detail.

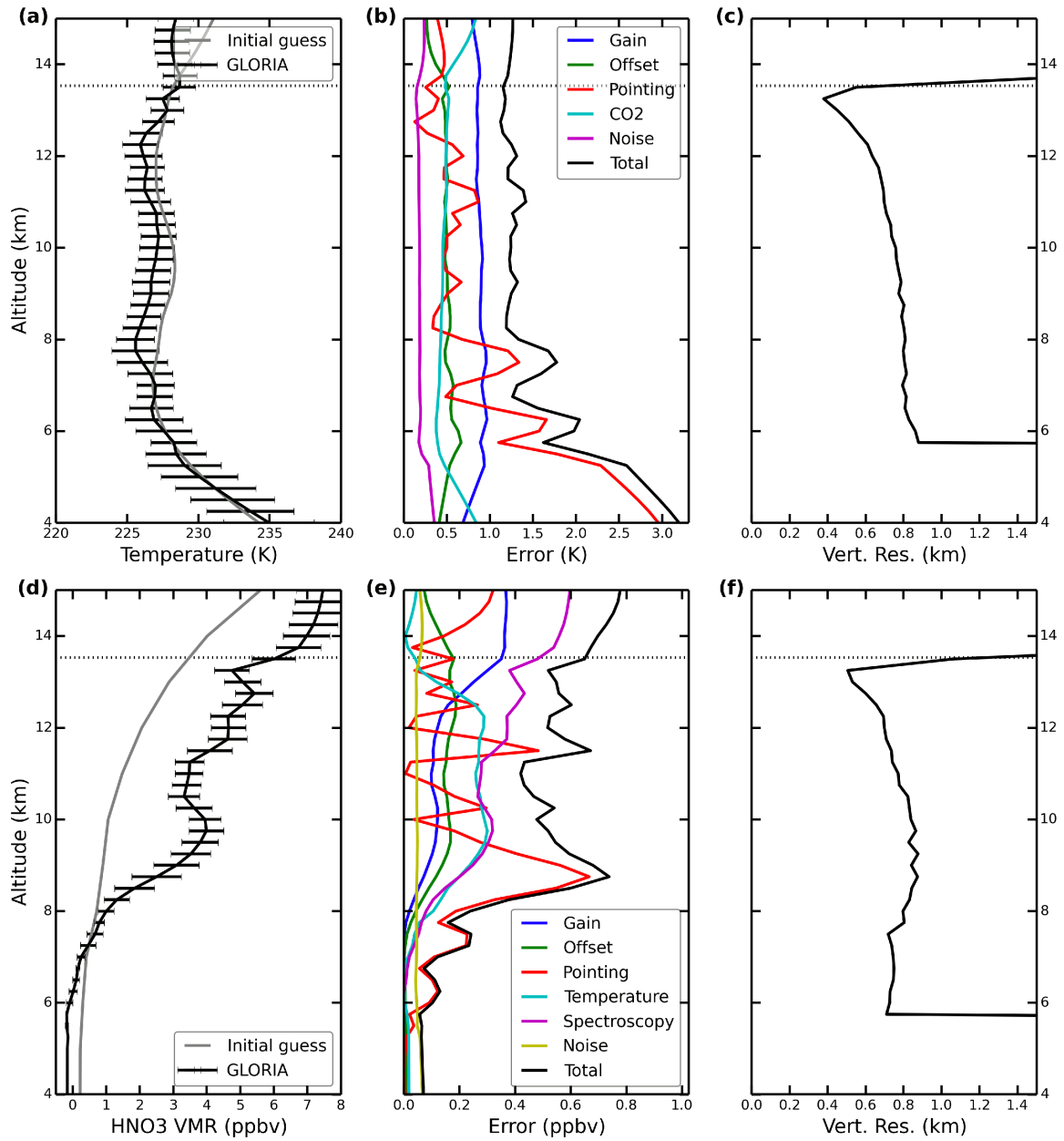


Figure 5.2: Illustration of the retrieval quality of temperature (a–c) and HNO₃ (d–f) of flight PGS19 on 13 March 2016 for a selected profile at 10:37:06 UTC. (a, d) Retrieved vertical profiles with total estimated error (black) and initial-guess profile (gray). The retrieved profiles have 14.9 and 12.5 degrees of freedom for temperature and HNO₃, respectively. (b, e) Different total error contributions and estimated total error. (c, f) Vertical resolution of this retrieval result. The dotted line represents the flight altitude of the aircraft.

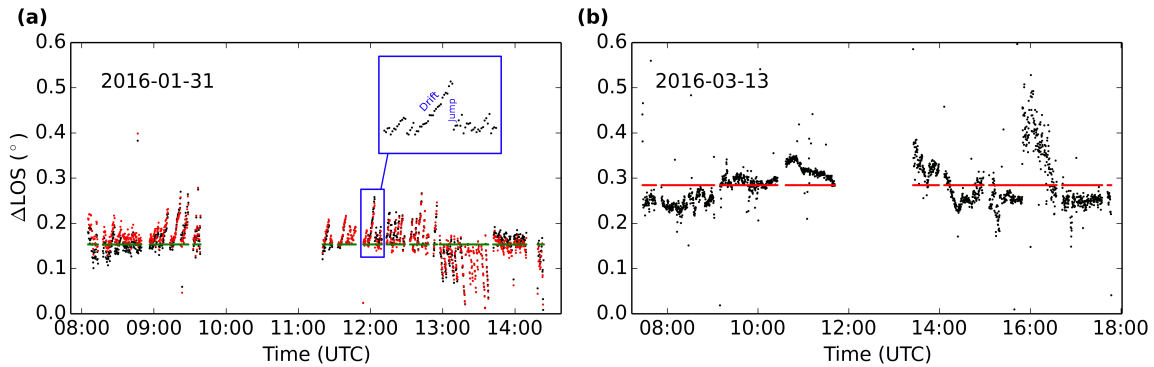


Figure 5.3: Line-of-sight correction of two flights (**a**: PGS12; **b**: PGS19) during the PGS campaign. The retrieved deviation of the **LOS** from the nominally set value is shown in black, the applied correction in red and for flight PGS12 the averaged **LOS** (before applying the correction of the drift) in green.

5.3 GLORIA results

5.3.1 Line of sight

For each flight, one systematic pointing correction is derived from the retrieval. The pointing elevation angle is retrieved to compensate for systematic misalignment of the pointing system of **GLORIA**. For this **LOS** retrieval, **ECMWF** temperature is set fixed. The **LOS** retrieval results for the flights on 31 January and on 13 March 2016 are shown as the difference between expected and retrieved elevation angle (black dots in Fig. 5.3). The difference can be caused by a systematic **LOS** calibration error, thermal deformation of the instrument during flight, or differences in the atmospheric state compared to the **ECMWF** fields (which also affect the intensity of the CO_2 spectral lines that are used for the **LOS** retrieval). While a constant **LOS** offset can be attributed to a systematic **LOS** calibration error, it is not possible to distinguish between atmospheric variations and thermal deformations of the instrument. For that reason, generally only one average **LOS** correction value per flight is used to correct for the systematic, time-independent **LOS** calibration error. For future campaigns it is planned to ensure the quality of the pointing by ground-based absolute pointing calibrations and by in-flight measurements of the moon on a regular basis. An example of this average correction, which is applied for flights between 2 February and 18 March 2016, is shown in Fig. 5.3b (red dots).

For flights between 21 December 2015 and 31 January 2016, a malfunction of the pointing control software caused the **LOS** to drift away from the commanded elevation. At certain points the software changed the instrument elevation back to its correct value, and steep steps in the retrieved pointing elevation angle are observed on these flights (see Fig. 5.3a, enlargement: “Drift” and “Jump”). A correction of this artifact can be calculated by interpolating the **LOS** between the points immediately after a steep step. This interpolated line between the correct elevation angles approximates the **LOS** that would have been retrieved for a measurement without this software malfunction. The

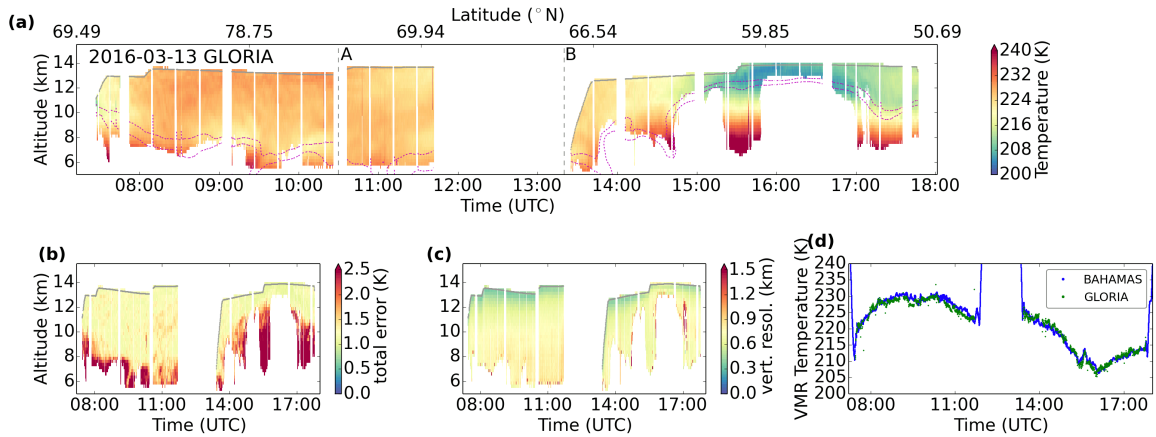


Figure 5.4: Temperature from flight PGS19: cross section of (a) retrieved temperature (the flight altitude is marked with a gray line, white spaces mark regions without data, the ECMWF potential vorticities of 2 and 4 PVU are marked with magenta dashed lines, and way points are marked with gray vertical dashed lines) and cross sections of (b) estimated total error and (c) vertical resolution, followed by (d) comparison of the GLORIA measurements (green) to the BAHAMAS in situ measurements (blue).

same average LOS correction, which is used for other flights, can be calculated from this interpolated LOS (Fig. 5.3a, green points). This is the first part of the LOS correction for these flights. In the second part, the influence of the software malfunction can be extracted by subtraction of the interpolated LOS from the retrieved LOS. For an idealized measurement (without any further error in the LOS), this method separates the effect of the software malfunction from long-term variations (which have been corrected for in the first part). For subsequent retrievals of temperature and volume mixing ratios, both corrections, the average LOS correction and the correction of the steps, have been applied (Fig. 5.3a, red points).

5.3.2 Temperature

The retrieved temperature along with characterization diagnostics and comparison to in situ observations for flight PGS19 is shown in Fig. 5.4. The retrieval results in panel (a) show the temperature profiles in a color-coded curtain plot. This type of plot is also used to present the curtains of volume mixing ratio results. The lower horizontal axis indicates the measurement time, and the upper horizontal axis the corresponding latitude of the aircraft. The vertical axis shows the absolute altitude of the retrieval grid points. The retrieval result is filtered according to the vertical resolution. Only data points with a vertical resolution better than 2 km are presented. For that reason, the data above flight level are filtered out. The measured spectra below cloud tops were also filtered out prior to the retrieval. The time between 12:00 and 13:00 UTC was spent on the ground due to a refueling stop of the aircraft. Smaller gaps between the profiles are due to radiometric calibration measurements. As a measure for the dynamical tropopause, the ECMWF potential vorticity interpolated to the GLORIA tangent

points is shown in magenta dashed lines, marking the values of 2 and 4 PVU. In the first part of the flight (until way point “B”), high temperatures are observed. The dynamical tropopause is at low altitudes down to 6 km, and mainly stratospheric air masses are sampled by GLORIA during this part of the flight. These stratospheric air masses at low altitudes suggest subsidence of air masses from the polar vortex during the late winter. The second part of this flight shows the transition to a higher tropopause up to 12 km and also stronger vertical gradients from higher temperatures (240 K) at lower altitudes, down to temperatures as low as 205 K at flight altitude. The last hour of measurements shows again a lower tropopause and less steep vertical gradients.

The total estimated error (b) indicates for most data points values in the range of 1.0 to 1.3 K. Especially in regions with higher temperature, the retrieval results are less accurate due to higher gain error contributions. The main error contribution is the pointing error because of vertical gradients. The vertical resolution (c) of the temperature retrieval is between 500 and 800 m. Altitudes closer to the aircraft usually show a better vertical resolution due to denser spacing of the tangent points.

In situ measurements taken at flight level are compared to the GLORIA retrieval results obtained close to the flight altitude. From each vertical profile retrieved from GLORIA, the grid point which is closest to the flight altitude (i.e., between 0 and 250 m underneath the flight altitude) and which has a vertical resolution better than 2 km is chosen for comparison. This assures the best possible match of sampled air masses with the in situ instrument. It is important to keep in mind that the data sets do not probe exactly the same air masses, since GLORIA measures at the limb and thus collects the radiation from a long path of ≈ 100 km through the atmosphere (Ungermaun et al., 2012, 2011). In Fig. 5.4d the comparison of GLORIA temperatures (green dots) to the BAHAMAS in situ measurements (blue dots) is presented. The two measurements show agreement to within 1.3 K, which is the estimated error of the GLORIA temperature retrieval.

5.3.3 Nitric acid

Due to the formation and sedimentation of polar stratospheric clouds and the resulting de- or re-nitrification (Peter and Grooß, 2012), nitric acid (HNO_3) is expected to display irregularly small structures in the UTLS region. For that reason, it is important to achieve spatially highly resolved and validated measurements of HNO_3 in the UTLS. The GLORIA retrieval results for flight PGS19 are presented in Fig. 5.5. The two-dimensional distribution of HNO_3 volume mixing ratios shows fine structures with maximum values up to 7 ppbv. The retrieval has a typical vertical resolution of 500 to 800 m, and the error is typically 0.5 ppbv. The comparison to the in situ data measured by AIMS is given in Fig. 5.5e. The strong fluctuations of HNO_3 are captured simultaneously by both instruments. The agreement between the instruments is often better than 0.5 ppbv. However, at some locations their differences reach up to 2.0 ppbv. These discrepancies reflect the large atmospheric variability in the horizontal direction due to denitrification processes along the GLORIA line of sight. The horizontal distribution of PV (Fig. 5.1b) suggests that at this part of the flight (from way point “B” to the final destination, Oberpfaffenhofen) air masses influenced by outflow of the polar vortex are

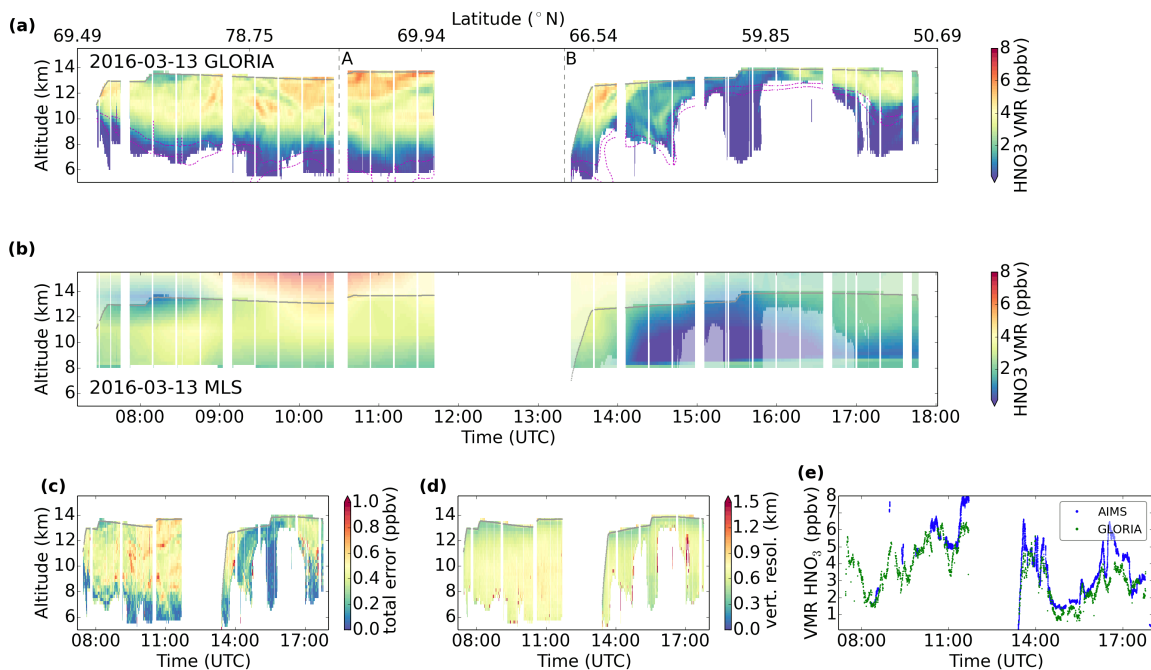


Figure 5.5: HNO₃ from flight PGS19: cross section of (a) retrieved HNO₃ volume mixing ratio (the flight altitude is marked with a gray line, the ECMWF potential vorticities of 2 and 4 PVU are marked with magenta dashed lines, and way points are marked with gray vertical dashed lines). Cross section of (b) MLS HNO₃ data interpolated to the GLORIA tangent points and latitude/longitude flight path coordinates above the aircraft. Regions with no corresponding GLORIA measurement are marked with fainter colors. Cross sections of (c) total estimated error, (d) vertical resolution and (e) comparison of the GLORIA measurements (green) to the AIMS in situ measurements (blue).

sampled, which explains higher variability in trace gas distributions. This atmospheric variability is also visible in the MLS HNO₃ horizontal distribution along the GLORIA viewing direction as shown in Fig. 5.1c. For a qualitative comparison to the airborne measurements, the gridded MLS HNO₃ data have been interpolated to the GLORIA tangent points (Fig. 5.5b). Considering the different spatial resolutions of the airborne and the spaceborne data, both HNO₃ distributions show relative minima and maxima at the same locations, and the absolute values are on the same order of magnitude. Due to the lower vertical resolution of MLS HNO₃ measurements, they are more influenced by air masses at higher altitudes, and small structures cannot be resolved. This difference in spatial resolution explains lower absolute HNO₃ in MLS compared to GLORIA. The advantage of the satellite product, though, is information about air masses above the HALO flight altitude and how these large-scale structures of HNO₃ are connected with the filaments measured by GLORIA.

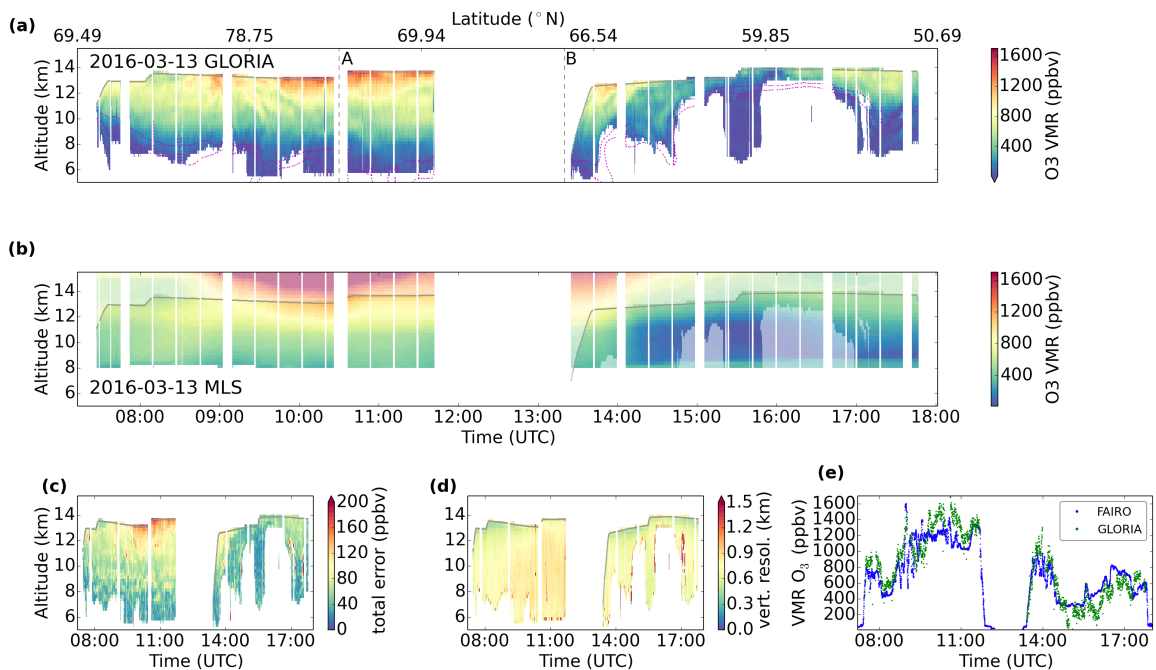


Figure 5.6: O₃ from flight PGS19: cross section of (a) retrieved O₃ volume mixing ratio (the flight altitude is marked with a gray line, the ECMWF potential vorticities of 2 and 4 PVU are marked with magenta dashed lines, and way points are marked with gray vertical dashed lines). Cross section of (b) MLS O₃ data interpolated to the GLORIA tangent points and latitude/longitude flight path coordinates above the aircraft. Regions with no corresponding GLORIA measurement are marked with fainter colors. Cross sections of (c) total estimated error, (d) vertical resolution and (e) comparison of the GLORIA measurements (green) to the FAIRO in situ measurements (blue).

5.3.4 Ozone

The measured ozone (O₃) distribution during flight PGS19 is shown in Fig. 5.6, where maximum values up to 1600 ppbv at altitudes of 13 km are observed. Below this maximum, finer structures are present. Spatial features are in agreement with the ones observed in HNO₃ (see Fig. 5.5), which is expected from atmospheric chemistry (Popp et al., 2009). This close correlation between the GLORIA measurements of both trace gases is an additional self-check for the validity of our results. The total estimated error (up to 150 ppbv) is dominated by spectroscopic and gain uncertainties. Vertical resolutions from 500 to 900 m are achieved. In comparison to the FAIRO in situ measurements, the GLORIA retrieval results follow both the long-term and the short-term variations. The agreement of the two measurements is typically better than 100 ppbv. In regions of maximum observed O₃ mixing ratios, high profile-to-profile variations up to 200 ppbv are visible. These variations are explained by the estimated total error and by the expected atmospheric variability along the GLORIA line of sight. In the second part of the flight, GLORIA and FAIRO ozone data show different structures and differences between the measurements up to 300 ppbv. This is the same region where the HNO₃ in situ comparison shows differences and where an inhomogeneous horizontal dis-

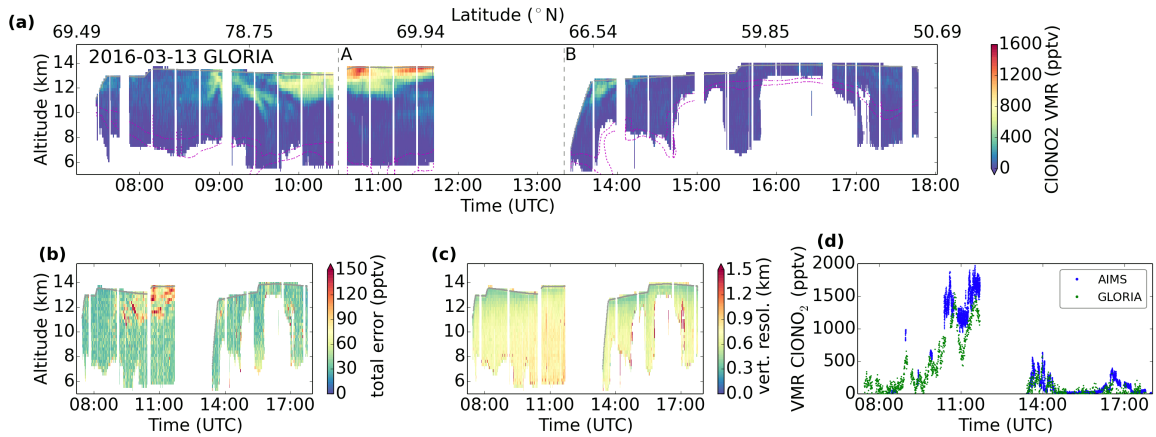


Figure 5.7: ClONO_2 from flight PGS19: cross section of (a) retrieved ClONO_2 volume mixing ratio (the flight altitude is marked with a gray line, the ECMWF potential vorticities of 2 and 4 PVU are marked with magenta dashed lines, and way points are marked with gray vertical dashed lines). (b) Cross sections of total estimated error, (c) vertical resolution and (d) in situ comparison of the GLORIA measurements (green) to the AIMS in situ measurements (blue).

tribution is suspected to distort the comparison of these measurements. The horizontal distribution of O_3 at 13 km altitude as derived from MLS measurements is illustrated in Fig. 5.1d. A horizontal gradient is seen above Baffin Bay (the region covered by the GLORIA tangent points between way points “A” and “B”; higher O_3 volume mixing ratios in the GLORIA line of sight compared to the aircraft position). The comparison of GLORIA O_3 to the MLS distributions interpolated to the GLORIA geolocations shows very similar large-scale structures in both data sets. Again, small-scale structures which are visible in GLORIA measurements are not captured in the lower-resolution MLS data.

5.3.5 Chlorine nitrate

Besides HCl, chlorine nitrate (ClONO_2) is the second reservoir species of chlorine in the stratosphere. As was initially shown by infrared limb-emission observations (von Clarmann et al., 1993; Oelhaf et al., 1994; Roche et al., 1994), chlorine deactivation in the Arctic spring region usually results in strong enhancement of ClONO_2 . The retrieved ClONO_2 distribution in Fig. 5.7 shows several fine structures and maximum values up to 1500 pptv in the flight section that reached the highest PV values (between way points “A” and “B”; see Fig. 5.1b), which can be interpreted as subsided deactivated chlorine in the form of ClONO_2 . The corresponding values of the total estimated error are 150 pptv. In the case of background values (< 100 pptv), the estimated errors are 30 pptv. The increased errors for enhanced values are caused by the impact of relatively increased gain errors. Vertical resolutions of 500 to 900 m are calculated for this retrieval. The comparison to the AIMS in situ measurements of ClONO_2 shows agreement of the two data products to within 200 pptv, except for the maximum values, where differences

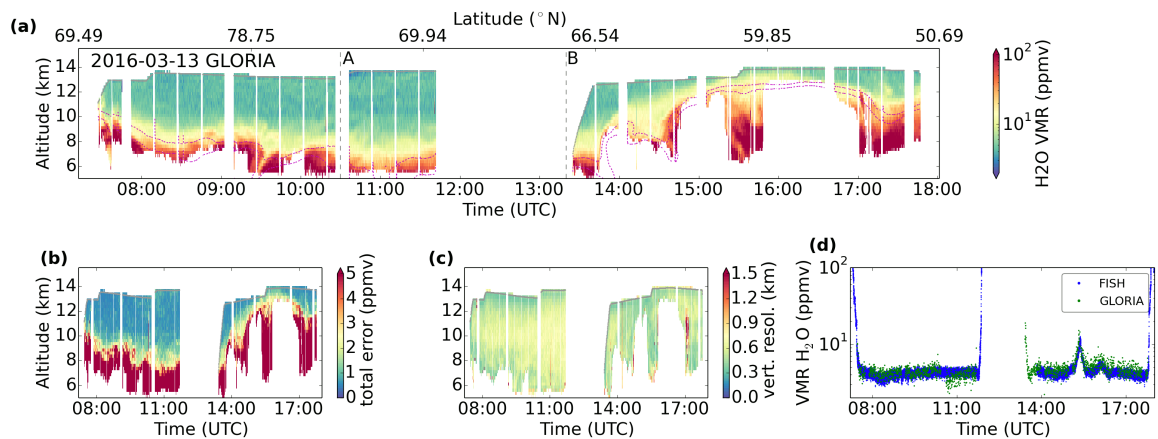


Figure 5.8: H₂O from flight PGS19: cross section of (a) retrieved H₂O volume mixing ratio (the flight altitude is marked with a gray line, the ECMWF potential vorticities of 2 and 4 PVU are marked with magenta dashed lines, and way points are marked with gray vertical dashed lines). Cross sections of (b) total estimated error, (c) vertical resolution and (d) comparison of the GLORIA measurements (green) to the FISH in situ measurements (blue).

are up to 500 pptv. Here, the GLORIA retrieval shows a lower absolute VMR but a similar structure. Again, this difference is attributed to an offset in altitude and a possible horizontal gradient, which averages the measured signal along the GLORIA line of sight.

5.3.6 Water vapor

Water vapor (H₂O) is mainly present in the troposphere. GLORIA H₂O distributions allow for investigations of mesoscale structures such as tropopause folds (Shapiro, 1980). In polar studies, H₂O is of interest because these distributions are used to understand the formation and decay of polar stratospheric ice clouds (dehydration and re-hydration) (Fahey et al., 1990). The distribution of H₂O (Fig. 5.8) reflects the tropopause altitude with very low stratospheric values (≈ 5 ppmv) in the region of the aged vortex (way point “A” to way point “B”) and high values (10–20 ppmv) above the intrusion of subtropical air where HALO was close to the tropopause (way point “B” to the final destination, Oberpfaffenhofen). The total estimated error shows higher values (> 5 ppmv) in regions with enhanced H₂O VMR compared to errors below 1 ppmv in regions with measured stratospheric background values. The vertical resolution is between 400 and 700 m. The comparison to the FISH in situ measurements shows agreement to within the GLORIA error of typically 1 ppmv. The enhancement at flight altitude at 15:30 UTC is well captured in both data sets.

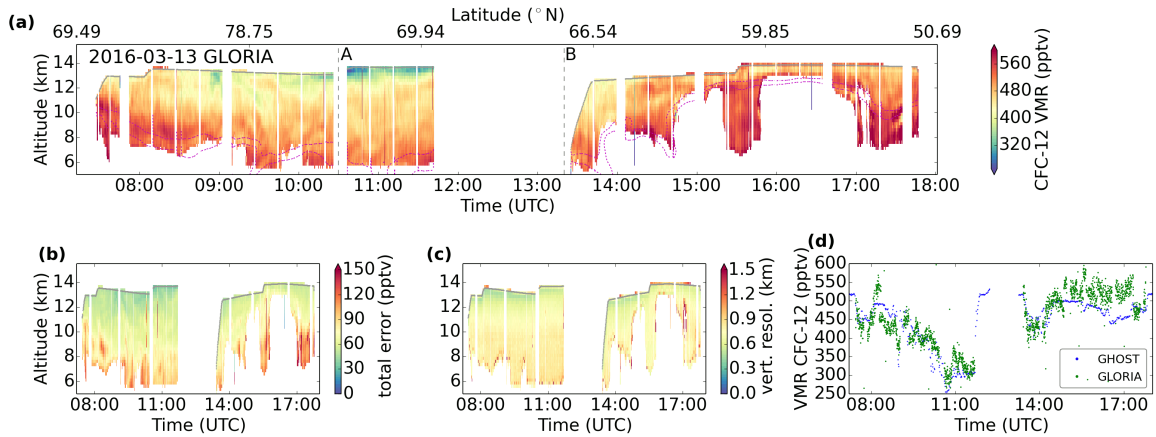


Figure 5.9: CFC-12 from flight PGS19: cross section of (a) retrieved CFC-12 volume mixing ratio (the flight altitude is marked with a gray line, the ECMWF potential vorticities of 2 and 4 PVU are marked with magenta dashed lines, and way points are marked with gray vertical dashed lines). Cross sections of (b) total estimated error, (c) vertical resolution and (d) comparison of the GLORIA measurements (green) to the GhOST-MS in situ measurements (blue).

5.3.7 Chlorofluorocarbon 12

Dichlorodifluoromethane (CFC-12) is a chlorofluorocarbon that has been artificially produced for usage as refrigerants and aerosols. Its production is regulated by the Montreal Protocol due to its potential for ozone depletion (WMO, 2015). Because of its vertical gradient, CFC-12 can be used as a tracer for tropospheric air and for the altitude of the air masses (Greenblatt et al., 2002). The VMR distribution along flight PGS19 of CFC-12 is presented in Fig. 5.9. Here, mainly volume mixing ratios of about 500 pptv are observed in the troposphere. In the area where aged subsided vortex air was reached (way point “A” to way point “B”), values as low as 320 pptv were found. The error is between 40 and 130 pptv. The vertical resolution is in the range of 500 to 1000 m. The comparison to the in situ measurements by GhOST-MS shows agreement to within 70 pptv. The high profile-to-profile variation up to 100 pptv of GLORIA CFC-12 that can be seen in this in situ comparison plot exceeds the total estimated error at flight altitude of ≈ 70 pptv. These fluctuations may be caused by the atmospheric variability along the GLORIA line of sight. This variability is also present in all other flights of this campaign (see Table 5.1). In addition, compared to other GLORIA retrievals, a higher number of extreme outlier points are observed in the GLORIA CFC-12 data. This is an indication that the retrieval for CFC-12 is more sensitive to perturbations in the spectra (e.g., high-altitude clouds that have not been effectively filtered) compared to the retrievals of temperature and other trace gases.

5.4 Overview of in situ comparisons for the PGS campaign

For an overview of comparisons of **GLORIA** high-spectral-resolution retrieval results to in situ measurements for all PGS flights, the median difference and the median absolute deviation (Rousseeuw and Croux, 1993) are presented in Table 5.1. The median difference gives a measure of the accuracy of the match between the data sets, and the median absolute deviation is a method for describing the spread around this median value. Both measures are robust methods, and a few extreme mismatches do not have a large influence. Detailed plots for flights that are not described as thoroughly as flight PGS19 are provided in the supplement of Johansson et al. (2018). Rather large deviations, in particular in temperature, are present in numerous flights in January 2016, which have been strongly affected by **PSCs** at and above flight level. From the **HALO** flight crew, **PSCs** were reported at these altitudes for PGS flights until PGS14 (26 February 2016). The influence of **PSC** and high-altitude cirrus clouds on the spectra are reflected in Fig. 3.9a as lower **CI** values at and below flight altitude. Except for the problems with clouds at or above flight altitude, the comparisons of **GLORIA** and in situ instruments over the whole campaign show reasonably low biases between the data sets. Atmospheric conditions influencing the measurement conditions for remote-sensing change during the winter: In January, many **PSCs** occur, which influence the measured infrared spectra and make temperature and trace gas retrievals challenging. Towards the end of the Arctic winter, more delicate structures in trace gases are present due to nitrification and related events, which make comparisons of measurements at different geolocations more difficult. These changing atmospheric conditions are also visible in the comparisons in Table 5.1: Deviations between **GLORIA** and **BAHAMAS** temperatures are larger for flights in January (due to the influence of **PSCs**). Another measure for the agreement between **GLORIA** and in situ instruments is the part of co-located measurements, of which the differences are within twice the combined estimated errors of the cross-compared instruments. For temperature 88%, for **HNO₃** 73%, for **O₃** 63%, for **ClONO₂** 53%, for **H₂O** 90%, for **CFC-12** 77% and in total 73% of the comparisons show this agreement. **ClONO₂**, **O₃**, and **HNO₃** show substantial variations at flight altitude (e.g., Figs. 5.7, 5.6, 5.5). The lower fraction of agreement is attributed to the higher atmospheric variability of those trace gases, thereby complicating the comparison due to the strongly differing instrumental sampling characteristics. **MLS O₃** and **HNO₃** values become increasingly smaller compared to the corresponding **GLORIA** measurements towards the end of the Arctic winter. This is explained by the fine structures which are visible in the **GLORIA** measurements but not resolved in **Aura/MLS** data due to their lower vertical resolution and horizontal gridding.

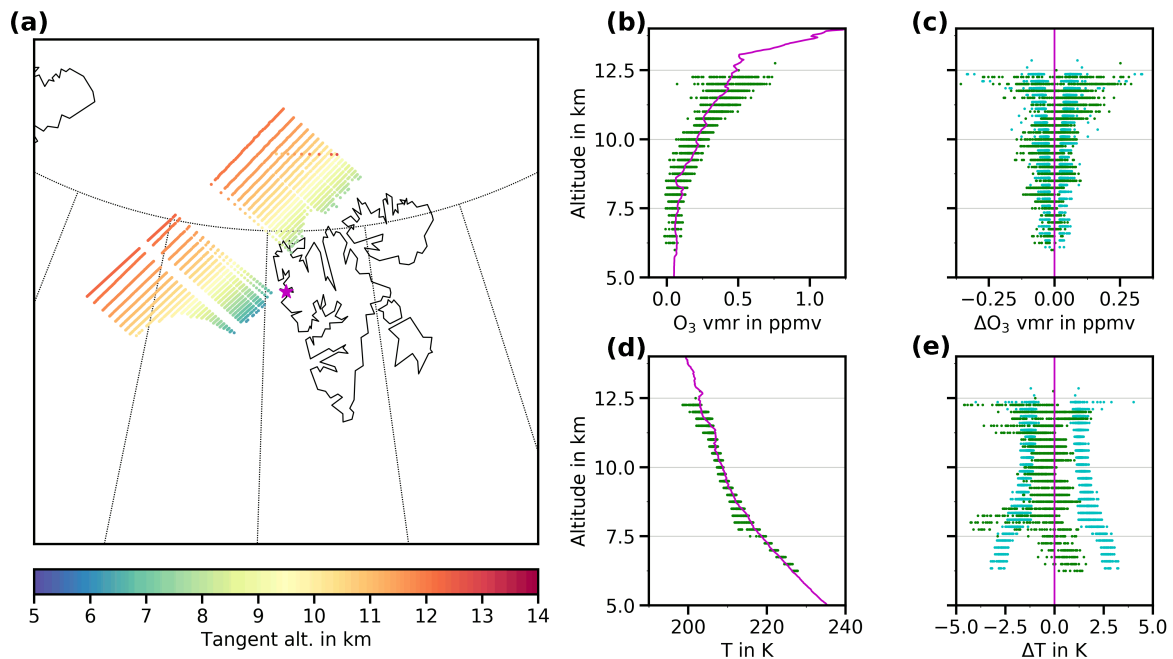


Figure 5.10: Comparison of O_3 and temperature from balloon-borne measurements and **GLORIA**: (a) shows on a map where the sonde was launched in Ny-Ålesund, Spitsbergen on 20 January 2016, 16:32 (magenta star), and where the **GLORIA** tangent points selected for comparison are located (colored dots, indicating the altitudes). (b) shows the O_3 VMR profile measured by the sonde (magenta line) and all selected **GLORIA** retrieval results (green points), and (c) shows the absolute differences between these measurements (**GLORIA** minus sonde, green points), together with the total estimated errors of the selected **GLORIA** measurements (cyan points, for better discrimination with the differences, these points are plotted 100 m higher than marked by the y-axis). Panels (d) and (e) show the same plots for temperature. Courtesy ozone sonde data: Peter von der Gathen (AWI).

5.5 Vertical validation of temperature and O₃ profiles

During flight PGS08 (20 January 2016), **GLORIA** collected measurements spatially and temporally close a balloon-borne ozone sonde (Vaisala, 2016, Vaisala RS41), launched on 20 January 2016, 16:32 from Ny-Ålesund, Spitsbergen. The location of the launch site and selected **GLORIA** measurement geolocations (average position of the profile closer than 300 km to the launch site) between 15:34 and 16:33 are shown in Fig. 5.10a. Flight PGS08 started westbound in Kiruna until Iceland, where it turned towards north of Spitsbergen, and then back to Kiruna. The late January phase was the coldest time during this Arctic winter (Manney and Lawrence, 2016). This flight was almost completely inside the polar vortex, and **PSCs** were observed down to flight altitudes (Braun et al., 2019).

Comparisons between the ozone sonde profile (magenta) and O₃ retrieved from **GLORIA** measurements are shown in Fig. 5.10b, and differences (green) together with total estimated errors in Fig. 5.10c. These profiles show that both measurements are in agreement, and for most altitudes the **GLORIA** profiles scatter around the ozone sonde profile. Most, but not all of the differences between the measurements are within the total estimated errors. This indicates that these differences are a result of both measurement uncertainty and atmospheric variability. Temperature comparisons also show an agreement between both data sets, again with a larger variation of the **GLORIA** profiles (see Fig. 5.10d). For most altitudes, these differences are smaller than the total estimated errors (Fig. 5.10e). Around 8 km altitude, **GLORIA** temperatures are particularly colder than sonde temperatures, which might indicate a strong temperature gradient at these altitudes.

Flight date	Temp. [K]	HNO ₃ [ppbv]		O ₃ [ppbv]		ClONO ₂ [ppbv]		H ₂ O [ppmv]	CFC-12 [pptv]
		BAHAMAS	AIMS	FAIRO	MLS	AIMS	MLS		
15-12-21	-0.97 ± 0.63	0.38 ± 0.33	0.99 ± 0.35	40.5 ± 89.9	197.4 ± 86.9	20.3 ± 64.9	-0.42 ± 0.52	-21.9 ± 25.6	
16-01-12	-1.15 ± 0.91	0.03 ± 0.68	1.31 ± 0.79	-123.4 ± 127.4	257.4 ± 176.7	-35.3 ± 84.5		-58.2 ± 21.7	
16-01-18	-2.04 ± 1.47	0.47 ± 1.15	1.39 ± 0.82	66.6 ± 80.2	261.0 ± 149.1	-11.2 ± 75.8	-0.67 ± 0.59	-66.5 ± 50.5	
16-01-20	-1.99 ± 1.21	-1.03 ± 0.80	1.41 ± 0.74	19.7 ± 129.0	266.4 ± 126.6	-33.3 ± 70.7	-0.71 ± 0.76	-44.6 ± 48.3	
16-01-22	-1.09 ± 1.15	-0.10 ± 1.30	1.83 ± 0.66	-21.2 ± 108.9	365.7 ± 101.2	-11.0 ± 84.3	-0.01 ± 0.70	-55.3 ± 46.1	
16-01-25	-2.18 ± 0.66	-0.82 ± 0.99	1.84 ± 0.63	4.5 ± 109.9	435.8 ± 170.3	-6.6 ± 85.3	-0.32 ± 0.49	-57.9 ± 29.4	
16-01-28	-1.78 ± 0.67	-0.48 ± 0.42	1.37 ± 0.58	4.4 ± 37.8	230.4 ± 104.3	56.0 ± 78.6	-0.69 ± 0.40	-28.0 ± 13.7	
16-01-31	-0.56 ± 0.60	-1.83 ± 1.52	2.26 ± 0.86	17.8 ± 76.9	397.1 ± 134.6	7.3 ± 67.6	-0.75 ± 0.52	-9.2 ± 26.2	
16-02-02	-0.45 ± 0.76	0.21 ± 0.79	1.94 ± 0.72	17.0 ± 50.7	324.0 ± 123.7	-17.4 ± 60.2	0.07 ± 0.64	-17.1 ± 32.3	
16-02-26	-0.98 ± 0.80	0.23 ± 0.66	2.12 ± 1.58	-42.4 ± 92.4	319.8 ± 210.3	-22.4 ± 88.9	-0.24 ± 0.68	7.6 ± 29.2	
16-03-06	-0.82 ± 0.66	0.10 ± 0.48	2.46 ± 1.26	12.8 ± 68.6	387.2 ± 194.5	1.7 ± 87.4	-0.16 ± 0.68	-21.9 ± 53.6	
16-03-09	-0.83 ± 0.74	-0.38 ± 0.88	2.64 ± 1.06	72.9 ± 144.2	418.3 ± 194.0	-35.0 ± 127.8	-0.05 ± 0.49	-41.8 ± 49.9	
16-03-13	-0.14 ± 0.86	-0.24 ± 0.95	3.04 ± 1.10	55.7 ± 139.6	465.3 ± 225.2	-18.4 ± 202.6	0.24 ± 0.55	2.4 ± 39.6	
16-03-16	-0.06 ± 0.78	0.02 ± 0.42	0.32 ± 0.53	-114.8 ± 120.1	113.2 ± 97.8	-9.9 ± 235.4	-0.06 ± 0.55	26.4 ± 41.0	
16-03-18	-0.64 ± 0.98	0.69 ± 0.60	3.57 ± 0.76	60.5 ± 152.8	549.0 ± 234.4	-47.0 ± 131.5	0.19 ± 0.53	18.1 ± 34.6	
Campaign	-0.75 ± 0.88	-0.03 ± 0.85	2.01 ± 1.33	-3.5 ± 116.8	346.0 ± 202.7	-15.4 ± 102.8	-0.13 ± 0.63	-19.8 ± 46.9	

Table 5.1: Median differences between **GLORIA** and in situ and **Aura/MLS** measurements with the median absolute deviation (as a measure of the spread of the difference around the median value) for each flight and the whole campaign. For the flight on 12 January 2016 (PGS06) no water vapor in situ measurements are available.

Chapter 6

Chlorine partitioning and ozone loss in the 2015/16 Arctic winter lowermost stratosphere

In this chapter, the unique **GLORIA** data set is used to validate the processes for the chemical transport model Chemical Lagrangian Model of the Stratosphere (**CLaMS**) and the chemistry climate model ECHAM/MESSy Atmospheric Chemistry (**EMAC**) at the lower boundary of the polar vortex. Satellite measurements are utilized to put the **GLORIA** measurements into context of the Arctic winter 2015/16, and to investigate the temporal evolution of chlorine activation and deactivation in the **LMS** in comparison to **CLaMS**. O_3 measurements of **MLS** are used to estimate profiles of chemical ozone loss during the 2004-2017 time period. Sensitivity simulations are performed to estimate the influence of the availability of O_3 and reactive nitrogen (NO_y) on chlorine deactivation into **HCl** or **ClONO₂**. **CLaMS** is also used to estimate chemical ozone loss in 2015/16, which has not been reported by other studies. In another **CLaMS** sensitivity study, the influence of low temperatures on ozone and chlorine is probed. Additionally, the deactivation of chlorine into **ClONO₂** in the measured air masses is investigated. **CLaMS** is used to estimate, which fraction of measured **ClONO₂** arises from in situ deactivation in the **LMS** and which fraction has been transported downwards over the timescale of several days.

6.1 Measurements and model evaluation

In this section, the Arctic winter of 2015/16 is put into climatological context by comparing time series of satellite measurements of the **LMS** in that year with those of other Arctic winters. The 2015/16 satellite time series is then compared to **CLaMS** simulation results in more detail. After that, three exemplary flights from the PGS campaign are discussed regarding **GLORIA** O_3 , **ClONO₂**, and **HNO₃ VMR** cross sections. These aircraft measurements are then used to validate **EMAC** and **CLaMS** simulations. The state of deactivation of reactive chlorine to **ClONO₂**, and the variability of **ClONO₂**

and O_3 in the LMS region are estimated using correlations of these trace gases with CFC-11.

6.1.1 Time series

Time series of MERRA2 temperature and trace gas data of MLS (HCl , daytime ClO , O_3 , HNO_3 , and CH_3Cl) and ACE-FTS (ClONO_2) are used to provide context for the aircraft based measurements. These time series are created by spatially averaging all reanalysis temperatures and all measured trace gas profiles within the polar cap (latitudes $> 55^\circ\text{N}$) and within the polar vortex. The vortex is defined according to the sPV criterion described in Sec. 2.2). The data is linearly interpolated to levels of potential temperature for each day. Because of the pronounced diurnal cycle of ClO , all ClO nighttime measurements have been filtered out using the solar zenith angle (threshold of 90°) associated with the measurement. In order to compare the time series of the Arctic winter 2015/16 with other winters, these time series are created for all Arctic winters of the MLS and ACE-FTS epoch from 2004/05 to 2017/18.

The time series at $\theta = 380$ K for temperature, ClONO_2 , HCl , ClO , O_3 , HNO_3 , and methyl chloride (CH_3Cl) are shown in Fig. 6.1. For each species, the black line marks the mean for each day for all years from 2004 to 2018 (excluding 2015/16), dark grey shading depicts the standard deviation around this mean value and light grey shading marks minimum/maximum values of all time series (excluding 2015/16). The time series for the Arctic winter 2015/16, which is the focus of this thesis, is presented in red. The Arctic winters 2004/05 (green) and 2010/11 (cyan) are also highlighted. These winters are known for extremely low stratospheric temperatures and have been discussed in detail previously (e.g., Santee et al., 2008b; Manney et al., 2011).

In 2015/16, MERRA2 temperatures at 380 K were near or below the climatological minima through mid-January (Fig. 6.1a). Then two minor warmings (end of January and mid of February) and the final warming (early March) are visible in the 2015/16 temperature curve. ClONO_2 from ACE-FTS measurements (Fig. 6.1b) exhibits lower abundances in January 2016 compared to the other winters in the ACE-FTS record. Measurements available for February and March show that ClONO_2 followed a course in 2016 comparable to or below the multi-year average. The other chlorine reservoir HCl (Fig. 6.1c) sets a new minimum of all Aura/MLS time series in January and February for the year 2016. Consistent with the picture from HCl , the MLS ClO (Fig. 6.1d) is above the average for the whole winter and also establishes new maximum values on many days. O_3 in the LMS is slightly above the MLS average (Fig. 6.1e) in the beginning of the Arctic winter 2015/16, while minimum O_3 values are observed from mid February 2016 onward at 380 K. As discussed by Manney and Lawrence (2016), such extremely low O_3 has not been observed at higher altitudes (490 K), where the ozone loss was maximum in 2011. HNO_3 (Fig. 6.1f) shows an extreme behavior in 2015/16 at $\theta = 380$ K: In December 2015, HNO_3 exhibits a strong increase, reaching maximum values above 6 ppbv, whereas in March values consistently below 3 ppbv are measured. Methyl chloride (CH_3Cl), a largely biogenic trace gas that is well mixed in the troposphere and photolyzed in the stratosphere, is a useful tracer of diabatic descent within the

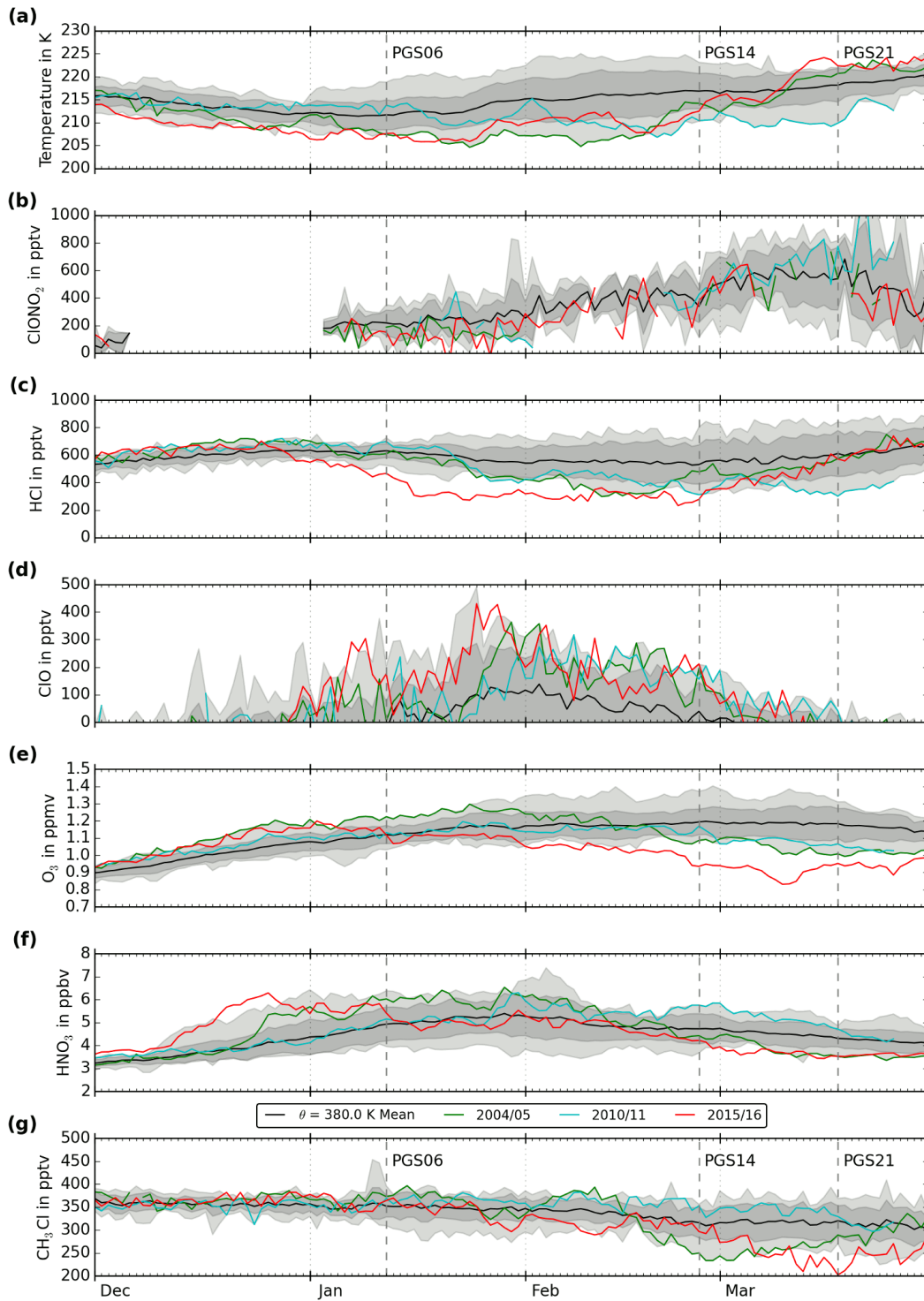


Figure 6.1: Vortex average time series of (a) temperature (MERRA2), and volume mixing ratios of (b) ClONO_2 (ACE-FTS), (c) HCl, (d) daytime ClO, (e) O_3 , (f) HNO_3 , (g) CH_3Cl (MLS) for the period 2004-2018 over the Arctic at $\theta=380\text{K}$ (≈ 15 km in January). The black line marks the average value for each day, the dark shaded area marks the standard deviation of each day between different years and the light shaded area marks minimum/maximum values within the time period. The Arctic winter 2015/16 has been excluded from all of these measures. Mean values for the Arctic winters 2004/05 (green), 2010/11 (cyan), and 2015/16 (red) are marked separately. Days with aircraft measurements discussed in this thesis are marked with dashed lines.

polar vortex. The time series of CH_3Cl is illustrated in Fig. 6.1g: The typically slow decrease of CH_3Cl due to diabatic descent is visible in the average VMR, which slowly decreases. During 2015/16, CH_3Cl followed a more or less climatological evolution until the beginning of March, when VMRs dropped rapidly and became highly variable with the onset of the major final warming.

Manney and Lawrence (2016) showed the extraordinary nature of the 2015/16 Arctic winter higher in the stratosphere (at 490 K). The contextual information from satellite observations in Fig. 6.1 illustrates how exceptional this winter also was in the LMS, where the PGS measurements were performed. At 380 K, the decrease in HCl and increase in ClO, indicative of substantial chlorine activation in the LMS, started earlier and reached more extreme levels in 2015/16 compared to any other year in the Aura/MLS record. The unusually strong chlorine activation at this level is also evident in the ClONO_2 abundances measured by ACE-FTS, which lie below the climatological mean in January 2016. Substantial chlorine activation in the Arctic LMS has rarely been reported previously (e.g., Santee et al., 2011). The unusually low O_3 abundances at 380 K towards the end of the winter can in principle either be caused by chemical ozone loss or by an unusual low diabatic descent. Since the diabatic descent at 380 K in 2015/16 essentially followed the climatological mean until the final warming in March, as seen in CH_3Cl , the unusually low O_3 abundances at 380 K indicate chemical ozone loss.

6.1.2 Comparison of satellite measurements to model simulations

For a comparison with the measured Arctic winter 2015/16 time series, the CLaMS simulations have been linearly interpolated to MLS geolocations (see Sec. 4.4.1). These data have been used to calculate vortex averaged profiles in the same manner as described in Sec. 6.1.1. In order to get a more complete picture of the CLaMS simulation, modeled ClONO_2 (which is measured by ACE-FTS) is also interpolated to the MLS geolocations. In addition, the daily PSC area is calculated and compared to CALIOP measurements. The comparison of the time series in the altitude range $\theta = 330 - 490$ K is illustrated in Fig. 6.2. Fig. 6.2a presents daily PSC area time series until the end of January 2016, when instrumental problems forced CALIOP to suspend measurements. The data product shown does not discriminate between cirrus clouds and PSCs in the UTLS region. Chlorine activation is also possible on cirrus clouds (e.g., Borrmann et al., 1996), and thus this panel indicates the area of potential heterogeneous chlorine activation. These cloud areas increase considerably at 490 K at the end of December 2015 and were also observed at potential temperatures as low as 380 K in the beginning of January 2016. The CLaMS simulation reveals the same temporal and spatial distribution of clouds as measured by CALIOP, but with slightly larger maximum cloud areas. For the rest of the winter (after CALIOP stopped measurements), CLaMS shows a rapid decrease of PSC area until the beginning of February and a short period with a small area of PSC occurrences at the end of February. ClONO_2 (Fig. 6.2b) displays enhancements of more than 1000 pptv at altitudes $\theta > 380$ K in March in both, the simulation

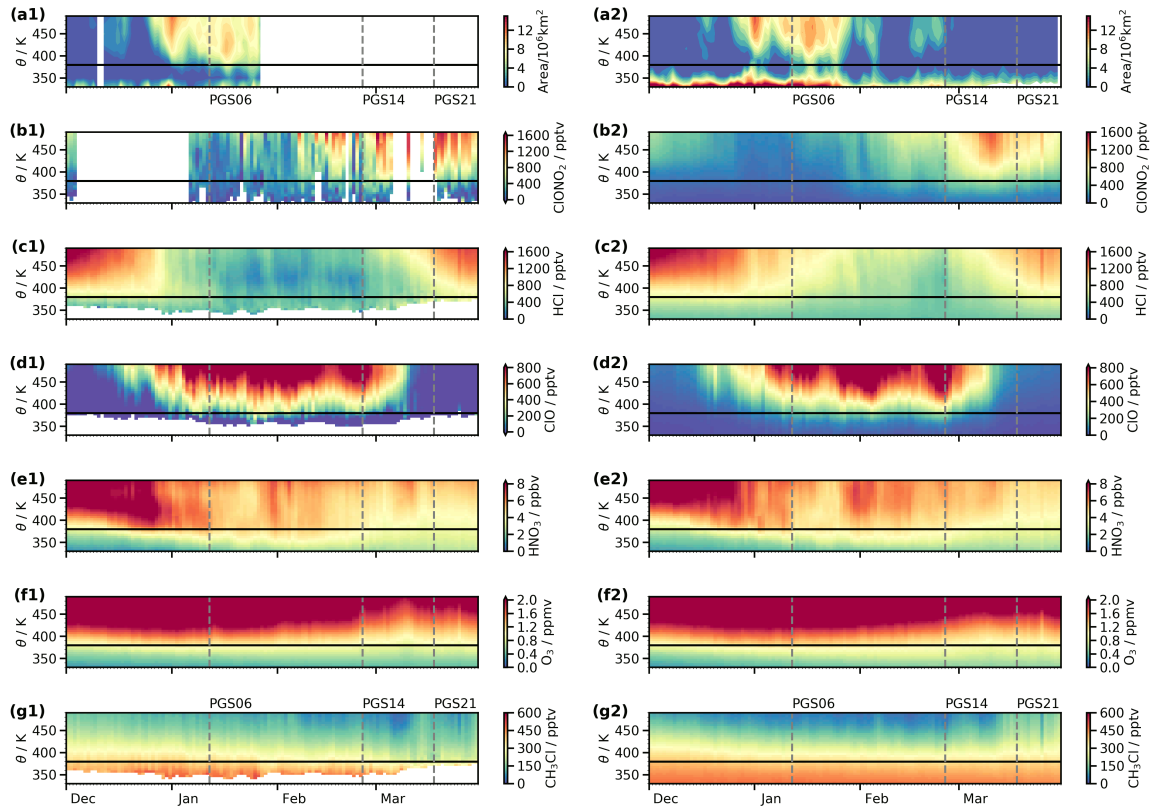


Figure 6.2: Comparison of MLS, ACE-FTS, and CALIOP time series (left) with CLaMS simulation results (right) for (a) PSC areas, (b) ClONO_2 , (c) HCl, (d) daytime ClO, (e) O_3 , (f) HNO_3 , and (g) CH_3Cl . The $\theta = 380$ K altitude is marked with a black line, and days with aircraft measurements discussed in this thesis are marked with dashed lines.

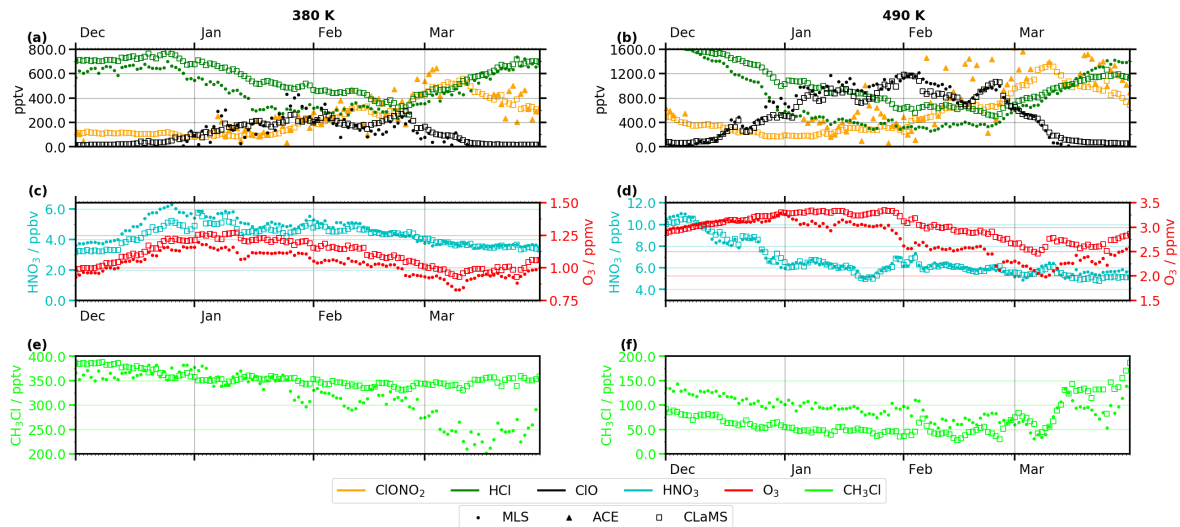


Figure 6.3: Time series of vortex averaged trace gases from satellite measurements and CLaMS simulation at 380 K (a,c,e) and 490 K (b,d,f). CLaMS data are shown as open squares, MLS as filled points and ACE-FTS as triangles. The evolution of chlorine species (ClONO_2 : orange, HCl : green, ClO : black) is illustrated in the first row (a,b), HNO_3 (cyan) and O_3 (red) in the second row (c,d), and CH_3Cl (light green) in the third row (e,f).

and measurements. In the ACE-FTS measurements, these enhancements already start in the middle of February, whereas the CLaMS simulation indicates weaker maxima of 500 pptv at that time. A direct comparison of these plots is difficult due to the sparse sampling of the ACE-FTS measurements. HCl (Fig. 6.2c) decreases from 1600 pptv starting in December in MLS observations and in simulated data. This decrease starts earlier and advances faster in the measurements. Also the minimum values of 200 pptv are lower compared to the simulation with minimum values of 400 pptv. The increase of HCl , starting in the beginning of March, exhibits the same temporal evolution in the measurement and the simulation with higher maximum values in the measurement (1400 pptv) than in the simulation (1200 pptv). Measured and modeled ClO (Fig. 6.2d) are enhanced in the same time periods and altitude levels, although in the CLaMS ClO increases later (as observed for HCl) and thus shows towards the end of December shows lower absolute values (400 pptv at 490 K) compared to MLS (800 pptv at 490 K). O_3 (Fig. 6.2e) displays very similar curtains over the course of the winter, although towards the end of the winter lower O_3 values are observed than simulated at altitudes of $\theta \approx 450$ K. HNO_3 (Fig. 6.2f) simulated by CLaMS compares well with the corresponding MLS measurement. The major difference is observed at the end of December, when HNO_3 values > 8 ppbv are measured at altitudes of $\theta \approx 400$ K, but only 6 ppbv are simulated at this time and altitude. Fig. 6.2g presents measured and modeled CH_3Cl with VMRs up to 500 pptv in the troposphere and VMRs measured as low as 50 pptv and simulated as low as 25 pptv in the stratosphere.

For a more quantitative comparison, cuts along $\theta = 380$ K and $\theta = 490$ K are presented in Fig. 6.3. The lower altitude curves are provided as an extension of Fig. 6.1, and to give context to the aircraft measurements in the following sections. The slice at θ

= 490 K is meant as a connection to previous discussions of this winter (Manney and Lawrence, 2016) and to compare to other extreme winters discussed at this altitude level (Santee et al., 2008b; Manney et al., 2011). In addition, showing both levels illuminates the differences between the LMS and the bulk of the stratosphere above. The chlorine species (Fig. 6.3a-b), HNO_3 (6.3c-d, left axis), and O_3 (6.3c-d, right axis) show in detail the overall agreement and specific differences between measurement and simulation, which have already been described for Fig. 6.2. At $\theta = 380$ K, large discrepancies between model and observation are noted for HCl ($\Delta\text{vmr}_{\text{max}} = 200$ pptv) and HNO_3 ($\Delta\text{vmr}_{\text{max}} = 1$ ppbv) until the middle of February, while at $\theta = 490$ K, discrepancies are visible for HCl ($\Delta\text{vmr}_{\text{max}} = 400$ pptv) starting from the beginning of the winter, and for O_3 ($\Delta\text{vmr}_{\text{max}} = 750$ ppbv) starting from January. CH_3Cl (Fig. 6.3e,f) shows agreement at 380 K until the end of January 2016, with slowly decreasing VMRs between 380 pptv and 340 pptv. From the end of January on, the measured CH_3Cl VMR decreases to values as low as 200 pptv in March, while the simulated VMR remains at about 340 pptv. At 490 K, a difference of 50 pptv between simulated and measured CH_3Cl is visible, with simulated VMRs lower than those measured until February, when the measured CH_3Cl VMRs approach the simulated values. Modeled and measured CH_3Cl then agree until the middle of March, after which the observed variations are not fully captured by the simulation.

In general, CLaMS succeeds in reproducing chlorine deactivation of the Arctic winter 2015/16, which has been identified to be unusual by the comparison to time series of other years in the MLS record: The deactivation of chlorine in the Arctic LMS typically starts with a decrease of ClO and an increase of ClONO_2 , followed by a slow increase of HCl until the equilibrium between the reservoirs is reestablished (Solomon, 1999). The 2015/16 time series of ClONO_2 is mostly at or below the 2004-2018 average in February and March, and an increase of HCl from exceptionally low values of 200 pptv at the end of February 2016 to the 2004-2018 average values of 600 pptv at 380 K is observed in the middle of March 2016 (Figs. 6.1 and 6.3).

CALIOP PSC area measurements agree with PSC areas simulated by CLaMS for the time CALIOP was able to collect measurements. ACE-FTS measurements and CLaMS simulation of ClONO_2 show agreement within the limited ACE-FTS sampling, which influences the daily mean profiles. The HCl time series exhibit differences similar to those discussed in detail by Grooß et al. (2018): In the beginning of the winter, activation of HCl is not simulated to the extent it is observed by the satellite instrument. This lack of chlorine activation is also visible in ClO , which indicates lower VMRs in the model in the beginning of the winter. Another result of the reduced chlorine activation of CLaMS is the overestimation of simulated O_3 compared to MLS observations, which is in particular visible at 490 K towards the end of the winter. HNO_3 shows agreement between MLS and CLaMS, but in the beginning of the winter, lower VMRs are simulated than observed at 380 K. This disagreement is considered to result from an underestimation by CLaMS of re-nitrification at this level from the sedimentation of HNO_3 containing PSC particles from above. It is known that denitrification and re-nitrification are difficult to simulate in the LMS (Braun et al., 2019). Comparisons of CH_3Cl show agreement between measurement and simulation for the beginning of the winter at 380 K, but starting in January measured CH_3Cl decreases notably,

while the simulated CH_3Cl remains almost constant. These differences indicate that diabatic descent is too weak in the model at 380 K. At 490 K, the persistent 50 pptv model-measurement discrepancy suggests that the CH_3Cl VMRs used to initialize the simulation (see Sec. 4.4.1) were too low, which does not allow for further conclusions at this altitude level.

6.1.3 Aircraft measurements

In order to complement the overview of the Arctic winter 2015/16 chemical composition of the LMS using satellite observations, the airborne GLORIA measurements of O_3 , ClONO_2 and HNO_3 aim to give detailed insights into the lowermost part of the polar vortex. Out of 14 scientific flights, 3 flights with particularly interesting trace gas distributions at different stages of the winter are discussed in this section. Measurements from other flights are provided in the supplement of Johansson et al. (2018).

Flight on 12 January 2016 (PGS06)

The flight on 12 January 2016 (PGS06, Fig. 6.4) during the early/mid winter was the transfer flight from the campaign base Oberpfaffenhofen (Germany) to Kiruna (Sweden) via southern Italy (way points “A” and “B”, marked in Fig. 6.4). As shown in Fig. 6.4a, the polar vortex (estimated by regions that are not marked with a shadow) extended over central Europe to the Arctic and Siberia. It can be seen from the higher MERRA2 potential temperature that air masses at the typical flight altitude of 13 km had subsided over southern France and northern Italy (close to way point “C”), where a tropopause fold was present along the polar front jet stream on the day of the flight (Woiwode et al., 2018). Towards the end of the flight (after way point “D”), high altitude clouds were observed along the GLORIA line of sight, and no retrievals were possible.

Two-dimensional trace gas distributions of O_3 (Fig. 6.4b), ClONO_2 (Fig. 6.4c) and HNO_3 (Fig. 6.4d) along the flight path are shown as a function of time and θ for PGS06 and in the following sections for PGS14 and PGS21. In order to compensate for dynamical features in the atmosphere, the trace gas cross sections are linearly interpolated on potential temperature levels. Additionally, the MERRA2 potential vorticity (2 and 4 PVU) along the measurement geolocations are plotted as magenta lines to identify the dynamical tropopause. Way points, marked by capital letters and dashed lines, help to arrange these curtain plots on the map. Trace gas retrievals are possible between cloud top and flight altitude. Regions outside this range are not shown. In addition, no retrieval results are available for time periods used for calibration measurements, refuel stops (only flight PGS21), and different measurement modes (only flight PGS21).

The measured O_3 concentrations reveal enhanced values up to 1200 ppbv at way point “C” at a potential temperature level of 370 K. Below this maximum, small-scale structures of ~ 800 ppbv are visible. Ozone values are low in tropospheric air masses over Italy (near way points “A” and “B”), but during the rest of the flight, mostly VMRs of ≈ 500 ppbv are observed at potential temperatures between 310 and 350 K. ClONO_2

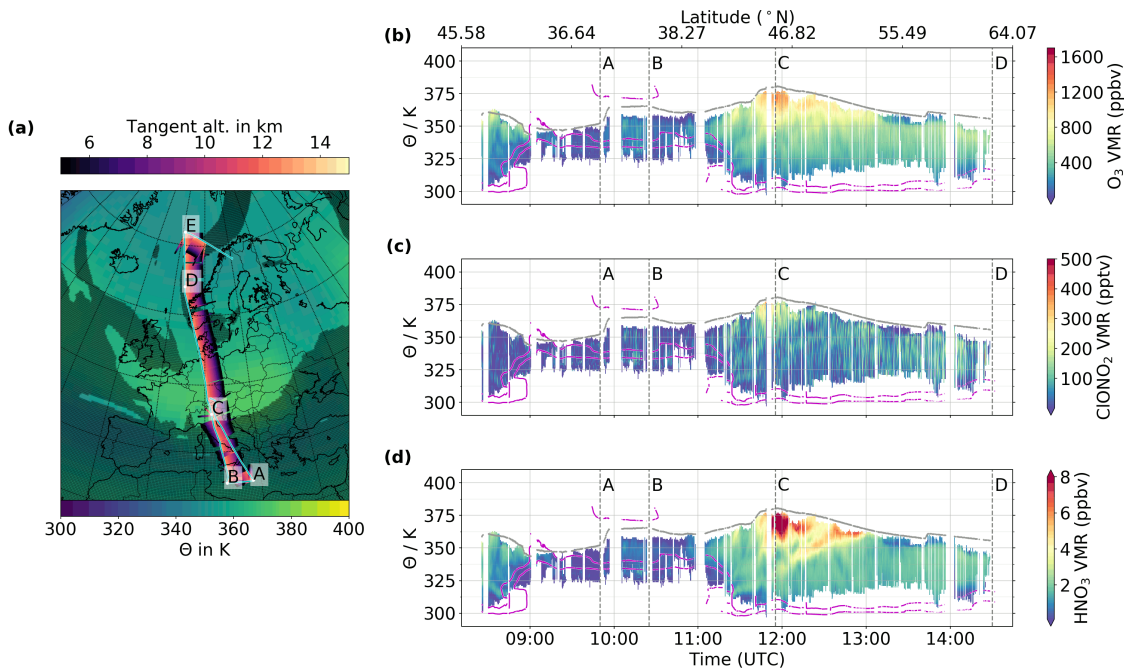


Figure 6.4: Flight PGS06 (12 January 2016): (a) Flight path (cyan) on a map with MERRA2 potential temperatures (lower color bar) at typical HALO cruise altitude of 13 km. Regions outside the polar vortex (according to Nash et al. (1996) at $\theta = 370$ K) are marked with a grey shadow. Way points are marked with capital letters. The tangent altitudes of **GLORIA** measurements are shown in the upper color bar. Right panels: **GLORIA** cross section of (b) O₃, (c) ClONO₂, and (d) HNO₃ (using potential temperature derived from GLORIA temperature). The flight level (approximated using **MERRA2** potential temperature) is marked with a grey line, and white spaces mark regions without data. The **MERRA2** potential vorticities of 2 and 4 PVU are marked with magenta lines and way points are marked with grey vertical dashed lines.

shows maximum values up to 250 pptv close to the maximum O₃ VMR at way point “C”, where the highest potential temperature levels were reached. In the second part of this flight (after 11:30 UTC), small ClONO₂ enhancements (< 200 pptv) are visible in small-scale horizontal structures at 310-350 K potential temperature. For HNO₃, maximum VMRs (> 8 ppbv) are observed at way point “C”, in line with the other discussed gases. After this way point (between 12:00 UTC and 13:00 UTC), more enhancements (up to 7 ppbv) are observed shortly below flight altitude, at 360 K. These enhancements show diagonal structures (e.g., from 12:00 UTC and 340 K to 12:45 UTC and 360 K) and are considered to be a result of recent re-nitrification events. Overall, the **GLORIA** observations show a long north-south transect through the Arctic **LMS** in mid-January 2016, with subsided ozone-rich air masses and first indications of chlorine deactivation into ClONO₂.

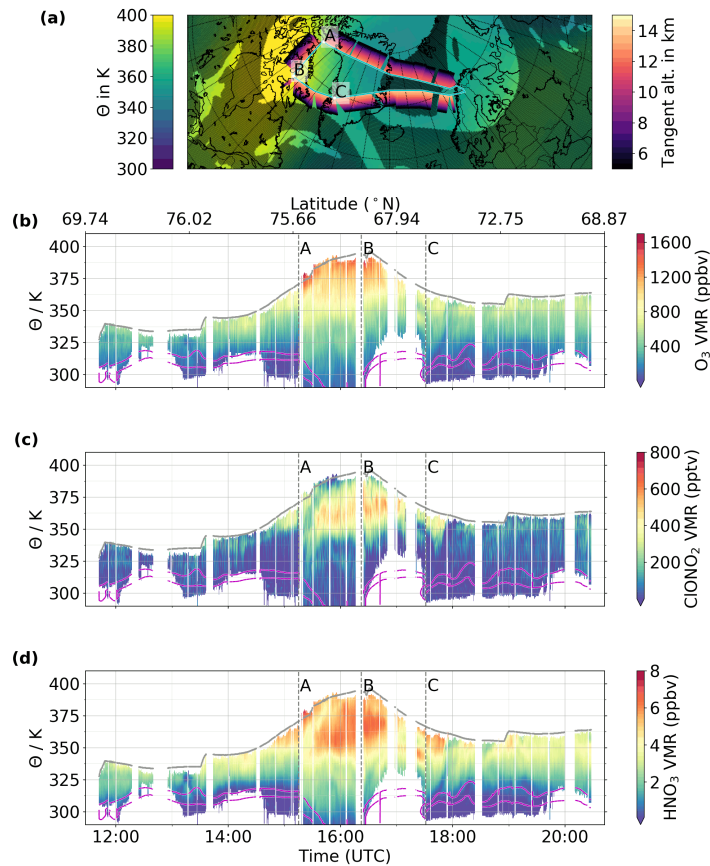


Figure 6.5: Same as in Fig. 6.4, but for Flight PGS14 (26 February 2016).

Flight on 26 February 2016 (PGS14)

In the middle of the Arctic winter, flight PGS14 was realized on 26 February 2016 as shown in Fig. 6.5a. From the campaign base in Kiruna, the flight headed towards the northern part of Greenland (way point “A”), continued until Baffin Bay (way point “B”), and turned at way point “C” to change direction towards Kiruna. At typical flight altitude of 13 km, the substantially subsided air masses are evident in the higher potential temperatures characterizing the portion of the flight track near way point “B”. The vortex criterion of Nash *et al.* (1996) at $\theta = 370$ K also shows that most of the flight path was within the polar vortex.

The cross sections of O_3 (Fig. 6.5b) and ClONO_2 (Fig. 6.5c) are presented in the same manner as for flight PGS06. Between way points “A” and “B”, maximum O_3 values of 1600 ppbv are measured at $\theta = 390$ K, and small-scale structures are visible at $\theta = 340$ K (in the vicinity of way point “C”). ClONO_2 developed a local maximum of 600 pptv below flight altitude at $\theta = 360$ K around way points “A” and “B”. The maximum that becomes visible just before way point “A” is discontinuous, reforming at slightly lower altitudes along the flight path (diagonal local minimum feature in Fig. 6.5c). HNO_3 shows a local maximum (up to 7 ppbv) at the same location as the local maximum in ClONO_2 . Also the discontinuity observed in this ClONO_2 local maximum is visible in

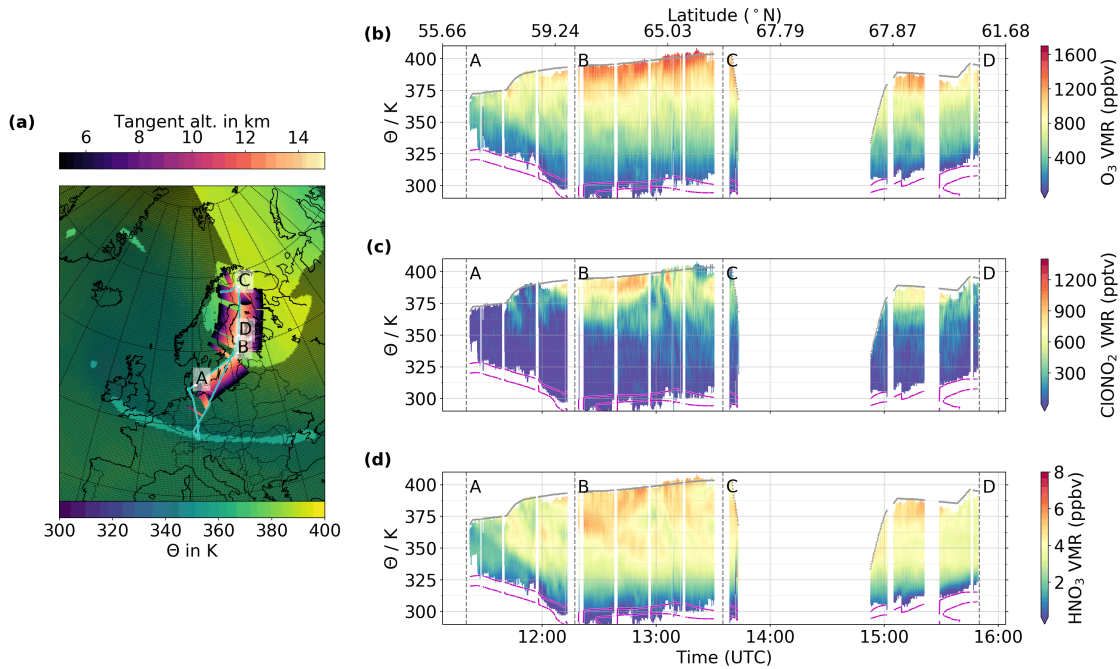


Figure 6.6: Same as in Fig. 6.4, but for Flight PGS21 (18 March 2016).

the HNO_3 cross section. After way point “C”, just below flight altitude a maximum of ≈ 6 ppbv is measured at the same geolocation as for O_3 and $ClONO_2$. This local enhancement in HNO_3 is directly followed by a series of two minima, separated by a local maximum. These minima are, in a less pronounced extent, also observed in O_3 . In addition, the MERRA2 4 PVU isoline, as shown in Fig. 6.5d, reveals enhanced modulations at the position of these minima. This modulation of the PV indicates a dynamical origin of the modulation in the trace gases.

Flight on 18 March 2016 (PGS21)

The flight path of the late winter flight on 18 March 2016 (PGS21) is shown in Fig. 6.6a on a map with MERRA2 potential temperature at the typical flight altitude of 13 km. This flight started at the campaign base in Oberpfaffenhofen and headed towards Denmark (way point “A”), where the GLORIA measurement mode was switched to the “chemistry mode” (high spectral resolution mode). Then the flight course followed the Baltic sea northeastwards until it reached remnants of the late winter polar vortex at way point “B”. Inside this region of high potential temperatures, the HALO aircraft continued northward until Kiruna for a refueling stop (shortly after way point “C”). On its way back to Oberpfaffenhofen, HALO took a similar flight path over the Baltic sea, where the measurement mode of GLORIA was changed (way point “D”).

Two-dimensional cross sections of O_3 and $ClONO_2$ are shown in Fig. 6.6b and c. Between way points “B” and “C”, maximum O_3 values of 1600 ppbv are observed, and filamentary structures are visible down to altitudes of $\theta = 340$ K. Between way points “A” and “B”, these filaments are visible close to flight altitude at $\theta = 360$ K. For $ClONO_2$,

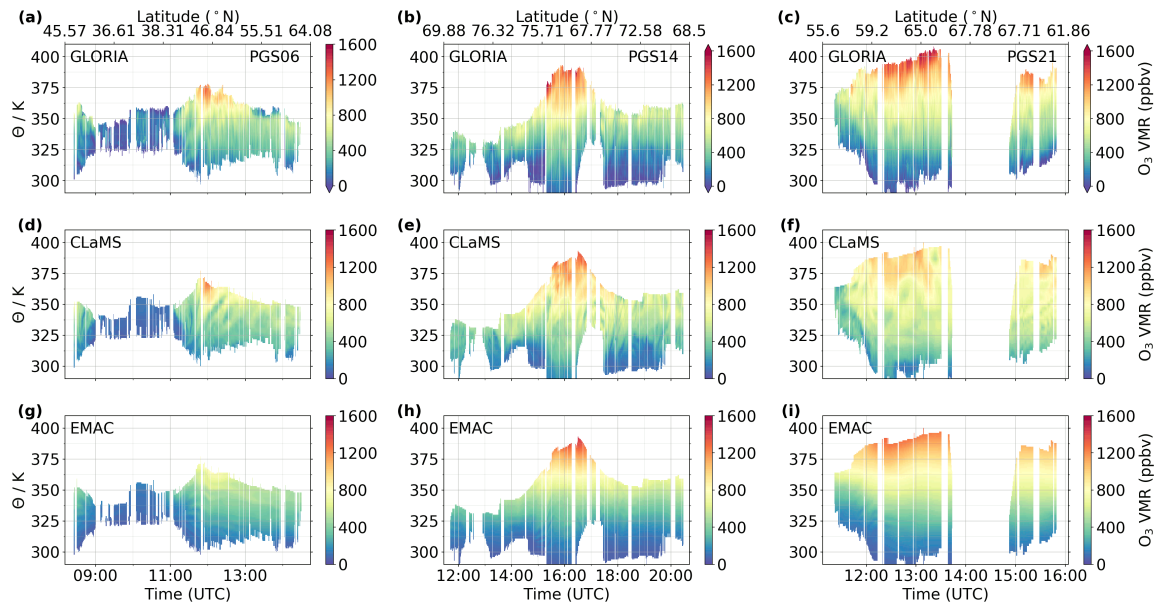


Figure 6.7: Comparison of GLORIA measured O_3 (first row, repeated from Figs. 6.4-6.6 with a different color bar) to CLaMS (second row) and EMAC (third row) simulated O_3 cross sections for flights PGS06 (12 January 2016, first column), PGS14 (26 February 2016, second column) and PGS21 (18 March 2016, third column). Color bars with top/bottom arrowheads indicate data greater/smaller than the color bar range.

enhanced values up to 1100 pptv are measured at $\theta = 380$ K altitude. ClONO_2 VMR values as high as 500 pptv are measured at altitudes as low as $\theta = 350$ K. Between way points “B” and “C”, where consistently high O_3 VMR is observed at $\theta = 370$ K, strong horizontal fluctuations in ClONO_2 are visible. These filaments in ClONO_2 are likely to be connected to the availability of NO_2 . Structures of enhanced HNO_3 (which is photolyzed to NO_2) and ClONO_2 in the collocated GLORIA measurements reveal similar shapes. In general, HNO_3 is observed with VMRs > 4 ppbv down to θ levels as low as 325 K, with filamentary enhancements up to 6 ppbv. These irregularly placed small structures are interpreted as a result of redistributed air masses after re-nitrification of sedimented PSC containing air masses.

6.1.4 Comparison of aircraft measurements to model simulations

The CLaMS results have been compared to various observations of Arctic winters, which led to important improvements of this model (e.g., Grooß et al., 2014, 2018; Tritscher et al., 2018). Also for the EMAC model, comparisons with different observations of Arctic winters have been performed (e.g., Khosrawi et al., 2017, 2018). Still, those previous comparisons focus on the stratosphere, and comparisons in the LMS are only marginally discussed. Complex dynamical situations, which may occur in the LMS, are challenging for atmospheric modeling. Therefore, comparisons in this altitude region are beneficial to benchmark the performance of these models.

The **GLORIA** cross sections of O_3 , ClONO_2 and HNO_3 are compared to the **CLaMS** and **EMAC** model results in Figs. 6.7, 6.8, and 6.9, respectively. The **CLaMS** output has been interpolated to **GLORIA** geolocations as described in Sec. 4.4.1. The globally available **EMAC** data have been interpolated linearly to the **GLORIA** tangent point geolocations. ECMWF operational analysis pressure, linearly interpolated to the **GLORIA** tangent point geolocations, is used to assign the **EMAC** model vertical levels (provided on pressure levels) to the **GLORIA** retrieval altitudes of the measurements. **EMAC** model output was provided every five hours.

For O_3 on flight PGS06 (Fig. 6.7a,d,g), the low tropospheric **VMR** values measured by **GLORIA** that can be found above Italy (9:00-11:00 **UTC**) are as well reproduced by **CLaMS** as enhanced values above central and northern Europe. Maximum modeled values at 12:00 **UTC** of 1200 ppbv are slightly lower than measured (1400 ppbv) but agree within the total estimated error of the instrument. A local minimum of O_3 observed at flight altitude after 13:00 **UTC** is not present in **CLaMS** or **EMAC**, but is suspected to be influenced by a slight degradation of the **GLORIA** measurements due to **PSCs** (see in situ comparisons in Johansson et al., 2018, supplement). The comparison with **EMAC** shows that the overall structure of measured O_3 (low values above northern Italy, enhanced values over northern Europe) is reproduced by the model, but maximum values at 12:00 **UTC** are lower in the model (700 ppbv) compared to the measurement (1400 ppbv).

For PGS14 (Fig. 6.7b,e,h), the measured distribution of O_3 over the course of the flight is well reproduced by **CLaMS**, and also fine structures (e.g., at 18:00 **UTC**) are clearly visible in both data sets. For the enhanced O_3 **VMRs** in the middle of the flight (15:00-17:00 **UTC**), the absolute measured values are higher but agree within their total estimated errors with **CLaMS**. In this region, structures are also visible in the model data that are less pronounced in the measurements. At $\theta = 300\text{-}350$ K altitude, higher **VMRs** are visible in the model data compared to the **GLORIA** observations. The O_3 **VMR** values simulated by **EMAC** reproduce the overall measured vertical structure, although finer features in the trace gas distributions are not visible due to the horizontal resolution of **EMAC** (≈ 125 km) compared to **GLORIA** (along-track sampling ≈ 3 km, horizontal resolution along viewing direction several 10 – 100 km, see also Woiwode et al. (2018)).

During the late winter flight PGS21 (Fig. 6.7c,f,i), again the modeled and measured two-dimensional distributions of O_3 generally agree between **CLaMS** and **GLORIA**, and anew higher **VMR** values are modeled than observed at $\theta = 300\text{-}350$ K altitude. Here again, finer structures are visible in the **CLaMS** data, and higher absolute **VMRs** (> 1600 ppbv) are measured than modeled (1100 ppbv) at 400 K, with the difference between them comparable to the total estimated error of the **GLORIA** data. The **EMAC** simulation of this flight shows maximum values of O_3 (up to 1500 ppbv) that are marginally higher than those of **CLaMS** and closer to the ones measured by **GLORIA**. Again, **EMAC** largely succeeds in reproducing the measured two-dimensional trace gas distribution, but with less detail in the small-scale structures than measured by **GLORIA** (see also Khosrawi et al., 2017).

ClONO_2 on flight PGS06 shows the same maximum of 250 pptv at $\theta = 370$ K altitude

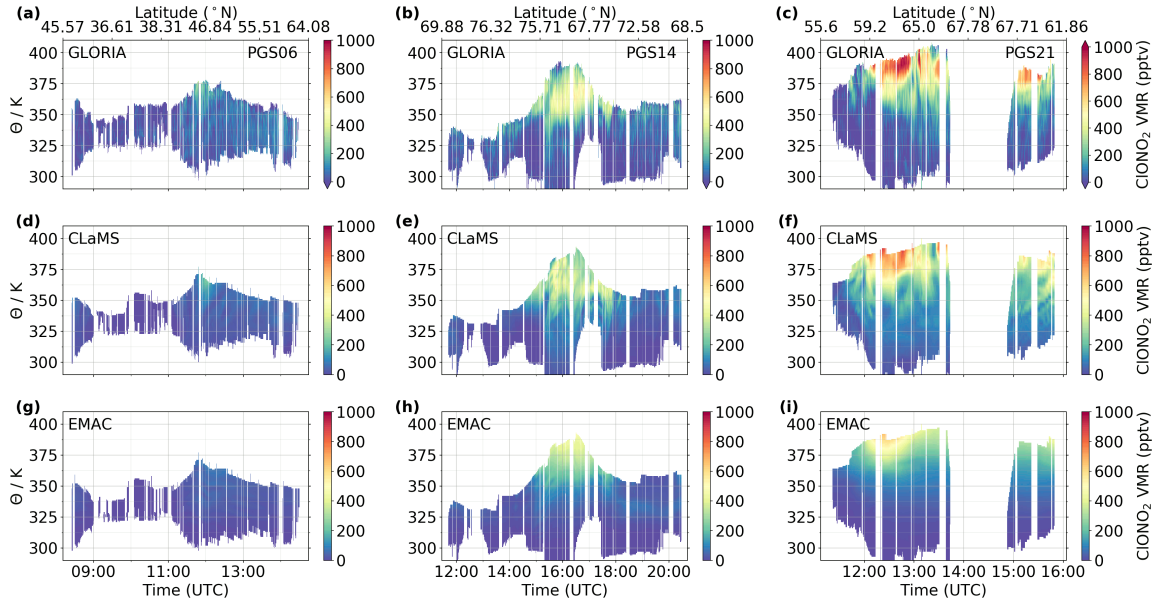


Figure 6.8: Same as Fig. 6.7, but for ClONO_2 . Please note that the first row is repeated from Figs. 6.4-6.6, but with a different color bar.

(12:00 UTC) for CLaMS as for GLORIA (see Fig. 6.8a,d). Two-dimensional structures with weak ClONO_2 enhancements are found at lower altitudes and show slightly different patterns in the two data sets. In EMAC, the simulated enhancement of ClONO_2 is smaller than the measured one (below < 100 pptv), and barely visible with the color bar used (Fig. 6.8a,g).

For flight PGS14, again the ClONO_2 small scale structures of GLORIA and CLaMS generally agree (see Fig. 6.8b,e). The maxima found in the ClONO_2 distribution around 16:00 UTC coincide in both data sets in terms of the position and absolute values. Compared to the GLORIA measurements, more structures are present in the area where ClONO_2 values are largest in the CLaMS data (as for O_3), but all measured structures are also apparent in the model. The comparison to EMAC (see Fig. 6.8b,h) shows similar maximum values, but the two-dimensional structure of ClONO_2 is different: The measured local maximum below flight altitude is not reproduced by the model, which shows the ClONO_2 maximum at 370 K flight altitude, while GLORIA shows a local maximum at 360 K.

Flight PGS21 shows higher values in measured ClONO_2 compared to CLaMS (see Fig. 6.8c,f). Besides the overall agreement of the data, the increased ClONO_2 values at $\theta = 330$ -350 K altitude in the model simulation do not match the measured patterns well. For this flight, EMAC simulates the maximum of ClONO_2 at a similar position compared to the measurements, and most measured enhancements are also evident in the model data (see Fig. 6.8c,i). Though this agreement in structure is within expectations, given the horizontal resolution of EMAC, the absolute values of ClONO_2 in the model (up to 600 pptv) differ substantially from the measured VMRs (1100 pptv), indicating an underestimation of ClONO_2 in the model simulation.

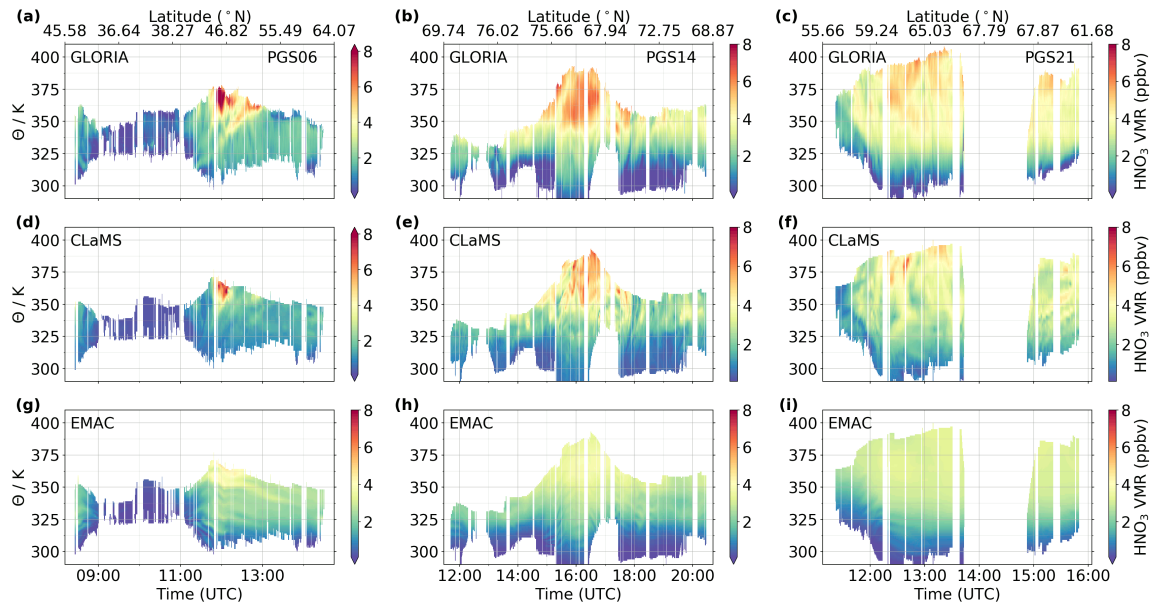


Figure 6.9: Same as Fig. 6.7, but for HNO_3 .

Comparisons of the HNO_3 cross sections with **CLaMS** and **EMAC** simulations generally reveal similar conclusions as for the other discussed trace gases (Fig. 6.9): Both models succeed within their limitations to reproduce the general picture of the HNO_3 distributions. For flight PGS06, **CLaMS** is able to simulate the correct geolocation of the greatest HNO_3 enhancement with similar VMRs > 8 ppbv. The second, diagonally located enhancement in the **GLORIA** measurement is not reproduced by the model. At other regions than the ones with maximum values, **CLaMS** and **GLORIA** show comparable VMRs. **EMAC** also is able to reproduce the location of the highest measured HNO_3 maximum, but with a notably lower absolute VMR of 4 ppbv. Similar to **CLaMS**, **EMAC** is not able to reproduce the second measured enhancement. Generally, **EMAC** shows marginally larger background HNO_3 values (≈ 2 -3 ppbv) than measured (≈ 1 -2 ppbv).

HNO_3 for flight PGS14 is reproduced in great detail by the **CLaMS** simulation. Notable differences are more filamentary structures modeled than observed, marginally lower background VMRs and small displacements of mesoscale structures. **EMAC** does not reproduce these small structures, but the maximum in the simulated cross section coincides with the **GLORIA** cross section, although it is significantly lower (6 ppbv measured compared to 4 ppbv simulated).

This general picture is similar for flight PGS21: **EMAC** shows the same regions of enhancements as the measurement, again with lower VMRs modeled (3 ppbv) than observed (5 ppbv). **CLaMS** shows similar structures of enhanced HNO_3 , but introduces more structures, which are not measured. As already noted for ClONO_2 and HNO_3 , maximum values are lower in **CLaMS** (5 ppbv) than in **GLORIA** measurements (6 ppbv).

These comparisons show that the measured two-dimensional structures in O_3 , ClONO_2

and HNO_3 are well captured in the **CLaMS** simulation, albeit with some differences in the magnitude of the features. The comparisons to **EMAC** show general agreement with the measurements, considering the spatial resolution of the model. **CLaMS** is a Lagrangian CTM, in which transport and chemical reactions are simulated along trajectories following specified meteorological fields. **EMAC** is an Eulerian CCM, which uses a defined grid on which the chemical processes are simulated. Transport and dynamical processes are taken into account by the coupling between grid points (Khosrawi et al., 2005; Morgenstern et al., 2017). These different model approaches are also reflected in the comparison of simulated trace gases to **GLORIA** measurements. While the **EMAC** simulation used here has been performed on a grid with $1.125^\circ \times 1.125^\circ$ resolution, in the Lagrangian model **CLaMS** the number of trajectories in the region of interest can be optimized for advanced interpolation methods. For this reason, **EMAC** succeeds in generally reproducing the chemical composition (for O_3 , ClONO_2 and HNO_3) of the measured UTLS regions, while **CLaMS** is able to reproduce even small-scale structures in these trace gases. Better agreement is expected for an **EMAC** simulation with higher horizontal resolution (e.g., T255). Improvements are desirable for both models in the simulation of ClONO_2 in the late winter (flight PGS21), when maximum measured VMRs are underestimated. **EMAC** is known to underestimate downward transport in the lower parts of the polar vortex (Brühl et al., 2007; Khosrawi et al., 2017), and also **CLaMS** shows diabatic descent that is too weak towards the end of the Arctic winter (see Sec. 6.1.2). Together with the strong vertical gradient of all gases in this region, less downward transport of the model results in smaller trace gas abundances at lower altitudes. Differences in maximum values between **GLORIA** and **EMAC** for flight PGS06 appear in all discussed trace gases and can most likely be attributed to the limited horizontal resolution of **EMAC**, because the enhancement seen on flight PGS06 appears to be spatially very confined. **CLaMS** data for flight PGS21 shows higher VMRs of O_3 at $\theta = 325$ K and of ClONO_2 at $\theta = 340$ K compared to the measurements, despite the observed lack of descent at 380 K. This enhanced **CLaMS** O_3 is also visible in the passive O_3 tracer (not shown), which indicates that this disagreement with the **GLORIA** measurements is caused by problems in horizontal transport or in the lower boundary conditions of **CLaMS**. These problems are not unexpected, as **CLaMS** is a stratospheric model by design. In addition, mixing is difficult to model, but **CLaMS** has been proven to successfully reproduce mixing during the Arctic winter 2015/16 (Krause et al., 2018).

6.1.5 Correlations

For comparisons of the chemical composition of the probed atmosphere during different flights, correlations of O_3 and ClONO_2 with **CFC-11** are used. **CFC-11** is well accessible with **GLORIA** and characterized by a long atmospheric life time. Therefore it is used as reference to analyze variations of O_3 and ClONO_2 in the **LMS**. As described by e.g., Müller et al. (1996), a long-lived species with a vertical gradient of VMR (such as **CFC-11**) can be used to represent measurements over the course of a winter accounting for the dynamical behavior of the atmosphere. Correlations of **GLORIA** **CFC-11** with O_3 and ClONO_2 are based on collocated measurements that are vortex-filtered (according to the Nash- and sPV-criteria described in Sec. 2.2), and only data points with a

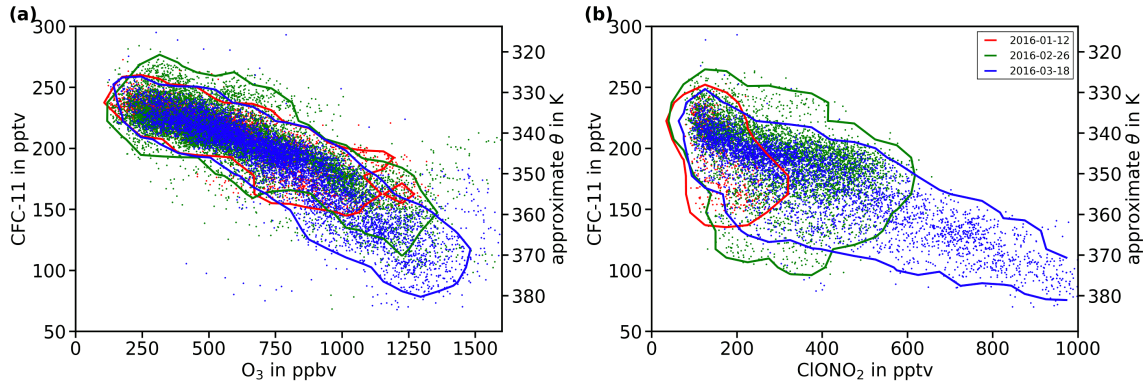


Figure 6.10: Correlation of (a) O₃ and (b) ClONO₂ with CFC-11 measured by GLORIA for flights PGS06 (red), PGS14 (green) and PGS21 (blue). The correlations are shown as scatter plot and as RNFD (solid lines). An estimated potential temperature (based on GLORIA CFC-11 and temperature measurements) is shown.

relative estimated error better than 20% are considered. For correlations with CLaMS data, interpolations to GLORIA measurement geolocations are done as described in Sec. 6.1.4. The CLaMS data shown in the following are interpolated as described in Sect. 6.1.4 and are filtered for geolocations where GLORIA data points are available in the correlations.

Due to the scattering and the large amount of available GLORIA data points, RNFD as discussed by Eckstein et al. (2017) are used for a well-arranged representation of the cloud of single correlation points: A two-dimensional histogram density is calculated for the single correlation points within a VMR grid motivated by the variation of the trace gases ($\Delta\text{VMR}_{\text{CFC-11}} = 15$ pptv, $\Delta\text{VMR}_{\text{ClONO}_2} = 50$ pptv, $\Delta\text{VMR}_{\text{O}_3} = 70$ ppbv). From this normalized density histogram, a contour line at 3% of the maximum density is shown to quantify the distribution of points. These correlations are shown in Fig. 6.10.

The correlations of individual points are characterized by large variability, which is also visible in the RNFD. Partly, this variability is caused by the estimated GLORIA uncertainty (< 200 ppbv for O₃, < 100 pptv for ClONO₂, and < 40 pptv for CFC-11), while the remaining variability is caused by atmospheric variation, as also suggested by the spread of the model correlations (see below). In the O₃ correlation (Fig. 6.10a) it can be seen that at lower altitudes (250-200 pptv CFC-11, $\theta \approx 330$ -340 K) the majority of correlated single points are located in the same area, whatever flight these points belong to. Where measurements were possible at higher altitudes (150-100 pptv CFC-11, $\theta \approx 360$ -370 K), this correlation shows on average different slopes for the late flight PGS21 compared to the other, earlier flights. For all flights, variations up to 400 ppbv are observed at altitudes of 150 pptv CFC-11 ($\theta \approx 360$ K).

For the ClONO₂ correlation, again many points cluster at 250-200 pptv CFC-11 altitude ($\theta \approx 330$ -340 K), but significant differences between the different parts of the winter are observed. While in the beginning of January (PGS06) only 100-300 pptv of ClONO₂ are measured at 150 pptv CFC-11 ($\theta \approx 360$ K), in the middle of March (PGS21)

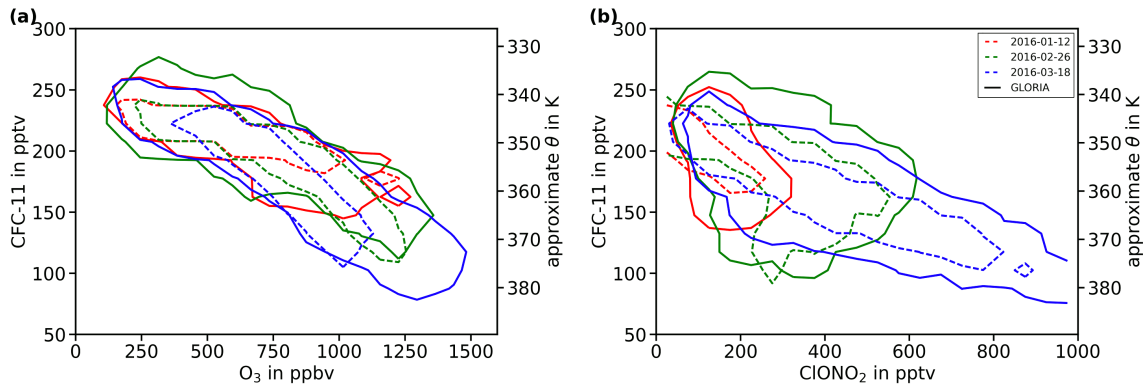


Figure 6.11: Correlation of (a) O_3 and (b) $ClONO_2$ with CFC-11 for flights PGS06 (red), PGS14 (green) and PGS21 (blue). The correlations are shown as RNFD for GLORIA (solid lines) and CLaMS (dashed lines). An estimated potential temperature (based on GLORIA CFC-11 and temperature measurements) is shown.

approximately 200 - 800 pptv are measured at this level, which indicates a chlorine deactivation of ≈ 300 pptv on average into $ClONO_2$. For flight PGS14 strong variability of $ClONO_2$ for altitudes lower than 170 pptv CFC-11 ($\theta \approx 350$ K) is visible. A similar tracer-tracer correlation is shown in Fig. 6.11 for CLaMS, which succeeds in reproducing the measured two-dimensional structures of O_3 and $ClONO_2$. For this analysis only one model, namely CLaMS, is used because of the better agreement with observations and because of problems in this specific EMAC simulation (see Khosrawi et al., 2017). As in Fig. 6.10, the RNFD lines for the GLORIA data are shown as solid lines, while those for the CLaMS data are shown as dashed lines. For O_3 (Fig. 6.11a) the model data shows a more distinct difference between the earlier PGS06 and the later PGS14 and PGS21 flights at 180 pptv CFC-11 ($\theta \approx 365$ K). The model and the measurement O_3 distributions agree regarding the average, while GLORIA data shows a larger variation. This larger variability in the GLORIA data compared to CLaMS is also apparent in the comparison of the $ClONO_2$ correlation with CFC-11 (Fig. 6.11b). Despite the different spread of data, the model and observation RNFD lines agree on average and similar changes in the $ClONO_2$ distributions demonstrate the stages of chlorine deactivation into $ClONO_2$ over the course of the winter.

6.2 Chemical ozone loss

The unusually low O_3 abundances at 380 K in the Arctic winter 2015/16 (as shown in Fig. 6.1) suggests that a high amount of O_3 was depleted in the Arctic LMS in this particular winter. However, for determining the chemical ozone loss, also dynamical effects such as transport, mixing and subsidence, need to be separated from low O_3 abundances due to chemical ozone depletion. Many, in particular model based, studies compute the chemical ozone loss as the difference between ozone and a so-called “passive ozone” (Manney et al., 1995a,b). This passive ozone is calculated either from a correlation with a chemically inert trace gas (e.g., CFCs, N_2O) or from an artificial

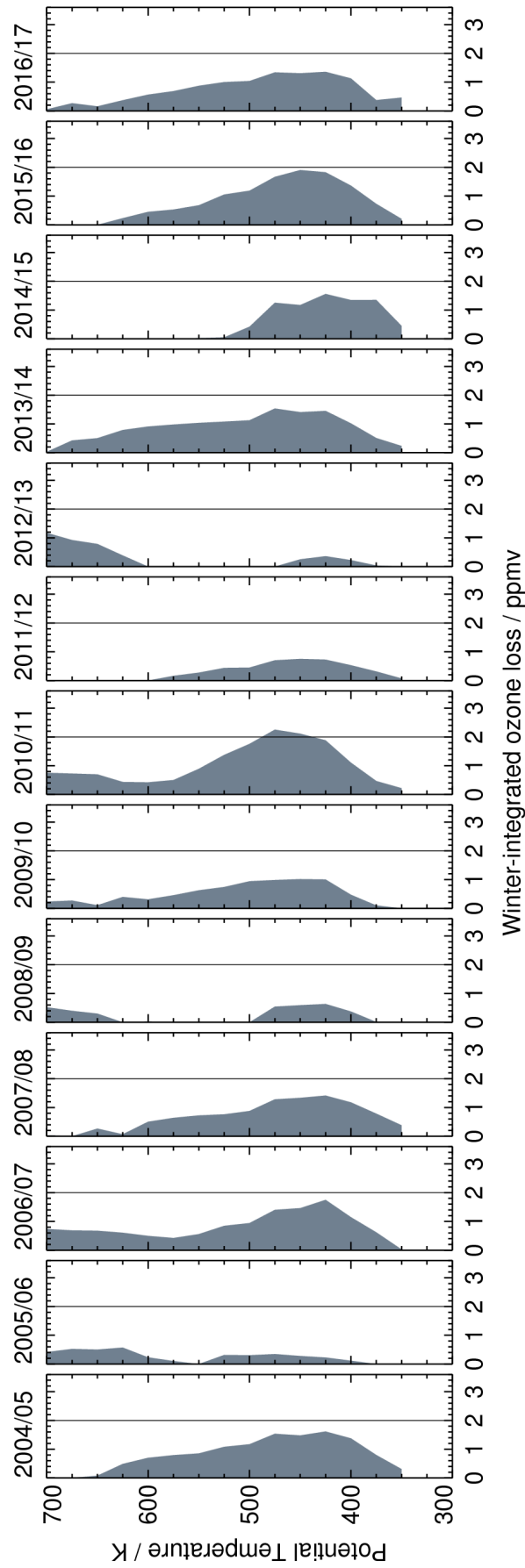


Figure 6.12: Ozone loss profiles per potential temperature level calculated with a Match based approach on MLS ozone data. Profiles are presented for Arctic winters between 2004 and 2017. Approved modified reprint from Santee (2017).

model tracer, which is initialized, transported and mixed as “regular” ozone, but not involved in any chemical reaction. The latter approach is applied by the CLaMS model and with this method chemical ozone loss is estimated in Sec. 6.13.

Another well-established method to estimate the chemical ozone loss is the so-called “Match” approach (Gathen et al., 1995). This technique applies trajectories to monitor the paths of air masses within the polar vortex. These trajectories are compared to measurement geolocations, and in case the same air mass is measured multiple times, it is possible to deduce the chemical evolution of these air masses. Mixing processes, e.g., with air masses from mid latitudes, are typically not considered for such trajectory based approaches and introduce an error source. Livesey et al. (2015) used this Match-based technique with Aura/MLS measurements of ozone to calculate profiles of chemical ozone loss for each winter of the Aura measurement epoch. For an error estimation, they use the chemically inert N₂O trace gas to estimate the effect of mixing and the effect of uncertainties in the descent prescribed from the meteorological data. These errors in O₃ loss are estimated as 0.5 ppmv.

As an extension of Livesey et al. (2015), Santee (2017) presented Match-based ozone loss profiles for Arctic winters until 2017, as shown in Fig. 6.12. In this comparison of profiles, the extreme nature of the Arctic winter 2010/11 is clearly visible: Chemical ozone loss of more than 2.0 ppbv at 475 K potential temperature is estimated by the MLS Match approach and this particular winter is also known as an “Arctic ozone hole” (Santee et al., 2011). Other Arctic winters with remarkable stratospheric ozone loss during the MLS measurement period are 2004/05, 2006/07, 2007/08, 2013/14 and 2015/16. Note that all of these winters show ozone losses lower than 2.0 ppbv in the stratosphere. In the LMS, which is in focus of this work, notable ozone loss occurred in the Arctic winters 2004/05 with 0.8 ppmv, 2007/08 with 0.8 ppmv, 2014/15 with 1.3 ppmv, and 2015/16 with 0.8 ppmv of chemical ozone loss at 375 K potential temperature. For the extraordinarily high estimated ozone loss at 375 K in 2014/15, the unusually early final stratospheric sudden warming (SSW; early January 2015; Manney et al., 2015a) needs to be considered, which makes the Match-estimated ozone loss 2014/15 implausible and is neglected for further analysis.

However, this analysis of ozone loss based on MLS data implies that chemical ozone loss in the LMS during the Arctic winter 2015/16 was not as exceptional as the time series in Fig. 6.1 suggests. According to Fig. 6.12, among others, the Arctic winter 2004/05 was comparable regarding chemical ozone loss in the LMS. In Fig. 6.1e, the O₃ concentrations in the late winter 2004/05 is considerably greater than O₃ in 2015/16, but also the descent (indicated by the strong decrease of CH₃Cl in Fig. 6.1g) until the final warming (Manney et al., 2006, 10 March 2005,) was unusually strong in 2004/05. This strong descent resulted in greater replenishment of O₃, which compensated for chemical ozone loss at 380 K (assuming that mixing and other transport processes are of minor importance at these altitudes). Analyses of other winters with chemical ozone loss comparable to 2015/16 in the LMS (according to Fig. 6.12) suggest that 2015/16 was exceptional in the LMS regarding the combination of unusually strong chemical ozone loss with non-extraordinary diabatic descent (unlike other winters with unusually strong chemical ozone loss).

6.3 CLaMS investigations of chemical evolution

The measurements presented in Sec. 6.1 revealed unusual chlorine deactivation in the satellite time series and interesting mesoscale structures with unusually high ClONO_2 VMRs for the Arctic in the GLORIA measurements. It was shown that CLaMS successfully reproduces structures in the LMS measured by MLS and GLORIA. For this reason, these validated model simulations are applied to examine the influence of ozone depletion and PSC sedimentation on chlorine deactivation. Then, the influence of considerably lower temperatures is shown with a CLaMS sensitivity simulation. In the third part of this section, the origin of measured ClONO_2 in the LMS is investigated.

6.3.1 Influence of ozone depletion and denitrification on chlorine deactivation

NO_y and O_3 abundances are known to have a major influence on chlorine deactivation pathways, and those abundances are strongly affected by denitrification and ozone loss, respectively. In Sec. 6.1.1, the partitioning of chlorine reservoirs in 2016 was identified to be unusual for an Arctic winter, and therefore CLaMS sensitivity simulations have been performed to understand and quantify the influence of ozone depletion and PSC sedimentation on chlorine deactivation.

The sensitivity run without ozone depletion has been facilitated by replacing the CLaMS O_3 with the passive O_3 tracer at the beginning of each simulation step. This passive O_3 tracer is initialized, transported and mixed in the same way as the regular O_3 field, but it does not experience ozone-depleting processes. The difference between the passive O_3 and the standard O_3 is a measure of chemical ozone loss and is presented as time series at 380 K and 490 K (Fig. 6.13a) and as a cross section between 330 K and 600 K (Fig. 6.13c). These time series of differences show that ozone depletion starts in the beginning of January and reaches its maximum in the middle of March. The largest ozone depletion is simulated at 490 K, with maximum VMR differences of 1.75 ppmv. The influence of ozone depletion on HCl and ClONO_2 is illustrated in Fig. 6.13e,g as differences between the reference and the sensitivity simulation without ozone depletion. Negative differences (shades of blue) indicate how much the chlorine reservoir is diminished due to the effect of ozone depletion, while positive differences (shades of red) show enhancements due to this effect. HCl exhibits a positive response to ozone depletion, and starting from the beginning of March, more than 500 pptv additional chlorine is deactivated into HCl under ozone-depleted conditions. At the same time, ClONO_2 is reduced by more than 500 pptv due to ozone depletion. These differences for both reservoir gases peak at altitudes of 440 K towards the end of March. Interestingly, this peak altitude is lower than the altitude of greatest ozone loss (490 K).

For the sensitivity run without PSC sedimentation, a CLaMS simulation was performed without the sedimentation module (see Sec. 4.4.1). Differences in NO_y between the reference and the sensitivity simulation are presented in Fig. 6.13b,d as time series at 380 K and 490 K and as cross sections. Nitrification up to 4 ppbv is seen at 380 K in

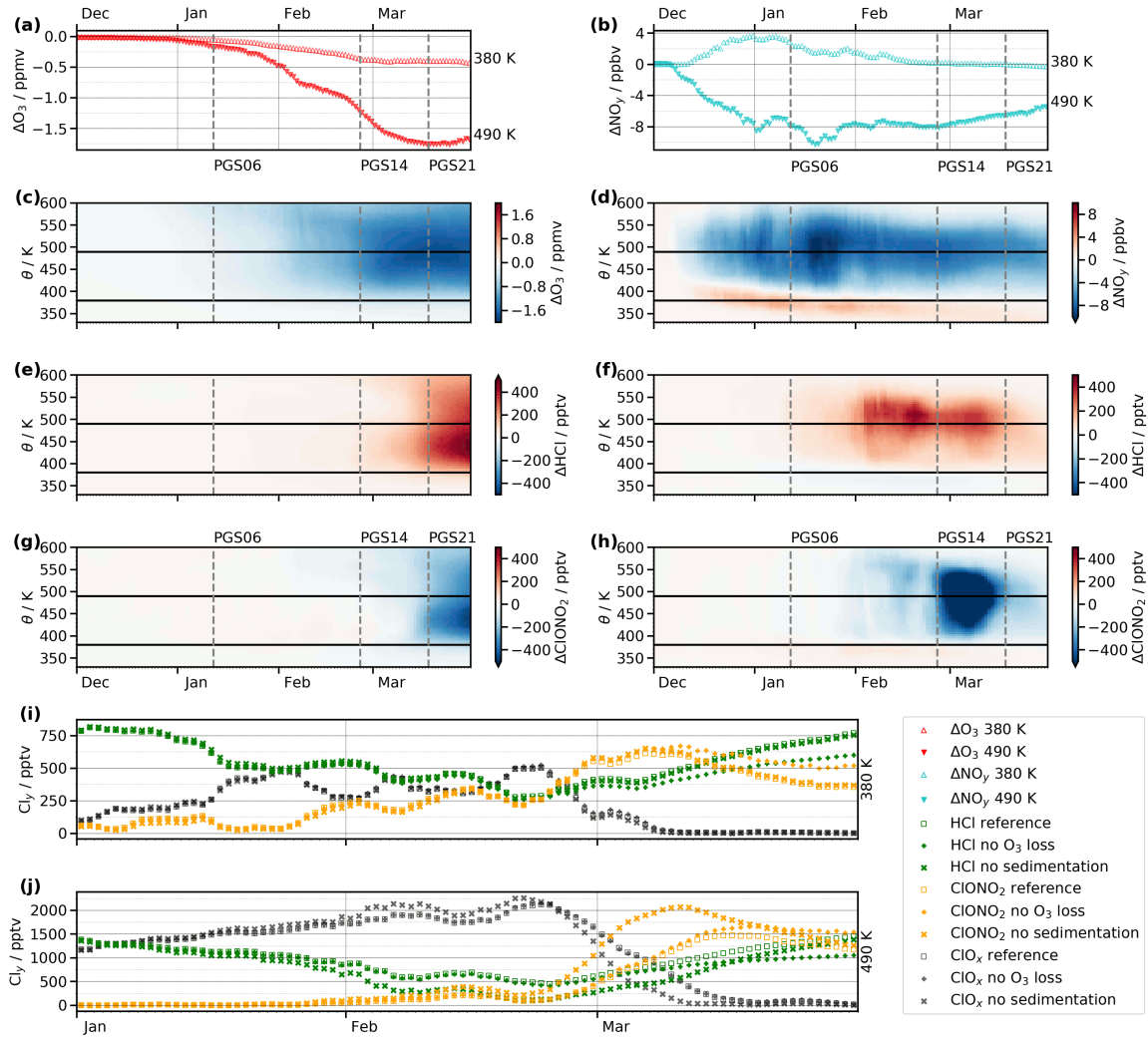


Figure 6.13: CLaMS vortex average (equivalent latitude $> 75^\circ N$) time series for ozone loss at 380 K and 490 K (a), and as cross section (c). Denitrification is presented in the same manner (b,d). Differences in HCl and $ClONO_2$ between a reference simulation and a simulation without the influence of ozone depletion (e,g) or PSC sedimentation (f,h). Altitudes of 380 K and 490 K, which are illustrated in other panels, are marked with horizontal lines. The bottom panels show ClO_x (black), HCl (green), and $ClONO_2$ (orange) for the reference simulation (open squares), and for the sensitivity simulations without ozone depletion (+) and without PSC sedimentation (x) at 380 K (i) and 490 K (j). Please note that these time series, in contrast to others in this figure, start in January.

early winter and later at lower altitudes, while denitrification is largest (up to 10 ppbv) at 490 K in the middle of January. The effect on **HCl** and **ClONO₂** (Fig. 6.13f,h) shows an enhancement of **HCl**, which reaches its maximum (500 pptv) in the middle of February, and a decrease in **ClONO₂**, which reaches its extreme (> 500 pptv) in the beginning of March. A weak opposite effect is observed at lower altitudes (< 380 K), where nitrification is observed.

Absolute values of **HCl**, **ClONO₂**, and **ClO_x** at 380 K and 490 K are presented in Fig. 6.13i,j for the reference and both sensitivity simulations. At 380 K, differences up to 200 pptv between the reference and the **O₃** sensitivity simulation (“+”) are visible in the reservoirs in March, with more **ClONO₂** and less **HCl** in the simulation without ozone depletion. **PSC** sedimentation (“x”) has only a weak influence at 380 K on the temporal evolution of the chlorine reservoirs and **ClO_x**, with small differences visible around the time of the final warming in the beginning of March. At 490 K, differences in the reservoirs between the reference and the **O₃** sensitivity run increase to 300 pptv, starting in the beginning of March. Again, more **ClONO₂** and less **HCl** is modeled for the sensitivity simulation without ozone depletion. A larger change in the chlorine partitioning is observed for the sensitivity simulation without **PSC** sedimentation: Starting towards the end of January, less **HCl** and more **ClO_x** is simulated, and by the beginning of March a substantial increase in **ClONO₂** with a difference of 1000 pptv compared to the reference is found. During that time, **ClO_x** decreases faster and **HCl** is consistently lower in comparison to the reference simulation. At the end of March, the sensitivity simulation without **PSC** sedimentation approaches the reference simulation for all presented species.

The sensitivity simulations by **CLaMS** help to quantify the effect of ozone depletion and **PSC** sedimentation on the observed unusual chlorine deactivation in 2016. The sensitivity simulation without ozone depletion showed that at 380 K, low ozone abundances (< 1.0 ppmv) caused 200 pptv of chlorine to be deactivated into **HCl** instead of **ClONO₂**. These ozone abundances are not as low (< 0.5 ppmv) as those found in previous studies (Prather and Jaffe, 1990; Douglass et al., 1995; Groöß et al., 1997, 2005; Mickley et al., 1997), but as demonstrated by Douglass and Kawa (1999), even higher ozone abundances than 0.5 ppmv together with cold temperatures are able to change chlorine deactivation. The different altitudes of the maxima observed in ozone loss (490 K) and changes in chlorine species (440 K) may be explained by the vertically increasing ozone **VMR** profile in the **LMS**. At 490 K, the absolute chemical ozone loss (≈ 1.75 ppmv) is larger than at 440 K (≈ 1.2 ppmv), but the total ozone **VMR** still is larger at 490 K (≈ 2.5 ppmv) than at 440 K (≈ 1.5 ppmv, see also Fig. 6.2). According to Douglass and Kawa (1999), the absolute ozone **VMR** is important for the chlorine deactivation partitioning, and not the chemical ozone loss. The availability of **NO_y** does not play a significant role in chlorine partitioning at 380 K. This may be explained by the fact that **CLaMS** does not simulate denitrification at 380 K (see Fig. 6.13b), and the availability of **NO_y** is not limited due to **PSC** sedimentation at this level. Thus there is little difference between the control and sensitivity simulations in this case. At 490 K, the reduced availability of **O₃** caused a relatively small proportion of chlorine (300 pptv) to be deactivated into **HCl** instead of **ClONO₂**. The decreased availability of **NO_y** (as a consequence of **PSC** sedimentation) induces major differences up to 1000 pptv in

ClONO₂.

The two sensitivity simulations reveal different time and altitude ranges in which they have the strongest impact on chlorine deactivation: While O₃ abundances affect the partitioning of the reservoirs from the beginning of March (with a maximum towards the end of March), the availability of NO_y has the maximum effect on HCl between February and the middle of March and on ClONO₂ around the major warming in the beginning of March. These sensitivity simulations also show impacts over different altitude ranges: The effect of O₃ depletion leads to notable differences between reference and sensitivity simulation starting from 380 K, with maximal differences at 440 K. The effect of sedimentation of HNO₃-containing particles on the chlorine reservoirs shows large impact between 400 K and 550 K. A small opposite effect is observed at altitudes below 380 K due to re-nitrification. The differences in HCl and ClONO₂ for ozone sensitivity appear to be very symmetric: positive differences in HCl correspond to negative differences in ClONO₂ at approximately the same time and altitude and with roughly the same magnitude. This is because O₃ abundances influence the partitioning of Cl and ClO, which directly determines whether chlorine is deactivated into HCl or ClONO₂ (Douglass and Kawa, 1999). For the sensitivity to PSC sedimentation, this symmetry between the differences in the chlorine reservoirs is not observed. Without PSC sedimentation, the chlorine activation is already changed by the end of January, while PSCs are present and chlorine activation is still possible. During this time, in the absence of denitrification, more ClONO₂ is produced due to the greater availability of NO_y, assuming that there is sufficient sunlight in the vortex to photolyze HNO₃ to produce NO₂. Together with available HCl, this regenerated ClONO₂ is then activated on PSCs, which results in net chlorine activation. In March, chlorine is deactivated into ClONO₂ to a considerably larger extent, again due to the greater availability of NO_y. The impact over different altitude ranges of the two sensitivity simulations implies that the observed unusually strong chlorine deactivation into HCl at 380 K (see Sec. 6.1.1) was predominantly driven by low O₃. At 490 K, where denitrification was much stronger than at 380 K, it was mainly the low NO_y that shifted chlorine deactivation towards HCl, while the low O₃ abundances only played a minor role.

The passive O₃ tracer of CLaMS also allows estimation of chemical ozone loss of 0.4 ppmv at 380 K and 1.75 ppmv at 490 K. Since the comparisons to MLS indicate that CLaMS overestimates O₃ towards the end of the winter, possibly because of deficiencies in its representation of dynamical processes, these estimates of ozone loss should be regarded as a lower boundary. As shown in Sec. 6.2, only a few other Arctic winters have experienced chemical ozone loss in the LMS as large as that in 2015/16 (Livesey et al., 2015; Santee, 2017).

6.3.2 Temperature sensitivity

In order to quantify the influence of temperature on the processes of chlorine activation and deactivation, an additional simulation of CLaMS with temperature reduced by 1 K globally has been performed to be compared to the “reference” simulation with temperatures given by the meteorological analysis. The reanalysis temperature usually

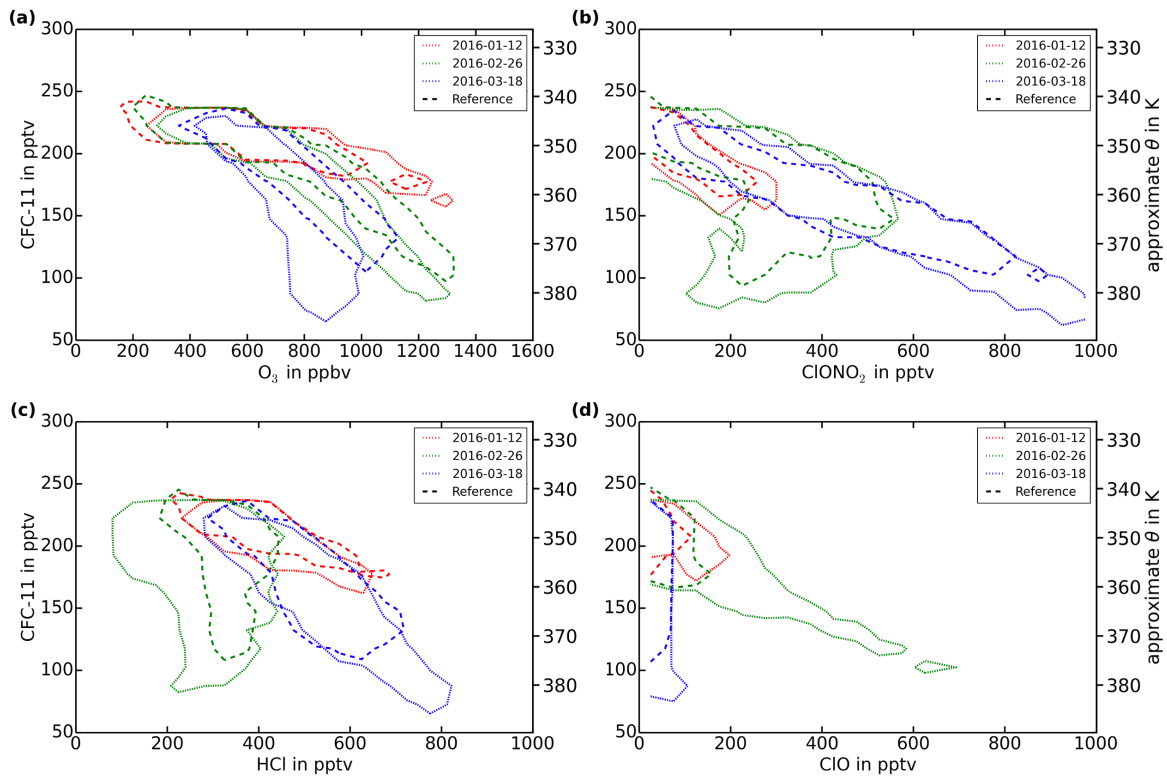


Figure 6.14: Correlation of CLaMS (a) O_3 , (b) $ClONO_2$, (c) HCl and (d) ClO with $CFC-11$ for flights PGS06 (red), PGS14 (green) and PGS21 (blue). The correlations are shown as RNFD for the reference run (dashed lines) and the sensitivity run with temperature reduced by 1 K globally (dotted) in the respective color of the flight.

used for the model simulation is not expected to have an error as high as 1 K (Hoffmann et al., 2017), but this sensitivity study is shown to estimate the response of ozone and chlorine species to significantly lower temperatures (see also Sinnhuber et al., 2011). This sensitivity run is shown as an RNFD correlation of O_3 , $ClONO_2$, HCl and ClO with $CFC-11$ in Fig. 6.14. In the O_3 correlation (Fig. 6.14a) it is apparent that the reduced temperature affects the extent of ozone depletion: While the correlation for the early flight PGS06 shows little change, the later flights PGS14 and PGS21 show considerably lower O_3 VMRs at higher altitudes (lower $CFC-11$ VMRs).

In contrast to the changes in O_3 due to the decreased temperature, few differences between the reference and the sensitivity run are visible for $ClONO_2$ (Fig. 6.14b). The main difference for $ClONO_2$ due to the decreased temperature is slightly increased variability, which in some regions more closely resembles that for the GLORIA correlations (see Fig. 6.10). For HCl (Fig. 6.14c) the reduced temperature leads to decreased VMRs for the earlier flights PGS06 and PGS14, while results for PGS21 remain almost unchanged. ClO (Fig. 6.14d) also shows notable changes for the two earlier flights PGS06 and PGS14 and no remarkable change for flight PGS21. For all flights in the temperature sensitivity run, it can be seen that the RNFD lines extend to lower $CFC-11$ abundances and thus to higher altitudes.

The modeled enhanced ozone depletion due to the decreased temperature (visible in the lower O_3 VMRs at higher altitudes during mid- and late winter flights PGS14 and PGS21) is expected as the lower temperatures also increase the time period during which PSC formation and chlorine activation may occur. With this earlier and longer chlorine activation in mind, one would assume that the sensitivity run would also show a decrease of the chlorine reservoirs ClONO_2 and HCl . This decrease for the early- and mid-winter is visible for HCl but not for ClONO_2 , which only changes marginally compared to the CLaMS reference run. This goes along with a substantial increase of simulated ClO during these flights. Due to the location of the polar vortex (see Sec. 6.1.3: the vortex reached as far south as the Alps) sunlight was available during the time of the flight and therefore the production of ClO was possible, which then could form ClONO_2 with ambient available NO_2 (see Sec. 2.5). The availability of NO_2 is indicated by record high HNO_3 abundances in early winter 2015/16, measured by MLS at 380 K (see Fig. 6.1). These high HNO_3 values are possible evidence of substantial re-nitrification through sedimentation of PSC particles. Such re-nitrification likely produced larger abundances of gas-phase HNO_3 at 380 K than typical, at least in early winter, thus making more NO_2 available. ClONO_2 gets “recycled” (converted into active chlorine via R 2.8 but then reformed via R 2.15) whereas HCl does not, so its abundances just continue to decline over the winter (as already shown by Müller et al., 1994). The extension of the RNFD isolines to lower CFC-11 values for flights PGS14 and PGS21 also indicates a change in the descent due to the decreased temperature. This was expected, because the diabatic part of the downwelling inside the stratospheric vortex (see Sec. 2.2) is driven by low temperatures.

6.3.3 Origin of ClONO_2 measured by GLORIA

In order to investigate the temporal evolution of the chemical composition at geolocations measured by GLORIA, CLaMS is used to calculate 11-day backward trajectories from these measurement geolocations. Then the model variables from the global model run are interpolated to these geolocations 11 days before the measurement, and CLaMS performs its Lagrangian simulation along the trajectory leading to the measurement. Along this trajectory, variables are saved at a temporal resolution of one hour. Because the chemical composition is simulated only along the trajectories, mixing was not considered for this simulation. As discussed by Konopka et al. (2003), mixing is regarded to have a weak influence on chlorine deactivation. This explains differences in CLaMS ClONO_2 cross sections between Figs. 6.8 and 6.15. A similar approach to investigate chlorine activation along backward trajectories has been reported by Lelieveld et al. (1999), but based on in situ measurements of HCl and with a focus on chlorine activation on cirrus clouds.

The cross sections at the trajectory ending points are shown in Fig. 6.15(a-d) for flight PGS14 for ClONO_2 and HCl as the reservoir gases and for ClO as one of the major active chlorine species at these altitudes. According to the validated ClONO_2 cross section, regions of interest are identified and marked: The local maximum of ClONO_2 at 16:00 UTC and $\theta = 360$ K is marked with a magenta “star” symbol, another local

maximum at 16:40 UTC and $\theta = 370$ K is marked green and the last substantial local maximum at 17:45 UTC and $\theta = 355$ K is marked blue. In the ClO cross section a maximum is modeled at 16:35 UTC and $\theta = 385$ K which is marked cyan. CLaMS backward trajectories within a horizontal distance of 25 km and a vertical distance of $\theta = 5$ K from these marked geolocations are selected for further analysis. These selected trajectories are projected on a map in Fig. 6.15d. It can be seen that the majority of these air parcels stay confined within a well defined region which is expected to be the polar vortex.

For flight PGS21, results from this trajectory analysis are presented in the same manner (Fig. 6.15e-h). Regions of interest are identified at different locations of enhanced ClONO₂ values at 12:10 UTC and $\theta = 380$ K (red), 13:25 UTC and $\theta = 390$ K (dark blue) and 15:20 UTC and $\theta = 380$ K (light green). Trajectories in the vicinity of these points are selected as described for flight PGS14. In the map projection of these trajectories (Fig. 6.15h), it can be seen that these air masses have been confined above Greenland (red) or have been circulating above Siberia (dark blue, light green) until they migrated to Scandinavia, where they were measured. The tracks of these trajectories are consistent with the meteorological situation of an eroding polar vortex during the time of flight PGS21.

The temporal evolution along these selected trajectories is shown for both flights in Fig. 6.16 for (a) potential temperature, (b) the solar zenith angle (SZA), (c) ClONO₂, (d) HCl, (e) ClO_x (= ClO+2Cl₂O₂+2Cl₂), (f) ClO, (g) Cl₂O₂ and (h) Cl₂. The mean of all selected trajectories belonging to a point of interest is presented as a solid line in the corresponding color, while minimum and maximum values are marked with shading in the same color.

Flight on 26 February 2016 (PGS14)

Potential temperatures (Fig. 6.16a1) show persistent downwelling along all selected trajectories, and the SZA (Fig. 6.16b1) indicates long periods in darkness. These first two panels provide context for the temporal evolution of the chlorine species.

The magenta curves, which have been defined to end at the region with the highest ClONO₂ in the cross section, show persistently high VMRs for ClONO₂ between 250 and 500 pptv and HCl values around 375 pptv. These persistently high VMRs in the chlorine reservoir species indicate that chlorine deactivation mainly occurred prior to the end point of the 11-day back trajectory and that these deactivated air masses have been transported to the GLORIA measurement location. Both chlorine reservoirs slightly increase during the first four days until 18 February 2016, then decrease for three days (until 20 February 2016) and then increase again, with a stronger increase seen in ClONO₂. The active chlorine species (as a sum shown in ClO_x) for the magenta curves remain at low levels (< 250 pptv), and show enhancements when the chlorine reservoirs are at lower values.

The green curves end at a local maximum of 340 pptv of ClONO₂ at $\theta = 370$ K. This enhanced value was reached due to an increase within the last five days. In the beginning

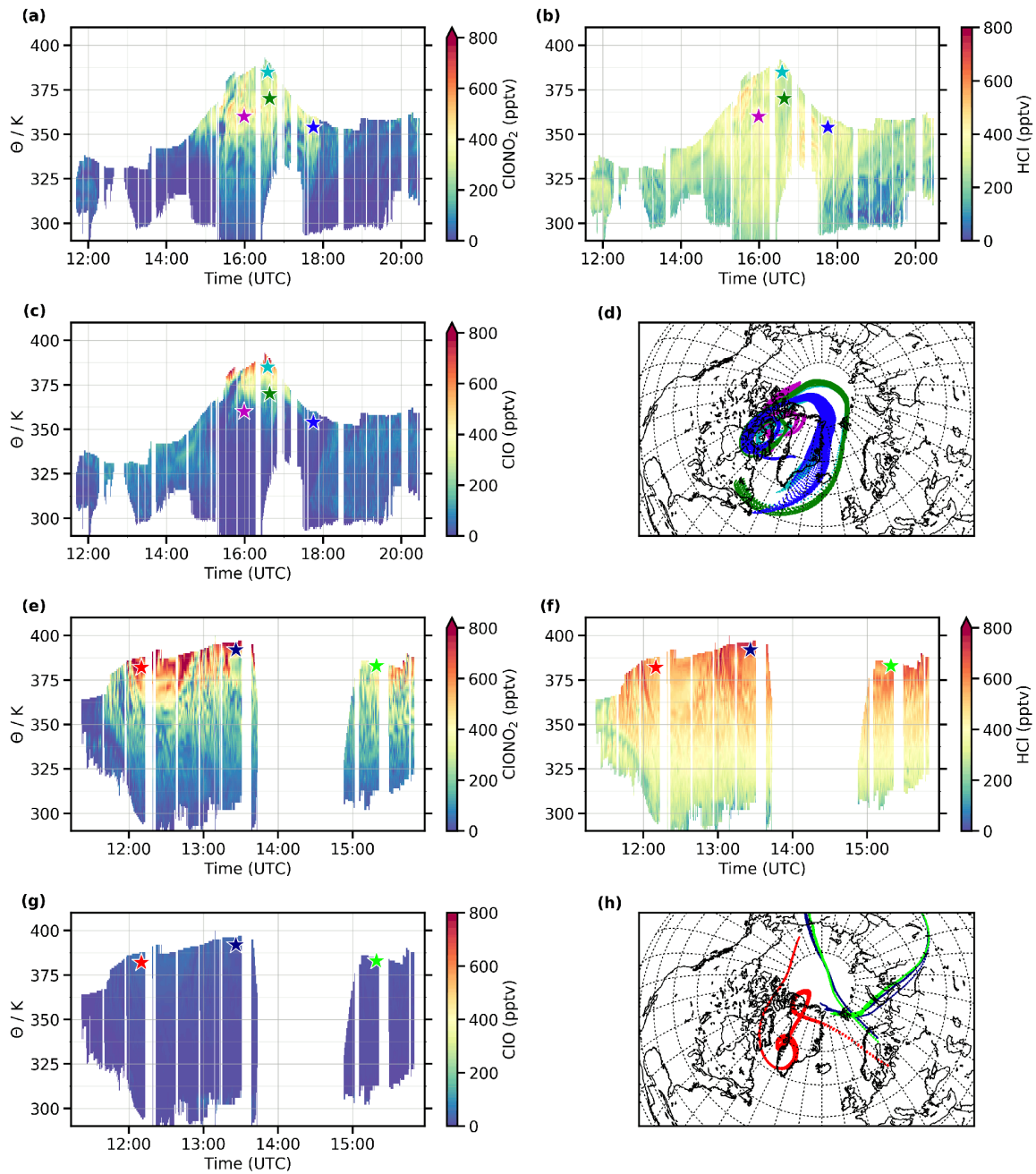


Figure 6.15: Cross sections for (a,e) ClONO_2 , (b,f) HCl and (c,g) ClO at the end of CLaMS trajectories leading to the GLORIA tangent point geolocations for flights PGS14 (a-d) and PGS21 (e-h). Regions of interest are marked with colored star symbols. 11-day backward trajectories calculated for each flight by CLaMS are shown on the map (d,h) in corresponding colors.

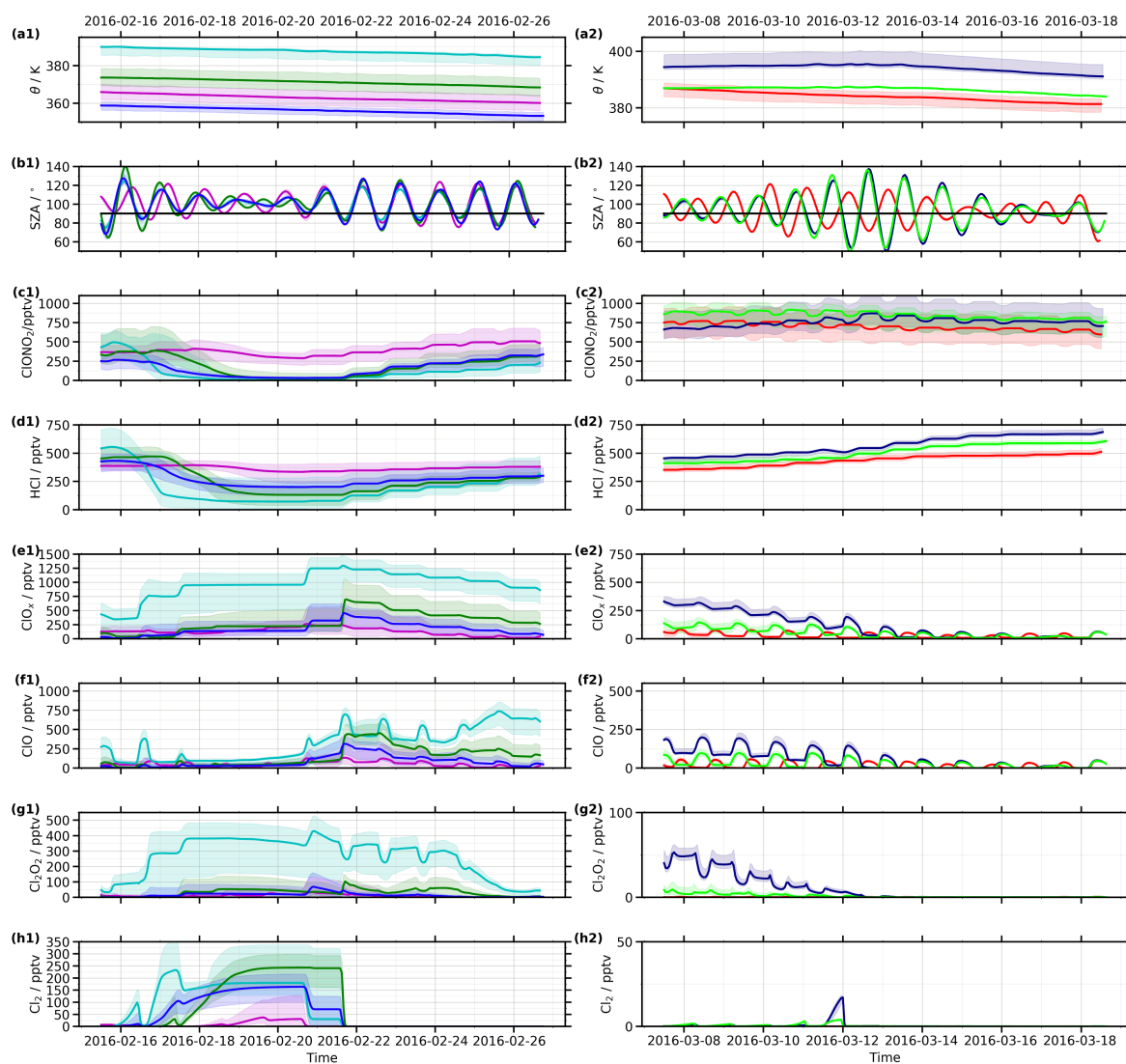


Figure 6.16: Modeled temporal evolution of (a) potential temperature, (b) solar zenith angle (SZA, the 90° threshold is marked with a black line), (c) ClONO_2 , (d) HCl , (e) ClO_x , (f) ClO , (g) Cl_2O_2 , and (h) Cl_2 for (1) flight PGS14 (left) and (2) flight PGS21 (right). These trajectories are color-coded as defined in Fig. 6.15 a-c and e-g. Solid lines show the mean of all trajectories connected with these regions and the light colors show minimum/maximum values among those trajectories. Please note different ordinate scales in each column.

of these 11-day trajectories, ClONO_2 started at VMRs of approximately 375 pptv until 17 February 2016 and then decreased to minimum values on 20 February 2016. The temporal evolution of HCl shows a similar slope: The mean value of these trajectories starts at a VMR of 470 pptv, which increases on the same time scale as ClONO_2 to 500 pptv, decreases to 125 pptv and finally increases to 320 pptv. During the time of ClONO_2 and HCl decrease, Cl_2 builds up to 270 pptv until it suddenly decreases to 0 pptv on 21 February 2016. At the same time, which coincides with the first exposure of this air parcel to sunlight since 16 February 2016 (according to the SZA), the VMR of ClO rapidly increases and then decreases again (with signatures of its diurnal cycle), while the reservoirs (ClONO_2 and HCl) increase again along with the decrease of ClO_x . The ClO -dimer increases first on 17 February 2016, when Cl_2 starts to rise, and increases again on 18 February 2016. In addition to the substantial increase of ClO on 21 February 2016, also the ClO -dimer rapidly increases to 100 pptv but then decreases again.

The blue curves show a similar course compared to the green ones but at lower potential temperature altitudes. Due to these different altitudes, the blue curves start with lower availability of chlorine reservoirs. At first (17 February 2016 and beginning of 18 February 2016) Cl_2 along the blue trajectory exceeds that on the green one, but ultimately less chlorine is activated (see Cl_2), because the blue parcels saw less sunlight than the green ones on 16 February 2016 and none on 17 February 2016. This also results in less ClO after the exposure to sunlight (21 February 2016), but these lower amounts of ClO are initially deactivated slightly more rapidly into ClONO_2 compared to the green curve. During the last three days of this trajectory, the green and the blue curves are almost identical for the chlorine reservoirs.

As an example of enhanced ClO values at the end of the trajectories, the cyan curves (which are at higher potential temperature altitudes of 385 K) show also a similar course compared to the green curves during the last five days before the measurement. In the beginning of the presented 11 days, the reservoir gases decrease earlier (16 February 2016) to low VMR levels than they did for the green point. ClO_x values are highest compared to other trajectory sets. The amount of accumulated Cl_2 is similar to that in the blue parcels (175 pptv) with the same times of sunlight exposure on 21 February 2016 and 22 February 2016. ClO also shows a similar evolution compared to the green course (if one considers the different altitudes, which are presumably the reason for the higher VMRs in the beginning) until the last three days, when ClO increases considerably along the cyan trajectory. This increase goes along with a decrease of the ClO -dimer, which is significantly higher along the entire trajectory compared to all other curves, reaching mean values up to 440 pptv on 20 February 2016.

For all selected points, there are regions in which the minimum/maximum values (indicated by the colored shading) vary substantially from the mean value, which indicates strong variability even for trajectories that end at geolocations within a horizontal distance of 25 km and $\theta = 5$ K altitude.

Flight on 18 March 2016 (PGS21)

In contrast to flight PGS14, sunlight is available along all selected trajectories of flight PGS21 on a daily basis, according to the SZA (Fig. 6.16b2). Based on the potential temperature, continuous subsidence is observed for the red trajectory set, while for the light-green and dark-blue trajectories the air parcels are slightly uplifted until 13 March 2016 and then subside with a similar slope compared to the other trajectories. ClO_x (Fig. 6.16e2) predominantly consists of ClO for all selected trajectories during that time of the year.

The red set of trajectories was selected due to the enhanced ClONO_2 values at the measurement location. The history of this enhancement in ClONO_2 shows a slight overall decrease (from 760 pptv to 630 pptv) with decreasing and increasing features due to the diurnal cycle. HCl increases step-wise from 380 pptv to 500 pptv, and ClO_x shows diurnal enhancements during the sunlit periods up to 60 pptv.

For the light-green air parcels, ClONO_2 slowly decreases from 900 to 750 pptv with fluctuations due to the diurnal cycle. HCl starts at 400 pptv and ends at 600 pptv by increasing in small steps. ClO shows a small diurnal cycle with maximum values up to 100 pptv.

The highest potential temperature trajectory end point for this flight is marked in dark blue. ClONO_2 increases from 670 to 870 pptv and then decreases again to 700 pptv with fluctuations due to the diurnal cycle. These dark-blue trajectories show the largest increase in HCl (from 450 pptv to 700 pptv). The diurnal cycle also dominates the evolution of ClO , with maximum values up to 200 pptv superimposed on a baseline value of 100 pptv that persists until 13 March 2016. During this period also small (50 pptv) remnants of Cl_2O_2 are visible.

For most of these selected trajectory sets it can be observed that the variability is smaller compared to the ones for PGS14, especially for chlorine species other than ClONO_2 .

Discussion

According to chemical tracers along CLaMS backward trajectories, enhanced ClONO_2 measured by GLORIA on 26 February 2016 was mainly a result of chlorine deactivation within the last five days before the measurement. An example of air masses has been presented that had been deactivated prior to the end point of the 11-day back trajectory and then transported to the GLORIA measurement location. These results also revealed substantial variability among trajectories initialized within a given region of interest (marked by the shaded area: 25 km horizontal and $\theta = 5$ K vertical coincidence). This variability indicates that small changes in the ending point of the trajectories result from different chemical histories of the air parcels.

For flight PGS21 in mid March, the ClONO_2 along the trajectories shows constantly high VMRs, modulated by the diurnal cycle. Since this flight took place well after the final warming (5-6 March; Manney and Lawrence, 2016), there had been no recent PSC formation or chlorine activation, and almost all of the measured enhanced ClONO_2

had been produced by chlorine deactivation that took place at least 11 days before the measurement. Changes in ClONO_2 , ClO_x (which is nearly all ClO at this time) and HCl can be explained by the photolysis of ClONO_2 , which results in a diurnal cycle (Brasseur and Solomon, 2005). This photolysis diminishes ClONO_2 and creates Cl (or a small fraction of ClO) during sunlit portions of the trajectories (Burkholder et al., 2015). These products can either react in ozone loss cycles, during which the fractions of Cl and ClO may change (see Solomon, 1999), or build chlorine reservoirs again: ClO reacts with NO_2 to ClONO_2 , while Cl reacts to HCl . Therefore not all of the ClONO_2 photolysis products ultimately go on to regenerate ClONO_2 . Thus HCl increases in a stepwise fashion, while ClONO_2 decreases. As was demonstrated with CLaMS sensitivity simulations, preferential deactivation into HCl is caused by low O_3 abundances as a consequence of ozone depletion.

In summary, for the most part enhanced ClONO_2 measured in February had been recently (within the prior few days) deactivated in situ in the LMS, while in March almost all of the measured enhanced ClONO_2 had been transported longer than 11 days.

Chapter 7

Summary and conclusions

In this thesis, a new data set based on recent measurements of the airborne imaging Fourier transform spectrometer **GLORIA** during the Arctic winter 2015/16 has been presented and discussed. These data have been applied in this work for scientific studies on chlorine deactivation processes in the Arctic **LMS**.

The retrieval results for **LOS**, temperature and trace gases have been characterized, and detailed error estimations have been motivated and discussed. As an example, flight PGS19 on 13 March 2016 has been discussed in detail, showing the retrieval results of temperature and the trace gases **HNO₃**, **O₃**, **ClONO₂**, **H₂O** and **CFC-12**, which have been compared to in situ measurements and to **MLS** data if applicable. It has been demonstrated that valuable information at high spatial resolution can be retrieved from infrared limb imaging data even in the **UTLS** with high clouds and **PSCs** present. The vertical resolution is 400 to 1000 m reached for most trace gases, which is unique for passive remote sensing instruments. With this high resolution, fine vertical structures can be examined. Typical estimated errors are in the range of 1–2K for temperature and 10%–20% relative error for the discussed trace gases. An approach for post-flight **LOS** correction has been successfully established to account for limited in-flight **LOS** knowledge and stabilization due to technical and software problems.

The comparisons of **HNO₃** and **O₃** measured by **MLS** and **GLORIA** show the synergies of air- and spaceborne measurements: The aircraft measurements with high spatial resolution reveal small-scale structures in the trace gas distributions. In contrast, the satellite measurements provide a continuous time series of global measurements up to high altitudes, which helps to put the structures observed by **GLORIA** into context. The same structures in **O₃** and **HNO₃** are visible in both data sets, and the measured mixing ratios are consistent, considering the different measurement characteristics. Towards the end of the winter, **O₃** and **HNO₃** are underestimated by **MLS**, which is an effect of lower vertical resolution of the spaceborne instrument and horizontal gridding. This lower resolution does not resolve spatially confined enhancements in these trace gases. Due to only partial overlap of vertically resolved information from **GLORIA** and the width of the **MLS** averaging kernels, it is not possible to perform a more refined comparison.

Comparisons of the **GLORIA** retrieval results with in situ measurements on board

HALO show the consistency of these data sets, taking into account the error, vertical and horizontal resolution of **GLORIA** and atmospheric variability, which are pronounced by the different measurement techniques and the inferred different geolocations of the measurements. Also comparisons with a balloon borne ozone and temperature sonde show a high consistency of the **GLORIA** data with independent observations.

This newly presented **GLORIA** data set benefits from aero-acoustic improvements of the instrument compared to previous **GLORIA** campaigns (Kaufmann et al., 2015; Woiwode et al., 2015; Ungermann et al., 2015). It is based on a much higher number of measured profiles and also has been compared to additional in situ trace gas measurements. Compared to the data set by Woiwode et al. (2015), which is also based on measurements in the high-spectral-resolution mode, the vertical resolutions of this **GLORIA** data set are significantly better, and a more detailed approach for error estimation is introduced. Furthermore, **GLORIA** measurements discussed in this work provide temperature and trace gas information down to 5 km, which is lower compared to the majority of previously discussed infrared limb sounders.

The second major part of this thesis is dedicated to the analysis of chlorine activation and deactivation in the Arctic winter 2015/16 **LMS** by utilizing time series of satellite measurements, aircraft remote sensing measurements from **GLORIA** during the **PGS** campaign and simulations by the atmospheric models **CLaMS** and **EMAC**. The analysis of **ACE-FTS** and **MLS** time series shows the extreme nature of the Arctic winter 2015/16: **HCl** has reached a new minimum in the Arctic at $\theta = 380$ K during the **Aura/MLS** epoch, followed by an unusually rapid increase of **HCl**. For several parts of the winter, **ClO** showed maximum values also within the instrument's record. Although ozone loss was greater in 2010/11, 2015/16 was a winter with extraordinary large chemical ozone loss (Livesey et al., 2015; Santee, 2017), estimated by **CLaMS** to be at least 0.4 ppmv at 380 K and 1.75 ppmv at 490 K. Estimations of chemical ozone loss with a "Match-based" analysis of **MLS O₃** measurements even reveal chemical ozone loss of 0.8 ppmv at 375 K and 1.7 ppmv at 475 K. The chemical process of chlorine deactivation, which was unusual for the Arctic, has been identified through **CLaMS** sensitivity studies to result at 380 K from low **O₃** abundances due to ozone depletion rather than from low **NO_y** availability as a result of **PSC** sedimentation. At higher potential temperatures (as shown at 490 K), denitrification played a greater role with 1000 pptv less chlorine deactivated into **ClONO₂** due to denitrification.

During this exceptional Arctic winter, the **GLORIA** instrument observed enhanced **ClONO₂** in the **LMS**. **GLORIA** measurements of both **O₃** and **ClONO₂** show meso-scale structures in the two-dimensional vertical cross sections. The comparisons of the highly resolved **GLORIA** cross sections of **O₃**, **ClONO₂** and **HNO₃** with the models **EMAC** and **CLaMS** serve as useful evaluations of two different approaches (Eulerian **CCM** and Lagrangian **CTM**) for modeling the chemical composition of the **UTLS**. The comparison of **EMAC** model data with measurements shows agreement within the limitations expected due to its relatively coarse resolution compared to **CLaMS** and **GLORIA**. In addition, deficiencies of **EMAC**'s diabatic descent are revealed in the comparisons. **CLaMS** benefits from its higher spatial resolution and reproduces the measurements even for detailed small-scale structures. For the late winter flight **PGS21**, **CLaMS** shows more **O₃** and

ClONO_2 than **GLORIA** at low potential temperature altitudes (330-340 K), which indicates that **CLaMS** could be improved concerning boundary conditions at low altitudes, horizontal transport and mixing. Discrepancies at 380 K between measurements (**MLS** CH_3Cl and **GLORIA** O_3 and ClONO_2) and **CLaMS** data also suggest potential for improvement in the model's representation of diabatic descent in the **LMS**. Generally, comparisons of **CLaMS** with **MLS** demonstrate overall agreement, while differences in **HCl** reflect well known problems with modeled chlorine activation, which also have consequences for O_3 and **ClO**.

A sensitivity study with the **CLaMS** model simulates this winter with temperature decreased globally by 1 K. As expected, this decreased temperature results in enhanced ozone depletion due to the earlier and longer presence of PSCs even at lower altitude levels, which leads to chlorine activation. Such an enhanced chlorine activation is not observed in ClONO_2 due to the position of the polar vortex outside the polar night. Thus sunlight was available to break up chlorine molecules. Atomic chlorine forms **ClO**, which then can react with NO_2 to "recycle" ClONO_2 which was reacting with **HCl** during chlorine activation. This process impedes the usage of ClONO_2 as a tracer of the extent of chlorine activation during an Arctic winter. From the correlation between **CFC-11** and O_3 for exemplary **PGS** flights, an additional ozone loss of 200 ppbv at 370 K is estimated at the end of the winter if temperature decreases by 1 K.

The origin of observed enhanced ClONO_2 at selected points in the **LMS** is reconstructed with an analysis of the chemical composition along trajectories leading to the measurement geolocations provided by **CLaMS**. As expected, this analysis shows that both transport of ClONO_2 and in situ chlorine deactivation at lower altitudes are simulated in the model for the selected February flight. Large variability among trajectories ending in the same vicinity shows that small changes in the path of an air parcel may strongly influence its course of chlorine activation/deactivation due to different encounters with PSCs, and different amounts of available NO_y , O_3 , and sunlight. For the flight in March 2016, the enhanced measured ClONO_2 is a result of transport, as illustrated by the chemical composition along the **CLaMS** trajectories.

Due to climate change, exceptionally cold winters are expected to occur more frequently in the future (Fels et al., 1980; Hartmann et al., 2014; WMO, 2015), which may in particular impact ozone in the Arctic **LMS**. These expected changes in ozone and chlorine activation and deactivation processes emphasize the importance of regular observations of the chemical composition of the atmosphere, with a particular focus on the **LMS**.

Outlook

This work sets the basis for a variety of consecutive studies. The results demonstrate the performance and quality of the **GLORIA** data set of the **UTLS** during the Arctic winter 2015/2016. In terms of data evaluation, first studies to explore additional retrieval targets for the **GLORIA** **PGS** spectra show the feasibility to retrieve ethane (C_2H_6), acetylene (C_2H_2), peroxyacyl nitrate (PAN), and formic acid (HCOOH). These tropospheric trace gases indicate pollution and allow for investigations of transport

of pollution plumes in the mid- and upper troposphere. The comparison of **GLORIA** and satellite trace gas measurements to model data shows room for improvements for both atmospheric models **EMAC** and **CLaMS**. For the **EMAC** model, simulations with higher spatial resolution would allow for better comparisons with **GLORIA** data, as in the present comparisons, the limited resolution of **EMAC** was dominant. In addition, more detailed analyses of the downward transport in the **LMS** which is underestimated by **EMAC** (as already mentioned by Brühl et al. (2007)) would be of interest. Also for **CLaMS**, comparisons with **MLS** and **GLORIA** indicate that the downward transport in the **LMS** is underestimated in the simulation. Discrepancies in **UTLS O₃** and **ClONO₂** between **CLaMS** and **GLORIA** indicate that the lower boundary conditions, which **CLaMS** uses for initialization, need to be reviewed in order to better represent atmospheric processes for these stratospheric trace gases. Of particular interest are further studies on the discrepancy of the onset of chlorine activation in the beginning of the polar winter. Grooß et al. (2018) already emphasized that this discrepancy is shown in many atmospheric models which indicates that at least one process related to chlorine activation is not fully understood and integrated in atmospheric models.

A new data set of spatially highly resolved trace gas distributions during polar winter is expected from **GLORIA** during the Antarctic SouthTRAC¹ **HALO** mission, scheduled in 2019. With such measurements, comparable to **GLORIA** PGS observations, new insights to spatial distributions of trace gases related to ozone depletion are expected. In order to globally monitor the influences of advancing climate change to the chemical composition of the atmosphere, new satellite missions with imaging limb emission instruments would be of great importance.

¹Transport and Composition of the Southern Hemisphere UTLS

List of Abbreviations

ACE-FTS	Atmospheric Chemistry Experiment – Fourier Transform Spectrometer
AIMS	Airborne (chemical ionization) Mass Spectrometer
BAHAMAS	Basic HALO Measurement and Data System
BDC	Brewer Dobson circulation
CALIOP	Cloud-Aerosol Lidar with Orthogonal Polarization
CALIPSO	Cloud-Aerosol Lidar and Infrared Pathfinder Satellite Observations
CCM	chemistry climate model
CFC-11	trichlorofluoromethane
CFC-12	dichlorodifluoromethane
CH₃Cl	methyl chloride
CI	cloud index
CLaMS	Chemical Lagrangian Model of the Stratosphere
Cl	atomic chlorine
Cl₂	molecular chlorine
Cl_y	sum of all chlorine species ($Cl_y = ClO_x + HCl + ClONO_2$)
Cl₂O₂	ClO-dimer
ClO	chlorine monoxide
ClO_x	sum of all reactive chlorine species ($ClO_x \approx ClO + 2Cl_2O_2 + 2Cl_2$)
ClONO₂	chlorine nitrate
CRISTA	CRyogenic Infrared Spectrometers and Telescopes for the Atmosphere
CRISTA-NF	CRISTA – New Frontiers

CTM	chemistry transport model
ECHAM5	fifth-generation European Centre HAmburg general circulation Model
ECMWF	European Centre for Medium-Range Weather Forecasts
EMAC	ECHAM/MESSy Atmospheric Chemistry
EqL	equivalent latitude
ESMVal	Earth System Model Validation
ESSenCe	ESA Sounder Campaign
FAIRO	Fast AIRborne Ozone instrument
FISH	Fast In-situ Stratospheric Hygrometer
FTIR	Fourier transform infrared spectrometry
FTS	Fourier transform spectrometer
GHG	greenhouse gas
GhOST-MS	Gas chromatograph for the Observation of Stratospheric Tracers Mass Spectrometer
GLORIA	Gimballed Limb Observer for Radiance Imaging of the Atmosphere
GWEX	Gravity Wave EXperiment
GW-LCYCLE II	Gravity Wave Life Cycle
H₂O	water vapor
HALO	High Altitude and LOng range research aircraft
HCl	hydrogen chloride
HITRAN	high-resolution transmission molecular absorption database
HNO₃	nitric acid
IASI	Infrared Atmospheric Sounding Interferometer
iFTS	imaging FTS
KOPRA	Karlsruhe Optimized and Precise Radiative transfer Algorithm
LIDAR	light detection and ranging
LOS	line of sight
LMS	lowermost stratosphere

LTE	local thermodynamic equilibrium
M55	Geophysica
MAD	median absolute deviation
MESSy	Modular Earth Submodel System
MERRA2	Modern-Era Retrospective analysis for Research and Applications, Version 2
MIPAS	Michelson Interferometer for Passive Atmospheric Sounding
MIPAS-STR	MIPAS-STRatospheric aircraft
MIPAS-B	MIPAS-Balloon
MIPAS-Envisat	MIPAS-environmental satellite
MkIV	Mark 4
MLS	Microwave Limb Sounder
NAT	nitric acid trihydrate
NDACC	Network for the Detection of Atmospheric Composition Change
NO_y	reactive nitrogen
O₃	ozone
ODS	ozone depleting substances
OMI	Ozone Monitoring Instrument
OMPS	Ozone Mapping Profiler Suite
OPD	optical path difference
PGS	POLSTRACC / GW-LCYCLE II / GWEX / SALSA
POLSTRACC	POLar STRAtosphere in a Changing Climate
PSC	polar stratospheric cloud
θ	potential temperature
PV	potential vorticity
PVU	potential vorticity unit
RECONCILE	Reconciliation of essential process parameters for an enhanced predictability of Arctic stratospheric ozone loss and its climate interactions
RNFD	relative normalized frequency distributions

SALSA	Seasonality of Air mass transport and origin in the Lowermost Stratosphere using the HALO Aircraft
SOLVE / THESEO	Stratospheric Aerosol and Gas Experiment (SAGE) III Ozone Loss and Validation Experiment / Third European Stratospheric Experiment on Ozone
sPV	scaled potential vorticity
SSW	stratospheric sudden warming
STE	stratosphere-troposphere exchange
StratoClim	Stratospheric and upper tropospheric processes for better climate predictions
STS	supercooled ternary solution
SZA	solar zenith angle
TAT	Total Air Temperature
TACTS	Transport and Composition in the UTLS
TOMS	Total Ozone Mapping Spectrometer
UARS	Upper Atmosphere Research Satellite
UTC	Universal Time, Coordinated
UTLS	upper troposphere lower stratosphere
UV	ultraviolet
VMR	volume mixing ratio
WISE	Wave-driven ISentropic Exchange
WMO	World Meteorological Organization

List of Figures

2.1	Temperature and θ profile of U.S. standard atmosphere.	4
2.2	Schematic of the transport and mixing processes in the UTLS.	5
2.3	Polar vortex evolution: potential vorticity at different potential temperature levels.	7
2.4	Climatological temperature and trace gas profiles for the Arctic.	9
2.5	Observed and simulated total ozone column anomalies as time series between 1960 and 2100.	11
2.6	Exemplary time series that show chlorine partitioning in the Arctic and Antarctic.	13
2.7	Total ozone columns for a “World avoided” without reduction of CFCs.	14
2.8	Climate impacts due to Antarctic ozone depletion.	16
3.1	Interferogram and corresponding spectrum measured by GLORIA.	20
3.2	Schematic of off-axis beams in a FTS.	21
3.3	Comparison of sampling of MIPAS-STR and GLORIA.	22
3.4	GLORIA mounted below the HALO research aircraft.	23
3.5	Example of an atmospheric limb emission infrared spectrum measured by GLORIA.	25
3.6	Close-up of the example of an atmospheric limb emission infrared spectrum measured by GLORIA with contributions of single trace gases.	26
3.7	Spectrum for a CO ₂ molecule showing the P, Q and R branches.	27
3.8	Schematic representation of the limb measurement geometry.	28
3.9	Vertical distribution of cloud indices along flights PGS12 and PGS19.	30
4.1	Flight paths of all PGS flights with GLORIA measurements.	36
5.1	Temperature, PV, HNO ₃ , and O ₃ at 13 km typical flight altitude together with GLORIA tangent points.	43
5.2	Illustration of the error budget of the temperature and HNO ₃ retrieval.	45
5.3	Line-of-sight corrections of flights PGS12 and PGS19.	46
5.4	GLORIA temperature, corresponding estimated error and vertical resolution, and comparison to BAHAMAS in situ measurements.	47
5.5	GLORIA HNO ₃ , corresponding estimated error and vertical resolution, comparison to MLS measurements, and to AIMS in situ measurements.	49
5.6	GLORIA O ₃ , corresponding estimated error and vertical resolution, comparison to MLS measurements, and to FAIRO in situ measurements.	50

5.7	GLORIA ClONO ₂ , corresponding estimated error and vertical resolution, and comparison to AIMS in situ measurements.	51
5.8	GLORIA H ₂ O, corresponding estimated error and vertical resolution, and comparison to FISH in situ measurements.	52
5.9	GLORIA CFC-12, corresponding estimated error and vertical resolution, and comparison to GhOST-MS in situ measurements.	53
5.10	Comparison of O ₃ and temperature from balloon-borne measurements and GLORIA.	55
6.1	Vortex average time series of temperature, and volume mixing ratios of ClONO ₂ , HCl, daytime ClO, O ₃ , HNO ₃ , CH ₃ Cl for the period 2004-2018 over the Arctic at $\theta=380\text{K}$	61
6.2	Comparison of MLS, ACE-FTS, and CALIOP time series with CLaMS simulation results for PSC areas, ClONO ₂ , HCl, daytime ClO, O ₃ , HNO ₃ , and CH ₃ Cl.	63
6.3	Time series of vortex averaged trace gases from satellite measurements and CLaMS simulation at 380 K and 490 K.	64
6.4	Flight PGS06 (12 January 2016): Flight path on a map with θ at typical HALO cruise altitude of 13 km together with GLORIA tangent points. GLORIA cross section of O ₃ , ClONO ₂ , and HNO ₃	67
6.5	Same as in Fig. 6.4, but for Flight PGS14 (26 February 2016).	68
6.6	Same as in Fig. 6.4, but for Flight PGS21 (18 March 2016).	69
6.7	Comparison of GLORIA measured O ₃ to CLaMS and EMAC simulated O ₃ cross sections for flights PGS06 (12 January 2016), PGS14 (26 February 2016) and PGS21 (18 March 2016).	70
6.8	Same as Fig. 6.7, but for ClONO ₂	72
6.9	Same as Fig. 6.7, but for HNO ₃	73
6.10	Correlation of O ₃ and ClONO ₂ with CFC-11 measured by GLORIA for flights PGS06, PGS14 and PGS21.	75
6.11	Correlation of CLaMS O ₃ and ClONO ₂ with CFC-11 for flights PGS06, PGS14 and PGS21.	76
6.12	Ozone loss profiles calculated with a Match based approach on MLS ozone data.	77
6.13	CLaMS vortex average time series for ozone loss, denitrification, differences in HCl and ClONO ₂ between a reference simulation and a simulation without the influence of ozone depletion or PSC sedimentation.	80
6.14	Correlation of CLaMS (temperature sensitivity simulation) O ₃ , ClONO ₂ , HCl and ClO with CFC-11 for flights PGS06, PGS14 and PGS21.	83
6.15	Cross sections for ClONO ₂ , HCl and ClO at the end of CLaMS trajectories leading to the GLORIA tangent point geolocations for flights PGS14 and PGS21.	86
6.16	Modeled temporal evolution of potential temperature, solar zenith angle, ClONO ₂ , HCl, ClO _{<i>x</i>} , ClO, Cl ₂ O ₂ , and Cl ₂ for flights PGS14 and PGS21.	87

List of Tables

3.1	Spectral windows for the different target species of the GLORIA high-spectral-resolution-mode PGS retrieval.	31
4.1	Approximate vertical resolution, typical estimated error, and recommended lowest (i.e., highest pressure) retrieval surface for MLS version 4 trace gases in the UTLS.	38
5.1	Median differences between GLORIA and in situ and Aura/MLS measurements with the median absolute deviation for each flight and the whole campaign.	57

Bibliography

- Andersson, M. E., Verronen, P. T., Marsh, D. R., Päivärinta, S., and Plane, J. M. C.: WACCM-D—Improved modeling of nitric acid and active chlorine during energetic particle precipitation, *Journal of Geophysical Research: Atmospheres*, 121, 10,328–10,341. doi:10.1002/2015JD024173, 2016. (cited on page 18).
- Armstrong, B. H.: Spectrum line profiles: The Voigt function, *Journal of Quantitative Spectroscopy and Radiative Transfer*, 7, 61–88. doi:10.1016/0022-4073(67)90057-X, 1967. (cited on page 26).
- Baldwin, M. P. and Dunkerton, T. J.: Stratospheric harbingers of anomalous weather regimes, *Science (New York, N.Y.)*, 294, 581–584. doi:10.1126/science.1063315, 2001. (cited on page 4).
- Ball, W. T., Alsing, J., Mortlock, D. J., Staehelin, J., Haigh, J. D., Peter, T., Tummon, F., Stübi, R., Stenke, A., Anderson, J., Bourassa, A., Davis, S. M., Degenstein, D., Frith, S., Froidevaux, L., Roth, C., Sofieva, V., Wang, R., Wild, J., Yu, P., Ziemke, J. R., and Rozanov, E. V.: Evidence for a continuous decline in lower stratospheric ozone offsetting ozone layer recovery, *Atmospheric Chemistry and Physics*, 18, 1379–1394. doi:10.5194/acp-18-1379-2018, 2018. (cited on page 11).
- Bange, J., Esposito, M., Lenschow, D. H., Brown, P. R. A., Dreiling, V., Giez, A., Mahrt, L., Malinowski, S. P., Rodi, A. R., Shaw, R. A., Siebert, H., Smit, H., and Zöger, M.: Measurement of Aircraft State and Thermodynamic and Dynamic Variables: 2, in: *Airborne Measurements for Environmental Research*, pp. 7–75, Wiley-Blackwell. ISBN:9783527653218, 2013. (cited on page 37).
- Bates, D. R. and Nicolet, M.: The photochemistry of atmospheric water vapor, *Journal of Geophysical Research*, 55, 301–327, 1950. (cited on page 10).
- Beaver, G. M. and Russell, J. M.: The climatology of stratospheric HCL and HF observed by HALOE, *Advances in Space Research*, 21, 1373–1382. doi:10.1016/S0273-1177(97)00745-X, 1998. (cited on page 18).
- Beer, R.: Remote sensing by Fourier transform spectrometry, vol. 120 of *Chemical analysis*, Wiley, New York. ISBN:0-471-55346-8, 1992. (cited on page 19).
- Berman, R.: Direct measurements of line mixing, line broadening, and translational line shape in the v_1+v_2 Q-branch of pure CO₂, Graduate Department of Physics, University of Toronto, Toronto, 1998. (cited on page 27).

- Bernath, P. F.: Spectra of Atoms and Molecules, Oxford University Press USA, Oxford, 2nd ed. edn. ISBN:978-0-19-517759-6, 2005. (cited on pages 24, 25).
- Bernath, P. F.: The Atmospheric Chemistry Experiment (ACE), Journal of Quantitative Spectroscopy and Radiative Transfer, 186, 3–16. doi:10.1016/j.jqsrt.2016.04.006, 2017. (cited on pages 18, 27, 38).
- Birk, M. and Wagner, G.: Voigt profile introduces optical depth dependent systematic errors – Detected in high resolution laboratory spectra of water, Journal of Quantitative Spectroscopy and Radiative Transfer, 170, 159–168. doi:10.1016/j.jqsrt.2015.11.008, 2016. (cited on page 26).
- Blom, C. E., Gulde, T., Höpfner, M., Keim, C., Kimmig, W., Liu, G. Y., Piesch, C., and Sartorius, C.: MIPAS-STR: Ein Fernerkundungsinstrument für Stratosphärenflugzeuge, Nachrichten - Forschungszentrum Karlsruhe, 35, 46–50, 2003. (cited on page 19).
- Bönisch, H., Engel, A., Birner, T., Hoor, P., Tarasick, D. W., and Ray, E. A.: On the structural changes in the Brewer-Dobson circulation after 2000, Atmospheric Chemistry and Physics, 11, 3937–3948. doi:10.5194/acp-11-3937-2011, 2011. (cited on page 6).
- Borrmann, S., Solomon, S., Dye, J. E., and Luo, B.: The potential of cirrus clouds for heterogeneous chlorine activation, Geophysical Research Letters, 23, 2133–2136. doi:10.1029/96GL01957, 1996. (cited on page 62).
- Brasseur, G. and Solomon, S.: Aeronomy of the middle atmosphere: Chemistry and physics of the stratosphere and mesosphere, vol. 32 of *Atmospheric and oceanographic sciences library*, Springer, Dordrecht and [Great Britain], 3rd rev. and enl. edn. ISBN:9781402032844, 2005. (cited on pages 3, 12, 12, 90).
- Brault, J. W.: New approach to high-precision Fourier transform spectrometer design, Applied Optics, 35, 2891–2896. doi:10.1364/AO.35.002891, 1996. (cited on page 23).
- Braun, M., Groß, J.-U., Woiwode, W., Johansson, S., Höpfner, M., Friedl-Vallon, F., Oelhaf, H., Preusse, P., Ungermann, J., Sinnhuber, B.-M., Ziereis, H., and Braesicke, P.: Nitrification of the lowermost stratosphere during the exceptionally cold Arctic winter 2015/16: Manuscript in preparation, Atmospheric Chemistry and Physics Discussions, 2019. (cited on pages 56, 65).
- Brewer, A. W.: Evidence for a world circulation provided by the measurements of helium and water vapour distribution in the stratosphere, Quarterly Journal of the Royal Meteorological Society, 75, 351–363. doi:10.1002/qj.49707532603, 1949. (cited on page 4).
- Brühl, C., Steil, B., Stiller, G., Funke, B., and Jöckel, P.: Nitrogen compounds and ozone in the stratosphere: Comparison of MIPAS satellite data with the chemistry climate model ECHAM5/MESy1, Atmospheric Chemistry and Physics, 7, 5585–5598. doi:10.5194/acp-7-5585-2007, 2007. (cited on pages 74, 94).

- Browell, E. V., Butler, C. F., Ismail, S., Robinette, P. A., Carter, A. F., Higdon, N. S., Toon, O. B., Schoeberl, M. R., and Tuck, A. F.: Airborne lidar observations in the wintertime Arctic stratosphere: Polar stratospheric clouds, *Geophysical Research Letters*, 17, 385–388. doi:10.1029/GL017i004p00385, 1990. (cited on page 8).
- Brown, A. T., Volk, C. M., Schoeberl, M. R., Boone, C. D., and Bernath, P. F.: Stratospheric lifetimes of CFC-12, CCl₄, CH₄, CH₂Cl and N₂O from measurements made by the Atmospheric Chemistry Experiment-Fourier Transform Spectrometer (ACE-FTS), *Atmospheric Chemistry and Physics*, 13, 6921–6950. doi:10.5194/acp-13-6921-2013, 2013. (cited on page 39).
- Burkholder, J. B., Sander, S. P., Abbatt, J., Barker, J. R., Huie, R. E., Kolb, C. E., Kurylo, M. J., Orkin, V. L., Wilmouth, D. M., and Wine, P. H.: Chemical Kinetics and Photochemical Data for Use in Atmospheric Studies, Evaluation No. 18, JPL Publication, 15-10. <http://jpldataeval.jpl.nasa.gov>, 2015. (cited on page 90).
- Butchart, N.: The Brewer-Dobson circulation, *Reviews of Geophysics*, 52, 157–184. doi:10.1002/2013RG000448, 2014. (cited on pages 4, 6, 17).
- Carslaw, K. S., Luo, B. P., Clegg, S. L., Peter, T., Brimblecombe, P., and Crutzen, P. J.: Stratospheric aerosol growth and HNO₃ gas phase depletion from coupled HNO₃ and water uptake by liquid particles, *Geophysical Research Letters*, 21, 2479–2482. doi:10.1029/94GL02799, 1994. (cited on page 40).
- Carslaw, K. S., Luo, B., and Peter, T.: An analytic expression for the composition of aqueous HNO₃-H₂SO₄ stratospheric aerosols including gas phase removal of HNO₃, *Geophysical Research Letters*, 22, 1877–1880. doi:10.1029/95GL01668, 1995. (cited on page 8).
- Chapman, S.: On ozone and atomic oxygen in the upper atmosphere, *The London, Edinburgh, and Dublin Philosophical Magazine and Journal of Science*, 10, 369–383. doi:10.1080/14786443009461588, 1930. (cited on page 10).
- Charlton, A. J., O'Neill, A., Lahoz, W. A., and Berrisford, P.: The Splitting of the Stratospheric Polar Vortex in the Southern Hemisphere, September 2002: Dynamical Evolution, *Journal of the Atmospheric Sciences*, 62, 590–602. doi:10.1175/JAS-3318.1, 2005. (cited on page 8).
- Charney, J. G., Arakawa, A., Baker, D. J., Bolin, B., and Dickson, R. E.: Carbon Dioxide and Climate, National Academies Press, Washington, D.C. doi:10.17226/12181, 1979. (cited on page 15).
- Chubachi, S. et al.: Preliminary result of ozone observations at Syowa station from February 1982 to January 1983, internal note, 1984. (cited on page 3).
- Crutzen, P. J.: The influence of nitrogen oxides on the atmospheric ozone content, *Quarterly Journal of the Royal Meteorological Society*, 96, 320–325, 1970. (cited on page 10).

- Crutzen, P. J., Müller, R., Brühl, C., and Peter, T.: On the potential importance of the gas phase reaction $\text{CH}_3\text{O}_2 + \text{ClO} \rightarrow \text{ClOO} + \text{CH}_3\text{O}$ and the heterogeneous reaction $\text{HOCl} + \text{HCl} \rightarrow \text{H}_2\text{O} + \text{Cl}_2$ in “ozone hole” chemistry, *Geophysical Research Letters*, 19, 1113–1116. doi:10.1029/92GL01172, 1992. (cited on page 12).
- Dameris, M. and Baldwin, M. P.: Chapter 8. Impact of Climate Change on the Stratospheric Ozone Layer, in: *Stratospheric Ozone Depletion and Climate Change*, edited by Müller, R., pp. 214–252, The Royal Society of Chemistry. ISBN:978-1-84973-002-0, 2012. (cited on pages 1, 15, 16, 16, 16).
- Dessler, A. E., Considine, D. B., Morris, G. A., Schoeberl, M. R., Russell, J. M., Roche, A. E., Kumer, J. B., Mergenthaler, J. L., Waters, J. W., Gille, J. C., and Yue, G. K.: Correlated observations of HCl and ClONO₂ from UARS and implications for stratospheric chlorine partitioning, *Geophysical Research Letters*, 22, 1721–1724. doi:10.1029/95GL01593, 1995. (cited on page 18).
- Dicke, R. H.: The Effect of Collisions upon the Doppler Width of Spectral Lines, *Physical Review*, 89, 472. doi:10.1103/PhysRev.89.472, 1953. (cited on page 26).
- Dobson, G. M. B.: Origin and Distribution of the Polyatomic Molecules in the Atmosphere, *Proceedings of the Royal Society A: Mathematical, Physical and Engineering Sciences*, 236, 187–193. doi:10.1098/rspa.1956.0127, 1956. (cited on page 4).
- Dobson, G. M. B. and Harrison, D. N.: Measurements of the Amount of Ozone in the Earth’s Atmosphere and Its Relation to Other Geophysical Conditions, *Proceedings of the Royal Society A: Mathematical, Physical and Engineering Sciences*, 110, 660–693. doi:10.1098/rspa.1926.0040, 1926. (cited on page 10).
- Douglass, A. R. and Kawa, S. R.: Contrast between 1992 and 1997 high-latitude spring Halogen Occultation Experiment observations of lower stratospheric HCl, *Journal of Geophysical Research: Atmospheres*, 104, 18 739–18 754. doi:10.1029/1999JD900281, 1999. (cited on pages 13, 14, 81, 81, 82).
- Douglass, A. R., Schoeberl, M. R., Stolarski, R. S., Waters, J. W., Russell, J. M., Roche, A. E., and Massie, S. T.: Interhemispheric differences in springtime production of HCl and ClONO₂ in the polar vortices, *Journal of Geophysical Research*, 100, 13967. doi:10.1029/95JD00698, 1995. (cited on pages 13, 14, 81).
- Dufour, G., Nassar, R., Boone, C. D., Skelton, R., Walker, K. A., Bernath, P. F., Rinsland, C. P., Semeniuk, K., Jin, J. J., McConnell, J. C., and Manney, G. L.: Partitioning between the inorganic chlorine reservoirs HCl and ClONO₂ during the Arctic winter 2005 from the ACE-FTS, *Atmospheric Chemistry and Physics*, 6, 2355–2366. doi:10.5194/acp-6-2355-2006, 2006. (cited on pages 18, 38).
- Dunkerton, T. J. and Delisi, D. P.: Evolution of potential vorticity in the winter stratosphere of January-February 1979, *Journal of Geophysical Research: Atmospheres* (1984–2012), 91, 1199–1208. doi:10.1029/JD091iD01p01199, 1986. (cited on page 6).

- Eckstein, J., Ruhnke, R., Pfahl, S., Christner, E., Dyroff, C., Reinert, D., Rieger, D., Schneider, M., Schröter, J., Zahn, A., and Braesicke, P.: From climatological to small scale applications: Simulating water isotopologues with ICON-ART-Iso (version 2.1), *Geoscientific Model Development Discussions*, pp. 1–31. doi:10.5194/gmd-2017-280, 2017. (cited on page 75).
- Eriksson, P.: Analysis and comparison of two linear regularization methods for passive atmospheric observations, *Journal of Geophysical Research: Atmospheres*, 105, 18 157–18 167. doi:10.1029/2000JD900172, 2000. (cited on page 30).
- Eyring, V., Cionni, I., Bodeker, G. E., Charlton-Perez, A. J., Kinnison, D. E., Scinocca, J. F., Waugh, D. W., Akiyoshi, H., Bekki, S., Chipperfield, M. P., Dameris, M., Dhomse, S., Frith, S. M., Garny, H., Gettelman, A., Kubin, A., Langematz, U., Mancini, E., Marchand, M., Nakamura, T., Oman, L. D., Pawson, S., Pitari, G., Plummer, D. A., Rozanov, E., Shepherd, T. G., Shibata, K., Tian, W., Braesicke, P., Hardiman, S. C., Lamarque, J. F., Morgenstern, O., Pyle, J. A., Smale, D., and Yamashita, Y.: Multi-model assessment of stratospheric ozone return dates and ozone recovery in CCMVal-2 models, *Atmospheric Chemistry and Physics*, 10, 9451–9472. doi:10.5194/acp-10-9451-2010, 2010. (cited on page 11).
- Fahey, D. W., Kelly, K. K., Kawa, S. R., Tuck, A. F., Loewenstein, M., Chan, K. R., and Heidt, L. E.: Observations of denitrification and dehydration in the winter polar stratospheres, *Nature*, 344, 321–324. doi:10.1038/344321a0, 1990. (cited on pages 14, 52).
- Fahey, D. W., Gao, R.-S., Möhler, O., Saathoff, H., Schiller, C., Ebert, V., Krämer, M., Peter, T., Amarouche, N., Avallone, L. M., Bauer, R., Bozóki, Z., Christensen, L. E., Davis, S. M., Durr, G., Dyroff, C., Herman, R. L., Hunsmann, S., Khaykin, S. M., Mackrodt, P., Meyer, J., Smith, J. B., Spelten, N., Troy, R. F., Vömel, H., Wagner, S., and Wienhold, F. G.: The AquaVIT-1 intercomparison of atmospheric water vapor measurement techniques, *Atmospheric Measurement Techniques*, 7, 3177–3213. doi:10.5194/amt-7-3177-2014, 2014. (cited on page 37).
- Farman, J. C., Gardiner, B. G., and Shanklin, J. D.: Large losses of total ozone in Antarctica reveal seasonal ClO_x/NO_x interaction, *Nature*, 315, 207 EP –. doi:10.1038/315207a0, 1985. (cited on page 3).
- Fels, S. B., Mahlman, J. D., Schwarzkopf, M. D., and Sinclair, R. W.: Stratospheric Sensitivity to Perturbations in Ozone and Carbon Dioxide: Radiative and Dynamical Response, *Journal of the Atmospheric Sciences*, 37, 2265–2297. doi:10.1175/1520-0469(1980)037<2265:SSTPIO>2.0.CO;2, 1980. (cited on pages 2, 15, 93).
- Fischer, H. and Oelhaf, H.: Remote sensing of vertical profiles of atmospheric trace constituents with MIPAS limb-emission spectrometers, *Applied Optics*, 35, 2787–2796. doi:10.1364/AO.35.002787, 1996. (cited on page 19).
- Fischer, H., Birk, M., Blom, C., Carli, B., Carlotti, M., von Clarmann, T., Delbouille, L., Dudhia, A., Ehhalt, D., Endemann, M., Flaud, J. M., Gessner, R., Kleinert, A.,

- Koopman, R., Langen, J., López-Puertas, M., Mosner, P., Nett, H., Oelhaf, H., Perron, G., Remedios, J., Ridolfi, M., Stiller, G., and Zander, R.: MIPAS: An instrument for atmospheric and climate research, *Atmospheric Chemistry and Physics*, 8, 2151–2188. doi:10.5194/acp-8-2151-2008, 2008. (cited on pages 18, 19, 28).
- Flaud, J. M.: Spectroscopic parameters of atmospheric gases, *Atmospheric Research*, 31, 299–313. doi:10.1016/0169-8095(94)90005-1, 1994. (cited on page 25).
- Flaud, J.-M., Piccolo, C., and Carli, B.: A Spectroscopic Database for MIPAS, in: *Proceedings of the ENVISAT validation workshop*, ESRIN, ESA, Italy, 2002. (cited on page 31).
- Flaud, J.-M., Piccolo, C., Carli, B., Perrin, A., Coudert, L. H., Teffo, J. L., and Brown, L. R.: Molecular line parameters for the MIPAS (Michelson Interferometer for Passive Atmospheric Sounding) experiment, *Atmos. Ocean. Opt.*, 16, 172–182, 2003. (cited on page 26).
- Flaud, J.-M., Brizzi, G., Carlotti, M., Perrin, A., and Ridolfi, M.: MIPAS database: Validation of HNO₃ line parameters using MIPAS satellite measurements, *Atmospheric Chemistry and Physics*, 6, 5037–5048. doi:10.5194/acp-6-5037-2006, 2006. (cited on page 31).
- Forster, P. and Shine, K. P.: Radiative forcing and temperature trends from stratospheric ozone changes, *Journal of Geophysical Research: Atmospheres*, 102, 10 841–10 855. doi:10.1029/96JD03510, 1997. (cited on pages 1, 17).
- Friedl-Vallon, F., Maucher, G., Seefeldner, M., Trieschmann, O., Kleinert, A., Lengel, A., Keim, C., Oelhaf, H., and Fischer, H.: Design and characterization of the balloon-borne Michelson Interferometer for Passive Atmospheric Sounding (MIPAS-B2), *Applied Optics*, 43, 3335–3355. doi:10.1364/AO.43.003335, 2004. (cited on page 19).
- Friedl-Vallon, F., Gulde, T., Hase, F., Kleinert, A., Kulesa, T., Maucher, G., Neubert, T., Olschewski, F., Piesch, C., Preusse, P., Rongen, H., Sartorius, C., Schneider, H., Schönfeld, A., Tan, V., Bayer, N., Blank, J., Dapp, R., Ebersoldt, A., Fischer, H., Graf, F., Guggenmoser, T., Höpfner, M., Kaufmann, M., Kretschmer, E., Latzko, T., Nordmeyer, H., Oelhaf, H., Orphal, J., Riese, M., Schardt, G., Schillings, J., Sha, M. K., Suminska-Ebersoldt, O., and Ungermann, J.: Instrument concept of the imaging Fourier transform spectrometer GLORIA, *Atmospheric Measurement Techniques*, 7, 3565–3577. doi:10.5194/amt-7-3565-2014, 2014. (cited on pages 19, 21).
- Froidevaux, L., Jiang, Y. B., Lambert, A., Livesey, N. J., Read, W. G., Waters, J. W., Browell, E. V., Hair, J. W., Avery, M. A., McGee, T. J., Twigg, L. W., Sunnicht, G. K., Jucks, K. W., Margitan, J. J., Sen, B., Stachnik, R. A., Toon, G. C., Bernath, P. F., Boone, C. D., Walker, K. A., Filipiak, M. J., Harwood, R. S., Fuller, R. A., Manney, G. L., Schwartz, M. J., Daffer, W. H., Drouin, B. J., Cofield, R. E., Cuddy, D. T., Jarnot, R. F., Knosp, B. W., Perun, V. S., Snyder, W. V., Stek, P. C., Thurstans, R. P., and Wagner, P. A.: Validation of Aura Microwave Limb Sounder stratospheric

- ozone measurements, *Journal of Geophysical Research: Atmospheres*, 113, D15S20. doi:10.1029/2007JD008771, 2008a. (cited on page 38).
- Froidevaux, L., Jiang, Y. B., Lambert, A., Livesey, N. J., Read, W. G., Waters, J. W., Fuller, R. A., Marcy, T. P., Popp, P. J., Gao, R. S., Fahey, D. W., Jucks, K. W., Stachnik, R. A., Toon, G. C., Christensen, L. E., Webster, C. R., Bernath, P. F., Boone, C. D., Walker, K. A., Pumphrey, H. C., Harwood, R. S., Manney, G. L., Schwartz, M. J., Daffer, W. H., Drouin, B. J., Cofield, R. E., Cuddy, D. T., Jarnot, R. F., Knosp, B. W., Perun, V. S., Snyder, W. V., Stek, P. C., Thurstans, R. P., and Wagner, P. A.: Validation of Aura Microwave Limb Sounder HCl measurements, *Journal of Geophysical Research: Atmospheres*, 113. doi:10.1029/2007JD009025, 2008b. (cited on pages 18, 38).
- Froidevaux, L., Livesey, N. J., and Read, W. G.: MLS/Aura L2 Hydrogen Chloride (HCl) Mixing Ratio - Version 4. <https://doi.org/10.5067/AURA/MLS/DATA2010>, 2015. (cited on page 38).
- Fueglistaler, S., Luo, B. P., Voigt, C., Carslaw, K. S., and Peter, T.: NAT-rock formation by mother clouds: A microphysical model study, *Atmospheric Chemistry and Physics*, 2, 93–98. doi:10.5194/acp-2-93-2002, 2002. (cited on page 18).
- Galatry, L.: Simultaneous Effect of Doppler and Foreign Gas Broadening on Spectral Lines, *Physical Review*, 122, 1218. doi:10.1103/PhysRev.122.1218, 1961. (cited on page 27).
- Gandrud, B. W., Dye, J. E., Baumgardner, D., Ferry, G. V., Loewenstein, M., Chan, K. R., Sanford, L., Gary, B., and Kelly, K.: The January 30, 1989 Arctic polar stratospheric clouds (PSC) event: Evidence for a mechanism of dehydration, *Geophysical Research Letters*, 17, 457–460. doi:10.1029/GL017i004p00457, 1990. (cited on page 13).
- Gathen, P. v. d., Rex, M., Harris, N. R. P., Lucic, D., Knudsen, B. M., Braathen, G. O., Backer, H. D., Fabian, R., Fast, H., Gil, M., Kyrö, E., Mikkelsen, I. S., Rummukainen, M., Stähelin, J., and Varotsos, C.: Observational evidence for chemical ozone depletion over the Arctic in winter 1991/92, *Nature*, 375, 131. doi:10.1038/375131a0, 1995. (cited on page 78).
- Gelaro, R., McCarty, W., Suárez, M. J., Todling, R., Molod, A., Takacs, L., Randles, C. A., Darmenov, A., Bosilovich, M. G., Reichle, R., Wargan, K., Coy, L., Cullather, R., Draper, C., Akella, S., Buchard, V., Conaty, A., da Silva, A. M., Gu, W., Kim, G.-K., Koster, R., Lucchesi, R., Merkova, D., Nielsen, J. E., Partyka, G., Pawson, S., Putman, W., Rienecker, M., Schubert, S. D., Sienkiewicz, M., and Zhao, B.: The Modern-Era Retrospective Analysis for Research and Applications, Version 2 (MERRA-2), *Journal of Climate*, 30, 5419–5454. doi:10.1175/JCLI-D-16-0758.1, 2017. (cited on page 40).
- Genest, J. and Tremblay, P.: Instrument line shape of Fourier transform spectrometers: Analytic solutions for nonuniformly illuminated off-axis detectors, *Applied Optics*, 38, 5438–5446. doi:10.1364/AO.38.005438, 1999. (cited on page 20).

- Gerber, E. P. and Son, S.-W.: Quantifying the Summertime Response of the Austral Jet Stream and Hadley Cell to Stratospheric Ozone and Greenhouse Gases, *Journal of Climate*, 27, 5538–5559. doi:10.1175/JCLI-D-13-00539.1, 2014. (cited on page 17).
- Gettelman, A., Hoor, P., Pan, L. L., Randel, W. J., Hegglin, M. I., and Birner, T.: The extratropical Upper Troposphere and Lower Stratosphere, *Reviews of Geophysics*, 49, 2011RG000355. doi:10.1029/2011RG000355, 2011. (cited on pages 1, 5, 6).
- Giez, A., Mallaun, C., Zöger, M., Dörnbrack, A., and Schumann, U.: Static Pressure from Aircraft Trailing-Cone Measurements and Numerical Weather-Prediction Analysis, *Journal of Aircraft*, 54, 1728–1737. doi:10.2514/1.C034084, 2017. (cited on page 37).
- Gille, J. C. and House, F. B.: On the Inversion of Limb Radiance Measurements I: Temperature and Thickness, *Journal of the Atmospheric Sciences*, 28, 1427–1442. doi:10.1175/1520-0469(1971)028<1427:OTIOLR>2.0.CO;2, 1971. (cited on page 27).
- Glatthor, N., von Clarmann, T., Fischer, H., Grabowski, U., Höpfner, M., Kellmann, S., Kiefer, M., Linden, A., Milz, M., Steck, T., Stiller, G. P., Tsidu, G. M., Wang, D., and Funke, B.: Spaceborne ClO observations by the Michelson Interferometer for Passive Atmospheric Sounding (MIPAS) before and during the Antarctic major warming in September/October 2002, *Journal of Geophysical Research: Atmospheres*, 109. doi:10.1029/2003JD004440, 2004. (cited on page 18).
- Günther, A., Höpfner, M., Sinnhuber, B.-M., Griessbach, S., Deshler, T., Clarmann, T. V., and Stiller, G.: MIPAS observations of volcanic sulphate aerosol and sulphur dioxide in the stratosphere, *Atmospheric Chemistry and Physics Discussions*, pp. 1–32. doi:10.5194/acp-2017-538, 2017. (cited on page 24).
- Gordley, L. L. and Russell Iii, J. M.: Rapid inversion of limb radiance data using an emissivity growth approximation, *Applied optics*, 20, 807–813. doi:10.1364/AO.20.000807, 1981. (cited on page 27).
- Gordon, I. E., Rothman, L. S., Hill, C., Kochanov, R. V., Tan, Y., Bernath, P. F., Birk, M., Boudon, V., Campargue, A., Chance, K. V., Drouin, B. J., Flaud, J. M., Gamache, R. R., Hodges, J. T., Jacquemart, D., Perevalov, V. I., Perrin, A., Shine, K. P., Smith, M. A. H., Tennyson, J., Toon, G. C., Tran, H., Tyuterev, V. G., Barbe, A., Császár, A. G., Devi, V. M., Furtenbacher, T., Harrison, J. J., Hartmann, J. M., Jolly, A., Johnson, T. J., Karman, T., Kleiner, I., Kyuberis, A. A., Loos, J., Lyulin, O. M., Massie, S. T., Mikhailenko, S. N., Moazzen-Ahmadi, N., Müller, H. S. P., Naumenko, O. V., Nikitin, A. V., Polyansky, O. L., Rey, M., Rotger, M., Sharpe, S. W., Sung, K., Starikova, E., Tashkun, S. A., Auwera, J. V., Wagner, G., Wilzewski, J., Weislo, P., Yu, S., and Zak, E. J.: The HITRAN2016 molecular spectroscopic database, *Journal of Quantitative Spectroscopy and Radiative Transfer*, 203, 3–69. doi:10.1016/j.jqsrt.2017.06.038, 2017. (cited on page 26).
- Greenblatt, J. B., Jost, H., Loewenstein, M., Podolske, J. R., Bui, T. P., Hurst, D. F., Elkins, J. W., Herman, R. L., Webster, C. R., Schauffler, S. M., Atlas, E. L., Newman, P. A., Lait, L. R., Müller, M., Engel, A., and Schmidt, U.: Defining the polar

- vortex edge from an N₂O:potential temperature correlation, *Journal of Geophysical Research: Atmospheres*, 107, 2001JD000575. doi:10.1029/2001JD000575, 2002. (cited on page 53).
- Groß, J.-U., Pierce, R. B., Crutzen, P. J., Grose, W. L., and Russell, J. M.: Reformation of chlorine reservoirs in southern hemisphere polar spring, *Journal of Geophysical Research*, 102, 13 141–13 152. doi:10.1029/96JD03505, 1997. (cited on pages 13, 14, 81).
- Groß, J.-U., Günther, G., Müller, R., Konopka, P., Bausch, S., Schlager, H., Voigt, C., Volk, C. M., and Toon, G. C.: Simulation of denitrification and ozone loss for the Arctic winter 2002/2003, *Atmospheric Chemistry and Physics*, 5, 1437–1448. doi:10.5194/acp-5-1437-2005, 2005. (cited on pages 13, 14, 81).
- Groß, J.-U., Brauttsch, K., Pommrich, R., Solomon, S., and Müller, R.: Stratospheric ozone chemistry in the Antarctic: What determines the lowest ozone values reached and their recovery?, *Atmospheric Chemistry and Physics*, 11, 12 217–12 226. doi:10.5194/acp-11-12217-2011, 2011. (cited on page 14).
- Groß, J.-U., Engel, I., Borrmann, S., Frey, W., Günther, G., Hoyle, C. R., Kivi, R., Luo, B. P., Mollenker, S., Peter, T., Pitts, M. C., Schlager, H., Stiller, G., Vömel, H., Walker, K. A., and Müller, R.: Nitric acid trihydrate nucleation and denitrification in the Arctic stratosphere, *Atmospheric Chemistry and Physics*, 14, 1055–1073. doi:10.5194/acp-14-1055-2014, 2014. (cited on pages 39, 39, 70).
- Groß, J.-U., Müller, R., Spang, R., Tritscher, I., Wegner, T., Chipperfield, M. P., Feng, W., Kinnison, D. E., and Madronich, S.: On the discrepancy of HCl processing in the core of the wintertime polar vortices, *Atmospheric Chemistry and Physics*, 18, 8647–8666. doi:10.5194/acp-18-8647-2018, 2018. (cited on pages 18, 39, 39, 65, 70, 94).
- Guggenmoser, T., Blank, J., Kleinert, A., Latzko, T., Ungermann, J., Friedl-Vallon, F., Höpfner, M., Kaufmann, M., Kretschmer, E., Maucher, G., Neubert, T., Oelhaf, H., Preusse, P., Riese, M., Rongen, H., Sha, M. K., Sumińska-Ebersoldt, O., and Tan, V.: New calibration noise suppression techniques for the GLORIA limb imager, *Atmospheric Measurement Techniques*, 8, 3147–3161. doi:10.5194/amt-8-3147-2015, 2015. (cited on page 24).
- Haenel, F. J., Stiller, G. P., von Clarmann, T., Funke, B., Eckert, E., Glatthor, N., Grabowski, U., Kellmann, S., Kiefer, M., Linden, A., and Reddman, T.: Reassessment of MIPAS age of air trends and variability, *Atmospheric Chemistry and Physics*, 15, 13 161–13 176. doi:10.5194/acp-15-13161-2015, 2015. (cited on page 16).
- Haken, H. and Wolf, H. C.: *Molekülphysik und Quantenchemie: Einführung in die experimentellen und theoretischen Grundlagen*, Springer-Lehrbuch, Springer-Verlag Berlin Heidelberg, Berlin, Heidelberg, 5., völlig neubearbeitete und erw. Aufl. edn. ISBN:3540303154, 2006. (cited on page 25).

- Hanson, D. and Mauersberger, K.: Laboratory studies of the nitric acid trihydrate: Implications for the south polar stratosphere, *Geophysical Research Letters*, 15, 855–858, 1988. (cited on page 8).
- Hartmann, D. L., Wallace, J. M., Limpasuvan, V., Thompson, D. W. J., and Holton, J. R.: Can ozone depletion and global warming interact to produce rapid climate change?, *Proceedings of the National Academy of Sciences*, 97, 1412–1417. doi:10.1073/pnas.97.4.1412, 2000. (cited on page 1).
- Hartmann, D. L., Klein Tank, A., Rusticucci, M., Alexander, L. V., Brönnimann, S., Charabi, Y., Dentener, F. J., Dlugokencky, E. J., Easterling, D. R., Kaplan, A., Soden, B. J., Thorne, P. W., Wild, M., and Zhai, P. M.: Observations: Atmosphere and Surface, in: *Climate Change 2013 – The Physical Science Basis*, edited by IPCC, Cambridge University Press. ISBN:9781139917193, 2014. (cited on pages 17, 93).
- Herzberg, G.: *Molecular spectra and molecular structure, Molekülspektren und Molekülstruktur*, van Nostrand Reinhold, New York [u.a.], 1939. (cited on page 25).
- Hoffmann, L., Hertzog, A., Rößler, T., Stein, O., and Wu, X.: Intercomparison of meteorological analyses and trajectories in the Antarctic lower stratosphere with Concordiasi superpressure balloon observations, *Atmospheric Chemistry and Physics*, 17, 8045–8061. doi:10.5194/acp-17-8045-2017, 2017. (cited on page 83).
- Hollas, J. M.: *Modern spectroscopy*, Wiley, Chichester, 4. ed., reprinted. edn. ISBN:978-0470844168, 2010. (cited on pages 25, 26).
- Holton, J. R., Haynes, P. H., McIntyre, M. E., Douglass, A. R., Rood, R. B., and Pfister, L.: Stratosphere-troposphere exchange, *Reviews of Geophysics*, 33, 403–439. doi:10.1029/95RG02097, 1995. (cited on page 6).
- Höpfner, M.: Derivatives and interface to the retrieval, in: *The Karlsruhe Optimized and Precise Radiative transfer Algorithm (KOPRA)*, edited by Stiller, G. P., *Wissenschaftliche Berichte*, pp. 133–144, Forschungszentrum Karlsruhe, 2000. (cited on page 29).
- Höpfner, M., von Clarmann, T., Fischer, H., Glatthor, N., Grabowski, U., Kellmann, S., Kiefer, M., Linden, A., Tsidu, G. M., Milz, M., Steck, T., Stiller, G. P., Wang, D. Y., and Funke, B.: First spaceborne observations of Antarctic stratospheric ClONO₂ recovery: Austral spring 2002, *Journal of Geophysical Research: Atmospheres*, 109. doi:10.1029/2004JD004609, 2004. (cited on page 18).
- Höpfner, M., Luo, B. P., Massoli, P., Cairo, F., Spang, R., Snels, M., Di Donfrancesco, G., Stiller, G., von Clarmann, T., Fischer, H., and Biermann, U.: Spectroscopic evidence for NAT, STS, and ice in MIPAS infrared limb emission measurements of polar stratospheric clouds, *Atmospheric Chemistry and Physics*, 6, 1201–1219. doi:10.5194/acp-6-1201-2006, 2006. (cited on page 10).
- Höpfner, M., Deshler, T., Pitts, M., Poole, L., Spang, R., Stiller, G., and von Clarmann, T.: *The MIPAS/Envisat climatology (2002-2012) of polar stratospheric cloud (PSC)*

- volume density profiles, *Atmospheric Measurement Techniques Discussions*, 2018, 1–29. doi:10.5194/amt-2018-163, 2018. (cited on pages 10, 24).
- Ivy, D. J., Solomon, S., Kinnison, D., Mills, M. J., Schmidt, A., and Neely, R. R.: The influence of the Calbuco eruption on the 2015 Antarctic ozone hole in a fully coupled chemistry-climate model, *Geophysical Research Letters*, 44, 2556–2561. doi:10.1002/2016GL071925, 2017. (cited on page 14).
- Jöckel, P., Kerkweg, A., Pozzer, A., Sander, R., Tost, H., Riede, H., Baumgaertner, A., Gromov, S., and Kern, B.: Development cycle 2 of the Modular Earth Submodel System (MESSy2), *Geoscientific Model Development*, 3, 717–752. doi:10.5194/gmd-3-717-2010, 2010. (cited on page 40).
- Johansson, S., Woiwode, W., Höpfner, M., Friedl-Vallon, F., Kleinert, A., Kretschmer, E., Latzko, T., Orphal, J., Preusse, P., Ungermann, J., Santee, M. L., Jurkat-Witschas, T., Marsing, A., Voigt, C., Giez, A., Krämer, M., Rolf, C., Zahn, A., Engel, A., Sinnhuber, B.-M., and Oelhaf, H.: Airborne limb-imaging measurements of temperature, HNO₃, O₃, ClONO₂, H₂O and CFC-12 during the Arctic winter 2015/2016: Characterization, in situ validation and comparison to Aura/MLS, *Atmospheric Measurement Techniques*, 11, 4737–4756. doi:10.5194/amt-11-4737-2018, 2018. (cited on pages 2, 41, 54, 66, 71).
- Johansson, S., Santee, M. L., Groß, J.-U., Höpfner, M., Braun, M., Friedl-Vallon, F., Khosrawi, F., Kirner, O., Kretschmer, E., Oelhaf, H., Orphal, J., Sinnhuber, B.-M., Ungermann, J., Walker, K. A., and Woiwode, W.: Unusual chlorine partitioning in the 2015/16 Arctic winter lowermost stratosphere: Observations and simulations, *Atmospheric Chemistry and Physics Discussions*, 2019. (cited on page 2).
- Junge, C. E., Chagnon, C. W., and Manson, J. E.: A World-wide Stratospheric Aerosol Layer, *Science*, 133, 1478–1479. doi:10.1126/science.133.3463.1478-a, 1961. (cited on page 8).
- Jurkat, T., Kaufmann, S., Voigt, C., Schäuble, D., Jeßberger, P., and Ziereis, H.: The airborne mass spectrometer AIMS – Part 2: Measurements of trace gases with stratospheric or tropospheric origin in the UTLS, *Atmospheric Measurement Techniques*, 9, 1907–1923. doi:10.5194/amt-9-1907-2016, 2016. (cited on page 37).
- Jurkat, T., Voigt, C., Kaufmann, S., Groß, J., Ziereis, H., Dörnbrack, A., Hoor, P., Bozem, H., Engel, A., Bönisch, H., Keber, T., Hüneke, T., Pfeilsticker, K., Zahn, A., Walker, K. A., Boone, C. D., Bernath, P. F., and Schlager, H.: Depletion of ozone and reservoir species of chlorine and nitrogen oxide in the lower Antarctic polar vortex measured from aircraft, *Geophysical Research Letters*, 44, 6440–6449. doi:10.1002/2017GL073270, 2017. (cited on pages 18, 37).
- Kaufmann, M., Blank, J., Guggenmoser, T., Ungermann, J., Engel, A., Ern, M., Friedl-Vallon, F., Gerber, D., Groß, J. U., Guenther, G., Höpfner, M., Kleinert, A., Kretschmer, E., Latzko, T., Maucher, G., Neubert, T., Nordmeyer, H., Oelhaf, H., Olschewski, F., Orphal, J., Preusse, P., Schlager, H., Schneider, H., Schuette-meyer, D., Stroh, F., Suminska-Ebersoldt, O., Vogel, B., M. Volk, C., Woiwode,

- W., and Riese, M.: Retrieval of three-dimensional small-scale structures in upper-tropospheric/lower-stratospheric composition as measured by GLORIA, *Atmospheric Measurement Techniques*, 8, 81–95. doi:10.5194/amt-8-81-2015, 2015. (cited on pages 24, 92).
- Kaufmann, S., Voigt, C., Jurkat, T., Thornberry, T., Fahey, D. W., Gao, R.-S., Schlage, R., Schäuble, D., and Zöger, M.: The airborne mass spectrometer AIMS - Part 1: AIMS-H₂O for UTLS water vapor measurements, *Atmospheric Measurement Techniques*, 9, 939–953. doi:10.5194/amt-9-939-2016, 2016. (cited on page 37).
- Khosrawi, F., Grooß, J.-U., Müller, R., Konopka, P., Kouker, W., Ruhnke, R., Reddmann, T., and Riese, M.: Intercomparison between Lagrangian and Eulerian simulations of the development of mid-latitude streamers as observed by CRISTA, *Atmospheric Chemistry and Physics*, 5, 85–95. doi:10.5194/acp-5-85-2005, 2005. (cited on page 74).
- Khosrawi, F., Kirner, O., Sinnhuber, B.-M., Johansson, S., Höpfner, M., Santee, M. L., Froidevaux, L., Ungermann, J., Ruhnke, R., Woiwode, W., Oelhaf, H., and Braesicke, P.: Denitrification, dehydration and ozone loss during the 2015/2016 Arctic winter, *Atmospheric Chemistry and Physics*, 17, 12 893–12 910. doi:10.5194/acp-17-12893-2017, 2017. (cited on pages 24, 35, 40, 70, 71, 74, 76).
- Khosrawi, F., Kirner, O., Stiller, G., Höpfner, M., Santee, M. L., Kellmann, S., and Braesicke, P.: Comparison of ECHAM5/MESSEy Atmospheric Chemistry (EMAC) simulations of the Arctic winter 2009/2010 and 2010/2011 with Envisat/MIPAS and Aura/MLS observations, *Atmospheric Chemistry and Physics*, 18, 8873–8892. doi:10.5194/acp-18-8873-2018, 2018. (cited on page 70).
- Kirner, O., Müller, R., Ruhnke, R., and Fischer, H.: Contribution of liquid, NAT and ice particles to chlorine activation and ozone depletion in Antarctic winter and spring, *Atmospheric Chemistry and Physics*, 15, 2019–2030. doi:10.5194/acp-15-2019-2015, 2015. (cited on page 12).
- Kleinert, A., Friedl-Vallon, F., Guggenmoser, T., Höpfner, M., Neubert, T., Ribalda, R., Sha, M. K., Ungermann, J., Blank, J., Ebersoldt, A., Kretschmer, E., Latzko, T., Oelhaf, H., Olschewski, F., and Preusse, P.: Level 0 to 1 processing of the imaging Fourier transform spectrometer GLORIA: Generation of radiometrically and spectrally calibrated spectra, *Atmospheric Measurement Techniques*, 7, 4167–4184. doi:10.5194/amt-7-4167-2014, 2014. (cited on pages 23, 24, 32).
- Kochanov, V. P.: On systematic errors in spectral line parameters retrieved with the Voigt line profile, *Journal of Quantitative Spectroscopy and Radiative Transfer*, 113, 1635–1641. doi:10.1016/j.jqsrt.2012.03.024, 2012. (cited on page 26).
- Konopka, P. and Pan, L. L.: On the mixing-driven formation of the Extratropical Transition Layer (ExTL), *Journal of Geophysical Research: Atmospheres*, 117, 2012JD017 876. doi:10.1029/2012JD017876, 2012. (cited on page 6).

- Konopka, P., Groöß, J.-U., Günther, G., McKenna, D. S., Muller, R., Elkins, J. W., Fahey, D. W., and Popp, P. J.: Weak impact of mixing on chlorine deactivation during SOLVE/THESEO 2000: Lagrangian modeling (CLaMS) versus ER-2 in situ observations, *Journal of Geophysical Research*, 108. doi:10.1029/2001JD000876, 2003. (cited on page 84).
- Konopka, P., Günther, G., Müller, R., dos Santos, F. H. S., Schiller, C., Ravegnani, F., Ulanovsky, A., Schlager, H., Volk, C. M., Viciani, S., Pan, L. L., McKenna, D.-S., and Riese, M.: Contribution of mixing to upward transport across the tropical tropopause layer (TTL), *Atmospheric Chemistry and Physics*, 7, 3285–3308. doi:10.5194/acp-7-3285-2007, 2007. (cited on page 39).
- Krause, J., Hoor, P., Engel, A., Plöger, F., Groöß, J.-U., Bönisch, H., Keber, T., Sinnhuber, B.-M., Woiwode, W., and Oelhaf, H.: Mixing and ageing in the polar lower stratosphere in winter 2015–2016, *Atmospheric Chemistry and Physics*, 18, 6057–6073. doi:10.5194/acp-18-6057-2018, 2018. (cited on pages 6, 74).
- Krautstrunk, M. and Giez, A.: The Transition From FALCON to HALO Era Airborne Atmospheric Research, in: *Atmospheric physics*, edited by Schumann, U., *Research topics in aerospace*, pp. 609–624, Springer, Berlin. ISBN:978-3-642-30183-4, 2012. (cited on page 37).
- Kretschmer, E.: *Modelling of the Instrument Spectral Response of Conventional and Imaging Fourier Transform Spectrometers: Doctorat en génie électrique*, Université Laval, Québec, Canada, 2014. (cited on pages 20, 21).
- Kretschmer, E., Bachner, M., Blank, J., Dapp, R., Ebersoldt, A., Friedl-Vallon, F., Guggenmoser, T., Gulde, T., Hartmann, V., Lutz, R., Maucher, G., Neubert, T., Oelhaf, H., Preusse, P., Schardt, G., Schmitt, C., Schönfeld, A., and Tan, V.: In-flight control and communication architecture of the GLORIA imaging limb sounder on atmospheric research aircraft, *Atmospheric Measurement Techniques*, 8, 2543–2553. doi:10.5194/amt-8-2543-2015, 2015. (cited on page 24).
- Krisch, I., Preusse, P., Ungermann, J., Dörnbrack, A., Eckermann, S. D., Ern, M., Friedl-Vallon, F., Kaufmann, M., Oelhaf, H., Rapp, M., Strube, C., and Riese, M.: First tomographic observations of gravity waves by the infrared limb imager GLORIA, *Atmospheric Chemistry and Physics*, 17, 14937–14953. doi:10.5194/acp-17-14937-2017, 2017. (cited on pages 23, 24).
- Krisch, I., Ungermann, J., Preusse, P., Kretschmer, E., and Riese, M.: Limited angle tomography of mesoscale gravity waves by the infrared limb-sounder GLORIA, *Atmospheric Measurement Techniques*, 11, 4327–4344. doi:10.5194/amt-11-4327-2018, 2018. (cited on page 23).
- Lawrence, Z. D., Manney, G. L., and Wargan, K.: Reanalysis intercomparisons of stratospheric polar processing diagnostics, *Atmospheric Chemistry and Physics*, 18, 13547–13579. doi:10.5194/acp-18-13547-2018, 2018. (cited on page 6).

- Lelieveld, J., Bregman, A., Scheeren, H. A., Ström, J., Carslaw, K. S., Fischer, H., Siegmund, P. C., and Arnold, F.: Chlorine activation and ozone destruction in the northern lowermost stratosphere, *Journal of Geophysical Research: Atmospheres*, 104, 8201–8213. doi:10.1029/1998JD100111, 1999. (cited on pages 1, 18, 84).
- Liou, K.-N.: Radiation and cloud processes in the atmosphere: Theory, observation, and modeling, vol. 20 of *Oxford monographs on geology and geophysics*, Oxford Univ. Press, New York. ISBN:9780195049107, 1992. (cited on page 28).
- Livesey, N.: Limb Sounding, Atmospheric, in: *Encyclopedia of Remote Sensing*, pp. 344–348, Springer, 2014. (cited on page 27).
- Livesey, N. J., Santee, M. L., and Manney, G. L.: A Match-based approach to the estimation of polar stratospheric ozone loss using Aura Microwave Limb Sounder observations, *Atmospheric Chemistry and Physics*, 15, 9945–9963. doi:10.5194/acp-15-9945-2015, 2015. (cited on pages 78, 78, 82, 92).
- Livesey, N. J., Read, W. G., Wagner, P. A., Froidevaux, L., Lambert, A., Manney, G. L., Millán, L. F., Pumphrey, Hugh, C., Santee, M. L., Schwartz, M. J., Wang, S., Fuller, R. A., Jarnot, R. F., Knosp, B. W., and Martinez, E.: Version 4.2x Level 2 data quality and description document. Earth Observing System (EOS) Aura Microwave Limb Sounder (MLS). https://mls.jpl.nasa.gov/data/v4-2_data_quality_document.pdf, 2018. (cited on pages 38, 38, 42).
- Lopez-Puertas, M.: Non-LTE radiative transfer in the atmosphere, vol. v. 3 of *Series on atmospheric, oceanic and planetary physics*, World Scientific Pub. Co, Singapore and River Edge, N.J. ISBN:9789810245665, 2001. (cited on page 28).
- Mahieu, E., Duchatelet, P., Demoulin, P., Walker, K. A., Dupuy, E., Froidevaux, L., Randall, C., Catoire, V., Strong, K., Boone, C. D., Bernath, P. F., Blavier, J.-F., Blumenstock, T., Coffey, M., Mazière, M. D., Griffith, D., Hannigan, J., Hase, F., Jones, N., Jucks, K. W., Kagawa, A., Kasai, Y., Mebarki, Y., Mikuteit, S., Nassar, R., Notholt, J., Rinsland, C. P., Robert, C., Schrems, O., Senten, C., Smale, D., Taylor, J., Tétard, C., Toon, G. C., Warneke, T., Wood, S. W., Zander, R., and Servais, C.: Validation of ACE-FTS v2.2 measurements of HCl, HF, CCl₃F and CCl₂F₂ using space-, balloon- and ground-based instrument observations, *Atmospheric Chemistry and Physics*, 8, 6199–6221. doi:10.5194/acp-8-6199-2008, 2008. (cited on page 18).
- Manney, G. L. and Lawrence, Z. D.: The major stratospheric final warming in 2016: Dispersal of vortex air and termination of Arctic chemical ozone loss, *Atmospheric Chemistry and Physics*, 16, 15 371–15 396. doi:10.5194/acp-16-15371-2016, 2016. (cited on pages 35, 56, 60, 62, 65, 89).
- Manney, G. L., Zurek, R. W., O’Neill, A., and Swinbank, R.: On the Motion of Air through the Stratospheric Polar Vortex, *Journal of the Atmospheric Sciences*, 51, 2973–2994. doi:10.1175/1520-0469(1994)051<2973:OTMOAT>2.0.CO;2, 1994. (cited on page 8).

- Manney, G. L., Zurek, R. W., Froidevaux, L., Waters, J. W., O'Neill, A., and Swinbank, R.: Lagrangian Transport Calculations Using UARS Data. Part II: Ozone, *Journal of the Atmospheric Sciences*, 52, 3069–3081. doi:10.1175/1520-0469(1995)052<3069:LTCUDP>2.0.CO;2, 1995a. (cited on page 76).
- Manney, G. L., Zurek, R. W., Lahoz, W. A., Harwood, R. S., Gille, J. C., Kumer, J. B., Mergenthaler, J. L., Roche, A. E., O'Neill, A., Swinbank, R., and Waters, J. W.: Lagrangian Transport Calculations Using UARS Data. Part I. Passive Tracers, *Journal of the Atmospheric Sciences*, 52, 3049–3068. doi:10.1175/1520-0469(1995)052<3049:LTCUDP>2.0.CO;2, 1995b. (cited on page 76).
- Manney, G. L., Santee, M. L., Froidevaux, L., Hoppel, K., Livesey, N. J., and Waters, J. W.: EOS MLS observations of ozone loss in the 2004–2005 Arctic winter, *Geophysical Research Letters*, 33. doi:10.1029/2005GL024494, 2006. (cited on page 78).
- Manney, G. L., Harwood, R. S., MacKenzie, I. A., Minschwaner, K., Allen, D. R., Santee, M. L., Walker, K. A., Hegglin, M. I., Lambert, A., Pumphrey, H. C., Bernath, P. F., Boone, C. D., Schwartz, M. J., Livesey, N. J., Daffer, W. H., and Fuller, R. A.: Satellite observations and modeling of transport in the upper troposphere through the lower mesosphere during the 2006 major stratospheric sudden warming, *Atmospheric Chemistry and Physics*, 9, 4775–4795. doi:10.5194/acp-9-4775-2009, 2009. (cited on pages 6, 8).
- Manney, G. L., Santee, M. L., Rex, M., Livesey, N. J., Pitts, M. C., Veefkind, P., Nash, E. R., Wohltmann, I., Lehmann, R., Froidevaux, L., Poole, L. R., Schoeberl, M. R., Haffner, D. P., Davies, J., Dorokhov, V., Gernandt, H., Johnson, B., Kivi, R., Kyrö, E., Larsen, N., Levelt, P. F., Makshtas, A., McElroy, C. T., Nakajima, H., Parrondo, M. C., Tarasick, D. W., Gathen, P. v. d., Walker, K. A., and Zinoviev, N. S.: Unprecedented Arctic ozone loss in 2011, *Nature*, 478, 469–475. doi:10.1038/nature10556, 2011. (cited on pages 14, 15, 60, 65).
- Manney, G. L., Lawrence, Z. D., Santee, M. L., Read, W. G., Livesey, N. J., Lambert, A., Froidevaux, L., Pumphrey, H. C., and Schwartz, M. J.: A minor sudden stratospheric warming with a major impact: Transport and polar processing in the 2014/2015 Arctic winter, *Geophysical Research Letters*, 42, 7808–7816. doi:10.1002/2015GL065864, 2015a. (cited on page 78).
- Manney, G. L., Santee, M. L., Froidevaux, L., Livesey, N. J., and Read, W. G.: MLS/Aura L2 Nitric Acid (HNO₃) Mixing Ratio - Version 4. <https://doi.org/10.5067/AURA/MLS/DATA2012>, 2015b. (cited on page 38).
- Matthewman, N. J., Esler, J. G., Charlton-Perez, A. J., and Polvani, L. M.: A New Look at Stratospheric Sudden Warmings. Part III: Polar Vortex Evolution and Vertical Structure, *Journal of Climate*, 22, 1566–1585. doi:10.1175/2008JCLI2365.1, 2009. (cited on page 6).

- Matthias, V., Dörnbrack, A., and Stober, G.: The extraordinarily strong and cold polar vortex in the early northern winter 2015/2016, *Geophysical Research Letters*, 43. doi:10.1002/2016GL071676, 2016. (cited on page 35).
- Mazière, M. D., Thompson, A. M., Kurylo, M. J., Wild, J. D., Bernhard, G., Blumenstock, T., Braathen, G. O., Hannigan, J. W., Lambert, J.-C., Leblanc, T., McGee, T. J., Nedoluha, G., Petropavlovskikh, I., Seckmeyer, G., Simon, P. C., Steinbrecht, W., and Strahan, S. E.: The Network for the Detection of Atmospheric Composition Change (NDACC): History, status and perspectives, *Atmospheric Chemistry and Physics*, 18, 4935–4964. doi:10.5194/acp-18-4935-2018, 2018. (cited on page 17).
- McElroy, M. B., Salawitch, R. J., Wofsy, S. C., and Logan, J. A.: Reductions of Antarctic ozone due to synergistic interactions of chlorine and bromine, *Nature*, 321, 759. doi:10.1038/321759a0, 1986. (cited on page 12).
- McKenna, D. S., Groöß, J., Günther, G., Konopka, P., Müller, R., Carver, G., and Sasano, Y.: A new Chemical Lagrangian Model of the Stratosphere (CLaMS) 2. Formulation of chemistry scheme and initialization, *Journal of Geophysical Research: Atmospheres*, 107. doi:10.1029/2000JD000113, 2002a. (cited on page 39).
- McKenna, D. S., Konopka, P., Groöß, J., Günther, G., Müller, R., Spang, R., Offermann, D., and Orsolini, Y.: A new Chemical Lagrangian Model of the Stratosphere (CLaMS) 1. Formulation of advection and mixing, *Journal of Geophysical Research: Atmospheres*, 107. doi:10.1029/2000JD000114, 2002b. (cited on page 39).
- McPeters, R. D., Heath, D. F., and Bhartia, P. K.: Average ozone profiles for 1979 from the NIMBUS 7 SBUV instrument, *Journal of Geophysical Research: Atmospheres*, 89, 5199–5214. doi:10.1029/JD089iD04p05199, 1984. (cited on page 29).
- Meyer, J., Rolf, C., Schiller, C., Rohs, S., Spelten, N., Afchine, A., Zöger, M., Sitnikov, N., Thornberry, T. D., Rollins, A. W., Bozóki, Z., Tátraí, D., Ebert, V., Kühnreich, B., Mackrodt, P., Möhler, O., Saathoff, H., Rosenlof, K. H., and Krämer, M.: Two decades of water vapor measurements with the FISH fluorescence hygrometer: A review, *Atmospheric Chemistry and Physics*, 15, 8521–8538. doi:10.5194/acp-15-8521-2015, 2015. (cited on page 37).
- Mickley, L. J., Abbatt, J. P. D., Frederick, J. E., and Russell, J. M.: Evolution of chlorine and nitrogen species in the lower stratosphere during Antarctic spring: Use of tracers to determine chemical change, *Journal of Geophysical Research*, 102, 21 479–21 491. doi:10.1029/97JD00422, 1997. (cited on pages 14, 81).
- Müller, R., ed.: *Stratospheric Ozone Depletion and Climate Change*, The Royal Society of Chemistry. ISBN:978-1-84973-002-0, 2012. (cited on page 3).
- Müller, R., Peter, T., Crutzen, P. J., Oelhaf, H., Adrian, G. P., Clarmann, T., Wegner, A., Schmidt, U., and Lary, D.: Chlorine chemistry and the potential for ozone depletion in the Arctic stratosphere in the winter of 1991/92, *Geophysical Research Letters*, 21, 1427–1430. doi:10.1029/94GL00465, 1994. (cited on page 84).

- Müller, R., Crutzen, P. J., Grooß, J., Brühl, C., Russell, J. M., and Tuck, A. F.: Chlorine activation and ozone depletion in the Arctic vortex: Observations by the Halogen Occultation Experiment on the Upper Atmosphere Research Satellite, *Journal of Geophysical Research: Atmospheres*, 101, 12 531–12 554. doi:10.1029/95JD00220, 1996. (cited on page 74).
- Molina, L. T. and Molina, M. J.: Production of chlorine oxide (Cl₂O₂) from the self-reaction of the chlorine oxide (ClO) radical, *Journal of Physical Chemistry*, 91, 433–436, 1987. (cited on pages 10, 12).
- Molina, M. J. and Rowland, F. S.: Stratospheric sink for chlorofluoromethanes: Chlorine atom-catalysed destruction of ozone, *Nature*, 249, 810–812. doi:10.1038/249810a0, 1974. (cited on page 10).
- Montzka, S. A., Dutton, G. S., Yu, P., Ray, E., Portmann, R. W., Daniel, J. S., Kuijpers, L., Hall, B. D., Mondeel, D., Siso, C., Nance, J. D., Rigby, M., Manning, A. J., Hu, L., Moore, F., Miller, B. R., and Elkins, J. W.: An unexpected and persistent increase in global emissions of ozone-depleting CFC-11, *Nature*, 557, 413. doi:10.1038/s41586-018-0106-2, 2018. (cited on page 11).
- Moore, D. P., Waterfall, A. M., and Remedios, J. J.: The potential for radiometric retrievals of halocarbon concentrations from the MIPAS-E instrument, *Advances in Space Research*, 37, 2238–2246. doi:10.1016/j.asr.2005.06.058, 2006. (cited on page 31).
- Morgenstern, O., Hegglin, M. I., Rozanov, E., O’Connor, F. M., Abraham, N. L., Akiyoshi, H., Archibald, A. T., Bekki, S., Butchart, N., Chipperfield, M. P., Deushi, M., Dhomse, S. S., Garcia, R. R., Hardiman, S. C., Horowitz, L. W., Jöckel, P., Josse, B., Kinnison, D., Lin, M., Mancini, E., Manyin, M. E., Marchand, M., Maréchal, V., Michou, M., Oman, L. D., Pitari, G., Plummer, D. A., Revell, L. E., Saint-Martin, D., Schofield, R., Stenke, A., Stone, K., Sudo, K., Tanaka, T. Y., Tilmes, S., Yamashita, Y., Yoshida, K., and Zeng, G.: Review of the global models used within phase 1 of the Chemistry–Climate Model Initiative (CCMI), *Geoscientific Model Development*, 10, 639–671. doi:10.5194/gmd-10-639-2017, 2017. (cited on page 74).
- Murphy, D. M. and Koop, T.: Review of the vapour pressures of ice and supercooled water for atmospheric applications, *Quarterly Journal of the Royal Meteorological Society*, 131, 1539–1565. doi:10.1256/qj.04.94, 2005. (cited on page 8).
- Nakajima, H., Sugita, T., Irie, H., Saitoh, N., Kanzawa, H., Oelhaf, H., Wetzel, G., Toon, G. C., Sen, B., Blavier, J., Traub, W. A., Jucks, K., Johnson, D. G., Yokota, T., and Sasano, Y.: Measurements of ClONO₂ by the Improved Limb Atmospheric Spectrometer (ILAS) in high-latitude stratosphere: New products using version 6.1 data processing algorithm, *Journal of Geophysical Research: Atmospheres*, 111. doi:10.1029/2005JD006441, 2006. (cited on page 18).
- NASA GSFC: NASA Ozone Watch. <https://ozonewatch.gsfc.nasa.gov/>, 2018. (cited on page 17).

- Nash, E. R., Newman, P. A., Rosenfield, J. E., and Schoeberl, M. R.: An objective determination of the polar vortex using Ertel's potential vorticity, *Journal of Geophysical Research: Atmospheres* (1984–2012), 101, 9471–9478. doi:10.1029/96JD00066, 1996. (cited on pages 6, 6, 42, 67, 68).
- Newman, P. A., Harris, N. R. P., Adriani, A., Amanatidis, G. T., Anderson, J. G., Braathen, G. O., Brune, W. H., Carslaw, K. S., Craig, M. S., DeCola, P. L., Guirlet, M., Hipskind, R. S., Kurylo, M. J., Küllmann, H., Larsen, N., Mégie, G. J., Pommereau, J., Poole, L. R., Schoeberl, M. R., Stroh, F., Toon, O. B., Trepte, C. R., and van Roozendaal, M.: An overview of the SOLVE/THESEO 2000 campaign, *Journal of Geophysical Research: Atmospheres*, 107, SOL 1–1–SOL 1–26. doi:10.1029/2001JD001303, 2002. (cited on page 18).
- Newman, P. A., Oman, L. D., Douglass, A. R., Fleming, E. L., Frith, S. M., Hurwitz, M. M., Kawa, S. R., Jackman, C. H., Krotkov, N. A., Nash, E. R., Nielsen, J. E., Pawson, S., Stolarski, R. S., and Velders, G. J. M.: What would have happened to the ozone layer if chlorofluorocarbons (CFCs) had not been regulated?, *Atmospheric Chemistry and Physics*, 9, 2113–2128. doi:10.5194/acp-9-2113-2009, 2009. (cited on pages 14, 15).
- NOAA: U.S. standard atmosphere, 1976: United States Committee on Extension to the Standard Atmosphere, National Oceanic and Atmospheric Administration : for sale by the Supt. of Docs., U.S. Govt. Print. Off. <https://books.google.de/books?id=x488AAAAIAAJ>, 1976. (cited on page 4).
- Norton, R. H. and Beer, R.: New apodizing functions for Fourier spectrometry, *JOSA*, 66, 259–264. doi:10.1364/JOSA.66.000259, 1976. (cited on page 23).
- Norton, R. H. and Beer, R.: Errata: New Apodizing Functions For Fourier Spectrometry, *JOSA*, 67, 419. doi:10.1364/JOSA.67.000419, 1977. (cited on page 23).
- Obersteiner, F., Bönisch, H., and Engel, A.: An automated gas chromatography time-of-flight mass spectrometry instrument for the quantitative analysis of halocarbons in air, *Atmospheric Measurement Techniques*, 9, 179–194. doi:10.5194/amt-9-179-2016, 2016. (cited on page 37).
- Oelhaf, H., v. Clarmann, T., Fischer, H., Friedl-Vallon, F., Fritzsche, C., Linden, A., Piesch, C., Seefeldner, M., and Völker, W.: Stratospheric ClONO₂ and HNO₃ profiles inside the Arctic vortex from MIPAS-B limb emission spectra obtained during EA-SOE, *Geophysical Research Letters*, 21, 1263–1266. doi:10.1029/93GL01303, 1994. (cited on page 51).
- Oelhaf, H., Sinnhuber, B.-M., and Woiwode, W.: POLSTRACC - POLar STRATosphere in a Changing Climate. <https://www.polstracc.kit.edu/>, 2015. (cited on page 35).
- Offermann, D., Grossmann, K., Barthol, P., Knieling, P., Riese, M., and Trant, R.: Cryogenic Infrared Spectrometers and Telescopes for the Atmosphere (CRISTA) experiment and middle atmosphere variability, *Journal of Geophysical Research: At-*

- mospheres, 104, 16 311–16 325. doi:10.1029/1998JD100047, 1999. (cited on pages 18, 19).
- Olschewski, F., Ebersoldt, A., Friedl-Vallon, F., Gutschwager, B., Hollandt, J., Kleinert, A., Monte, C., Piesch, C., Preusse, P., Rolf, C., Steffens, P., and Koppmann, R.: The in-flight blackbody calibration system for the GLORIA interferometer on board an airborne research platform, *Atmospheric Measurement Techniques*, 6, 3067–3082. doi:10.5194/amt-6-3067-2013, 2013. (cited on page 23).
- Pachauri, R. K. and Mayer, L., eds.: *Climate change 2014: Synthesis report*, Intergovernmental Panel on Climate Change, Geneva, Switzerland. ISBN:978-92-9169-143-2, 2015. (cited on page 15).
- Pawson, S. and Global Modeling and Assimilation Office: MERRA-2 inst6_3d_ana_Np: 3d,6-Hourly,Instantaneous,Pressure-Level,Analysis,Analyzed Meteorological Fields V5.12.4, 2015. (cited on page 40).
- Perlwitz, J., Pawson, S., Fogt, R. L., Nielsen, J. E., and Neff, W. D.: Impact of stratospheric ozone hole recovery on Antarctic climate, *Geophysical Research Letters*, 35. doi:10.1029/2008GL033317, 2008. (cited on page 1).
- Persky, M. J.: A review of spaceborne infrared Fourier transform spectrometers for remote sensing, *Review of Scientific Instruments*, 66, 4763–4797. doi:10.1063/1.1146154, 1995. (cited on page 19).
- Peter, T. and Groß, J.-U.: Chapter 4 Polar Stratospheric Clouds and Sulfate Aerosol Particles: Microphysics, Denitrification and Heterogeneous Chemistry, in: *Stratospheric Ozone Depletion and Climate Change*, edited by Müller, R., pp. 108–144, The Royal Society of Chemistry. ISBN:978-1-84973-002-0, 2012. (cited on pages 12, 48).
- Phillips, D. L.: A Technique for the Numerical Solution of Certain Integral Equations of the First Kind, *Journal of the ACM (JACM)*, 9, 84–97. doi:10.1145/321105.321114, 1962. (cited on page 29).
- Piesch, C., Gulde, T., Sartorius, C., Friedl-Vallon, F., Seefeldner, M., Wölfel, M., Blom, C. E., and Fischer, H., eds.: *Design of a MIPAS instrument for high-altitude aircraft*, Proc. of the 2nd Internat. Airborne Remote Sensing Conference and Exhibition, 1996. (cited on page 19, 19).
- Piesch, C., Sartorius, C., Friedl-Vallon, F., Gulde, T., Heger, S., Kretschmer, E., Maucher, G., Nordmeyer, H., Barthel, J., Ebersoldt, A., Graf, F., Hase, F., Kleinert, A., Neubert, T., and Schillings, H. J.: The mechanical and thermal setup of the GLORIA spectrometer, *Atmospheric Measurement Techniques*, 8, 1773–1787. doi:10.5194/amt-8-1773-2015, 2015. (cited on page 22).
- Pitts, M. C., Poole, L. R., and Gonzalez, R.: Polar stratospheric cloud climatology based on CALIPSO spaceborne lidar measurements from 2006 to 2017, *Atmospheric Chemistry and Physics*, 18, 10 881–10 913. doi:10.5194/acp-18-10881-2018, 2018. (cited on pages 8, 35, 39).

- Planck, M.: The theory of heat radiation: Authorized translation by M. Masius of 'Wärmestrahlung', P. Plakiston's son & co., Philadelphia, Pa., 2 edn., 1914. (cited on page 29).
- Popp, P. J., Marcy, T. P., Gao, R. S., Watts, L. A., Fahey, D. W., Richard, E. C., Oltmans, S. J., Santee, M. L., Livesey, N. J., Froidevaux, L., Sen, B., Toon, G. C., Walker, K. A., Boone, C. D., and Bernath, P. F.: Stratospheric correlation between nitric acid and ozone, *Journal of Geophysical Research: Atmospheres*, 114, 2008JD010875. doi:10.1029/2008JD010875, 2009. (cited on page 50).
- Prather, M. and Jaffe, A. H.: Global impact of the Antarctic ozone hole: Chemical propagation, *Journal of Geophysical Research*, 95, 3473. doi:10.1029/JD095iD04p03473, 1990. (cited on pages 13, 14, 81).
- Rabitz, H.: Rotation and rotation-vibration pressure-broadened spectral lineshapes, *Annual Review of Physical Chemistry*, 25, 155–177, 1974. (cited on page 26).
- Randel, W. J., Shine, K. P., Austin, J., Barnett, J., Claud, C., Gillett, N. P., Keckhut, P., Langematz, U., Lin, R., Long, C., Mears, C., Miller, A., Nash, J., Seidel, D. J., Thompson, D. W. J., Wu, F., and Yoden, S.: An update of observed stratospheric temperature trends, *Journal of Geophysical Research*, 114, 9479. doi:10.1029/2008JD010421, 2009. (cited on page 15).
- Rautian, S. G. and Sobel'man, I. I.: The effect of collisions on the Doppler broadening of spectral lines, *Soviet Physics Uspekhi*, 9, 701. doi:10.1070/PU1967v009n05ABEH003212, 1967. (cited on page 27).
- Remedios, J. J., Leigh, R. J., Waterfall, A. M., Moore, D. P., Sembhi, H., Parkes, I., Greenhough, J., Chipperfield, M. P., and Hauglustaine, D.: MIPAS reference atmospheres and comparisons to V4.61/V4.62 MIPAS level 2 geophysical data sets, *Atmospheric Chemistry and Physics Discussions*, pp. 9973–10017. doi:10.5194/acpd-7-9973-2007, 2007. (cited on pages 9, 30).
- Revercomb, H. E., Buijs, H., Howell, H. B., LaPorte, D. D., Smith, W. L., and Sromovsky, L. A.: Radiometric calibration of IR Fourier transform spectrometers: Solution to a problem with the High-Resolution Interferometer Sounder, *Applied Optics*, 27, 3210–3218. doi:10.1364/AO.27.003210, 1988. (cited on page 23).
- Rex, M., Salawitch, R. J., von der Gathen, P., Harris, N. R. P., Chipperfield, M. P., and Naujokat, B.: Arctic ozone loss and climate change, *Geophysical Research Letters*, 31. doi:10.1029/2003GL018844, 2004. (cited on pages 14, 15, 15).
- Rex, M., Salawitch, R. J., Deckelmann, H., von der Gathen, P., Harris, N. R. P., Chipperfield, M. P., Naujokat, B., Reimer, E., Allaart, M., Andersen, S. B., Bevilacqua, R., Braathen, G. O., Claude, H., Davies, J., de Backer, H., Dier, H., Dorokhov, V., Fast, H., Gerding, M., Godin-Beekmann, S., Hoppel, K., Johnson, B., Kyrö, E., Litynska, Z., Moore, D., Nakane, H., Parrondo, M. C., Risley, A. D., Skrivankova, P., Stübi, R., Viatte, P., Yushkov, V., and Zerefos, C.: Arctic winter 2005: Implications for stratospheric ozone loss and climate change, *Geophysical Research Letters*, 33, 221. doi:10.1029/2006GL026731, 2006. (cited on pages 14, 15).

- Riese, M., Ploeger, F., Rap, A., Vogel, B., Konopka, P., Dameris, M., and Forster, P.: Impact of uncertainties in atmospheric mixing on simulated UTLS composition and related radiative effects, *Journal of Geophysical Research: Atmospheres*, 117. doi:10.1029/2012JD017751, 2012. (cited on page 1).
- Riese, M., Oelhaf, H., Preusse, P., Blank, J., Ern, M., Friedl-Vallon, F., Fischer, H., Guggenmoser, T., Höpfner, M., Hoor, P., Kaufmann, M., Orphal, J., Plöger, F., Spang, R., Suminska-Ebersoldt, O., Ungermann, J., Vogel, B., and Woiwode, W.: Gimballed Limb Observer for Radiance Imaging of the Atmosphere (GLORIA) scientific objectives, *Atmospheric Measurement Techniques*, 7, 1915–1928. doi:10.5194/amt-7-1915-2014, 2014. (cited on page 19).
- Roche, A. E., Kumer, J. B., Mergenthaler, J. L., Nightingale, R. W., Uplinger, W. G., Ely, G. A., Potter, J. F., Wuebbles, D. J., Connell, P. S., and Kinnison, D. E.: Observations of Lower-Stratospheric CIONO₂, HNO₃, and Aerosol by the UARS CLAES Experiment between January 1992 and April 1993, *Journal of the Atmospheric Sciences*, 51, 2877–2902. doi:10.1175/1520-0469(1994)051<2877:OOLSCH>2.0.CO;2, 1994. (cited on pages 18, 51).
- Rodgers, C. D.: *Inverse Methods for Atmospheric Sounding*, WORLD SCIENTIFIC. doi:10.1142/3171, 2000. (cited on pages 28, 28, 29, 29, 32, 32, 33).
- Roeckner, E., Brokopf, R., Esch, M., Giorgetta, M., Hagemann, S., Kornblueh, L., Manzini, E., Schlese, U., and Schulzweida, U.: Sensitivity of Simulated Climate to Horizontal and Vertical Resolution in the ECHAM5 Atmosphere Model, *Journal of Climate*, 19, 3771–3791. doi:10.1175/JCLI3824.1, 2006. (cited on page 40).
- Roedel, W. and Wagner, T.: *Physik unserer Umwelt: Die Atmosphäre*, Springer Berlin Heidelberg, Berlin, Heidelberg. doi:10.1007/978-3-662-54258-3, 2017. (cited on page 3).
- Rolf, C., Afchine, A., Bozem, H., Buchholz, B., Ebert, V., Guggenmoser, T., Hoor, P., Konopka, P., Kretschmer, E., Müller, S., Schlager, H., Spelten, N., Sumińska-Ebersoldt, O., Ungermann, J., Zahn, A., and Krämer, M.: Transport of Antarctic stratospheric strongly dehydrated air into the troposphere observed during the HALO-ESMVal campaign 2012, *Atmospheric Chemistry and Physics*, 15, 9143–9158. doi:10.5194/acp-15-9143-2015, 2015. (cited on page 24).
- Rosenfield, J. E., Newman, P. A., and Schoeberl, M. R.: Computations of diabatic descent in the stratospheric polar vortex, *Journal of Geophysical Research: Atmospheres*, 99, 16 677–16 689. doi:10.1029/94JD01156, 1994. (cited on page 6).
- Rosenkranz, P.: Shape of the 5 mm oxygen band in the atmosphere, *IEEE Transactions on Antennas and Propagation*, 23, 498–506. doi:10.1109/TAP.1975.1141119, 1975. (cited on page 27).
- Rousseuw, P. J. and Croux, C.: Alternatives to the Median Absolute Deviation, *Journal of the American Statistical Association*, 88, 1273–1283. doi:10.1080/01621459.1993.10476408, 1993. (cited on page 54).

- Rowland, F. S., Spencer, J. E., and Molina, M. J.: Stratospheric formation and photolysis of chlorine nitrate, *The Journal of Physical Chemistry*, 80, 2711–2713, 1976. (cited on page 12).
- Sander, S. P., Friedl, R. R., Barker, J. R., Golden, D. M., Kurylo, M. J., Wine, P. H., Abbatt, J., Burkholder, J. B., Kolb, C. E., Moortgat, G. K., Huie, R. E., and Orkin, V. L.: Chemical kinetics and photochemical data for use in atmospheric studies, Evaluation no. 17, JPL Publication, 10-6. <http://jpldataeval.jpl.nasa.gov>, 2011. (cited on page 40).
- Santee, M. L.: Quantifying and confirming our understanding of processes controlling stratospheric ozone: Insights from UARS and Aura MLS. http://www.montreal30.io3c.org/sites/montreal30.io3c.org/files/pictures/19apm/Santee_MPSymp-MLS_Overview.pdf, 2017. (cited on pages 77, 78, 82, 92).
- Santee, M. L., Tabazadeh, A., Manney, G. L., Salawitch, R. J., Froidevaux, L., Read, W. G., and Waters, J. W.: UARS Microwave Limb Sounder HNO₃ observations: Implications for Antarctic polar stratospheric clouds, *Journal of Geophysical Research*, 103, 13 285–13 313. doi:10.1029/98JD00365, 1998. (cited on pages 13, 14).
- Santee, M. L., Manney, G. L., Livesey, N. J., and Waters, J. W.: UARS Microwave Limb Sounder observations of denitrification and ozone loss in the 2000 Arctic late winter, *Geophysical Research Letters*, 27, 3213–3216. doi:10.1029/2000GL011738, 2000. (cited on page 14).
- Santee, M. L., Lambert, A., Read, W. G., Livesey, N. J., Cofield, R. E., Cuddy, D. T., Daffer, W. H., Drouin, B. J., Froidevaux, L., Fuller, R. A., Jarnot, R. F., Knosp, B. W., Manney, G. L., Perun, V. S., Snyder, W. V., Stek, P. C., Thurstans, R. P., Wagner, P. A., Waters, J. W., Muscari, G., de Zafra, R. L., Dibb, J. E., Fahey, D. W., Popp, P. J., Marcy, T. P., Jucks, K. W., Toon, G. C., Stachnik, R. A., Bernath, P. F., Boone, C. D., Walker, K. A., Urban, J., and Murtagh, D.: Validation of the Aura Microwave Limb Sounder HNO₃ measurements, *Journal of Geophysical Research: Atmospheres*, 112, 2007JD008 721. doi:10.1029/2007JD008721, 2007. (cited on page 38).
- Santee, M. L., Lambert, A., Read, W. G., Livesey, N. J., Manney, G. L., Cofield, R. E., Cuddy, D. T., Daffer, W. H., Drouin, B. J., Froidevaux, L., Fuller, R. A., Jarnot, R. F., Knosp, B. W., Perun, V. S., Snyder, W. V., Stek, P. C., Thurstans, R. P., Wagner, P. A., Waters, J. W., Connor, B., Urban, J., Murtagh, D., Ricaud, P., Barret, B., Kleinböhl, A., Kuttippurath, J., Küllmann, H., von Hobe, M., Toon, G. C., and Stachnik, R. A.: Validation of the Aura Microwave Limb Sounder ClO measurements, *Journal of Geophysical Research: Atmospheres*, 113. doi:10.1029/2007JD008762, 2008a. (cited on pages 18, 38).
- Santee, M. L., MacKenzie, I. A., Manney, G. L., Chipperfield, M. P., Bernath, P. F., Walker, K. A., Boone, C. D., Froidevaux, L., Livesey, N. J., and Waters, J. W.: A study of stratospheric chlorine partitioning based on new satellite

- measurements and modeling, *Journal of Geophysical Research: Atmospheres*, 113. doi:10.1029/2007JD009057, 2008b. (cited on pages 13, 13, 14, 18, 38, 60, 65).
- Santee, M. L., Manney, G. L., Livesey, N. J., Froidevaux, L., Schwartz, M. J., and Read, W. G.: Trace gas evolution in the lowermost stratosphere from Aura Microwave Limb Sounder measurements, *Journal of Geophysical Research: Atmospheres*, 116. doi:10.1029/2011JD015590, 2011. (cited on pages 62, 78).
- Santee, M. L., Livesey, N. J., Manney, G. L., Lambert, A., and Read, W. G.: Methyl chloride from the Aura Microwave Limb Sounder: First global climatology and assessment of variability in the upper troposphere and stratosphere, *Journal of Geophysical Research: Atmospheres*, 118, 13,532–13,560. doi:10.1002/2013JD020235, 2013. (cited on pages 38, 39).
- Santee, M. L., Livesey, N. J., and Read, W. G.: MLS/Aura L2 Methyl Chloride (CH₃Cl) Mixing Ratio - Version 4. <https://doi.org/10.5067/AURA/MLS/DATA2002>, 2015a. (cited on page 38).
- Santee, M. L., Livesey, N. J., and Read, W. G.: MLS/Aura L2 Chlorine Monoxide (ClO) Mixing Ratio - Version 4. <https://doi.org/10.5067/AURA/MLS/DATA2004>, 2015b. (cited on page 38).
- Schoeberl, M. R. and Hartmann, D. L.: The dynamics of the stratospheric polar vortex and its relation to springtime ozone depletions, *Science (New York, N.Y.)*, 251, 46–52. doi:10.1126/science.251.4989.46, 1991. (cited on page 6, 6).
- Schoeberl, M. R., Lait, L. R., Newman, P. A., and Rosenfield, J. E.: The structure of the polar vortex, *Journal of Geophysical Research*, 97, 7859–7882. doi:10.1029/91JD02168, 1992. (cited on page 6, 6).
- Schrödinger, E.: An Undulatory Theory of the Mechanics of Atoms and Molecules, *Phys. Rev.*, 28, 1049–1070. doi:10.1103/PhysRev.28.1049, 1926. (cited on page 25).
- Schwartz, M. J., Froidevaux, L., Livesey, N. J., and Read, W. G.: MLS/Aura L2 Ozone (O₃) Mixing Ratio - Version 4. <https://doi.org/10.5067/AURA/MLS/DATA2017>, 2015. (cited on page 38).
- Seinfeld, J. H. and Pandis, S. N.: *Atmospheric Chemistry and Physics: From Air Pollution to Climate Change*, John Wiley & Sons, Incorporated, New York, UNITED STATES. ISBN:9781119221166, 2016. (cited on page 3).
- Shapiro, M. A.: Turbulent Mixing within Tropopause Folds as a Mechanism for the Exchange of Chemical Constituents between the Stratosphere and Troposphere, *Journal of the Atmospheric Sciences*, 37, 994–1004. doi:10.1175/1520-0469(1980)037<0994:TMWTFA>2.0.CO;2, 1980. (cited on pages 6, 52).
- Sheese, P. E., Walker, K. A., Boone, C. D., McLinden, C. A., Bernath, P. F., Bourassa, A. E., Burrows, J. P., Degenstein, D. A., Funke, B., Fussen, D., Manney, G. L., McElroy, C. T., Murtagh, D., Randall, C. E., Raspollini, P., Rozanov, A., Russell III, J. M., Suzuki, M., Shiotani, M., Urban, J., Clarmann, T. V., and Zawodny, J. M.: Validation

- of ACE-FTS version 3.5 NO_y species profiles using correlative satellite measurements, *Atmospheric Measurement Techniques*, 9, 5781–5810. doi:10.5194/amt-9-5781-2016, 2016. (cited on page 38).
- Shindell, D. T., Rind, D., and Lonergan, P.: Increased polar stratospheric ozone losses and delayed eventual recovery owing to increasing greenhouse-gas concentrations, *Nature*, 392, 589. doi:10.1038/33385, 1998. (cited on page 15).
- Sinnhuber, B., Stiller, G., Ruhnke, R., von Clarmann, T., Kellmann, S., and Aschmann, J.: Arctic winter 2010/2011 at the brink of an ozone hole, *Geophysical Research Letters*, 38. doi:10.1029/2011GL049784, 2011. (cited on page 83).
- Solomon, S.: Stratospheric ozone depletion: A review of concepts and history, *Reviews of Geophysics*, 37, 275–316. doi:10.1029/1999RG900008, 1999. (cited on pages 3, 10, 10, 13, 65, 90).
- Solomon, S., Garcia, R. R., Rowland, F. S., and Wuebbles, D. J.: On the depletion of Antarctic ozone, *Nature*, 321, 755 EP –. doi:10.1038/321755a0, 1986. (cited on page 12, 12).
- Solomon, S., Kinnison, D., Bandoro, J., and Garcia, R.: Simulation of polar ozone depletion: An update, *Journal of Geophysical Research: Atmospheres*, 120, 7958–7974. doi:10.1002/2015JD023365, 2015. (cited on page 3).
- Solomon, S., Kinnison, D., Garcia, R. R., Bandoro, J., Mills, M., Wilka, C., Neely, R. R., Schmidt, A., Barnes, J. E., Vernier, J., and Höpfner, M.: Monsoon circulations and tropical heterogeneous chlorine chemistry in the stratosphere, *Geophysical Research Letters*. doi:10.1002/2016GL071778, 2016. (cited on page 14).
- Spang, R., Remedios, J. J., and Brarkley, M. P.: Colour indices for the detection and differentiation of cloud types in infra-red limb emission spectra, *Advances in Space Research*, 33, 1041–1047. doi:10.1016/S0273-1177(03)00585-4, 2004. (cited on page 30).
- Spang, R., Hoffmann, L., Müller, R., Groß, J.-U., Tritscher, I., Höpfner, M., Pitts, M., Orr, A., and Riese, M.: A climatology of polar stratospheric cloud composition between 2002 and 2012 based on MIPAS/Envisat observations, *Atmospheric Chemistry and Physics*, 18, 5089–5113. doi:10.5194/acp-18-5089-2018, 2018. (cited on page 10).
- Spencer, N. D. and Moore, J. H.: *Encyclopedia of Chemical Physics and Physical Chemistry: Fundamentals*, Institute of Physics Pub. ISBN:9780750307987, 2001. (cited on page 26).
- Stiller, G. P., ed.: *The Karlsruhe Optimized and Precise Radiative transfer Algorithm (KOPRA)*, vol. FZKA 6487 of *Wissenschaftliche Berichte*, Forschungszentrum Karlsruhe, 2000. (cited on pages 26, 29).
- Stiller, G. P., von Clarmann, T., Haenel, F., Funke, B., Glatthor, N., Grabowski, U., Kellmann, S., Kiefer, M., Linden, A., Lossow, S., and López-Puertas, M.: Observed temporal evolution of global mean age of stratospheric air for the 2002 to 2010 period,

- Atmospheric Chemistry and Physics, 12, 3311–3331. doi:10.5194/acp-12-3311-2012, 2012. (cited on page 16).
- Stohl, A., Bonasoni, P., Cristofanelli, P., Collins, W., Feichter, J., Frank, A., Forster, C., Gerasopoulos, E., Gäggeler, H., James, P., Kentarchos, T., Kromp-Kolb, H., Krüger, B., Land, C., Meloan, J., Papayannis, A., Priller, A., Seibert, P., Sprenger, M., Roelofs, G. J., Scheel, H. E., Schnabel, C., Siegmund, P., Tobler, L., Trickl, T., Wernli, H., Wirth, V., Zanis, P., and Zerefos, C.: Stratosphere-troposphere exchange: A review, and what we have learned from STACCATO, *Journal of Geophysical Research: Atmospheres*, 108. doi:10.1029/2002JD002490, 2003. (cited on page 6).
- Stolarski, R. S. and Cicerone, R. J.: Stratospheric chlorine: A possible sink for ozone, *Canadian journal of Chemistry*, 52, 1610–1615, 1974. (cited on pages 10, 12).
- Stolarski, R. S., Krueger, A. J., Schoeberl, M. R., McPeters, R. D., Newman, P. A., and Alpert, J. C.: Nimbus 7 satellite measurements of the springtime Antarctic ozone decrease, *Nature*, 322, 808. doi:10.1038/322808a0, 1986. (cited on pages 13, 17).
- Stone, K. A., Solomon, S., and Kinnison, D. E.: On the Identification of Ozone Recovery, *Geophysical Research Letters*, pp. 5158–5165. doi:10.1029/2018GL077955, 2018. (cited on page 11).
- Swart, N. C., Gille, S. T., Fyfe, J. C., and Gillett, N. P.: Recent Southern Ocean warming and freshening driven by greenhouse gas emissions and ozone depletion, *Nature Geoscience*, 11, 836. doi:10.1038/s41561-018-0226-1, 2018. (cited on pages 1, 17).
- Tabazadeh, A., Turco, R. P., Drdla, K., Jacobson, M. Z., and Toon, O. B.: Correction [to “A study of type I polar stratospheric cloud formation,”], *Geophysical Research Letters*, 21, 2869. doi:10.1029/94GL02763, 1994a. (cited on page 8).
- Tabazadeh, A., Turco, R. P., Drdla, K., Jacobson, M. Z., and Toon, O. B.: A study of type I polar stratospheric cloud formation, *Geophysical Research Letters*, 21, 1619–1622. doi:10.1029/94GL01368, 1994b. (cited on page 8).
- Tabazadeh, A., Toon, O. B., and Jensen, E. J.: Formation and implications of ice particle nucleation in the stratosphere, *Geophysical Research Letters*, 24, 2007–2010. doi:10.1029/97GL01883, 1997. (cited on page 8).
- Thompson, D. W. J. and Solomon, S.: Interpretation of Recent Southern Hemisphere Climate Change, *Science*, 296, 895–899. doi:10.1126/science.1069270, 2002. (cited on page 1).
- Thornton, B. F., Toohey, D. W., Avallone, L. M., Harder, H., Martinez, M., Simpas, J. B., Brune, W. H., and Avery, M. A.: In situ observations of ClO near the winter polar tropopause, *Journal of Geophysical Research: Atmospheres*, 108. doi:10.1029/2002JD002839, 2003. (cited on page 15).

- Tikhonov, A. N. and Arsenin, V. I.: Solutions of ill-posed problems, Scripta series in mathematics, Winston and Distributed solely by Halsted Press, Washington and New York. ISBN:9780470991244, 1977. (cited on page 29).
- Toon, G. C.: The JPL MkIV interferometer, Optics and Photonics News, 2, 19. doi:10.1364/OPN.2.10.000019, 1991. (cited on page 18).
- Toon, O. B., Browell, E. V., Kinne, S., and Jordan, J.: An analysis of lidar observations of polar stratospheric clouds, Geophysical Research Letters, 17, 393–396. doi:10.1029/GL017i004p00393, 1990. (cited on page 13).
- Tritscher, I., Groß, J.-U., Spang, R., Pitts, M. C., Poole, L. R., Müller, R., and Riese, M.: Lagrangian simulation of ice particles and resulting dehydration in the polar winter stratosphere, Atmospheric Chemistry and Physics Discussions, pp. 1–32. doi:10.5194/acp-2018-337, 2018. (cited on pages 39, 70).
- Ungermann, J., Blank, J., Lotz, J., Leppkes, K., Hoffmann, L., Guggenmoser, T., Kaufmann, M., Preusse, P., Naumann, U., and Riese, M.: A 3-D tomographic retrieval approach with advection compensation for the air-borne limb-imager GLORIA, Atmospheric Measurement Techniques, 4, 2509–2529. doi:10.5194/amt-4-2509-2011, 2011. (cited on pages 23, 48).
- Ungermann, J., Kalicinsky, C., Olschewski, F., Knieling, P., Hoffmann, L., Blank, J., Woiwode, W., Oelhaf, H., Hösen, E., Volk, C. M., Ulanovsky, A., Ravegnani, F., Weigel, K., Stroh, F., and Riese, M.: CRISTA-NF measurements with unprecedented vertical resolution during the RECONCILE aircraft campaign, Atmospheric Measurement Techniques, 5, 1173–1191. doi:10.5194/amt-5-1173-2012, 2012. (cited on pages 19, 31, 48).
- Ungermann, J., Pan, L. L., Kalicinsky, C., Olschewski, F., Knieling, P., Blank, J., Weigel, K., Guggenmoser, T., Stroh, F., Hoffmann, L., and Riese, M.: Filamentary structure in chemical tracer distributions near the subtropical jet following a wave breaking event, Atmospheric Chemistry and Physics, 13, 10 517–10 534. doi:10.5194/acp-13-10517-2013, 2013. (cited on page 28).
- Ungermann, J., Blank, J., Dick, M., Ebersoldt, A., Friedl-Vallon, F., Giez, A., Guggenmoser, T., Höpfner, M., Jurkat, T., Kaufmann, M., Kaufmann, S., Kleinert, A., Krämer, M., Latzko, T., Oelhaf, H., Olschewski, F., Preusse, P., Rolf, C., Schillings, J., Suminska-Ebersoldt, O., Tan, V., Thomas, N., Voigt, C., Zahn, A., Zöger, M., and Riese, M.: Level 2 processing for the imaging Fourier transform spectrometer GLORIA: Derivation and validation of temperature and trace gas volume mixing ratios from calibrated dynamics mode spectra, Atmospheric Measurement Techniques, 8, 2473–2489. doi:10.5194/amt-8-2473-2015, 2015. (cited on pages 24, 92).
- United Nations: Paris Agreement. https://treaties.un.org/Pages/ViewDetails.aspx?src=TREATY&mtdsg_no=XXVII-7-d&chapter=27&lang=_en&clang=_en, 2015. (cited on page 1).

- Urban, J., Lautié, N., Le Flochmoën, E., Jiménez, C., Eriksson, P., La Noë, J. d., Dupuy, E., Ekström, M., Amraoui, L. E., Frisk, U., Murtagh, D., Olberg, M., and Ricaud, P.: Odin/SMR limb observations of stratospheric trace gases: Level 2 processing of ClO, N₂O, HNO₃, and O₃, *Journal of Geophysical Research: Atmospheres*, 110. doi:10.1029/2004JD005741, 2005. (cited on page 18).
- Vaisala: User's guide: Ozone Sounding with Vaisala Radiosonde RS41, 2016. (cited on page 56).
- Valipour, H.: Messung druckinduzierter Effekte an Absorptionslinien von Acetylen, Fachbereich Physik, Technischen Universität Berlin, Berlin, 2001. (cited on pages 26, 27).
- Voigt, C., Schreiner, J., Kohlmann, A., Zink, P., Mauersberger, K., Larsen, N., Deshler, T., Kröger, C., Rosen, J., Adriani, A., Cairo, F., Di Donfrancesco, G., Viterbini, M., Ovarlez, J., Ovarlez, H., David, C., and Dörnbrack, A.: Nitric Acid Trihydrate (NAT) in Polar Stratospheric Clouds, *Science (New York, N.Y.)*, 290, 1756–1758. doi:10.1126/science.290.5497.1756, 2000. (cited on page 8).
- Voigt, C., Schumann, U., Minikin, A., Abdelmonem, A., Afchine, A., Borrmann, S., Boettcher, M., Buchholz, B., Bugliaro, L., Costa, A., Curtius, J., Dollner, M., Dörnbrack, A., Dreiling, V., Ebert, V., Ehrlich, A., Fix, A., Forster, L., Frank, F., Fütterer, D., Giez, A., Graf, K., Groß, J.-U., Groß, S., Heimerl, K., Heinold, B., Hüneke, T., Järvinen, E., Jurkat, T., Kaufmann, S., Kenntner, M., Klingebiel, M., Klimach, T., Kohl, R., Krämer, M., Krisna, T. C., Luebke, A., Mayer, B., Mertes, S., Molleker, S., Petzold, A., Pfeilsticker, K., Port, M., Rapp, M., Reutter, P., Rolf, C., Rose, D., Sauer, D., Schäfler, A., Schlage, R., Schnaiter, M., Schneider, J., Spelten, N., Spichtinger, P., Stock, P., Walser, A., Weigel, R., Weinzierl, B., Wendisch, M., Werner, F., Wernli, H., Wirth, M., Zahn, A., Ziereis, H., and Zöger, M.: ML-CIRRUS: The Airborne Experiment on Natural Cirrus and Contrail Cirrus with the High-Altitude Long-Range Research Aircraft HALO, *Bulletin of the American Meteorological Society*, 98, 271–288. doi:10.1175/BAMS-D-15-00213.1, 2017. (cited on page 37).
- Voigt, C., Dörnbrack, A., Wirth, M., Groß, S. M., Pitts, M. C., Poole, L. R., Baumann, R., Ehard, B., Sinnhuber, B.-M., Woiwode, W., and Oelhaf, H.: Widespread polar stratospheric ice clouds in the 2015–2016 Arctic winter – implications for ice nucleation, *Atmospheric Chemistry and Physics*, 18, 15 623–15 641. doi:10.5194/acp-18-15623-2018, 2018. (cited on page 35).
- von Clarmann, T.: Chlorine in the Stratosphere, *Atmósfera*, 26. <http://www.revistascca.unam.mx/atm/index.php/atm/article/download/38656/36823>, 2013. (cited on page 3).
- von Clarmann, T. and Johansson, S.: Chlorine nitrate in the atmosphere, *Atmospheric Chemistry and Physics*, 18, 15 363–15 386. doi:10.5194/acp-18-15363-2018, 2018. (cited on page 12).
- von Clarmann, T., Fischer, H., Friedl-Vallon, F., Linden, A., Oelhaf, H., Piesch, C., Seefeldner, M., and Völker, W.: Retrieval of stratospheric O₃, HNO₃ and

- CLONO2 profiles from 1992 MIPAS-B limb emission spectra: Method, results, and error analysis, *Journal of Geophysical Research: Atmospheres*, 98, 20 495–20 506. doi:10.1029/93JD02261, 1993. (cited on page 51).
- von Clarmann, T., Linden, A., Oelhaf, H., Fischer, H., Friedl-Vallon, F., Piesch, C., Seefeldner, M., Völker, W., Bauer, R., Engel, A., and Schmidt, U.: Determination of the stratospheric organic chlorine budget in the spring arctic vortex from MIPAS B limb emission spectra and air sampling experiments, *Journal of Geophysical Research: Atmospheres*, 100, 13 979–13 997. doi:10.1029/95JD01048, 1995. (cited on page 18).
- von Clarmann, T., Glatthor, N., Grabowski, U., Höpfner, M., Kellmann, S., Kiefer, M., Linden, A., Tsidu, G. M., Milz, M., Steck, T., Stiller, G. P., Wang, D. Y., Fischer, H., Funke, B., Gil-López, S., and López-Puertas, M.: Retrieval of temperature and tangent altitude pointing from limb emission spectra recorded from space by the Michelson Interferometer for Passive Atmospheric Sounding (MIPAS), *Journal of Geophysical Research: Atmospheres*, 108, 2003JD003 602. doi:10.1029/2003JD003602, 2003. (cited on page 29).
- von Hobe, M. and Stroh, F.: Chapter 3. Stratospheric Halogen Chemistry, in: *Stratospheric Ozone Depletion and Climate Change*, edited by Müller, R., pp. 78–107, The Royal Society of Chemistry. ISBN:978-1-84973-002-0, 2012. (cited on pages 1, 10).
- von Hobe, M., Bekki, S., Borrmann, S., Cairo, F., D’Amato, F., Di Donfrancesco, G., Dörnbrack, A., Ebersoldt, A., Ebert, M., Emde, C., Engel, I., Ern, M., Frey, W., Genco, S., Griessbach, S., Groöß, J.-U., Gulde, T., Günther, G., Hösen, E., Hoffmann, L., Homonnai, V., Hoyle, C. R., Isaksen, I. S. A., Jackson, D. R., Jánosi, I. M., Jones, R. L., Kandler, K., Kalicinsky, C., Keil, A., Khaykin, S. M., Khosrawi, F., Kivi, R., Kuttippurath, J., Laube, J. C., Lefèvre, F., Lehmann, R., Ludmann, S., Luo, B. P., Marchand, M., Meyer, J., Mitev, V., Molleker, S., Müller, R., Oelhaf, H., Olschewski, F., Orsolini, Y., Peter, T., Pfeilsticker, K., Piesch, C., Pitts, M. C., Poole, L. R., Pope, F. D., Ravegnani, F., Rex, M., Riese, M., Röckmann, T., Rognerud, B., Roiger, A., Rolf, C., Santee, M. L., Scheibe, M., Schiller, C., Schlager, H., Siciliani de Cumis, M., Sitnikov, N., Søvde, O. A., Spang, R., Spelten, N., Stordal, F., Sumińska-Ebersoldt, O., Ulanovski, A., Ungermann, J., Viciani, S., Volk, C. M., Vom Scheidt, M., von der Gathen, P., Walker, K., Wegner, T., Weigel, R., Weinbruch, S., Wetzel, G., Wienhold, F. G., Wohltmann, I., Woiwode, W., Young, I. A. K., Yushkov, V., Zobrist, B., and Stroh, F.: Reconciliation of essential process parameters for an enhanced predictability of Arctic stratospheric ozone loss and its climate interactions (RECONCILE): Activities and results, *Atmospheric Chemistry and Physics*, 13, 9233–9268. doi:10.5194/acp-13-9233-2013, 2013. (cited on pages 13, 18, 18, 18).
- Wagner, G. and Birk, M.: New infrared spectroscopic database for chlorine nitrate, *Journal of Quantitative Spectroscopy and Radiative Transfer*, 82, 443–460. doi:10.1016/S0022-4073(03)00169-9, 2003. (cited on page 31).
- Waibel, A. E., Peter, T., Carslaw, K. S., Oelhaf, H., Wetzel, G., Crutzen, P. J., Pöschl, U., Tsias, A., Reimer, E., and Fischer, H.: Arctic Ozone Loss Due to Denitrification, *Science*, 283, 2064–2069. doi:10.1126/science.283.5410.2064, 1999. (cited on page 14).

- Wang, J.: Dicke narrowing and speed-dependent effects in dispersion signals: Influence on assessment of concentration and spectral parameters by noise-immune cavity-enhanced optical heterodyne molecular spectrometry, Department of Physics, Umeå University, Umeå. ISBN:978-91-7459-628-1, 2013. (cited on page 26).
- Waters, J. W., Froidevaux, L., Read, W. G., Manney, G. L., Elson, L. S., Flower, D. A., Jarnot, R. F., and Harwood, R. S.: Stratospheric ClO and ozone from the Microwave Limb Sounder on the Upper Atmosphere Research Satellite, *Nature*, 362, 597. doi:10.1038/362597a0, 1993. (cited on page 18).
- Waters, J. W., Froidevaux, L., Harwood, R. S., Jarnot, R. F., Pickett, H. M., Read, W. G., Siegel, P. H., Cofield, R. E., Filipiak, M. J., Flower, D. A., Holden, J. R., Lau, G. K., Livesey, N. J., Manney, G. L., Pumphrey, H. C., Santee, M. L., Wu, D. L., Cuddy, D. T., Lay, R. R., Loo, M. S., Perun, V. S., Schwartz, M. J., Stek, P. C., Thurstans, R. P., Boyles, M. A., Chandra, K. M., Chavez, M. C., Chen, G.-S., Chudasama, B. V., Dodge, R., Fuller, R. A., Girard, M. A., Jiang, J. H., Jiang, Y., Knosp, B. W., LaBelle, R. C., Lam, J. C., Lee, K. A., Miller, D., Oswald, J. E., Patel, N. C., Pukala, D. M., Quintero, O., Scaff, D. M., van Snyder, W., Tope, M. C., Wagner, P. A., and Walch, M. J.: The Earth Observing System Microwave Limb Sounder (EOS MLS) on the Aura Satellite, *IEEE Transactions on Geoscience and Remote Sensing*, 44, 1075–1092. doi:10.1109/TGRS.2006.873771, 2006. (cited on pages 18, 28, 38).
- Waugh, D. W. and Randel, W. J.: Climatology of Arctic and Antarctic Polar Vortices Using Elliptical Diagnostics, *Journal of the Atmospheric Sciences*, 56, 1594–1613. doi:10.1175/1520-0469(1999)056<1594:COAAAP>2.0.CO;2, 1999. (cited on page 8).
- Wegner, T., Pitts, M. C., Poole, L. R., Tritscher, I., Groß, J.-U., and Nakajima, H.: Vortex-wide chlorine activation by a mesoscale PSC event in the Arctic winter of 2009/10, *Atmospheric Chemistry and Physics*, 16, 4569–4577. doi:10.5194/acp-16-4569-2016, 2016. (cited on page 15).
- Wetzel, G., Oelhaf, H., Ruhnke, R., Friedl-Vallon, F., Kleinert, A., Kouker, W., Maucher, G., Reddmann, T., Seefeldner, M., Stowasser, M., Trieschmann, O., von Clarmann, T., and Fischer, H.: NO_y partitioning and budget and its correlation with N₂O in the Arctic vortex and in summer midlatitudes in 1997, *Journal of Geophysical Research: Atmospheres*, 107. doi:10.1029/2001JD000916, 2002. (cited on pages 29, 31, 32).
- Wetzel, G., Oelhaf, H., Kirner, O., Friedl-Vallon, F., Ruhnke, R., Ebersoldt, A., Kleinert, A., Maucher, G., Nordmeyer, H., and Orphal, J.: Diurnal variations of reactive chlorine and nitrogen oxides observed by MIPAS-B inside the January 2010 Arctic vortex, *Atmospheric Chemistry and Physics*, 12, 6581–6592. doi:10.5194/acp-12-6581-2012, 2012. (cited on page 18).
- Wetzel, G., Oelhaf, H., Birk, M., Lange, A. d., Engel, A., Friedl-Vallon, F., Kirner, O., Kleinert, A., Maucher, G., Nordmeyer, H., Orphal, J., Ruhnke, R., Sinnhuber, B.-M.,

- and Vogt, P.: Partitioning and budget of inorganic and organic chlorine species observed by MIPAS-B and TELIS in the Arctic in March 2011, *Atmospheric Chemistry and Physics*, 15, 8065–8076. doi:10.5194/acp-15-8065-2015, 2015. (cited on page 18).
- Wilson, E. B., Decius, J. C., and Cross, P. C.: *Molecular Vibrations: The Theory of Infrared and Raman Vibrational Spectra*, McGraw-Hill book company, New York, 1955. (cited on page 25).
- Winker, D. M., Vaughan, M. A., Omar, A., Hu, Y., Powell, K. A., Liu, Z., Hunt, W. H., and Young, S. A.: Overview of the CALIPSO Mission and CALIOP Data Processing Algorithms, *Journal of Atmospheric and Oceanic Technology*, 26, 2310–2323. doi:10.1175/2009JTECHA1281.1, 2009. (cited on page 39).
- WMO: The Montreal protocol on substances that deplete the ozone layer. <http://ozone.unep.org/en/treaties-and-decisions/montreal-protocol-substances-deplete-ozone-layer>, 1987. (cited on pages 1, 10).
- WMO: International meteorological vocabulary: Vocabulaire météorologique internationale = Meždunarodnyj meteorologičeskij slovar' = Vocabulario meteorológico internacional, vol. 182 of *WMO*, Secretariat of the World Meteorological Organization, Geneva, 2nd ed. edn. ISBN:9263021821, 1992. (cited on page 4).
- WMO: Scientific Assessment of Ozone Depletion: 2006: report of the Montreal Protocol Scientific Assessment Panel, WMO, 2007. (cited on page 13).
- WMO, ed.: Scientific assessment of Ozone depletion: 2014. Pursuant to Article 6 of the Montreal Protocol on substances that deplete the ozone layer, vol. 55 of *Report / World Meteorological Organization, Global Ozone Research and Monitoring Project*, World Meteorological Organization, Geneva. http://www.wmo.int/pages/prog/arep/gaw/ozone_2014/documents/Full_report_2014_Ozone_Assessment.pdf, 2015. (cited on pages 1, 8, 10, 11, 11, 11, 11, 12, 12, 13, 14, 53, 93).
- WMO: Executive Summary: Scientific Assessment of Ozone Depletion: 2018, vol. Report No. 58., World Meteorological Organization, Geneva, Switzerland. ISBN:978-1-7329317-0-1, 2018. (cited on pages 11, 16, 17).
- Wohlmann, I., Lehmann, R., and Rex, M.: A quantitative analysis of the reactions involved in stratospheric ozone depletion in the polar vortex core, *Atmospheric Chemistry and Physics*, 17, 10 535–10 563. doi:10.5194/acp-17-10535-2017, 2017. (cited on page 12).
- Woiwode, W., Oelhaf, H., Gulde, T., Piesch, C., Maucher, G., Ebersoldt, A., Keim, C., Höpfner, M., Khaykin, S., Ravegnani, F., Ulanovsky, A. E., Volk, C. M., Hösen, E., Dörnbrack, A., Ungermann, J., Kalicinsky, C., and Orphal, J.: MIPAS-STR measurements in the Arctic UTLS in winter/spring 2010: Instrument characterization, retrieval and validation, *Atmospheric Measurement Techniques*, 5, 1205–1228. doi:10.5194/amt-5-1205-2012, 2012. (cited on pages 29, 30, 31).

- Woiwode, W., Sumińska-Ebersoldt, O., Oelhaf, H., Höpfner, M., Belyaev, G. V., Ebersoldt, A., Friedl-Vallon, F., Grooß, J.-U., Gulde, T., Kaufmann, M., Kleinert, A., Krämer, M., Kretschmer, E., Kulesa, T., Maucher, G., Neubert, T., Piesch, C., Preusse, P., Riese, M., Rongen, H., Sartorius, C., Schardt, G., Schönfeld, A., Schuette-meyer, D., Sha, M. K., Stroh, F., Ungermann, J., Volk, C. M., and Orphal, J.: Validation of first chemistry mode retrieval results from the new limb-imaging FTS GLORIA with correlative MIPAS-STR observations, *Atmospheric Measurement Techniques*, 8, 2509–2520. doi:10.5194/amt-8-2509-2015, 2015. (cited on pages 22, 24, 24, 30, 31, 92, 92).
- Woiwode, W., Höpfner, M., Bi, L., Pitts, M. C., Poole, L. R., Oelhaf, H., Molleker, S., Borrmann, S., Klingebiel, M., Belyaev, G., Ebersoldt, A., Griessbach, S., Grooß, J.-U., Gulde, T., Krämer, M., Maucher, G., Piesch, C., Rolf, C., Sartorius, C., Spang, R., and Orphal, J.: Spectroscopic evidence of large aspherical beta-NAT particles involved in denitrification in the December 2011 Arctic stratosphere, *Atmospheric Chemistry and Physics*, 16, 9505–9532. doi:10.5194/acp-16-9505-2016, 2016. (cited on page 13).
- Woiwode, W., Dörnbrack, A., Bramberger, M., Friedl-Vallon, F., Haenel, F., Höpfner, M., Johansson, S., Kretschmer, E., Krisch, I., Latzko, T., Oelhaf, H., Orphal, J., Preusse, P., Sinnhuber, B.-M., and Ungermann, J.: Mesoscale fine structure of a tropopause fold over mountains, *Atmospheric Chemistry and Physics*, 18, 15643–15667. doi:10.5194/acp-18-15643-2018, 2018. (cited on pages 6, 24, 66, 71).
- Wolff, M. A., Kerzenmacher, T., Strong, K., Walker, K. A., Toohy, M., Dupuy, E., Bernath, P. F., Boone, C. D., Brohede, S., Catoire, V., von Clarmann, T., Coffey, M., Daffer, W. H., Mazière, M. D., Duchatelet, P., Glatthor, N., Griffith, D. W. T., Hannigan, J., Hase, F., Höpfner, M., Huret, N., Jones, N., Jucks, K., Kagawa, A., Kasai, Y., Kramer, I., Küllmann, H., Kuttippurath, J., Mahieu, E., Manney, G., McElroy, C. T., McLinden, C., Mébarki, Y., Mikuteit, S., Murtagh, D., Piccolo, C., Raspollini, P., Ridolfi, M., Ruhnke, R., Santee, M., Senten, C., Smale, D., Tétard, C., Urban, J., and Wood, S.: Validation of HNO₃, ClONO₂, and N₂O₅ from the Atmospheric Chemistry Experiment Fourier Transform Spectrometer (ACE-FTS), *Atmospheric Chemistry and Physics*, 8, 3529–3562. doi:10.5194/acp-8-3529-2008, 2008. (cited on page 18).
- Xia, Y., Huang, Y., and Hu, Y.: On the Climate Impacts of Upper Tropospheric and Lower Stratospheric Ozone, *Journal of Geophysical Research: Atmospheres*. doi:10.1002/2017JD027398, 2017. (cited on pages 1, 17).
- Zahn, A., Weppner, J., Widmann, H., Schlote-Holubek, K., Burger, B., Kühner, T., and Franke, H.: A fast and precise chemiluminescence ozone detector for eddy flux and airborne application, *Atmospheric Measurement Techniques*, 5, 363–375. doi:10.5194/amt-5-363-2012, 2012. (cited on page 37).
- Zander, R., Rinsland, C. P., Farmer, C. B., Brown, L. R., and Norton, R. H.: Observation of several chlorine nitrate (ClONO₂) bands in stratospheric infrared spectra, *Geo-*

- physical Research Letters, 13, 757–760. doi:10.1029/GL013i008p00757, 1986. (cited on page 18).
- Zöger, M., Afchine, A., Eicke, N., Gerhards, M., Klein, E., McKenna, D. S., Mörschel, U., Schmidt, U., Tan, V., Tuitjer, F., Woyke, T., and Schiller, C.: Fast in situ stratospheric hygrometers: A new family of balloon-borne and airborne Lyman alpha photofragment fluorescence hygrometers, *Journal of Geophysical Research: Atmospheres*, 104, 1807–1816. doi:10.1029/1998JD100025, 1999. (cited on page 37).
- Zhu, Y., Toon, O. B., Kinnison, D., Harvey, V. L., Mills, M. J., Bardeen, C. G., Pitts, M., Bègue, N., Renard, J., Berthet, G., and Jégou, F.: Stratospheric aerosols, polar stratospheric clouds and polar ozone depletion after the Mt. Calbuco eruption in 2015, *Journal of Geophysical Research: Atmospheres*. doi:10.1029/2018JD028974, 2018. (cited on page 14).

Acknowledgments

During the past four years, many people contributed to the success of this work, and I would like to express my gratitude. First of all, I thank Michael Höpfner for his guidance and supervision. He introduced me to limb sounding and atmospheric science and fostered my scientific career. I was very happy that I had the chance to present my work at so many conferences and that the publication in scientific journals was that much supported. In addition, I thank Johannes Orphal for his valuable counsel and for serving as examiner.

The FFB group at KIT/IMK-ASF does not only consist of outstanding engineers and scientists, they also are adorable colleagues. During workaday life, campaigns or conferences I learned a lot from them and I also enjoyed social events in our group. In particular, I would like to thank Anne Kleinert for her remarkable efforts in proofreading this manuscript, Felix Friedl-Vallon as group leader, Gerald Wetzel, Erik Kretschmer and Wolfgang Woiwode for proofreading, valuable discussions and providing figures for this manuscript. From the Forschungszentrum Jülich part of the GLORIA team, I received not only high quality measurements, they also carefully explained instrumental and calibration aspects of GLORIA, and the scientific objectives of the GLORIA “dynamics mode”. In particular, I would like to thank Jörn Ungermann, Peter Preusse, Axel Schönfeld and Isabell Krisch. I also thank my colleagues from the SAT group for very good collaboration and for excellent company during the lunch breaks. In particular, I thank Thomas von Clarmann for inviting me to join the “Chlorine nitrate” paper, Gabriele Stiller as group leader, Norbert Glatthor for many discussions on GLORIA retrievals, and Udo Grabowski and Johannes Plieninger for their excellent administration of the IMK-ASF Unix cluster. Thanks a lot to all other (former) doctoral researchers at our institute, namely Jennifer Schröter, Florian Haenel, Marleen Braun, Annika Günther, Qiansi Tu, Garlich Fischbeck, Matthias Frey, Darko Dubravica, Ugur Cayoglu, Thomas Latzko, Sebastian Kazarski, Amirmahdi Zarboo, Christopher Diekmann, Michael Weimer, Matthäus Kiel and all I forgot to mention for their encouragement and social activities. I also thank Sandra Leist, Derya Cayiroglu and Regina Hühn for their guidance in many administrative issues in the KIT universe.

During my thesis project, I stayed three months at the Jet Propulsion Laboratory. Michelle L. Santee and the MLS team gave me a warm welcome to California and I learned how to use satellite data. After that time, she co-authored my two publications and besides insights into the English language, I learned a lot about polar chlorine chemistry.

Jens-Uwe Grooß and Ines Tritscher provided data from CLaMS simulations, Farahnaz Khosrawi and Oliver Kirner provided data from the EMAC model. Besides their precious simulation results, they contributed with very valuable discussions and comments on the model simulation results. Especially, I would like to express my gratitude to Jens-Uwe Grooß for many illuminating telephone conversations and tailored model simulations and data output for this work.

I gratefully thank Hermann Oelhaf, Björn-Martin Sinnhuber, Wolfgang Woiwode, the PGS coordination team and DLR-FX for successfully conducting the field campaign. The GLORIA results are based on the efforts of all members of the team, including the technology institutes ZEA-1 and ZEA-2 at FJZ and IPE at KIT. I thank ECMWF, NASA, the AIMS, BAHAMAS, FAIRO, FISH, GhOST-MS, and AWI teams for providing their high quality data.

For my PhD position, I received funding from the European Community's Seventh Framework Programme (FP7/2007-2013) under grant agreement 603557. I also gratefully thank the Graduate School for Climate and Environment (GRACE), KIT for funding my visit to NASA JPL to discuss the comparisons with the Aura/MLS measurements

In addition, I would like to thank my friends Inge Böhm for being a pleasant flatmate and for proofreading this manuscript, and Deeya Loram, Rory McKenna, and Juancarlos Chan for making my stay in California such a delightful time. I also appreciate very helpful discussions concerning English language with Kimberly Junmookda and Rory McKenna.

Finally, I would like to thank my parents Katharina and Thoralf, my sisters Annika and Birte, and my wife Ronja for their loving support and encouragement throughout the time of this thesis.